The Reactivity of Strained Carbocycles

Alistair J Sterling
University College

University of Oxford
A thesis presented for the degree of
Doctor of Philosophy

Trinity 2021

Abstract

The idea that increasing a reaction driving force will increase its rate is a central principle of chemistry. This principle has been used to great effect for the design of 'strain-release' reactions, in which a driving force is provided by building strain energy into the reactant. However, strain release alone is unable to account for the contrasting reactivity of even the simplest of systems, such as cyclopropane and cyclobutane which release near-identical amounts of strain energies but display stark differences in their rates of ring-opening. In this Thesis, the dominance of strain release is challenged by introducing the concept of electronic delocalisation to enhance reactivity: a more delocalised bond will be easier to break, and therefore incur a lower activation barrier to its cleavage resulting in a faster reaction rate. This idea is first explored through a computational study of the electronic structure and reactivity of [1.1.1]propellane (Chapter 2), before the importance of delocalisation is explored in the development of a new synthesis of α-chiral bicyclo[1.1.1]pentanes – important motifs in drug discovery (Chapter 3). The relationship between reaction rate, strain release and delocalisation is then quantified through the development of a predictive model for the reactivity of small rings in general (Chapter 4), where three-membered rings are found to be unique in their ability to cause delocalisation-enabled reactivity. In summary, this Thesis introduces a framework to better understand the relationship between ring strain and reactivity, and in doing so guide synthetic efforts towards new reaction design.

Declaration

I, Alistair Sterling, declare that the Thesis I am submitting is entirely my own work except where indicated in the text, caption, footnote or bibliography. This Thesis has not been submitted in whole or in part for any other academic degree or professional qualification.

8th November 2021

Signature *Date*

Acknowledgements

I owe a huge amount to Profs. Fernanda Duarte and Ed Anderson for their support and guidance throughout my time working towards this degree. Fernanda took me on as a total synthesis chemist with almost no experience in computational chemistry, for which I am grateful. This was a steep learning curve, and I appreciate the time she took and the encouragement she gave me to expand my knowledge and grow as a scientist. Ed probably didn't envisage the path that I ended up taking, but has been nothing but enthusiastic and accommodating from the very start. I feel fortunate to have had the chance to work with a synthetic chemist who has such a passion for understanding the basic principles of organic chemistry.

I would also like to thank Przemek and Alex, my early computational mentors who helped me submit my first jobs, and showed me the power of simulations to understand chemical reactions.

I have learned a great deal from the inaugural members of the Oxford Duarte group – Tom and Matina – as well as our honorary member Harry. Testing ridiculous ideas out on each other was a formative period for me, and has shaped my perspectives on chemistry. I have severely missed our conversations during the pandemic. I have also been lucky to have had the opportunity to work alongside a great many members of the Duarte group, both past and present – Kate, Tomasz, Tanya, Tristan, Said, Henry, Ally, Ema, Chloe, Bernie and Jon, to name just a few. I've also had the fortune of supervising a selection of very talented students, Nils, Miguel, Ben, Jacky and Damyan.

The Anderson group has also provided me with many years of support and friendship, in particular our team of BCP (and other small rings) chemists – Beth, Helena, Jeremy, Marie, Nils, Ryan, Felix, Dimitri and Carlos. A special mention

must also go to Eddie, Christian and Halli for introducing me to synthesis, and I’m grateful to my friends from other research groups and disciplines who have made my time in Oxford so special – Tom, Abdul, Xinlan, Lorel and Keith, to name a few.

Thank you to Kate, Tom and Nils for generously proofreading this Thesis.

I would especially like to thank my parents, Phil and Carol, and my sister, Hannah. To have grown up in such an inquisitive and nurturing family cannot be taken for granted, and this degree is as much theirs as it is mine.

Finally, to my wife Kayleigh. Your unwavering belief in me has helped me more than you could ever know.

Data availability

The data presented in this Thesis, including calculated energies, Cartesian coordinates and Python scripts used for data processing, has been submitted as Supplementary Material. The contents of the Supplementary Material are listed in Appendix A. This data is publicly-available on the Oxford University Research Archive (ORA) at https://doi.org/10.5287/bodleian:n6kdENEK5.

Publications

This Thesis is based upon the following publications:

1. Sterling, A.J., Dürr, A.B., Smith, R.C., Anderson, E.A.* and Duarte, F.*, Rationalizing the diverse reactivity of [1.1.1]propellane through σ–π-delocalization, *Chem. Sci.* **2020**, *11*, 4895–4903.

   Contribution: Conceptualisation, data generation and analysis, drafting, visualisation.

2. Wong, M.L.J, Sterling, A.J., Mousseau, J.J., Duarte, F.* and Anderson, E.A.*, Direct Catalytic Asymmetric Synthesis of α-Chiral Bicyclo[1.1.1]-pentanes, *Nat. Commun.* **2021**, *12*, 1644.

   Contribution: Conceptualisation, computational data generation and analysis, experimental mechanistic studies, drafting, visualisation.

Contributing-author articles published or submitted for publication during the course of this degree that do not form part of this Thesis are as follows:

3. Gouverneur, V.*, Szpera, R., Moseley, D.F.J.[†], Smith, L.B.[†], Sterling, A.J.[†], The Fluorination of C–H Bonds: Developments and Perspectives, *Angew. Chem. Int. Ed.*, **2019**, *58*, 14824-14848.

4. Nugent, J.[†], Arroniz, C.[†], Shire, B.R., Sterling, A.J., Pickford, H.D., Wong, M.L.J., Mansfield, S.J., Caputo, D.F.J., Owen, B., Mousseau, J.J., Duarte, F.* and Anderson, E.A.*, A General Route to Bicyclo[1.1.1]pentanes through Photoredox Catalysis *ACS Catal.* **2019**, *9*, 9568-9574.

5. Eland, J.H.D., Squibb, R.J., Sterling, A.J., Wallner, M., Hult Roos, A., Andersson, J., Axelsson, V., Johansson, E., Teichter, A., Stranges, S., Brunetti, B., Dyke, J.M., Duarte, F., Feifel, R.*, Double and triple ionization of isocyanic acid, *Sci. Rep.* **2020**, *10*, 2288.

[†] Equal author contribution

6. Bickerton, L.E., Sterling, A.J., Beer, P.D., Duarte, F.D.* and Langton, M.J.*, Transmembrane anion transport mediated by halogen bonding and hydrogen bonding triazole anionophores, *Chem. Sci.* **2020**, *11*, 4722–4729.

7. Costil, R., Sterling, A.J., Duarte, F. and Clayden, J.*, Atropisomerism in diarylamines: structural requirements and mechanisms of conformational interconversion, *Angew. Chem. Int. Ed.* **2020**, *59*, 18670–18678.

8. Scriven, L.M.†, Kaiser, K.†, Schulz, F., Sterling, A.J., Woltering, S.L., Gawel, P., Christensen, K., Anderson, H.L.* and Gross, L.*, Synthesis of cyclo[18]-carbon *via* debromination of $C_{18}Br_6$, *J. Am. Chem. Soc.* **2020**, *142*, 12921–12924.

9. Young, T.A., Silcock, J., Sterling, A.J. and Duarte, F.*, autodE: Automated Calculation of Reaction Energy Profiles – Application to Organic and Organometallic Reactions, *Angew. Chem. Int. Ed.* **2021**, *60*, 4266–4274.

10. Sterling, A.J.†, Zavitsanou, S.†, Ford, J. and Duarte, F.*, Selectivity in Organocatalysis – From Qualitative to Quantitative Predictive Models, *WIREs Comput. Mol. Sci.* **2021**, *11*, e1518.

11. Yu, P.*, Sterling, A.J.* and Hein, J.*, A Novel Automated Screening Method for Combinatorially Generated Small Molecules, *J. Chem. Inf. Model.* **2021**, *61*, 1637–1646.

12. Bickerton, L.E.†, Docker, A.†, Sterling, A.J., Kuhn, H., Duarte, F.*, Beer, P.D.* and Langton, M.J.*, Highly Active Halogen Bonding and Chalcogen Bonding Chloride Transporters with Non-Protonophoric Activity, *Chem. Eur. J* **2021**, *27*, 11738–11745.

13. Livesly, S., Sterling, A.J., Robertson, C.C., Goundry, W., Morris, J.A., Duarte, F.* and Aissa, C.*, Activation of [1.1.1]Propellane by Halogen Bond for the Synthesis of Nitrogen-substituted bicyclo[1.1.1]pentanes, *Angew. Chem. Int. Ed.* **2021**, https://doi.org/10.1002/anie.202111291.

14. Rojas, J.J.[†], Croft, R.A.[†], Sterling, A.J., Briggs, E.L., Antermite, D., Schmitt, D.C., Blagojevic, L., Haycock, P., White, A.J.P., Duarte, F., Choi, C., Mousseau, J.J. and Bull, J.A.*, Amino-Oxetanes as Amide Isosteres by an Alternative Click Reaction of Sulfonyl Fluorides, *Nat. Chem.* **2021**, *accepted.*
15. Nugent, J., Sterling, A. J., Frank, N., Mousseau, J. J. and Anderson, E. A., Synthesis of α-quaternary bicyclo[1.1.1]pentanes through synergistic organophotoredox and hydrogen atom transfer catalysis, *submitted.*
16. Ideböhn, V., Sterling, A.J., Wallner, M., Olsson, E., Squibb, R., Miniotaite, U., Forsmalm, E., Forsmalm, M., Stranges, S., Dyke, J.M., Duarte, F., Eland, J.H.D. and Feifel, R.*, Single photon double and triple ionisation of allene, *submitted.*

The following manuscripts were in preparation at the time of completion of this degree:

a. Sterling, A.J., Anderson, E.A.* and Duarte, F.*, Strain *vs* delocalisation: A general model to rationalise the reactivity of small rings.

b. Nugent, J., Sterling, A.J., Tay, M.Y., Mousseau, J.J., Duarte, F.* and Anderson, E.A.*, α-Amino Bicyclopentylation Using Organo-Photoredox Catalysis.

c. Smith, L.B., Armstrong, R.J., Hou, J., Sze, M., Sterling, A.J., Smith, A., Duarte, F.* and Donohoe, T.J.*, Regio, Stereo- and Chemoselective Synthesis of Multisubstituted Cyclohexenes via an Aluminium Mediated 1,5-Hydride Shift.

Table of Contents

List of Abbreviations

1-RDM	One-electron reduced density matrix
Å	Ångstrom
a.u.	Atomic units
ATRA	Atom transfer radical addition
BCP	Bicyclo[1.1.1]pentane
BDE	Bond dissociation energy
BEP	Bell-Evans-Polanyi
Boc	*tert*-Butyloxycarbonyl
bpy	2,2'-Bipyridyl
BTMG	2-*tert*-Butyl-1,1,3,3-tetramethylguanidine
Bu	Butyl
C	Celcius
CASSCF	Complete active space self consistent field
cat.	Catalyst
Cbz	Benzoyloxycarbonyl
CC	Coupled cluster
CI	Configuration interaction
cod	Cyclooctadiene
COSX	Chain-of-spheres exchange
CPCM	Conductor-like Polarizable Continuum Model
CSF	Configuration state function
DFT	Density functional theory
DIA	Distortion / interaction analysis
DLPNO	Domain based local pair natural orbital
dm	Decimeter
DME	1,2-Dimethoxyethane

dr	Diastereomeric ratio
dtbbpy	4,4’-Di-*tert*-butyl-2,2’-bipyridyl
E	Energy
e	Electron
E^+	Electrophile
ECP	Effective core potential
EDDP	Electron density difference plot
ee	Enantiomeric excess
ELF	Electron localisation function
Et	Ethyl
eV	Electron volt
EWG	Electron withdrawing group
FCI	Full configuration interaction
FMO	Frontier molecular orbital
g	Gram
GGA	Generalised gradient approximation
GPED	Gas-phase electron diffraction
H	Enthalpy
h	Planck’s constant
h	Hours
Ha	Hartree
HAT	H-atom transfer
HF	Hartree Fock
HOMO	Highest occupied molecular orbital
I	Intensity
IEPA	Independent electron pair approximation
k	Rate constant

K	Equilibrium constant
K	Kelvin
kcal mol^{-1}	Kilocalories per mole
KS-DFT	Kohn Sham density functional theory
LED	Light emitting diode
LFER	Linear free energy relationship
LP	Lone pair
LR	Linear regression
LSDA	Local spin density approximation
LUMO	Lowest unoccupied molecular orbital
M	mol dm^{-3}
ma	Minimally augmented
MAE	Mean absolute error
Me	Methyl
ME	Maximum error
MLR	Multiple linear regression
MO	Molecular orbital
Moc	Methoxycarbonyl
mol	Mole
MOM	Methoxymethyl
MP2	Second-order Møller-Plesset perturbation theory
MRCI	Multireference configuration interaction
MTBE	Methyl *tert*-Butyl ether
MUE	Mean unsigned error
ν	Frequency
n_3	Number of three-membered rings
NBO	Natural bond orbital

NCI	Non-covalent interaction
NHO	Natural hybrid orbital
NICS	Nucleus independent chemical shift
NMR	Nuclear magnetic resonance
NO	Natural orbital
N_{occ}	Natural bond orbital occupancy
NOON	Natural orbital occupation number
OITB	Orbital interactions through-bonds
PAO	Projected atomic orbital
Pc	Phthalocyanine
PES	Potential energy surface
Ph	Phenyl
pin	Pinacolato
PNO	Pair natural orbital
ppy	2-Phenylpyridyl
Pr	Propyl
PT2	Second-order perturbation theory
q	Charge
Q	Quencher
QM	Quantum mechanics
R	Alkyl
ρ	Electron density
R	Gas constant
RHF	Restricted Hartree Fock
RI	Resolution of the identity
RMSE	Root-mean-squared error
RRHO	Rigid rotor-harmonic oscillator

s	Reduced density gradient
SCF	Self consistent field
SET	Single electron transfer
SIE	Self interaction error
SMD	Solvent Model based on Density
SRE	Strain release energy
T	Temperature
T	Kinetic energy
TMS	Trimethylsilyl
TS	Transition state
TTMSS	Tris(trimethylsilyl)silane
UHF	Unrestricted Hartree Fock
V	Volt
V	Potential energy
VB	Valence bond
VIP	Vertical ionisation potential
WFT	Wavefunction theory
E_{xc}	Exchange-correlation functional
ZPVE	Zero-point vibrational energy

1 |

Introduction

1.1 Strain in organic chemistry

Strain is seemingly both an intuitive and an elusive concept. First described by Baeyer in 1885 in a footnote on the compressed bond angles in cyclopropane compared with methane (Figure 1.1a),[1] strain connects the reality of a given chemical structure to its (often) unattainable ideal: an 'unstrained' reference. Deviation from this ideal, however it may be defined, causes *thermodynamic* instability. In other words, a strained compound has the potential to release more energy upon its deconstruction, for example through combustion or reaction, than its unstrained reference. The formal connection between such a strain-releasing process and *kinetic* instability was first made in 1946 in Brown's landmark paper, "*A New Steric Effect in Organic Chemistry*".[2] It was proposed that steric clashes between tetrahedral carbon substituents ('B-strain', or back strain) would provide a "potent driving force" for processes which would relieve this B-strain (Figure 1.1b),[3] leading to the strain release hypothesis: destabilisation of reactants through strain energy enhancement increases the rate of any process which releases this strain. For example, Brown proposed that the tendency of tertiary alcohols to ionise could be explained using the combination of opposing trends in B-strain and inductive cation stabilisation, as could the increasing rate of alkyl halide hydrolysis with increasing numbers of substituents on the carbon atom.[4]

This Thesis explores the strain release hypothesis that connects the thermodynamics of strain energy to the kinetics of strain-release reactivity. To do this,

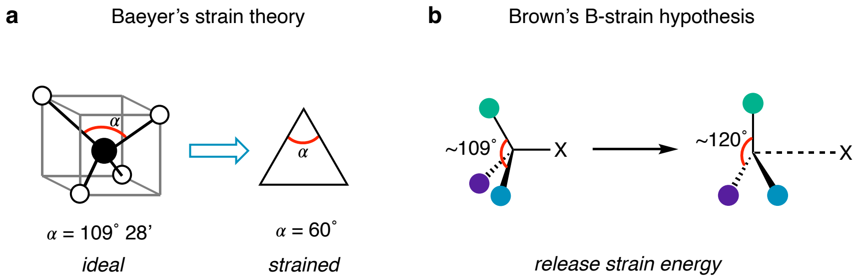

Figure 1.1: **a.** Baeyer's proposal that compression of the bond angles in cyclopropane compared with those in a tetrahedron would cause an increase in strain. **b.** Brown's hypothesis that the steric clash of substituents around a tetrahedral carbon is relieved upon planarisation, increasing the rate of ionisation.

two key concepts will be introduced: Firstly, the concept of *strain energy*, and the experimental and computational methods with which it may be quantified – with a particular focus on strain in small rings, which requires an overview of the electronic structure of these compounds – and secondly, *how strain energy and reactivity can be linked* through the use of linear free energy relationships (LFERs). The motivations for this Thesis are also laid out through a discussion of reactions of small rings, in particular for the development of caged hydrocarbons that have applications in medicinal and materials sciences.

1.1.1 Strain energy: Definitions and quantification

While Brown was developing the idea of B-strain, theoretical chemists were attempting to quantify, and therefore predict, the types and magnitudes of strain that could occur in molecules. As described above, strain energy is the excess energy contained within a molecule relative to an unstrained reference compound, which may be directly compared by, for example, calculating or measuring an energy while maintaining the number of atoms and bonds between the strained compound and the chosen reference compound. Four 'classical' types of strain exist: bond length strain, bond angle strain, torsional strain and steric (non-bonded, van der

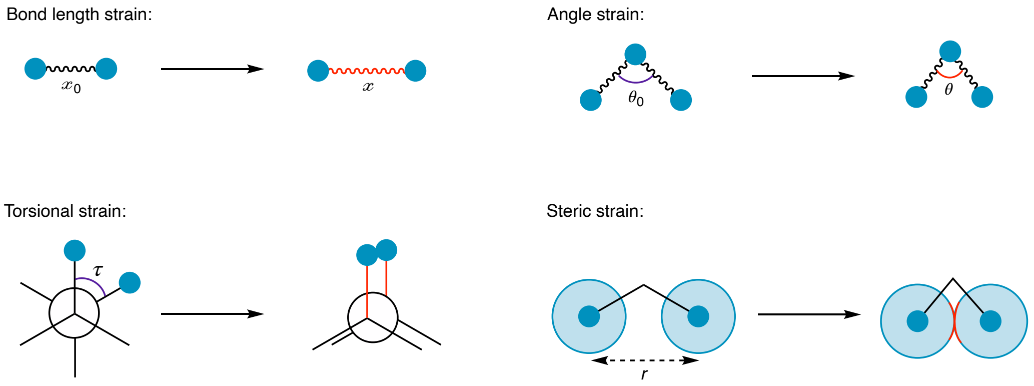

Figure 1.2: The four types of strain commonly encountered in organic molecules.

Waals) strain (Figure 1.2).[5] Bond length strain (ΔE_{bond}) arises through the extension or compression of a given bond length away from its ideal length, and can be approximated by Hooke's law

$$\Delta E_{bond} \propto (x - x_0)^2 \tag{1.1}$$

where x is the distance between the two atoms, and x_0 is the optimum distance between those atoms. Similarly, angle strain (ΔE_{angle}) can be described by the relationship

$$\Delta E_{angle} \propto (\theta - \theta_0)^2 \tag{1.2}$$

where θ is the angle between the three atoms, and θ_0 is the optimum angle between those atoms.

Torsional strain ($\Delta E_{torsion}$) is slightly more complex, since its origin has often been debated as the choice of method to characterise the contributions of steric, electrostatic and stereoelectronic effects can alter the interpretation.[6–10] Whatever its physical origin, torsional strain can be described using a combination of cosines of the torsional angle, τ, using

$$\Delta E_{torsion} = \frac{V_1^{\circ}}{2}(1+\cos\tau) + \frac{V_2^{\circ}}{2}(1+\cos 2\tau) + \frac{V_3^{\circ}}{2}(1+\cos 3\tau) \tag{1.3}$$

where V_1° and V_3°, the one- and threefold barriers, are suggested to correspond to steric repulsion, and V_2°, the twofold barrier, may be linked to stabilising hyperconjugative effects,[11] leading to the familiar preference for staggered and gauche conformers over eclipsed conformations. Lastly, steric strain (ΔE_{steric}) arises from non-covalent attractive (van der Waals forces) and repulsive (Pauli) interactions. ΔE_{steric} can be well-approximated by a Buckingham (1.4) or Lennard-Jones (1.5) potential (where A, B and C are constants, and ϵ is the dispersion energy found at distance $r = 2^{1/6}\sigma$).

$$\Delta E_{steric} = Ae^{-Br} - \frac{C}{r^6} \tag{1.4}$$

$$\Delta E_{steric} = 4\epsilon\left[\left(\frac{\sigma}{r}\right)^{12} - \left(\frac{\sigma}{r}\right)^{6}\right] \tag{1.5}$$

Independently, Hill, and Westheimer and Mayer were the first to recognise that each of these strain energies (bond length, bond angle, torsional, steric) could be combined to give a single quantitative measure of the energy of a structure in relation to the ideal ‘unstrained’ molecule.[12,13] This idea is the foundation of molecular mechanics, which uses each of the strain terms introduced above to estimate the potential energy of the system, playing a central role as one of the first computational tools employed to quantify strain.[14] For an excellent summary of these concepts, see Ref. [5].

Central to the quantification of strain energy through sums of individual strain

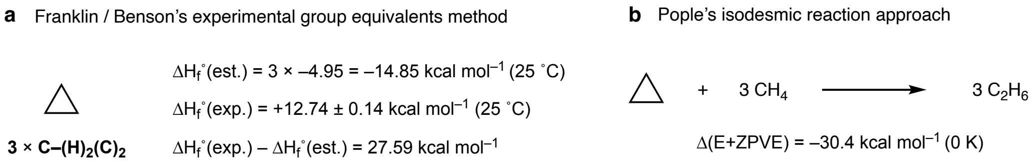

Figure 1.3: a. Estimated and experimental heats of formation of cyclopropane using Benson's values for $\Delta H_\mathrm{f}^\circ(\mathrm{est.})$[17] and Knowlton and Rossini's value for $\Delta H_\mathrm{f}^\circ(\mathrm{exp.})$[18] giving an estimate of the total strain energy. **b.** Isodesmic reaction to estimate the strain energy of cyclopropane, taken as the negative value of the reaction energy (corrected for the zero-point vibrational energy, at the HF/4-31G level).

contributions is the concept of the 'additivity of chemical properties' – *i.e.*, that properties of molecules can be represented by the sum of their individual atoms or groups of atoms. This was first realised in 1940 by Pitzer when he derived a general expression for the heat function $(H^\circ - H_0^\circ)/T$ of any linear hydrocarbon, in which he found dependence only on bond stretches, vibrations, torsions, a steric term, and the number of carbon atoms in the chain.[15] This idea was capitalised upon in 1949 when Franklin proposed a set of 'group equivalents' – molecular fragments (*e.g.*, CH, CH_2) with assigned heats of formation – that could be summed to obtain an estimate of the total heat formation of a molecule.[16] Benson later increased the range of fragments that could be employed, and defined a set of notation that allows the simple application of these group equivalents.[17] Group equivalents then provided a new definition of the unstrained reference needed to obtain a strain energy, where the predicted and measured heats of formation of a compound could be directly compared; the discrepancy between these two values is the strain energy (Figure 1.3a).

A significant limitation of this approach is the requirement of an experimental heat of formation, restricting analysis to compounds stable enough to be both (i) synthesised in significant quantities and (ii) measured. However, with rapid improvements in computational power in the 1960s[19] came the ability to calculate heats of formation and reaction of medium-sized molecules (10s of atoms) from first principles. While the absolute values obtained from these calculations were plagued by large errors ($\sim$10 kcal mol^{-1} using Hartree-Fock theory),[20] the relative heats of formation of similar compounds were found to be significantly more accurate due to error cancellation. Pople was an early proponent of the use of such an approach to compare the energies of similar compounds, introducing the ‘isodesmic reaction’ – a balanced theoretical reaction in which numbers and types of bonds are held constant (Figure 1.3b).[21] The power of the isodesmic reaction is that, by eliminating differences in bond energies, the strain energy can be easily estimated.

An alternative to Pople’s approach to calculate strain energy was introduced by Wiberg[22] and later adapted by Schleyer.[23] This approach employed a set of ‘computational group equivalents’, analogous to Franklin and Benson’s experimentally-obtained group equivalents, first featuring the calculation of electronic energies (with or without corrections for their zero-point vibrational energy and temperature) of reference compounds, from which a set of group equivalents could be extracted. An advantage of this approach over the Franklin and Benson approach is that, provided the same level of theory is used to calculate the group equivalent and the desired structure, significant errors arising from inaccuracies in the electronic structure method may be cancelled. Wiberg’s approach, recently reviewed and updated by Rablen,[24] allows the accurate prediction of the strain energy of any compound, whether or not it has been synthesised.

Perhaps surprisingly, all measures agree that the strain energies of cyclopropane and cyclobutane are rather similar (respectively 27.9 and 26.8 kcal mol^{-1}, according to recent theoretical estimates,[24] and 27.6 and 26.4 kcal mol^{-1} from experimental heats of formation[25]). The cause of this similarity, in the face of Baeyer’s angle strain argument, has resulted in much theoretical debate. One plausible explanation is that cyclobutane incurs 1,3-diaxial steric clashes (Figure 1.4a), which

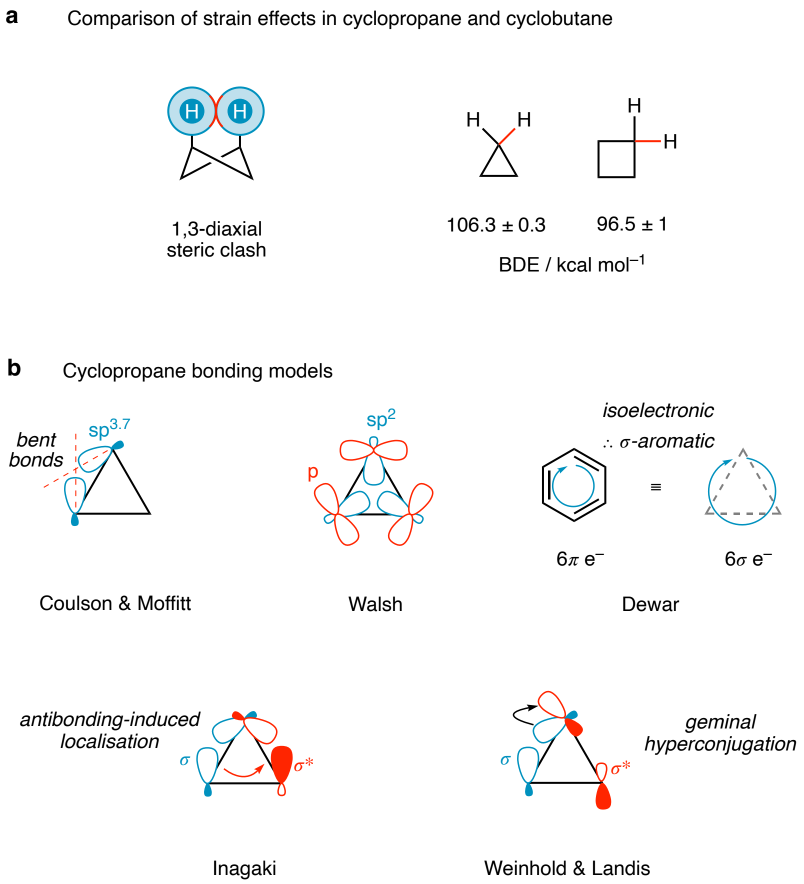

Figure 1.4: **a.** Transannular non-bonded repulsion, or rehybridisation-induced C–H bond strengthening, could explain the similar strain energies of cyclopropane and cyclobutane. Bond dissociation energies (BDEs) taken from Ref. [30]. **b.** Various bonding models for cyclopropane proposed over the past 75 years.

increases the non-bonded strain energy (the Dunitz-Schomaker hypothesis)[26] – although this puckering reduces torsional strain from eclipsing C–H bonds which is unavoidable in cyclopropane. Another argument is that the C–H bonds in cyclopropane are stronger than those in cyclobutane due to rehybridisation,[27] partially offsetting the increase in angle strain.[28] A third explanation is that cyclopropane is σ-aromatic[29] – an idea that will be discussed further below.

The argument of rehybridisation is corroborated by Coulson and Moffitt's 1947 study on the electronic structure of cyclopropane.[27,31] By assuming perfect pairing of electrons in each bond, they variationally optimised orbital hybridisation parameters to arrive at the conclusion that the C–C bonds were formed from $sp^{3.7}$ hybrids, and C–H bonds formed from C $sp^{2.3}$ hybrids.[27] The lobes of the C $sp^{3.7}$ hybrids do not lie along the shortest line connecting pairs of C atoms, but are deflected outwards, giving rise to 'bent' bonds (Figure 1.4b). Coulson and Moffitt concluded that this bent bonding describes electronic delocalisation – a property that could explain the ability of cyclopropane to conjugate with neighbouring π systems,[32] as well as the low dipole moment of cyclopropyl chloride compared with cyclopentyl chloride,[33] and the electrophilic character of the cyclopropane ring.[34]

Also in 1947, Walsh proposed an electronic structure for cyclopropane in which three sp^2 hybrids point towards the centre of mass of the ring like the spokes of a wheel, and the remaining p orbitals are perpendicular to these sp^2 orbitals (Figure 1.4b).[34,35] This leaves two sp^2 orbitals to bond with the two H atoms per methylene, explaining the slightly shorter and stronger C–H bonds observed experimentally than those in methane.[28,36,37] However, Coulson and Moffitt argued that Walsh's molecular orbital (MO)-type description was less intuitive than their own, concluding that the "considerable degree of delocalization in the cyclopropane bond system ... accounts for the chemical and spectroscopic conjugating effects rather more clearly than does Walsh's qualitative argument."[27]

While the cyclopropane models of Coulson, Moffitt and Walsh are widely taught in undergraduate Chemistry courses, some other more recent explanations for the properties of cyclopropane in terms of its electronic structure are also worth discussing. In 1980 Dewar put forward a radically new proposal: that cyclopropane was aromatic and isoconjugate with benzene (Figure 1.4b),[29] and that cyclobutane was isoconjugate with cycloocatetraene. He stated that "each carbon in the paraffin [cyclopropane or cyclobutane] plays the same role as a (=CH−CH=) unit in the polyene [benzene or cyclooctatetraene]", and that these paraffins are "hence liable to exhibit σ-aromaticity or σ-antiaromaticity". In other words, while cyclopropane and benzene can delocalise six electrons in a closed cycle and adhere to Hückel's '$4n + 2$' rule, cyclobutane and cyclooctatetraene instead contain eight electrons in a closed cycle and therefore obey the $4n$ rule. As well as explaining the unexpectedly low strain energy for cyclopropane in comparison with cyclobutane, Dewar pointed out, in the same manner as Coulson and Moffitt before him, that this cyclic delocalisation was consistent with the chemical properties of cyclopropane. However, Dewar appeared to hold Walsh's cyclopropane model in higher regard than Coulson and Moffitt's, remarking that the bond-shortening effect in cyclopropane was "not a mere "banana bond" effect", and that in order to understand the properties of cyclopropane, "one has to use a MO ("Walsh orbitals") description." The existence of σ-aromaticity in cyclopropane is still debated;[38,39] while its upfield ^{1}H chemical shifts and unexpectedly high diamagnetic susceptibility could be linked to aromaticity,[40,41] other explanations, such as a diamagnetism induced by the unique arrangement of C–H bonds,[42] have also been put forward that do not require aromaticity to be invoked.

In 1991, Inagaki countered previous suggestions the electron density is more delocalised in cyclopropane than cyclobutane.[43,44] He suggested that geminal delocalisation, in which each C–C σ bond may donate its electron pair into an adjacent C–C σ^* orbital, was in fact far smaller for cyclopropane than cyclobutane (Figure 1.4b). This result was used to explain the shorter C–C bond length in the former, and a smaller angle strain term than cyclobutane. Inagaki's interpretation, that geminal delocalisation causes molecular destabilisation, led to the conclusion that the "six electrons of the C–C σ-bonds in [cyclopropane] and the C=C π-bonds in [benzene] behave in an opposite manner" – in direct conflict with Dewar's explanation.

A similar approach to Inagaki's was taken by Weinhold and Landis in 2005,[45] where they employed their natural bond orbital (NBO) method to investigate geminal delocalisation in small rings. However, their results point strongly to the enhancement of stabilising hyperconjugative interactions in cyclopropane relative to cyclobutane. For example, using second order perturbation theory, they found that each geminal $\sigma_{\mathrm{C1–C2}} \rightarrow \sigma^{*}_{\mathrm{C2–C3}}$ interaction is worth 5.5 kcal mol^{-1} in cyclopropane (Figure 1.4b), leading to a total energy-lowering effect of 33 kcal mol^{-1}. The equivalent interaction in the equilibrium geometry of *n*-propane is worth only 0.5 kcal mol^{-1}, a value that rises to 6.6 kcal mol^{-1} when the formal C–C–C angle is compressed to 60°. This latter result illustrates the importance of angle compression in cyclopropane to enable this hyperconjugative delocalisation effect.

Each of these analyses strongly supports the idea that the electronic structures of cyclopropane and cyclobutane are different – most concluding that the former has a more delocalised density. This difference in electronic structure, and therefore bonding, has been suggested as one reason the strain energies of cyclopropane and cyclobutane are so similar. In the next section, we will introduce methods to quantitatively link strain energy and reactivity, setting the stage to ask the question of why ring-opening reactions of cyclopropane are so much faster than for cyclobutane.

1.1.2 Connecting strain release energy to reactivity

To connect strain and reactivity is to find a quantitative link between the thermodynamics and kinetics of a given process. This connection was made by Brønsted in 1924, who identified an empirical relationship between the strength of an acid and its catalytic effect on the rate of decomposition of nitramide into water and nitrous oxide (Figure 1.5a).[46] Bell was the first to propose a theoretical foundation for this relationship between the acidity / basicity of a catalyst, stating that "for acid catalysis a stronger acid means a less firmly bound proton and hence a greater ease of transfer."[47] He derived a model consistent with the experimental finding that a small change in the nature of the acid should have a linear effect on the activation energy for the proton transfer step. Evans and Polanyi[48] generalised these results by deriving the expected relationship between the activation energy and driving force for three-centre (A + B–C $\rightleftharpoons$ A–B + C) reactions, resulting in what is now often described as the Bell-Evans-Polanyi principle

$$\Delta E^{\ddagger} = -\alpha \Delta H \qquad 0 \leq \alpha \leq 1 \tag{1.6}$$

where $\Delta E^{\ddagger}$ is the difference in activation barrier between two similar reactions, and ΔH is the difference in reaction enthalpy for the two reactions. This equation provided the first quantitative expression for how an increase in reaction enthalpy through an increase in strain release might cause a decrease in activation barrier.

Further advances in the quest for such a relationship came from a different direction. In 1956, Marcus published a paper on the prediction of the rates of electron transfer in which there is minimal overlap of the donor and acceptor orbitals.[49] His equation linked the thermodynamic driving force of an elementary step and rate constants for electron self-exchange reactions to the rate of outer-sphere electron transfer between different species. However, he explicitly stated that his theory was "not applicable to any electron transfer reaction having a large-overlap activated complex."[49] While this might rule out any chance of applying this equation to chemical reactions, in 1966 Sutin found that Marcus' equation could accurately predict reaction rates for both outer sphere and inner sphere electron transfer processes.[50,51] Marcus addressed this new finding two years later, showing that a version of his theory could indeed be used to predict activation energies for chemical reactions involving significant orbital overlap.[52] This equation can be

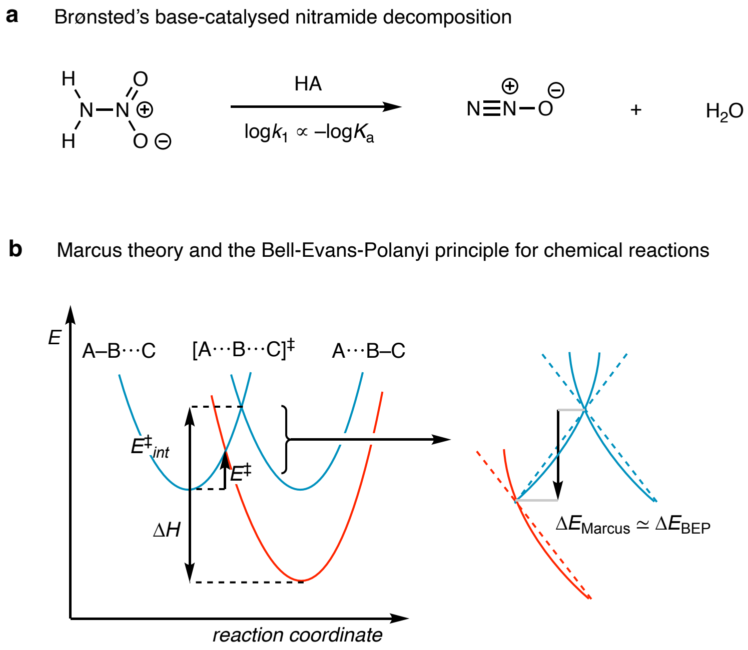

Figure 1.5: a. The acidity of a weak acid is anticorrelated with the rate of nitramide decomposition. **b.** Marcus theory describes the relationship between driving force and activation barrier using diabatic electronic states. For a small change in the driving force, the Bell-Evans-Polanyi principle follows the same behaviour as Marcus theory.

expressed as

$$\begin{aligned} \Delta E^{\ddagger} &= -\frac{1}{2}\Delta H + \frac{(\Delta H)^2}{16E^{\ddagger}_{\mathit{int}}} \\ \Delta E^{\ddagger} &= E^{\ddagger} - E^{\ddagger}_{\mathit{int}} \end{aligned} \tag{1.7}$$

where $E^{\ddagger}_{\mathit{int}}$ is the intrinsic activation barrier for the reaction in the absence of a thermodynamic driving force (*i.e.*, $\Delta H = 0$). Comparing equations (1.6) and (1.7), we see that the Bell-Evans-Polanyi equation is a truncation of Marcus' equation for chemical reactions. This corresponds to a change in the description of the A–B and B–C bond stretching curves from straight lines (Bell-Evans-Polanyi) to parabolas (Marcus) (Figure 1.5b). For similar reactions with a small span in ΔH

values, both models should therefore predict equivalent relationships between the reaction driving force and the activation barrier.

Application of these LFERs to link strain energy and activation barriers came almost 30 years later, when Hoz and co-workers first challenged the idea that the enhanced strain of a molecule was the cause of greater reactivity.[53,54] Their initial studies compared the activation barriers of reactions with strained and unstrained substrates, using a version of the Bell-Evans-Polanyi equation in which the percentage of strain release achieved at the TS is given by

$$\%\text{ Strain released at TS} = \frac{E^{\ddagger}_{\textit{unstrained}} - E^{\ddagger}_{\textit{strained}}}{\Delta E_{0,\textit{unstrained}} - \Delta E_{0,\textit{strained}}} \times 100\%. \tag{1.8}$$

For the addition of hydroxide to either the central or side bonds of bicyclo[1.1.0]-butane (Figure 1.6a), the reaction energies were found to be similar (–38.3 and –34.0 kcal mol^{-1}, respectively), yet the activation energies differ by more than 25 kcal mol^{-1} (4.4 and 30.6 kcal mol^{-1}, respectively). Hammond's postulate would indicate that the side-bond TS is more product-like than the central-bond TS,[55] and should therefore experience greater stabilisation from a release of strain. However, using the metric defined by (1.8), the strain energy relieved at the TS for cleavage of the central bond is 97%, compared with 32% for cleavage of the side bond. To explain this apparent contradiction, Hoz and co-workers suggested that geometric distortion forces a change in hybridisation of the central bond, resulting in a lower energy LUMO and earlier bond formation with the approaching nucleophile.

Around the same time, Houk and co-workers investigated the rates of [2 + 2 + 2] retro-cycloadditions of cyclohexanes (Figure 1.6b).[56,57] Employing a Bell-Evans-Polanyi-type correlation, they deduced that cyclopropane-substituted cyclohex-

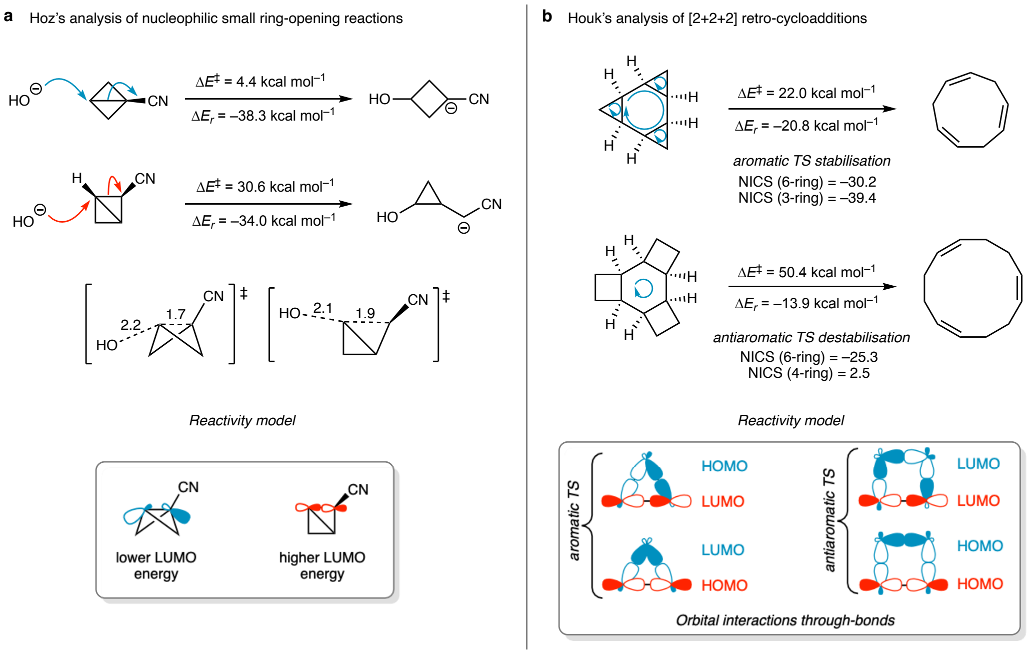

Figure 1.6: a. The enhanced reactivity of the central bond of bicyclo[1.1.0]butane with hydroxide can be explained in terms of the relative LUMO energies of the central and side bonds. Distances shown in Å. **b.** TS aromaticity results in lower activation barriers for [2 + 2 + 2] retro-cycloadditions of cyclopropane-substituted cyclohexanes relative to their cyclobutane-substituted counterparts. Verhoeven's 'orbital interactions through-bonds' (OITB) model provides an explanation for the origin of TS (anti)aromaticity.

anes enjoy activation energies up to 16 kcal mol^{-1} lower than expected, while cyclobutane-substituted systems have increased activation barriers. As these results could not be explained using classical strain-release arguments, the group turned to calculations of nucleus independent chemical shifts (NICS). Aromaticity at the TS was found for systems substituted with cyclopropanes, and antiaromaticity for systems with cyclobutanes.[58] In 1980 Verhoeven[59] discussed the implications of Hoffmann's[60] orbital interactions through-bonds (OITB) model on the enhanced reactivity of three-membered rings, and Houk used this idea to explain the NICS findings (Figure 1.6b). For substrates with three-membered rings, the highest occupied σ MO (HO-σ-MO) corresponding to the breaking bond is of the correct symmetry to overlap with the LUMO associated with the trimethylene ring. Similarly, the lowest unoccupied σ MO (LU-σ-MO) corresponding to the breaking bond can overlap constructively with the highest occupied trimethylene orbital. As a result, aromaticity stabilises the TS for the cyclopropane-substituted cyclohexane [2 + 2 + 2] retro-cycloadditions. For the cyclobutane-substituted cyclohexanes, the opposite is true – the HO-σ-MO of the breaking bond overlaps with the HOMO of the tetramethylene, resulting in a four-electron Pauli repulsion and an antiaromatic TS.

In response to Hoz and co-workers's LUMO-lowering argument for the enhanced reactivity of three-membered rings, Houk and co-workers also investigated the bicyclo[1.1.0]butane systems using the NICS/OITB approach.[58] They argued that aromaticity causes substrate distortion, which results in a lower energy LUMO of the central bond than the side bond. In this regard, Hoz's LUMO-lowering model could be considered as a special case of Houk's more general aromaticity model.

Hoz further explored the relationship between strain and reactivity using Marcus theory, quantifying an "additional factor" that enhances ring-opening reactivity of three-membered rings.[61,62] For a set of similar reactions, where at least one member of the set is absent of strain, the expected activation barrier for a given strain-relieving reaction could be calculated from the intrinsic activation barrier for the unstrained reaction, and the driving force for the strain-relieving reaction. Any discrepancy between the predicted and calculated activation energies could then be attributed to the "additional factor" – speculated to be electronic in origin, and related to the distortion-promoted LUMO lowering effect. A variety of carbo- and heterocyclic small-ring systems were studied using this method, leading to the findings that, in general, three-membered rings showed enhanced reactivity, while four-membered rings were well-described by the Marcus equation. This effect appears to be independent of reaction type – a similar "additional factor" is observed for both anionic and radical reactions.[62]

Regardless of the model used to explain the enhanced reactivity of three-membered rings over their four-membered counterparts, a wealth of experimental and computational studies support the existence of this phenomenon. A timeline that summarises some of the key scientific studies leading to our current understanding of the relationship between strain and reactivity is shown in Figure 1.7.

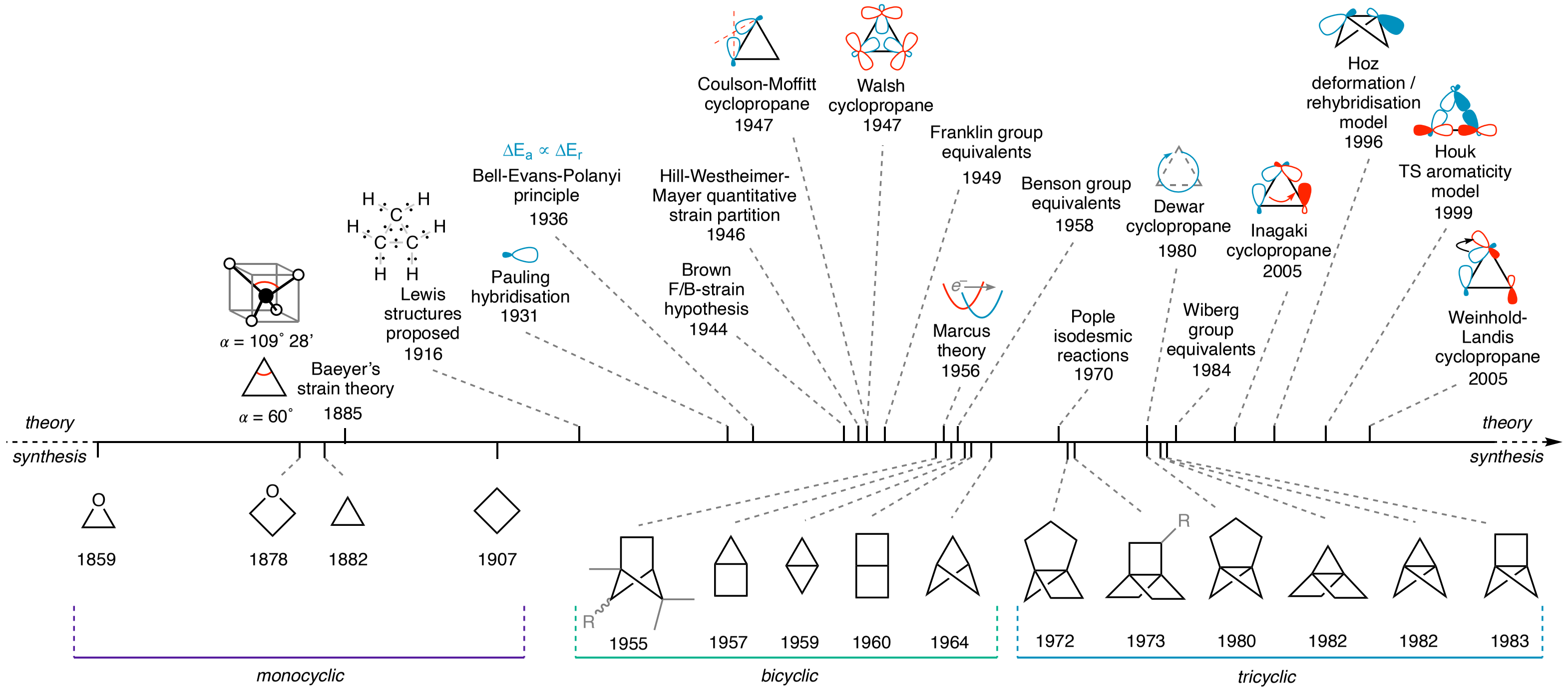

Figure 1.7: Timeline of important contributions to the field of strain release chemistry, with theoretical advances shown above, and synthetic progress shown below the line.

1.1.3 Contemporary applications of strain release reactivity

Strain release as a design principle in organic synthesis and chemical biology has seen a rapid rise over the past two decades (Figure 1.8a). A prime example in the latter field was reported in 2004 by Bertozzi and co-workers, where strain was engineered into Huisgen's [3 + 2] azide / alkyne click reaction[63] through the incorporation of the alkyne into an eight-membered ring (Figure 1.8b).[64] This had the effect of increasing the driving force for the cycloaddition, therefore increasing its rate and allowing the reaction to occur spontaneously under 'physiological' conditions, without the need for a catalyst or elevated temperature.

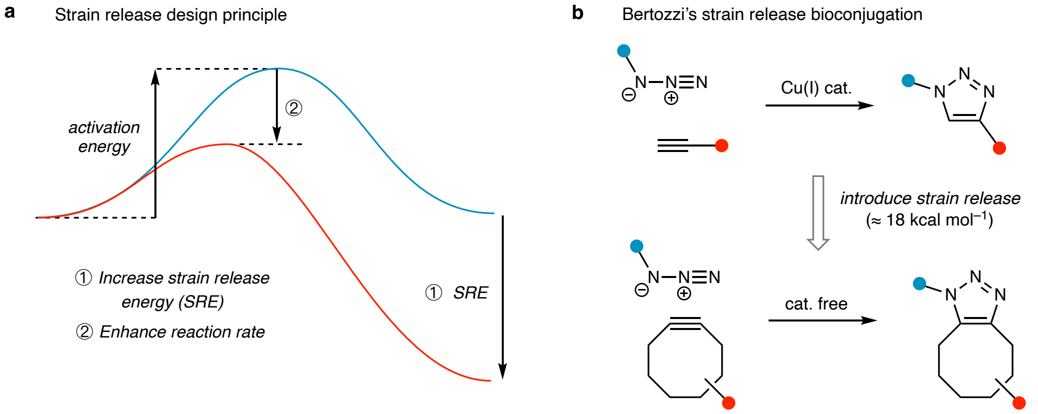

Figure 1.8: a. Introducing the release of strain into a reaction will increase its rate. **b.** The transformation of cyclooctyne into cis-cyclooctene releases 18 kcal mol^{-1} of strain energy, which is enough to enhance the rate of [3 + 2] cycloadditions with azides to negate the requirement for a catalyst or elevated temperature.

The application of the strain release principle in reaction design is exemplified by ring-opening reactions of systems containing at least one small ring. As a general rule, decreasing the number of small rings in a compound will decrease its strain energy – such that a reaction that removes a small ring will enjoy an inherent driving force for a process that may otherwise be thermodynamically disfavoured. For example, the ring-opening of ethylene oxide releases 27.2 kcal mol^{-1} of strain energy, but the same process for tetrahydrofuran releases only a fifth of this value

(5.6 kcal mol^{-1}).[65] The Bell-Evans-Polanyi principle (1.6) would predict ring-opening to occur with a $\approx$ 10 kcal mol^{-1} lower barrier for the former (taking an intermediate value of α = 0.5, which would be expected for the addition of an alkoxide), or a $\approx 10^7$ rate enhancement. Epoxides, and related structures such as cyclopropanes, have therefore found substantial use in total synthesis for the construction of fragments and complexity generation in synthesis.[66,67]

As noted above, ring strain effects are often roughly additive, and it can therefore be advantageous to design reactions in which a bond that belongs to two (or more) small rings is cleaved.[68] For example, cleavage of the central bond of bicyclo[1.1.0]butane to reveal cyclobutane is accompanied by the release of 39.7 kcal mol^{-1} strain energy,[24] offering a substantial driving force to accompany any reaction that involves this transformation. The key step in Fox's total synthesis of piperarborenine B was achieved using this strategy,[69] in which a rhodium-catalysed generation of a chiral bicyclo[1.1.0]butane, followed by organocuprate addition to its central bond, resulted in a 69% yield of the desired trisubstituted cyclobutane in 92% *ee* and a 4:1 *dr* (Figure 1.9a). Spearheaded initially by Wipf[70] and later by Aggarwal,[71–77] strain release chemistry with bicyclo[1.1.0]butanes and their *N*-substituted analogues (azabicyclo[1.1.0]butanes) is now general and can be used to synthesise a variety of densely-functionalised acyclic, mono- and bicyclic structures (Figure 1.9b). It is worth noting that some of these approaches were first developed for alkene substrates, leading to the question of whether the bicyclo[1.1.0]butane chemistry is indeed driven by strain release, or instead enabled by the olefinic electronic structure of the central C–C bond (or perhaps a combination of both factors).

Tricyclic hydrocarbons in which the three rings share a common bond (given the moniker 'propellanes' by Ginsberg due to their resemblance to a propeller)[78] have also enjoyed significant interest in the strain release literature.[79] Primarily of theo-

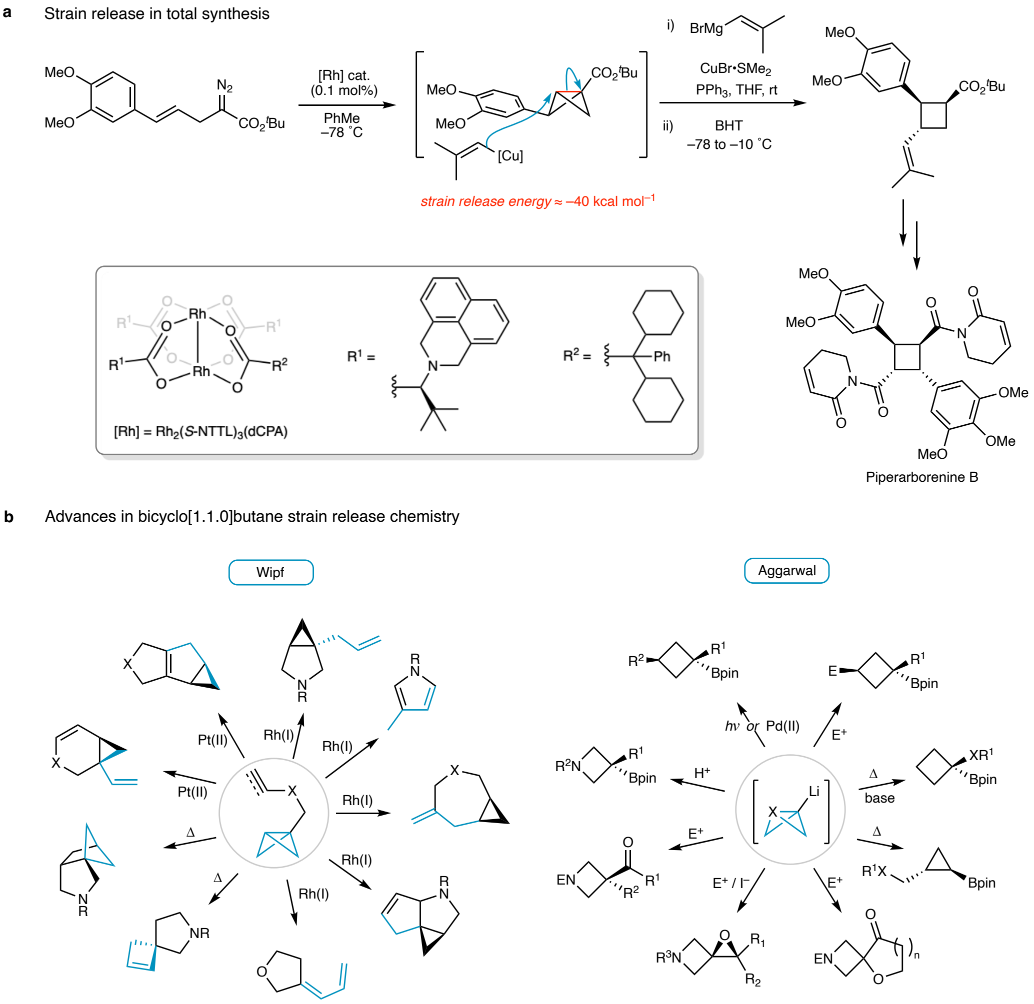

Figure 1.9: **a.** Fox's total synthesis of Piperarborenine B enabled by the strain release ring-opening of a bicyclo[1.1.0]butane. **b.** Contributions of Wipf and Aggarwal to the development of strain release chemistry with (aza)bicyclo[1.1.0]butanes. Left panel adapted with permission from Ref. [70].

retical interest in the 1960s and 70s, small-ring propellanes stretched the concepts of bonding and hybridisation and continue to do so today. In particular, [1.1.1]propellane (tricyclo[1.1.1.0^{1,3}]pentane, **1**) has long puzzled theorists since its inter-bridgehead C1–C3 'bond' is seemingly formed from the apparently non-existent inverted overlap of (approximately) C sp^3 orbitals (Figure 1.10a),[80] yet Hoffmann predicted the molecule to have a closed-shell singlet ground state due to symmetry constraints.[81] This prediction turned out to be correct when, in 1982, Wiberg successfully synthesised a sample of [1.1.1]propellane through dehalogenation of the corresponding 1,3-dibromobicyclo[1.1.1]pentane (Figure 1.10b).[82]

The strain energy of [1.1.1]propellane (99.2 kcal mol^{-1}) is almost identical to that of [2.1.1]propellane (tricyclo[2.1.1.0^{1,4}]hexane, 99.6 kcal mol^{-1}) and [2.2.1]propellane (tricyclo[2.2.1.0^{1,4}]heptane, 99.7 kcal mol^{-1}), yet their ring-opened hydrogenation products vary greatly: bicyclo[1.1.1]pentane has a strain energy of 66.9 kcal mol^{-1}, bicyclo[2.1.1]hexane contains 38.0 kcal mol^{-1}, and bicyclo[2.2.1]heptane contains 15.9 kcal mol^{-1} of strain energy (Figure 1.10c). Wiberg argued that the far greater stability of [1.1.1]propellane over [2.1.1] or [2.2.1]propellane was due to the ordering of strain release energies[83] – with the former being stable in solution at temperatures over 100 °C,[84] whereas the latter two spontaneously polymerise outside of a solid matrix.[85,86]

This strain release energy accompanying reactions of [1.1.1]propellane appears to be in a 'Goldilocks zone', where the addition of anions, radicals and cations are possible (and in many cases extremely facile),[79,87] yet spontaneous polymerisation is largely avoided under the reaction conditions. An expedited synthetic route towards [1.1.1]propellane by Szeimies in 1985,[84] slightly modified by Michl,[88] then permitted its synthesis on a practical scale (Figure 1.10d), opening the floodgates to several decades of reaction development for the synthesis of bicyclo[1.1.1]pentanes (BCPs).

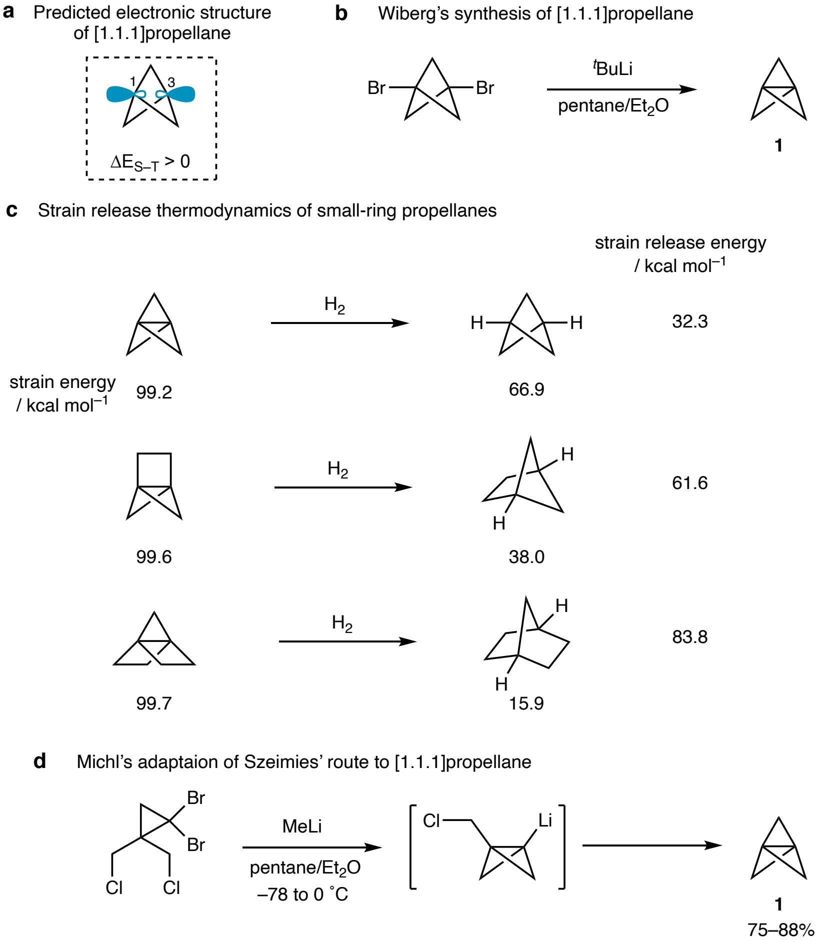

a Predicted electronic structure of [1.1.1]propellane

b Wiberg's synthesis of [1.1.1]propellane

c Strain release thermodynamics of small-ring propellanes

d Michl's adaptaion of Szeimies' route to [1.1.1]propellane

Figure 1.10: a. Stohrer and Hoffmann predicted a closed-shell singlet ground state, despite the apparent lack of C1–C3 orbital overlap. **b.** Debromination of 1,3-dibromobicyclo[1.1.1]pentane reveals [1.1.1]propellane. **c.** [1.1.1]Propellane relieves the least strain upon hydrogenation compared with similar small-ring analogues. **d.** Sequential lithium-halogen exchange / cyclisation reactions, *via* a bicyclo[1.1.0]butane, affords practical quantities of [1.1.1]propellane.

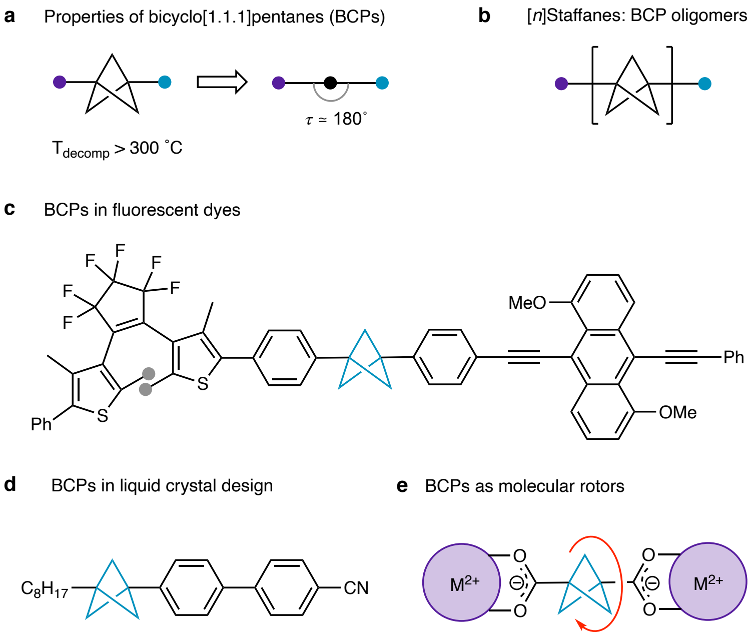

Figure 1.11: Applications of bicyclo[1.1.1]pentanes (BCPs) in materials science.

BCPs are of considerable synthetic interest because of their well-publicised 'wonder properties', such as rigidity, UV transparency, thermal stability, and 180° arrangement of bridgehead substituents (Figure 1.11a).[79,89] In the late 1980s, Michl developed a controlled oligomerisation of [1.1.1]propellane to generate oligo-BCPs, or [*n*]staffanes (Figure 1.11b), which exhibit higher melting points than the corresponding *n*-alkyl chains, as well as thermal stability up to 300 °C.[90] Hoz later calculated that the 1D Young's modulus of these [*n*]staffanes are greater than that of diamond.[91] As well as the oligomeric properties of BCPs, the monomeric units have also been explored as insulating spacers in fluorescent dye design to disrupt conjugation effects between the donor and acceptor motifs (Figure 1.11c).[87,92] The use of BCP backbones to develop liquid-crystalline materials has also been explored (Figure 1.11d).[93–95] More recently, the low barrier to rotation of the BCP unit was exploited as a low-temperature molecular rotor in a metal-organic framework (Figure 1.11e).[96] Further applications are discussed in Ref. [79].

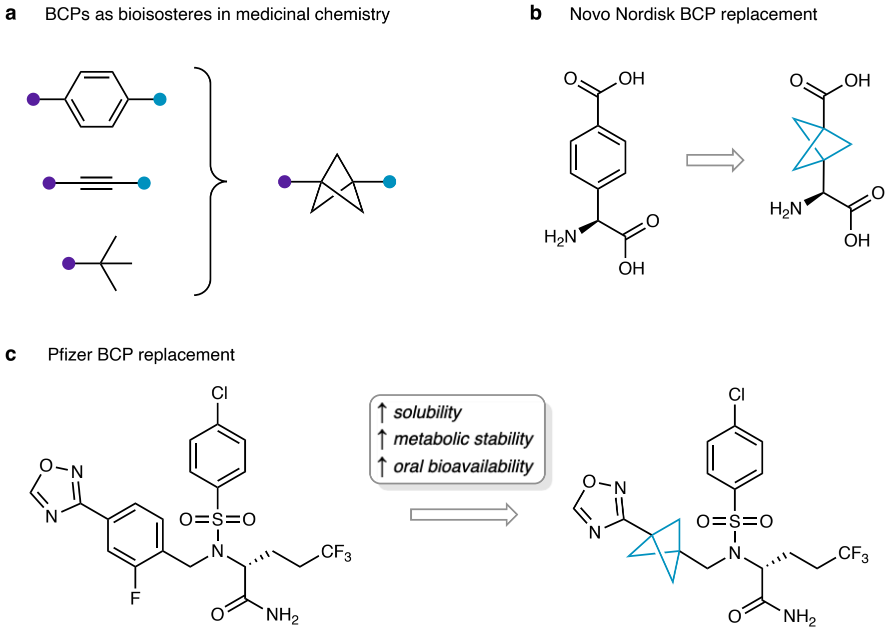

Figure 1.12: Applications of bicyclo[1.1.1]pentanes (BCPs) in medicinal chemistry.

The use of BCPs in materials science has been overshadowed by its expansion in popularity as a bioisostere for *para*-substituted phenyl,[97–104] *tert*-butyl[105] or alkyne[102] groups in medicinal chemistry (Figure 1.12a). Of these three replacements, the former has gained the most traction,[106] since it enables the so-called 'escape from flatland',[107] a phenomenon in which the fraction of sp^3 centres in a drug candidate has been found to correlate with clinical success. This idea was first demonstrated by Pellicciari and co-workers at Novo Nordisk in 1996 when the phenyl group of a (carboxyphenyl)glycine derivative, used for the study of a range of central nervous system disorders, was replaced by a BCP (Figure 1.12b).[97] The linear arrangement of BCP bridgehead substituents was found to match those of the phenyl derivative, and good activity was observed.

A direct comparison of the activity of a BCP-containing drug compared to the parent phenyl-substituted compound was made by Stepan and co-workers at Pfizer in 2012,[99] who synthesised and tested the pharmacological properties of a γ-

secretase inhibitor for the treatment of Alzheimer's disease (Figure 1.12c). Similar inhibition was observed for both the aryl and BCP derivatives in *in vitro* studies, while the BCP compound showed both enhanced solubility and metabolic stability. Further *in vivo* studies indicated improved oral bioavailability of the BCP compound. Brown has also recently highlighted the potential for abiotic scaffolds such as BCPs for the treatment of diseases prone to develop resistance.[108] While a BCP-containing drug is yet to be approved for clinical use, the number of patents featuring a BCP has risen sharply in recent years.[106]

Due to the rise in interest of the BCP motif in medicinal chemistry since the early 2010s, strategies for their synthesis have followed. Wiberg's classic synthesis of BCPs involved an intramolecular Wurtz coupling,[109] in the same spirit as the first synthesis of cyclopropane almost a century before;[110] however, low yields have prevented this approach from being synthetically useful. The reader is referred to Ref. [87] for a summary of other approaches to obtain BCPs, as this Thesis focuses instead on new methods that convert [1.1.1]propellane into the corresponding BCP.

Wiberg pioneered much of the ring-opening chemistry of [1.1.1]propellane, reporting a myriad of atom-transfer radical addition (ATRA) reactions including halogenation, halotrichloromethylation, thiyl and selenyl addition, acyl radical addition, hydrophosphination, nitration, radical-initiated oligomerisation, as well as the addition of electron-deficient alkenes and alkynes, ring-opening reactions with transition metal ions or acetic acid (Figure 1.13a).[111] Organolithium and Grignard additions to [1.1.1]propellane have also been reported by Della and Szeimies and later used by de Meijere for the synthesis of liquid crystals (Figure 1.13b).[112,113] However, it was only in 2016 that a scalable route to BCPs from [1.1.1]propellane was developed by Baran,[114] who employed 'turbo' amides as nucleophiles on a $>$100 g scale to synthesise 1-amino BCPs – bioisosteres for anilines (Figure

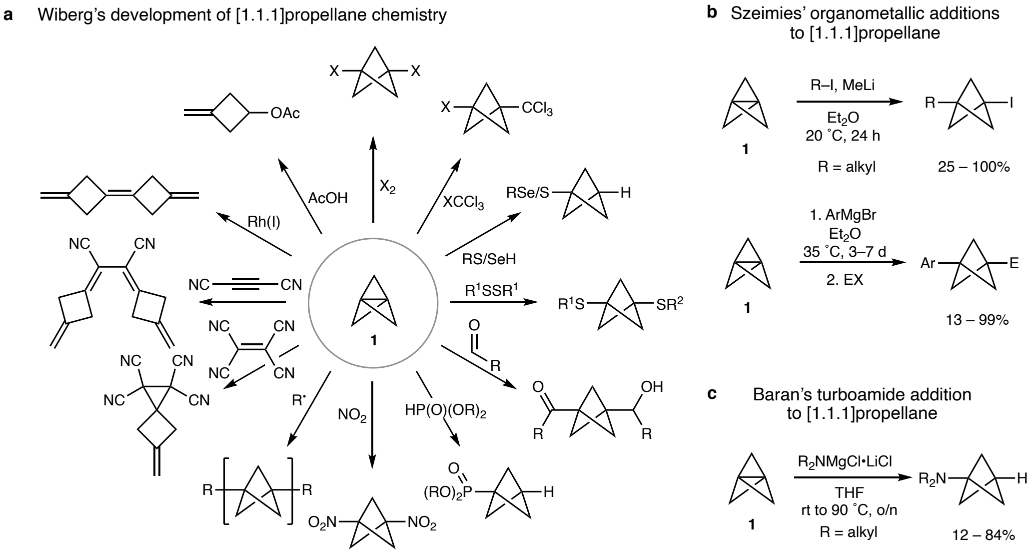

a Wiberg's development of [1.1.1]propellane chemistry

b Szeimies' organometallic additions to [1.1.1]propellane

c Baran's turboamide addition to [1.1.1]propellane

Figure 1.13: Radical, cationic and anionic addition reactions to [1.1.1]propellane.

1.13c). Notably, this synthetic strategy was based upon the "spring-loaded" nature of the interbridgehead C1–C3 bond of [1.1.1]propellane, citing the "$\sim$60 kcal mol^{-1} [energy] stored in this bond" (a value derived from Wiberg's estimate of the bond dissociation energy at the HF/6-31G* level).[†] It is therefore perhaps surprising that this reaction required elevated temperatures – as also found by Knochel for aryl Grignard additions,[102] and Walsh for the addition of 2-azaallyl anions.[115]

Milder conditions for ring opening of [1.1.1]propellane can be employed for radical reactions, as demonstrated in 2017 by Kanazawa and Uchiyama's multicomponent carboamination of [1.1.1]propellane at –20 °C (Figure 1.14a).[116] Anderson reported an efficient triethylborane-initiated synthesis of 1-halo-3-alkyl BCPs a year later, also finding that ambient temperatures (or below 0 °C) were ideal (Figure 1.14b).[117] A more general synthesis using this strategy was proposed by the same group shortly afterwards, where triethylborane was replaced by an iridium photocatalyst, enabling access to a wider range of radicals from alkyl and

---

[†] By this logic, ethane should be far more reactive than [1.1.1]propellane since its bond dissociation energy is $\approx$85 kcal mol^{-1}.[30]

aryl iodides for the ATRA process.[118] Sheikh and Leonori also contributed to the radical strain release toolkit, developing another multicomponent radical addition to [1.1.1]propellane using electron-deficient *N*-centred radicals (Figure 1.14c).[119] MacMillan capitalised upon this multicomponent difunctionalisation concept with metallaphotoredox catalysis,[120] employing activated carboxylic acids to generate *C*-centred radicals to add across [1.1.1]propellane, followed by copper-catalysed trapping and subsequent reductive elimination to form *N*-, *S*- and *P*-substituted BCPs (Figure 1.14d). A wide variety of bridgehead-functionalised BCPs can now be synthesised at will,[121] which we anticipate will further increase their popularity as building blocks in medicinal chemistry.

The use of bridge-substituted BCPs as bioisosteres for *ortho*- / *meta*-substituted arenes has also recently been explored.[122–124] Building on earlier work by Schlüter for the synthesis of bridge-substituted analogues of [1.1.1]propellane,[125] Ma and co-workers from Merck proposed a turbo amide addition to a 2-alkylpropellane, giving access to a range of 1,2-difunctionalised BCPs (Figure 1.14e).[122] Baran and co-workers from Pfizer were simultaneously developing a related approach, employing a 2-alkylpropellane in an ATRA reaction to synthesise the key BCP building block.[123] Further developments in the synthesis and application of bridge-substituted propellanes should be anticipated in the coming few years.

It is worth commenting on the lack of methods to synthesise BCPs from [1.1.1]propellane through cationic pathways. While reporting the first synthesis of [1.1.1]propellane, Wiberg noted its rapid reaction with acetic acid to form an exo-methylene cyclobutane.[82] The general instability of 1-bicyclo[1.1.1]pentyl cations has since become well-established,[126] therefore cationic methods to synthesise BCPs from [1.1.1]propellane are unknown. While a handful of methods invoke a bridgehead BCP cation to explain the mechanism of formation of intact BCP products, alternative mechanisms are far more likely.

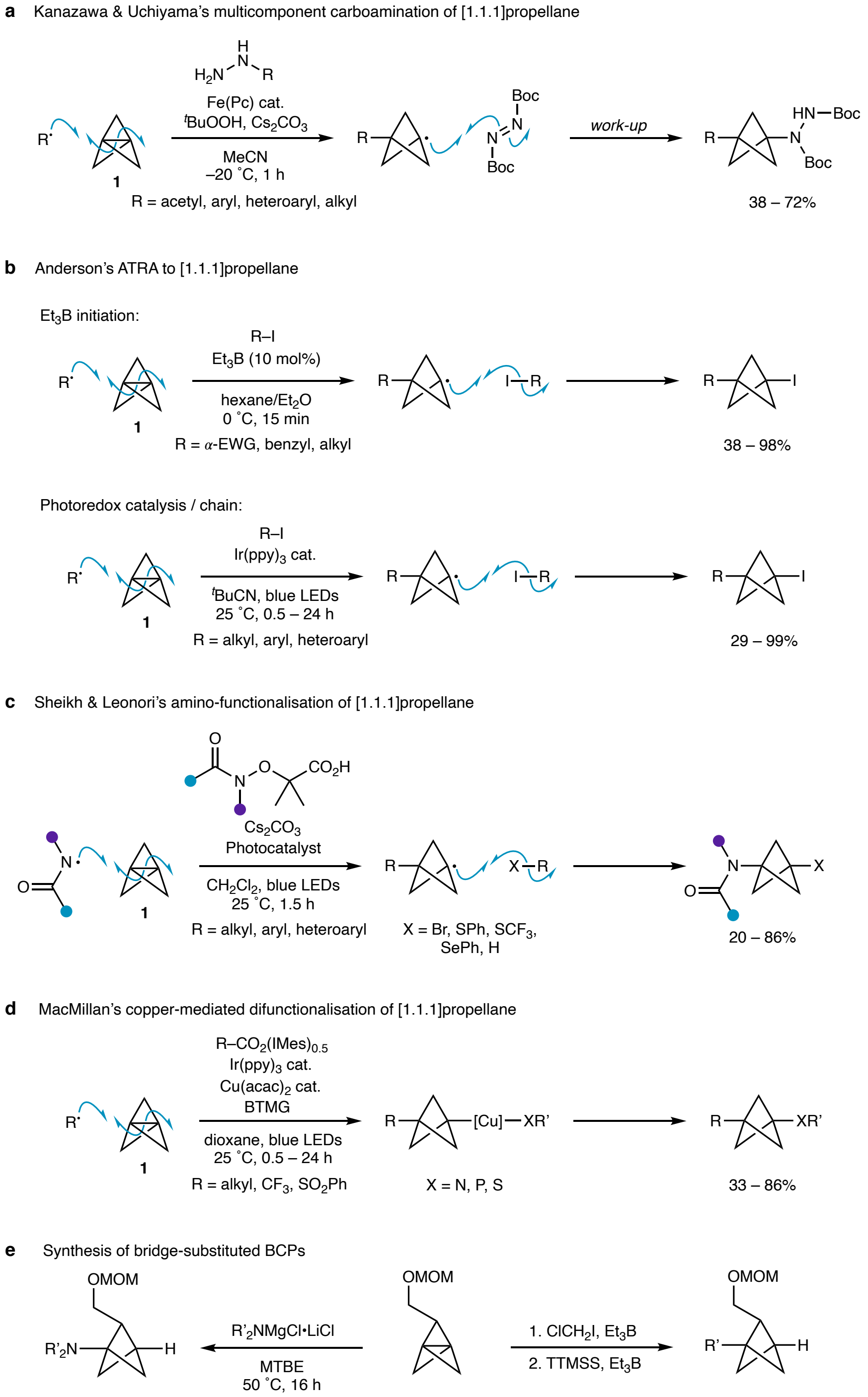

Figure 1.14: Radical difunctionalisation reactions of [1.1.1]propellane (**a**-**d**) and bridge-substituted BCP synthesis (**e**). Pc = phthalocyanine, BTMG = 2-tert-butyl-1,1,3,3-tetramethylguanidine, MTBE = methyl tert-butyl ether, TTMSS = tris(trimethylsilyl)silane, MOM = methoxymethyl.

1.2 Contributions of this Thesis

A brief history of the development of the concept of strain and its relationship with reactivity has been presented. From Baeyer's theory of strain in cycloalkanes, Brown's B-strain hypothesis, the use of LFERs to relate kinetics and thermodynamics, and the development of computational methods to calculate strain energies, physical organic chemists have developed the tools to routinely study the structure / activity relationships that underpin the development of new strain-release reactions. A sharp rise in the popularity of strain release as a synthetic tool, combined with our incomplete understanding of the role of thermodynamic and electronic factors determining the rates of these reactions, has inspired the investigations undertaken here.

In Chapter 2, the origins of the rich chemistry of [1.1.1]propellane (Figure 1.15a) are investigated. The rising popularity of BCPs in medicinal chemistry means that efficient methods for their synthesis are desirable, and strain release additions to the interbridgehead bond of [1.1.1]propellane by anions and radicals have shown great promise as a general approach to BCP synthesis. A phenomenal number of theoretical studies have probed the nature of the propellane interbridgehead bond, and a similarly impressive number of synthetic studies have made use of its unusual properties. However, a systematic study to elucidate the link between bonding and reactivity is yet to be undertaken. In this Chapter, we embark on such a study to uncover the reasons for its unusually broad reactivity profile with anions, radicals and cations. Introducing the idea of electronic delocalisation alongside strain release as factors that enhance the reactivity of [1.1.1]propellane, this study should find use in the synthetic community as a guide to consider when designing new BCP syntheses. The work presented in Chapter 2 was published in Chemical Science in 2020.[127]

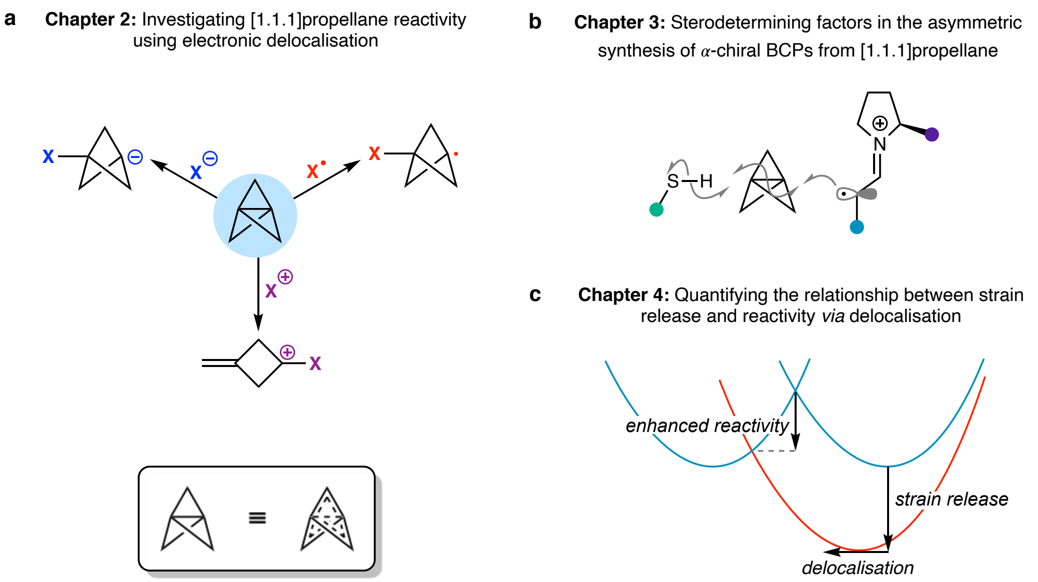

Figure 1.15: Overview of the content investigated in each of the Chapters in this Thesis.

In Chapter 3, the implications of the findings in Chapter 2 are explored through the development of a direct catalytic asymmetric synthesis of α-chiral BCPs from [1.1.1]propellane (Figure 1.15b); synthetic work in this project was carried out by Marie Wong in the group of Prof. Ed Anderson. In this Chapter, the key synthetic findings are summarised, including the important features of both the substrate and organocatalyst to achieve high enantioselectivity in the reaction, as well as an unusual dependence of the observed selectivity on the nature of the photocatalyst. Building from this data, the computational study of this reaction will be discussed, focusing on the stereodetermining step in which the key C–C bond is formed. A kinetic model that rationalises the observed results complements the combined synthetic and computational results, which is hoped to provide a guide for the design of future photoredox organocatalytic transformations, as well as highlighting the importance of delocalisation to fully appreciate the chemistry of [1.1.1]propellane. The work presented in Chapter 3 was published in Nature Communications in 2021.[128]

In Chapter 4, the scope of these investigations is broadened by studying the relationship between strain energy and reactivity of small rings in general. The idea of electronic delocalisation introduced in Chapter 2 is used alongside strain release to develop a quantitative model for predicting activation barriers in these reactions. To this end, the principles introduced in the early electronic structure studies of cyclopropane are employed to explore the origins of the differing reactivity of cyclopropane and cyclobutane, as well as bi- and tricyclic systems and heterocycles (Figure 1.15c). The results presented in this Chapter aim to counter the confusion around the origins of strain release reactivity, providing a general and simple model to interpret and predict reactivity trends.

In summary, this Thesis will propose a framework to understand and predict the behaviour, and in particular the reactivity, of small rings. The idea that electronic delocalisation stands as an equal alongside strain energy to describe reactivity is central to this framework – a more delocalised bond is easier to break, therefore a lower activation barrier accompanies the transformation. We hope that the ideas put forward here will contribute to the ongoing quest to synthesise better drugs and materials, as well as a fuller understanding of the fundamental chemistry that underpins the world around us.

1.3 Methods

A study of the reactivity of small organic molecules in solution using computation requires the use of electronic structure methods to characterise reaction intermediates and transition states (TSs). In this Thesis, we employ methods that can accurately describe challenging electronic structures, but are not so expensive that the calculations become impractical. There are, broadly, two approaches to solving electronic structure problems: wavefunction theory (WFT) and density functional theory (DFT). In the following sections, the methods employed in this Thesis will be briefly introduced, emphasising the strengths and limitations of each. A more detailed discussion of WFT methods is provided in Appendix E.

1.3.1 Wavefunction theory

Most common WFT methods are based on approximations to the time-independent many-electron Schrödinger equation

$$\hat{H}\Psi = E\Psi \tag{1.9}$$

where $\hat{H}$ is the non-relativistic many-electron Hamiltonian, Ψ is the wavefunction of the system that describes the spatial coordinates and spins of all particles, and the eigenvalue E is the total electronic energy. The Born-Oppenheimer approximation is made, which sets the nuclear kinetic energy to zero and the internuclear repulsion as a constant, since nuclear motion takes place on a much longer timescale than that of the electrons. The Born-Oppenheimer Hamiltonian then comprises

$$\hat{H} = -\frac{1}{2}\sum_{i=1}^{N}\nabla_i^2 - \sum_{i=1}^{N}\sum_{A=1}^{M}\frac{Z_A}{r_{iA}} + \sum_{i=1}^{N}\sum_{j>i}^{N}\frac{1}{r_{ij}} + \sum_{A=1}^{M}\sum_{B>A}^{N}\frac{Z_A Z_B}{r_{AB}} \tag{1.10}$$

where the first term determines the electron kinetic energy, the second defines the electron-nuclear Coulomb attraction, the third the electron-electron Coulomb repulsion, and the fourth the internuclear Coulomb repulsion (i, j represent electron indices, A, B are nuclear indices). While this equation cannot be solved exactly for more than one electron (hydrogenic wavefunctions), we can make the Hartree-Fock (HF) approximation, in which the many-electron wavefunction is approximated, using a Slater determinant, as an antisymmetrised product of one-electron wave-functions (orbitals χ_i, Figure 1.16a) given by

$$
\begin{aligned}
|\Phi\rangle &= \frac{1}{\sqrt{N!}} \begin{vmatrix} \chi_1(\mathbf{x}_1) & \dots & \chi_M(\mathbf{x}_1) \\ \vdots & \ddots & \vdots \\ \chi_1(\mathbf{x}_N) & \dots & \chi_M(\mathbf{x}_N) \end{vmatrix} \\
&= \frac{1}{\sqrt{N!}} \sum_{i=1}^{N!} (-1)^{p_i} \hat{P}_i(\chi_1(\mathbf{x}_1)\chi_2(\mathbf{x}_2)\dots\chi_M(\mathbf{x}_N))
\end{aligned}
\tag{1.11}
$$

where $\chi_i(\mathbf{x_1})$ denotes electron 1 occupying spin orbital i. $\hat{P}_i$ is an operator that generates the ith permutation of electrons 1, 2, ..., N (corresponding to switching rows of the determinant), and p_i is the number of row interchanges required to achieve a given electron permutation.

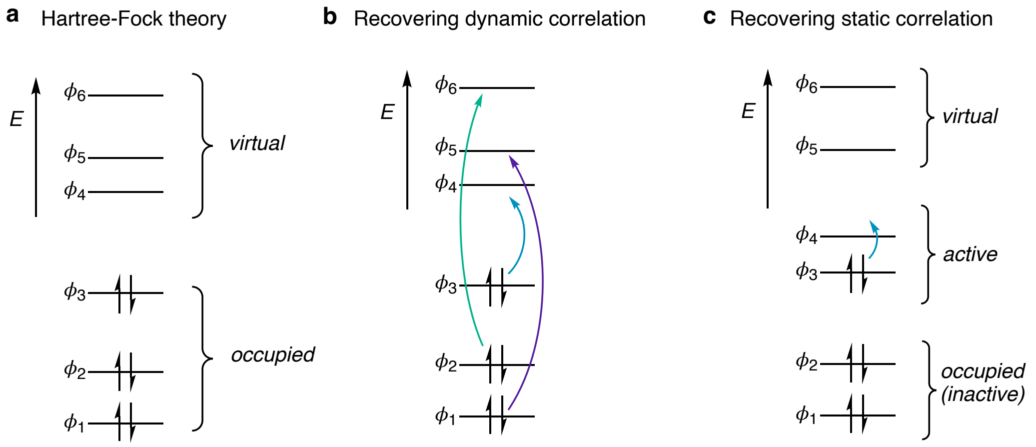

Figure 1.16: Wavefunction theory (WFT) for the description of molecular electronic structure: **a.** The Hartree-Fock (HF) energy depends on a set of occupied one-electron wavefunctions (orbitals) using a mean-field approximation; **b.** Excitations from the HF wavefunction recovers the correlated motion of electrons; **c.** A qualitatively incorrect HF wavefunction can be corrected using an active space from which multiple HF determinants are formed.

Each electron then experiences repulsion by the mean field of the remaining electrons (v_{HF}) through the equation

$$\begin{aligned}\left[-\frac{1}{2}\nabla_1^2 - \sum_{A=1}^{M}\frac{Z_A}{r_{A1}} + v_{HF}\right]\chi_i = \mathcal{E}_i\chi_i \\ v_{HF} = \sum_{b}^{N}(\hat{J}_b - \hat{K}_b)\end{aligned} \tag{1.12}$$

The eigenvalue $\mathcal{E}_i$ is the energy of the ith orbital χ_i. The operator $\hat{J}_b$ returns the Coulombic repulsion of an electron with the mean field of the remaining $N - 1$ electrons, where the superscript b denotes it is a two-electron operator. The operator $\hat{K}_b$, the exchange operator, lowers the total energy by swapping electrons of the same spin – a non-classical term arising from the indistinguishable nature of electrons. Through this machinery, the many-electron Schrödinger is turned into a one-electron problem, and can therefore be solved computationally. The total HF energy is then given by

$$E_{HF} = \sum_{i}^{N}\mathcal{E}_i - \frac{1}{2}v_{HF} \tag{1.13}$$

where the total energy is not simply equal to the sum of orbital energies since repulsions between pairs of electrons would be counted twice.

Electron correlation

HF theory is often described as being devoid of 'electron correlation' – a term used to describe how the instantaneous position of one electron will affect that of another – since the mean field approximation causes an electron to experience repulsion from the *average* position of any other electron in the system, not repulsion from the exact position of the electron at any given point in time. An unfortunate consequence of this approximation is that that two electrons (with opposite spins) may be found in the same volume element, so inter-electron repulsion is overestimated. The HF energy is therefore an upper limit (for a given basis set). It is not strictly true that HF theory is correlation-free; the use of an antisymmetrised wave-function does introduce same-spin (Fermi) correlation, however opposite-spin (Coulomb) correlation is completely unaccounted for. As a result, HF theory generally understabilises singlet states,[129] and gives bonds that are too short and too strong.[130] This is illustrated by the predicted –28.2 kcal mol^{-1} singlet-triplet energy gap and C–H bond lengths of 1.095 Å (singlet) / 1.069 Å (triplet) for CH_2 (cc-pVQZ basis set), compared with the experimental values of –9.0 kcal mol^{-1} and 1.107 Å (singlet) / 1.085 Å (triplet), respectively.[129]

Electron correlation is usually introduced into the HF wavefunction through the incorporation of excited configurations. There are many different approaches to this, but they can be broadly split into two. The first of these approaches uses a single HF determinant directly, adding small corrections to the total energy by variationally optimising the weights of the excited configurations (*e.g.*, configuration interaction methods, Figure 1.16b). The second approach uses multiple HF determinants, variationally optimising both the weights of all configurations *and* the orbitals in the wavefunction simultaneously to obtain an accurate description of the electronic structure (*e.g.*, complete active space methods, Figure 1.16c). These two methods serve different purposes: single-determinant methods recover so-called 'dynamic correlation' – the removal of the artificial repulsion arising from the naivety of an electron to the exact position of the others as described above, whereas multi-determinant methods recover 'static correlation' – energy arising from the inability of a single determinant to qualitatively describe the electronic structure.[131] Static correlation effects are most prominent in systems with (near-)degeneracies, such as diradical species,[132] low-spin metal complexes[133] or bond dissociations.[134]

It is worth noting that there is no physical distinction between dynamic and static correlation, but paradoxically the methods employed to describe correlation effects must be judiciously chosen to ensure each type of correlation is treated in a balanced way.[131] A simple test for the presence of static correlation in a system is to examine the natural orbital occupation number (NOON) from a correlated calculation; a NOON ≥ 1.98 likely indicates that a single HF determinant is sufficient to qualitatively describe the electronic structure, such that a perturbative treatment of dynamic correlation is sufficient (see below). However, if a NOON is < 1.98, it can be sometimes be wise to employ a multiconfigurational method, such as the complete active space self-consistent field (CASSCF) method (see below), to obtain a qualitatively correct wavefunction which can later be dressed with dynamic correlation if quantitative results are desired.

Recovering dynamic correlation. To correct the HF energy for dynamic correlation effects, (generally) small corrections are applied on top of a single HF wavefunction by incorporating excited configurations into the wavefunction (Figure 1.16b) to lower the total energy. While this might seem counterintuitive, electron exchange terms between the HF and excited configurations compensate for any increase in the one-electron energy (see Appendix E for further discussion). Of the multitude of methods that incorporate correlation in this way, the most common are the Møller-Plesset perturbation theory to second order (MP2) method[135] and the coupled cluster method with single, double and perturbative triple excitations [CCSD(T)].[136] The MP2 method performs well for most organic molecules, however can overestimate dispersion interactions[137] and struggle for open-shell systems with small occupied-virtual orbital energy gaps.[138] This latter shortcoming is particularly clear during bond dissociation, where the perturbation correction diverges and massively overstabilises species at large separation. MP2 scales as $\mathcal{O}(N^5)$, where N is the number of basis functions, restricting its use for large systems.[139]

Drastic improvements to electronic energies and properties are achieved with the CCSD(T) method,[136] often described as the 'gold standard' for benchmarking when experimental values are unavailable.[140] For this method to be accurate, the underlying HF determinant has to be qualitatively correct (*i.e.*, the system does not have strong multireference character, see below). In addition, CCSD(T) scales as $\mathcal{O}(N^7)$,[136] severely restricting its use in systems larger than 10s of atoms. Recent efforts to achieve linear-scaling coupled cluster methods have found reasonable success, notably the domain based local pair-natural orbital (DLPNO) approximation to CCSD(T) which has been applied to systems of hundreds of atoms.[141] This approach leverages the locality of correlation; correlation arising from the motion of two electrons at either end of a large molecule is essentially zero, so terms that include these interactions can be identified and neglected through the use of localised orbitals and pre-screening. The DLPNO-CCSD(T) method is employed throughout this Thesis as a benchmark for electronic energies.

Recovering static correlation. The CASSCF method is most commonly used to describe static correlation effects. A linear combination of HF determinants is variationally optimised to achieve the desired electronic structure. To limit the combinatorial explosion associated with the combinations of all electrons occupying all possible orbitals, the orbital space is divided into three parts (Figure 1.16c): an inactive subspace of occupied orbitals (treated at the HF level), an active subspace (treated at the full configuration interaction (FCI) level[†]), and a virtual subspace. The nomenclature used in this Thesis is CAS(*n*,*m*), where *n* is

---

[†] FCI is the exact solution to the electronic problem for a given basis, where all possible excitations from all possible occupied orbitals are considered

the number of electrons and *m* is the number of orbitals in the active space. In the CH_2 example above, the CASSCF method with two electrons in two active orbitals (CASSCF(2,2)/cc-pVQZ) predicts a singlet-triplet gap of –10.4 kcal mol^{-1} – much closer to the experimental value of –9.0 kcal mol^{-1}.

Unfortunately, there are significant downsides to this method, for example the active space is limited to only a dozen or so electrons and orbitals, and each calculation must be rigorously checked to ensure the desired orbitals are employed in the active space. There are no concrete rules for active orbital selection, but for organic species it is often sensible to choose bonding / antibonding combinations of orbitals where static correlation effects are believed to be important (e.g., the σ and σ^* orbitals of H_2 at large separation). In addition, while the electrons in the active space are in principle treated exactly, those in the inactive space suffer from the same problems as the HF method.

1.3.2 Density functional theory

WFT requires the explicit calculation of four-centre two-electron integrals, therefore incurs a baseline $\mathcal{O}(N^4)$ scaling. An elegant way to reduce this scaling is to instead calculate the total energy from the electron density, which is a function of only three spatial coordinates.[142] Hohenberg and Kohn demonstrated a one-to-one mapping between the total electron density and energy of a system, based on the idea that an 'energy functional' could extract this energy from the density using (1.14), where the first term represents the attraction between the electron density and the nuclei, and the second term describes the electronic kinetic energy and electron-electron repulsion.[143]

$$E[\rho] = \int v(\mathbf{r})\rho(\mathbf{r})d\mathbf{r} + F[\rho] \tag{1.14}$$

Unfortunately, the exact form of such an energy functional is unknown, and likely never will be. Modern density functional methods employ approximate functionals which have been shown to be sufficiently accurate and can often reproduce experimental trends and fundamental physical requirements to make their use widespread, stimulating an explosion in the popularity of simulations in chemistry.[144] In particular, for condensed-phase modelling (including molecular reactions) Kohn-Sham (KS) DFT (1.15) is the most commonly-employed approximation for achieving any sort of predictive accuracy.[145] In KS-DFT, the total electron density is approximated as a non-interacting density by introducing orbitals, as in WFT, which recovers accurate kinetic energies through $T_s[\rho]$ but requires a Coulomb functional ($E_{\mathrm{J}}[\rho]$) to obtain the inter-electron repulsion, and an exchange-correlation functional ($E_{\mathrm{xc}}[\rho]$) to calculate exchange and correlation interactions between electrons.

$$E[\rho] = T_s[\rho] + \int v(\mathbf{r})\rho(\mathbf{r})d\mathbf{r} + E_{\mathrm{J}}[\rho] + E_{\mathrm{xc}}[\rho] \tag{1.15}$$

The exact form of the exchange-correlation functional is unknown, but several decades of work have proved fruitful for the development of functionals that are practically useful and can recover much of the correct physical behaviour of the system.[144] A hierarchy of functionals was proposed by Perdew,[146] starting with the evaluation of the exchange-correlation energy using the density of the system (local spin density approximation, LSDA, Figure 1.17a). More accurate molecular calculations can be achieved through dependence of E_{xc} on both the density and its gradient (generalised gradient approximation, GGA), or the density, gradient, and second derivative of the density (meta-GGA). However, many commonly-employed functionals of these types suffer from using an approximate exchange-correlation functional: each electron can repel itself (commonly described as self-interaction error, SIE).[147] To correct for the over-delocalisation resulting from SIE, a fraction of HF exchange energy can be included in the functional. Error cancellation often results, giving rise to the enormous success of these 'hybrid' DFT functionals – although this error-cancellation is system-dependent.[144] Further accuracy can be gained by making the exchange-correlation functional depend on virtual orbitals ('double hybrid' DFT), in a manner akin to the MP2 correction to the HF energy.[148] While energies and other properties often systematically improve with greater sophistication of the DFT functional, this is not always the case, since KS-DFT is not variational.

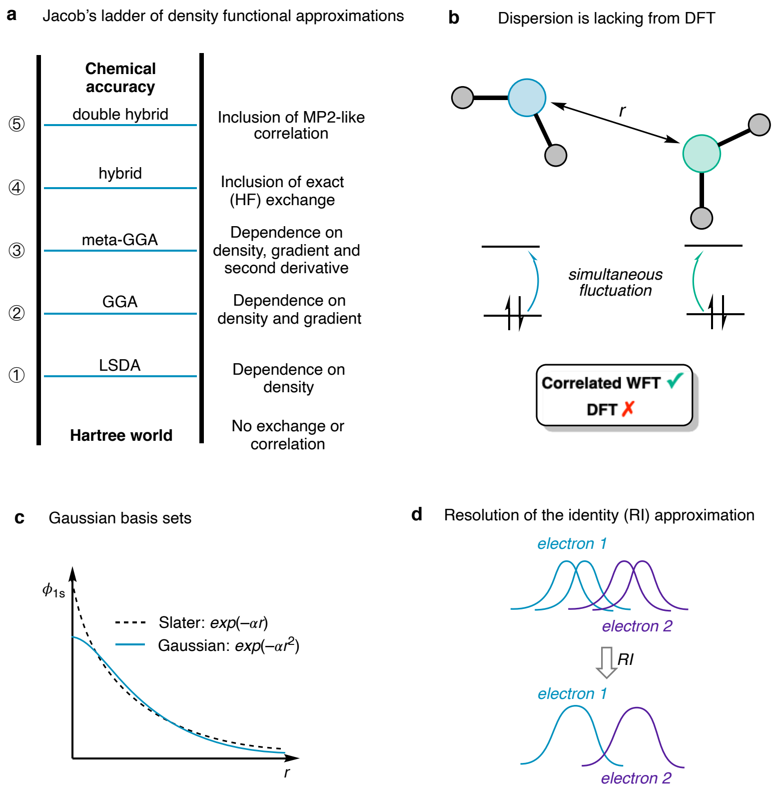

Figure 1.17: a. Perdew's DFT hierarchy; LSDA = local spin density approximation, GGA = generalised gradient approximation. **b.** Local DFT cannot describe the nonlocal fluctuations in density required for dispersion interactions. **c.** Linear combinations of Gaussians are routinely used to approximate Slater functions. **d.** Cartoon to describe the resolution of identity (RI) approximation for a Coulomb integral, where a four-centre two-electron integral is transformed into a two-centre integral *via* an auxiliary basis set.

An additional problem with many commonly-employed DFT functionals is their inability to describe nonlocal density fluctuations and therefore account for dispersion interactions (Figure 1.17b). At large interatomic separation, the dispersion energy should decay as $-1/R^6$, but this behaviour is not fulfilled by many common DFT functionals.[149] One solution to this problem is to add an empirical correction to the total energy which describes any long-range interactions as a function of the distance between atoms. For example, the D3BJ dispersion correction employed in this Thesis sums interactions arising from pairwise atomic interactions, using a damping function to remove short-range correlation effects that are already described by DFT.[150]

1.3.3 Practical considerations

Basis set

Both WFT and KS-DFT-based methods require a finite basis set to evaluate the integrals necessary to describe the electronic structure using computation. Hydrogenic orbitals decay exponentially with distance from the nucleus, therefore a Slater-type basis set can be employed which decays as $\exp(-\alpha r)$ and therefore has the correct short- and long-range physical behaviour (Figure 1.17c). However, greater computational efficiency can be achieved by using a Gaussian-type basis set, where the orbital instead decays as $\exp(-\alpha r^2)$, since the product of two Gaussians centred on different points is a sum of Gaussians centred at a point between those Gaussians (the Gaussian Product Theorem).[151] While many more Gaussians are required to approach the correct physical behaviour, Gaussian integrals can be evaluated analytically and therefore offer significant speed-up compared with Slater-type orbitals. The Gaussian-type ‘def2’ basis sets developed by Weigend and Ahlrichs are employed throughout this Thesis, given their strong performance across the periodic table and the ability to routinely employ the def2-ECP (effective core potential) for heavy elements.[152]

Resolution of identity (RI) approximation

Most of the computational cost in electronic structure calculations arises from the evaluation of four-centre two-electron repulsion integrals. This cost can be reduced by expanding the orbital basis functions over an auxiliary basis set[153–155] – in effect approximating these four-centre integrals as two-centre (Coulomb) and three-centre (exchange) integrals (Figure 1.17d). Since all calculations in this Thesis were carried out with the ORCA electronic structure package,[156] the RI-JCOSX approximation was employed as standard, which uses separate auxiliary basis sets for the Coulomb, exchange and correlation integrals.[154]

Solvent effects

Two computational approaches exist to describe solution-phase reactions: explicit or implicit solvation. Explicit solvation places the solute into a bath of discrete solvent molecules, and therefore includes explicit solute-solvent interactions such as hydrogen bonds. While explicit solvation would give the closest match to the experimental system, it can become prohibitively expensive with increasing system size. Moreover, the configuration of solvent molecules must be well-sampled to include multiple configurations of similar energy that may be partially populated at a given temperature. There is the potential for an enormous number of solvent configurations due to a lack of strong ordering interactions, and errors may also arise in the calculation of entropic contributions due to an abundance of low-energy vibrational modes. An alternative to the explicit solvation approach is to instead use an implicit solvent model, in which a solvent-accessible cavity is constructed around the solute, and charges are placed on the surface of the cavity to mimic the solvent medium. In this Thesis, the SMD solvent model is employed,[157] since it generally performs well for solvation free energies of both charged (MUE = 4 kcal mol^{-1}) and uncharged (MUE = 0.6 – 1.0 kcal mol^{-1}) systems. The distinct advantage of such a solvent model is that it is applied during the SCF cycle, such that the solute charge density is optimised for the given solvent environment. However, a drawback of this approach is that any explicit solvent-solute interactions, such as hydrogen bonds, are not accounted for.

1.3.4 Computational physical organic chemistry

To connect the electronic structure and reactivity of the systems studied in this Thesis, a series of analyses based on population analyses, molecular orbital (MO), distortion / interaction (DIA), and non-covalent interactions (NCI) were performed. These properties can then be used to inform our understanding of the important chemical interactions and trends that can be used to guide further experiments.

Population analysis

The accumulation or depletion of charges or spin density on individual atoms over the course of a reaction can reveal the flow of electrons that loosely corresponds to our understanding of reaction mechanisms using curly arrows. Partial charges are not physical observables, therefore there are multiple equally valid methods through which they can calculated; however, irrespective of the method employed, quantitative structure-activity relationships can be constructed which link trends in molecular properties or reactivity to partial charges. In this Thesis we employ Hirshfeld partial charge analysis,[158] which allocates charges to each atom by comparing the calculated molecular charge density with that of a promolecule formed from overlapping, but non-interacting, charge densities of the constituent atoms. The advantage of Hirshfeld charges over other methods is that the direct use of the charge density results in lower sensitivity to changes in basis set size, compared with partial charges obtained from atomic orbital contributions (e.g., Mulliken charges[159]) which can vary greatly.

It is also possible to use the diabatic fragments involved in an intermolecular reaction in the place of an atomic promolecule to observe changes in charge density over the course of a reaction. The charge density of each isolated fragment can be subtracted from the total charge density of the system and visualised. Positive lobes then represent a local increase in the electron density, and negative lobes represent a local decrease. An electron density difference plot (EDDP) for the addition of CN^- to acetone reveals the expected build-up of negative charge on the carbonyl oxygen (blue lobe, Figure 1.18a) and depletion of density on the cyanide fragment (red lobe). Additional chemical insight can be drawn from this analysis, for example the accumulation of electron density in the region corresponding to the forming C–C bond, depletion of density from the C=O π bond, polarisation of acetone charge density away from the approaching CN^- nucleophile, and disruption of $\sigma_{\mathrm{C-H}} \rightarrow \pi^*_{\mathrm{C-O}}$ hyperconjugation. Differences in Hirshfeld charges between the TS and isolated reactants (Δq) are also shown for reference.

Molecular orbitals

Additional insight into the origins of reactivity can be drawn from an examination of the molecular orbitals (MOs) involved in a reaction. There is debate over the physical significance of MOs,[160,161] since there is no unique definition and the connection to experiment is complex,[162] so care must be taken to ensure any chemical interpretations that result from their use depend as little on the chosen method as possible. Various methods exist to construct MOs and derive meaning from them, which can be broadly divided into two.

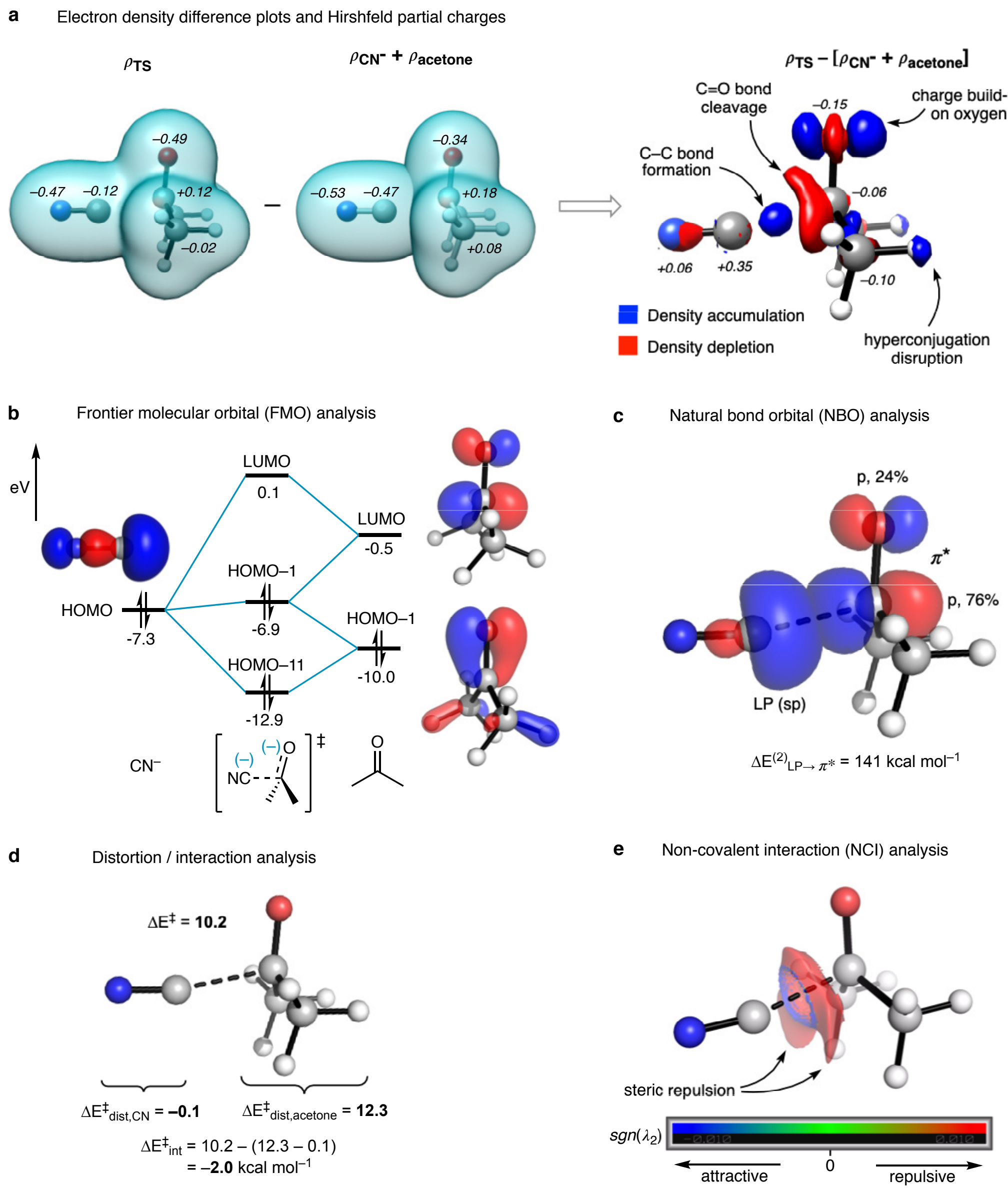

Figure 1.18: Analysis of the TS for the addition of CN⁻ to acetone, analysed using: **a.** Hirshfeld partial charges (q, in e) and an electron density difference plot (isovalue = 0.005 a.u.), **b.** frontier molecular orbital (FMO) analysis (isovalue = 0.1 a.u.), **c.** natural bond orbital (NBO) analysis (isovalue = 0.1 a.u.), **d.** distortion / interaction analysis, and **e.** non-covalent interaction (NCI) analysis (isovalue = 0.7 a.u.). Calculations at the CPCM(water)-PBE0-D3BJ/ma-def2-TZVP//CPCM(water)-PBE0-D3BJ/ma-def2-SVP level. Hirshfeld charges for hydrogens are summed into the nearest heavy atom. Unless specified, all energies are given in kcal mol^{-1}.

Delocalised MOs. The first of these categories, delocalised MOs, are obtained directly from a WFT or DFT calculation. They are often, by construction, symmetry-adapted and orthogonal, which can limit interpretability except in simple cases. However, delocalised MOs do have some important physical characteristics – for example, that the lowest vertical ionisation potential (VIP) of a molecule is approximately equal to the negative of the energy of the highest occupied MO (HOMO) within HF theory (Koopmans' theorem).[163] In addition, the HOMO-LUMO (lowest occupied molecular orbital) gap derived from DFT can be used as an approximation for the difference between the VIP and electron affinity.[164] The HOMO energy and HOMO-LUMO gap then inherit some physical meaning, relating to the ease with which a molecule may donate or accept electron density during a chemical reaction. For example, frontier molecular orbital (FMO) theory uses the energies and overlaps of the HOMO of a nucleophile and the LUMO of an electrophile to predict reactivity trends: minimising the HOMO-LUMO energy gap, or maximising the HOMO-LUMO overlap, leads to a lower energy TS (Figure 1.18b).[165–167] The HOMO-LUMO overlap term is especially significant for pericyclic reactions, where the relative phases of the HOMO and LUMO of a pair of reactants may lead to symmetry-allowed or symmetry-forbidden processes.[168,169] However, there are some disadvantages to using delocalised MOs to interpret reactivity: the fact that they are constructed to transform as the point group of the molecule results in artificial delocalisation effects that can confuse the connection to the chemist's view of bonding, and the choice of method can also strongly affect orbital energies and the extent of delocalisation. Nonetheless, delocalised MOs are undoubtedly a powerful tool for the prediction and rationalisation of chemical reactivity.

Localised MOs. The second category of MOs commonly used to analyse chemical reactions is localised MOs, where the orbitals are constructed such that they resemble electron (pairs), allowing a more direct comparison with familiar covalent / ionic representations of bonding.[170] One such localised MO framework is natural bond orbital (NBO) theory,[171] which takes delocalised MOs from a WFT or DFT calculation and transforms them into localised ones, first by constructing ‘natural atomic orbitals’ from the SCF first-order reduced density matrix, then forming directional ‘natural hybrid orbitals’ (NHOs), before allowing the overlap of these NHOs on different atoms to form NBOs (for an example see Figure 1.18c). The resultant bonding picture strongly resembles that described by Lewis,[170] where electrons are generally localised on one or two atoms only (for ordinary organic molecules). However, deviations from the localised picture, represented by an increase in the population of antibonding NBOs, represents a deviation from the Lewis representation of a molecule – commonly described as delocalisation. This delocalisation relates to conjugation and hyperconjugation concepts, for example in the description of the π-system of benzene using two cyclohexatriene resonance forms.

Donor-acceptor interactions, such as donation from bonding to antibonding orbitals, can be quantified using second order perturbation analysis of the NBO Fock matrix

$$\Delta E^{(2)}_{i \to j^*} = -n_i \frac{|\langle \phi_i^{(0)} | \hat{F} | \phi_j^{*(0)} \rangle|^2}{\epsilon_j^{*(0)} - \epsilon_i^{(0)}} \tag{1.16}$$

where n_i is the Lewis occupation number of the orbital (0, 1 or 2), $\phi_i^{(0)}$ is an occupied (Lewis) orbital, $\phi_j^{*(0)}$ is an unoccupied (non-Lewis) orbital, $\hat{F}$ is the Fock operator, and ϵ is the orbital energy. The NBO program is widely implemented in many popular electronic structure packages.

Distortion / interaction analysis

Further insight into the origins of reaction barriers can be derived by examing changes in geometry over the course of the reaction in terms of the energy; distortion / interaction analysis (DIA, also called the activation strain model)[172] is one such method. For an intermolecular reaction, the total energy at a given point on the potential energy surface (PES) can be described in terms of the energy required to distort each fragment into its geometry at that point ζ according to

$$\Delta E^{i}_{dist}(\zeta) = E^{i}(\zeta) - E^{i}(0) \tag{1.17}$$

where ΔE^{i}_{dist} is the distortion energy of the ith fragment, and the sum of all distortion energies is the total distortion energy (ΔE_{dist}). The distortion energy results from deviations from ideal bond lengths, angles, etc. (*i.e.*, increasing strain). The difference between the energy change resulting from fragment distortion and the total energy change, ΔE_{total}, corresponds to stabilisation through the formation of bonding and non-bonding intermolecular interactions, and is given by

$$\Delta E_{int}(\zeta) = \Delta E_{total}(\zeta) - \Delta E_{dist}(\zeta). \tag{1.18}$$

The position of a reacting complex on the PES is defined by a ‘critical geometry parameter’ – for example the forming C–C bond for the addition of CN^- to acetone (Figure 1.18d). In this case, at the TS the distortion energy of acetone dominates the activation barrier ($\Delta E^{\ddagger}_{dist,acetone}$ = 12.3 kcal mol^{-1}), and from the calculated activation energy of 10.2 kcal mol^{-1}, intermolecular interactions offer 2.0 kcal mol^{-1} stabilisation. In this example we have examined only the TS geometry for simplicity, however it is often necessary to calculate the distortion and interaction contributions along the entire reaction coordinate to draw correct conclusions about changes in activation energies between different systems.

Non-covalent interaction analysis

The methods of analysis discussed so far have focused on the effects of bonding on reactivity. However, non-covalent interactions (NCIs) can be equally important to unravel the impact of steric repulsion, dispersion, hydrogen bonding or attractive electrostatic interactions on reactivity and selectivity trends. The NCI method[173] makes possible the visualisation of these interactions by evaluating the electron density (ρ) and the reduced density gradient ($s \propto |\nabla\rho|/\rho^{4/3}$) on a grid spanning the molecule. This analysis provides a rough partition of real space into non-bonding regions (low-ρ, high-s), covalent bonds (high-ρ, low-s) and non-covalent interactions (low-ρ, low-s). The sign of the second-largest eigenvalue of the electron density Hessian at a particular point ($sgn(\lambda_2)\rho$) then reveals whether the interaction is attractive ($sgn(\lambda_2)\rho < 0$, local accumulation of density), repulsive ($sgn(\lambda_2)\rho > 0$, local depletion of density) or dispersive ($sgn(\lambda_2)\rho \approx 0$, weak accumulation of density). In the addition of cyanide to acetone, steric repulsion between the approaching anion and the methyl groups of the ketone destabilises the TS (Figure 1.18e).

Linear free energy relationships

LFERs work on the principle that there is a linear relationship between a physical organic parameter, for example a Hammett parameter (σ) that describe electron-withdrawal or donation,[174] and a free energy – usually a Gibbs free energy change ΔG, but sometimes approximated as an enthalpy change ΔH through neglect of changes in entropy. To obtain a predictive model from this data, linear regression (LR) can be used to predict a free energy based on a physical organic parameter, once the model has been fitted to some calculated or measured data. In the same way, multiple linear regression (MLR) can take multiple physical organic parameters simultaneously and return a predicted free energy, which is useful when multiple features, *e.g.*, sterics and stereoelectronics, are important to describe the observed trend in reactivity under study. LFERs are employed in Chapter 4, so a brief summary of the theory of LR and MLR is provided here.

Linear regression. LR is concerned with finding a linear relationship between two variables: an independent variable, x, which functions as the input, and a dependent variable, y, which functions as the output. LR then tests how well x describes y through the equation of a straight line

$$y = \beta_0 + \beta_1 x \tag{1.19}$$

where β_0 describes the y-intercept – the intrinsic value of y when x is zero (*i.e.* has no effect) – and β_1 is the gradient of the line – the effect size. To find β_0 and β_1, the squared error between the y values predicted by (1.19) and the true y values is minimised by least squares regression. One way of doing this is to introduce a term to (1.19) to account for the model error (residuals), $\epsilon = y - y_{pred}$, through

$$y = \beta_0 + \beta_1 x + \epsilon \tag{1.20}$$

then calculate ϵ_i for each pair (x_i, y_i) in the data set. The coefficients β_0 and β_1 can then be found by minimising the sum of square errors (residual sum of squares)

$$SS_{res}(\beta_0, \beta_1) = \sum_{i}^{N} \epsilon_i^2 \tag{1.21}$$

$$\frac{\partial SS_{res}}{\partial \beta_0} = 0 \tag{1.22}$$

$$\frac{\partial SS_{res}}{\partial \beta_1} = 0 \tag{1.23}$$

then solving the resultant simultaneous equations for β_0 and β_1. A metric is then required to quantify how well x describes y; this is most commonly done using the coefficient of determination, R^2, which is given by

$$\mathrm{R}^2 = 1 - \frac{SS_{res}}{SS_{tot}} \qquad SS_{tot} = \sum_{i}^{N} (y_i - \bar{y})^2 \tag{1.24}$$

where SS_{tot} is a normalising factor, and $\bar{y}$ is the mean of the true y values. An R^2 of zero then indicates no correlation, and $\mathrm{R}^2 = 1$ indicates perfect correlation. Other error metrics are commonly used, such as the mean absolute error (MAE), given by

$$MAE = \frac{1}{N} \sum_{i}^{N} |\epsilon_i| \tag{1.25}$$

where N is the sample size, and the root-mean-squared error (RMSE), which is given by

$$RMSE = \sqrt{\frac{1}{N} \sum_{i}^{N} \epsilon_i^2}. \tag{1.26}$$

RMSE punishes larger errors to a greater extent than MAE, and MAE is generally more interpretable.

Multiple linear regression. The LR approach that maps a single x onto y can be generalised to multiple x_i through the equation

$$y = \beta_0 + \sum_{i}^{N} \beta_i x_i + \epsilon \tag{1.27}$$

which describes MLR – the process of finding how well a *linear combination* of independent variables x_i describe the dependent variable y. The same process for finding the coefficients β_i can be used as for the LR case. Implicit in both LR and MLR are the assumptions that (1) there is a linear relationship between x and y, (2) the residuals ϵ are normally distributed, (3) each pair (x_i, y_i) is independent of all others, and (4) the residual ϵ does not depend on the value of x_i. In addition, MLR requires the assumption that the independent variables are uncorrelated.

A danger of MLR is that increasing the number of independent variables in the model will increase the correlation (R^2), but once unseen data is fed into the model the predictions may be poor. This is called overfitting, and can be avoided by minimising the number of independent variables included in the model. Additionally, an LFER should reproduce the chemical behaviour of the system under study, rather than simply provide a low prediction error, since this will provide chemical insight that can inform further improvements to the reaction or property under investigation. Worked examples of LR and MLR are shown in Appendix F.

1.3.5 Stern-Volmer quenching

Alongside the theoretical models and QM calculations carried out in this Thesis, we also investigated some aspects of reactivity using experimental techniques. In particular, in Chapter 3 we investigated rates of electron transfer between an excited photocatalyst and several components in the reaction mixture. We employed the Stern-Volmer method to quantify the kinetics of intermolecular luminescence quenching,[175] in which the decrease in luminescence intensity, represented as a normalised ratio (I_0/I), varies linearly with the concentration of a quencher Q according to the equation

$$\frac{I_0}{I} = 1 + k_q \tau_0 [Q] \tag{1.28}$$

where k_q is the quenching rate constant and τ_0 is the lifetime of the excited state. This result arises from the set of four processes that are assumed to completely define the kinetics of an excited state M^* formed upon irradiation of M:

Photoexcitation	$M + h\nu \rightarrow M^*$	$k_{abs}[M]$
Radiation	$M^* \rightarrow M + h\nu$	$k_r[M^*]$
Non-radiative decay	$M^* \rightarrow M$	$k_{nr}[M^*]$
Quenching	$M^* + Q \rightarrow M + Q$	$k_q[M^*][Q]$

Non-radiative decay includes processes such as vibrational relaxation and internal conversion. The radiation quantum yield (Φ) of M^* in the presence of Q is defined by the ratio of the radiation rate and all radiative and non-radiative processes

$$\Phi = \frac{k_r}{k_r + k_{nr} + k_q[Q]} \tag{1.29}$$

The ratio of quantum yields in the absence and presence of Q can be measured as a change in the emission intensity

$$\frac{\Phi_0}{\Phi} = \frac{I_0}{I} = \frac{k_r + k_{nr} + k_q[Q]}{k_r + k_{nr}} \tag{1.30}$$

which simplifies to (1.28), where $\tau_0 = (k_r + k_{nr})^{-1}$.

While τ_0 must be measured to obtain k_r, in this Thesis we are concerned only with relative quenching rates. In this case, ratios of the Stern-Volmer quenching gradient, $k_q\tau_0$, for different quenchers are sufficient, therefore explicit knowledge of τ_0 is not required.

2 |

Electronic structure and reactivity of [1.1.1]propellane

[1.1.1]Propellane (**1**) has attracted significant interest across many areas of chemistry over the past 50 years, from theoretical studies on its electronic structure to its use in organic synthesis as a precursor to bicyclo[1.1.1]pentanes. It exhibits a remarkably broad reactivity profile, undergoing additions of anions, radicals and cations to its highly-strained cage. Much of the recent [1.1.1]propellane literature discusses the importance of the release of strain energy to enable reactivity, yet this strain release is similar to cyclobutane and cyclopropane – which do not exhibit the same reactivity profile. In this Chapter, the relationship between the bonding and reactivity of [1.1.1]propellane will be explored, where a σ–π-delocalisation effect is proposed to work alongside strain release to enable such facile reactivity. A summary of computational benchmarking studies is also discussed to validate the approaches employed throughout this Thesis. This work was published in *Chemical Science* in 2020.[127]

2.1 Ground state electronic structure

To understand how the electronic structure of [1.1.1]propellane influences its reactivity, we carried out a detailed study of its electronic structure in the ground state and its change upon bond-stretching or ionisation. These analyses reveal the important features of the electronic structure of **1** that will determine its ability to react with anionic, radical or cationic species. Much experimental and computational effort has been put into understanding the nature of **1**, and some of the key studies will be summarised here.

The ground state geometry and electronic structure of **1** has been examined by low-temperature gas-phase electron diffraction (GPED),[176] vibrational spectroscopy,[177] X-ray diffraction,[178] photoelectron spectroscopy[179] and NMR,[180] which have been complemented by extensive computational studies.[80–82,181–186] The interbridgehead (C1–C3) bond length from GPED is estimated to be 1.594 Å,[176] which is only slightly elongated compared with ethane (1.524 Å),[187] suggestive of a covalent C1–C3 bond (Figure 2.1a). However, photoelectron spectroscopy revealed a very short vibrational progression through ionisation from the $3a_1'$ orbital responsible for the C1–C3 bond (Figure 2.1b),[179] in line with calculations of negligible orbital overlap[80] that would point to a complete lack of a σ bond between the bridgehead carbon atoms. Despite this latter evidence, the calculated singlet-triplet gap of **1** is large ($\approx$ 79 kcal mol^{-1} at the MP2/6-31G* level),[182] consistent with its resistance towards oligomerisation in solution.

Jackson and Allen proposed that the bonding energy apparently caused by a C1–C3 interaction is in fact a result of three-centre two-electron bonding (σ-bridged π bonding) involving bridgehead-bridge orbital interactions (Figure 2.1c),[181] although this was disputed by Davidson on the grounds that the C1–C3 interaction is net π-antibonding.[182] Studies of the electron density of **1** provided further insight; while a bond critical point was observed between C1 and C3, the Laplacian of the electron density at this point – which should be negative for a covalent interaction – was found to be positive through both computational and experimental studies.[177,188] Indicative of a depletion of electron density, this result led to the classification of the C1–C3 bond of **1** as a charge-shift bond using Valence Bond (VB) theory. This type of bonding is typified by the stabilisation energy arising from resonance between the covalent ([C1$^\bullet \cdots {}^\bullet$C3], repulsive) and

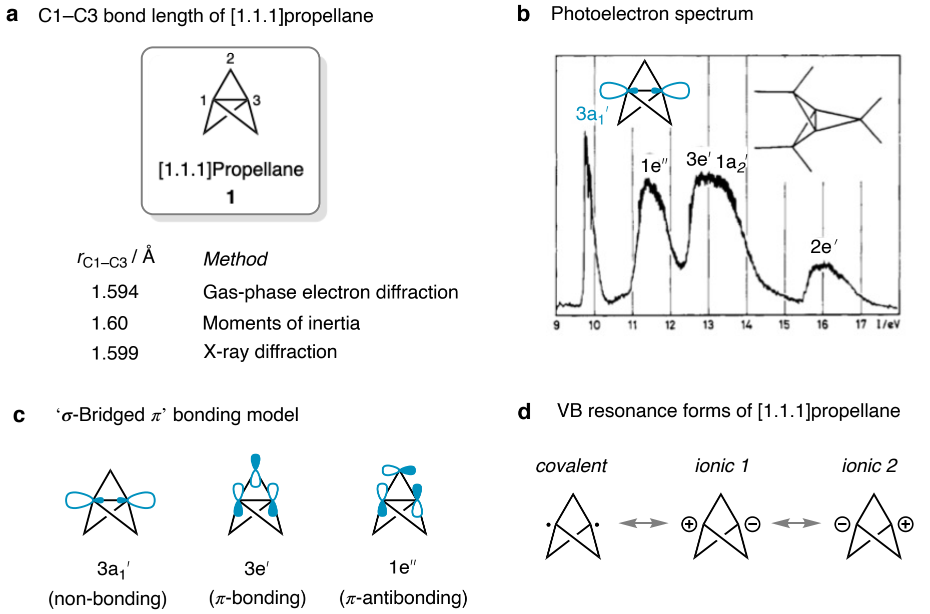

$r_{C1–C3}$ / Å	*Method*
1.594	Gas-phase electron diffraction
1.60	Moments of inertia
1.599	X-ray diffraction

Figure 2.1: a. Experimentally-determined C1–C3 bond lengths for [1.1.1]propellane from Refs. [176–178]. **b.** Photoelectron spectrum of [1.1.1]propellane, adapted with permission from Ref. [179]. **c.** Jackson and Allen's σ-bridged π bonding model for [1.1.1]propellane based on the $3e'$ MO, and the $1e''$ π-antibonding MO pointed out by Davidson. **d.** Valence bond (VB) resonance forms that describe the charge-shift bond of [1.1.1]propellane.

ionic ([C1$^{(-)}\cdots{}^{(+)}$C3] and [C1$^{(+)}\cdots{}^{(-)}$C3], attractive) structures (Figure 2.1d). In **1**, this situation is suggested to arise due to significant Pauli repulsion pressure between each of the C1/3–C2 ‘wing’ bonds and the C1–C3 bond.

Following these studies, we sought to further investigate the ground state electronic structure of **1** to ensure an accurate reference was available to determine changes in electronic structure through reactivity. We investigated this possibility with the complete active space (CASSCF) method, employing a (2,2) active space to allow two electrons to populate both the σ and σ^* orbitals such that any diradical character could be accurately described (Figure 2.2a) We found that $\Psi_{\text{CASSCF(2,2)}} = 0.95(a_1')^2(a_2'')^0 + 0.05(a_1')^0(a_2'')^2$, leading to a population of the C1–C3 σ orbital of 1.91 electrons. For context, ‘ordinary’ closed-shell organic molecules feature orbital occupation numbers in excess of 1.98 electrons, sug-

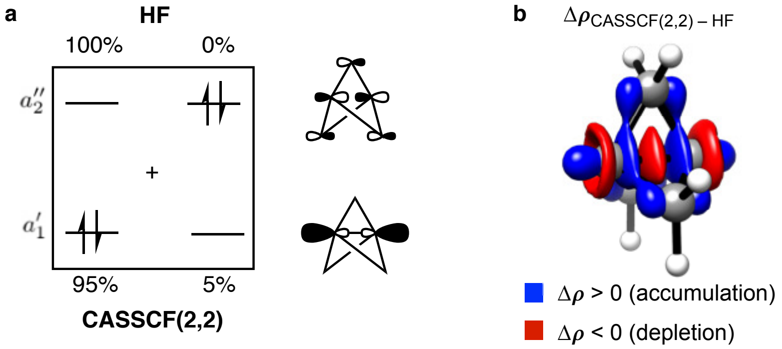

Figure 2.2: a. Active orbitals selected for the description of the interbridgehead bond of [1.1.1]propellane (**1**), and comparison of HF and CASSCF(2,2) configuration coefficients. **b.** Electron density difference plot for [1.1.1]propellane at the CASSCF(2,2) and HF levels (def2-QZVPP basis). Isovalue = 0.002 a.u.

gesting correlation effects must be carefully accounted for in our description of **1**. Perplexingly, the large HOMO-LUMO gap (E_{gap} = 13.0 eV, RHF/def2-QZVPP) is not typical of static correlation effects that might be expected from the CASSCF wavefunction. Expanding the active space to include the next set of bonding / antibonding degenerate orbitals (e'') with a CASSCF(6,6) calculation revealed an almost identical electronic structure and natural orbital occupation numbers (NOONs) of these e'' orbitals >1.98 / < 0.02, suggesting that the (2,2) active space is sufficient to describe any static correlation effects present in the molecule.

The calculated singlet-triplet gap ($\Delta E_{\text{S-T}}$) at the CASSCF(2,2)/def2-QZVPP level is 131 kcal mol^{-1}, but only 83 kcal mol^{-1} at the HF level. Since the triplet state is well-described by a single determinant, the increase in $\Delta E_{\text{S-T}}$ at the CASSCF level must occur due to stabilisation of the singlet state. To investigate this effect further, we visually compared the difference in total electron density (ρ) between the CASSCF(2,2) and HF wavefunctions ($\Delta\rho_{\text{CASSCF(2,2) - HF}}$). HF theory will be expected to overlocalise electron density in bonding regions due to a lack of Coulomb correlation, a contribution present in CASSCF. For [1.1.1]propellane, $\Delta\rho_{\text{CASSCF(2,2)}-\text{HF}}$ reveals the expected depletion of density from the centre of the cage – but a redistribution of electron density through the accumulation of the excess density onto the wing carbon atoms (Figure 2.2b). We interpret this redistribution as the sacrifice of the C1–C3 σ bond to form a C1–C2 π-bonding interaction. In terms of electronic configurations, this process can be thought of as a $\sigma \rightarrow [\sigma^* + \pi]$ stereoelectronic interaction, or 'σ–π-delocalisation'. The result of this delocalisation effect is two-fold: firstly, the expected electronic unpairing that would give an open-shell singlet state is avoided; and secondly, these π-bonding interactions may provide structural integrity to the propellane cage, increasing the activation barrier to unimolecular decomposition.

Localised representation. The σ–π-delocalisation effect in [1.1.1]propellane can be also analysed with a localised representation of the CASSCF(2,2) wavefunction. Here, we employ the Foster-Boys localisation[189] of the SCF orbitals, which reveals the expected bridgehead-centered orbital pair (Figure 2.3a), with three electronic configurations comprising one covalent [$\Psi_{\text{cov}} = (\phi_1)^1(\phi_2)^1$] and two ionic [$\Psi_{\text{ion,1}} = (\phi_1)^0(\phi_2)^2$ and $\Psi_{\text{ion,2}} = (\phi_1)^2(\phi_0)^0$] states. The resulting wavefunction: $\Psi_{\text{CASSCF(2,2),loc}} = 0.71\Psi_{\text{cov}} + 0.15\Psi_{\text{ion,1}} + 0.15\Psi_{\text{ion,2}}$, indicates a 30% contribution of ionicity to the bond, in good agreement with that obtained by Davidson at the two-configuration SCF level.[182] This representation is also in qualitative agreement with that arising from VB theory as described by Wu, Shaik, Hiberty and co-workers: $\Psi_{\text{VB}} = 0.62\Psi_{\text{cov}} + 0.19\Psi_{\text{ion,1}} + 0.19\Psi_{\text{ion,2}}$.[186] Interestingly, the weights of the ionic structures were found to be greater for ethane than **1**. However, the key difference between the two C–C bonds lies in the nature of the covalent interaction: it is attractive for ethane, but repulsive for **1**.

An alternative localisation scheme is available within NBO theory. In particular, second-order perturbation theory analysis of the NBO Fock matrix reveals that the σ–π-delocalisation effect is equivalent to geminal hyperconjugation, in which the $\sigma_{\text{C1–C3}}$ and $\sigma_{\text{C1–C2}}$ orbitals donates electron density into the $\sigma^*_{\text{C1–C2}}$ and $\sigma^*_{\text{C1–C3}}$

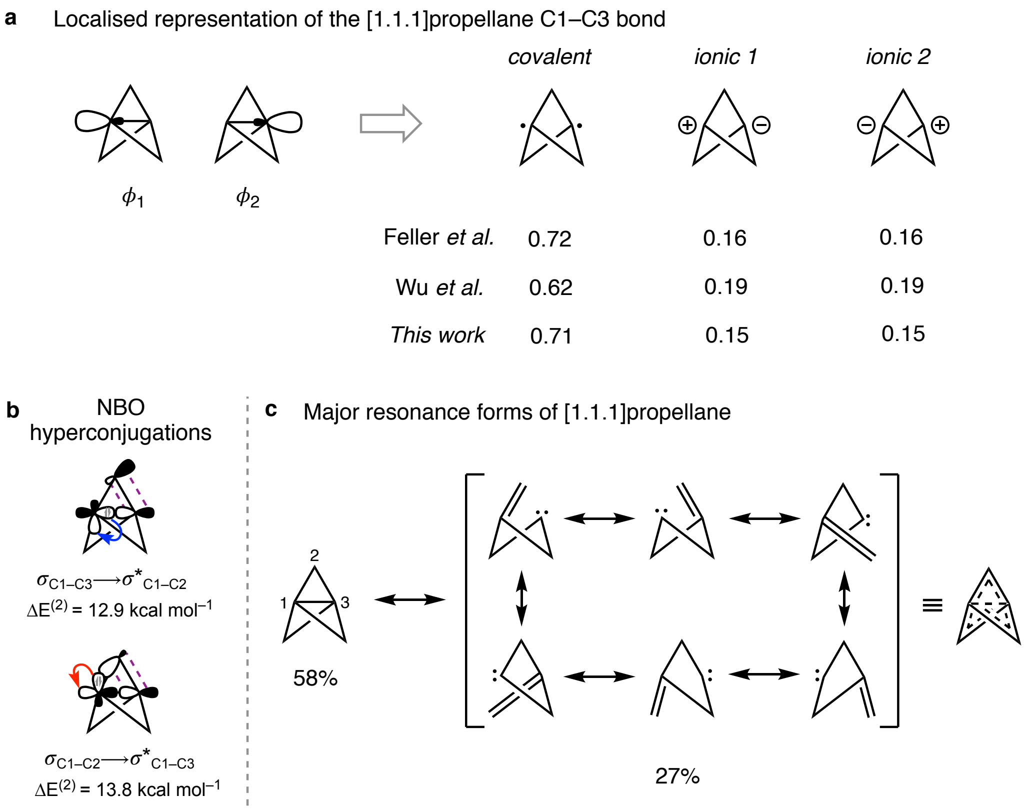

	covalent	ionic 1	ionic 2
Feller *et al.*	0.72	0.16	0.16
Wu *et al.*	0.62	0.19	0.19
This work	0.71	0.15	0.15

Figure 2.3: **a.** Localised CASSCF(2,2) active orbitals of [1.1.1]propellane, and weights of covalent and ionic resonance forms from Refs. [182] and [186]. **b.** Geminal hyperconjugation between the interbridgehead and wing bonds of [1.1.1]propellane. **c.** Resonance structures for [1.1.1]propellane.

orbitals, respectively (Figure 2.3b). These interactions are significant (12.9 and 13.8 kcal mol^{-1}, respectively) compared with the equivalent interactions in cyclopropane (5 kcal mol^{-1}), suggesting that geminal hyperconjugation, which has already been suggested to account for the low strain energy of cyclopropane,[45] plays an even more important role in stabilising the electronic structure of **1**. The geminal hyperconjugation model allows the representation of [1.1.1]propellane as a resonance between its Lewis structure, in which all C–C bonds are σ bonds, and six degenerate alkene/carbene pairs (Figure 2.3c). Natural resonance theory indicates that the Lewis structure contributes 58% to the total structure in [1.1.1]propellane, while each alkene/carbene pair contributes 4.5%, leading to a total contribution of 27%. These results confirm that the C1–C3 bond is delocalised over the cage.

2.1.1 Electronic structure methods

Since our CASSCF calculations revealed only a small contribution ($\approx$ 5%) of a doubly-excited determinant wavefunction of [1.1.1]propellane, we were confident that a robust single-reference approach would provide sufficient accuracy to compute the desired molecular properties. We settled on the approximately linear-scaling DLPNO-CCSD(T) method[141] with a large def2-QZVPP basis set[152] to calculate several properties of [1.1.1]propellane, such as the singlet-triplet energy gap, the ionisation potential and the electron density, and used these values as a reference method to benchmark a selection of density functionals for the reactivity studies.

C1–C3 bond distance. One of the first indicators of the behaviour of a given method is its ability to reproduce meaningful geometries. In particular, we evaluated how well the C1–C3 bond length of [1.1.1]propellane is described by a range of electronic structure methods (Figure 2.4). While different experimental values have been reported for this distance which differ in the technique employed, here we chose the value obtained from gas phase electron diffraction (1.594 Å) as our reference,[176] as it is free from crystal packing effects. At the HF level, this distance is underestimated (1.540 Å) due to overlocalisation of the electron density in this region. On the other hand, MP2 gives the smallest error among the methods tested; however, this may be coincidental as other properties are only poorly reproduced (*vide infra*). Pure DFT methods slightly underestimate the C1–C3 distance, which may seem surprising as one would expect that electron density in bonding regions should be underestimated due to self-interaction error.[190] Addi-

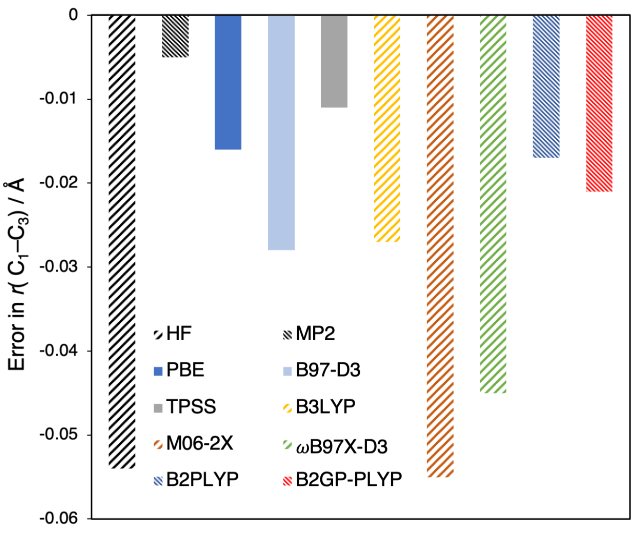

Figure 2.4: Error in interbridgehead (C1–C3) bond length compared with gas-phase electron diffraction measurements, employing a def2-QZVPP basis set.

tion of exact HF exchange causes further bond shortening, presumably due to the aforementioned localisation error. Finally, the inclusion of MP2-like correlation in double-hybrid functionals reduces the error, lengthening the C1–C3 bond but still falling short of the experimental value. We suspect the geometric constraints provided by the cage play a significant role in how well the C1–C3 bond length is described.

Singlet-triplet gap. The singlet-triplet gap of [1.1.1]propellane indicates the extent of electron pairing in the C1–C3 bond, and is therefore a description of σ–π-delocalisation. We calculated $\Delta E_{\text{S–T}}$ over a range of C1–C3 bond lengths for a selection of methods and compared these results to the those obtained at the DLPNO-CCSD(T)/def2-QZVPP level (Figure 2.5). As expected, HF theory greatly underestimates $\Delta E_{\text{S–T}}$ over the range of bond lengths. We attribute this behaviour to overlocalisation of the density at the centre of the propellane cage and consequently overestimation of electron-electron repulsion. While this is effect is somewhat corrected with MP2, $\Delta E_{\text{S–T}}$ is now overestimated by $\approx$ 10 kcal mol^{-1}.

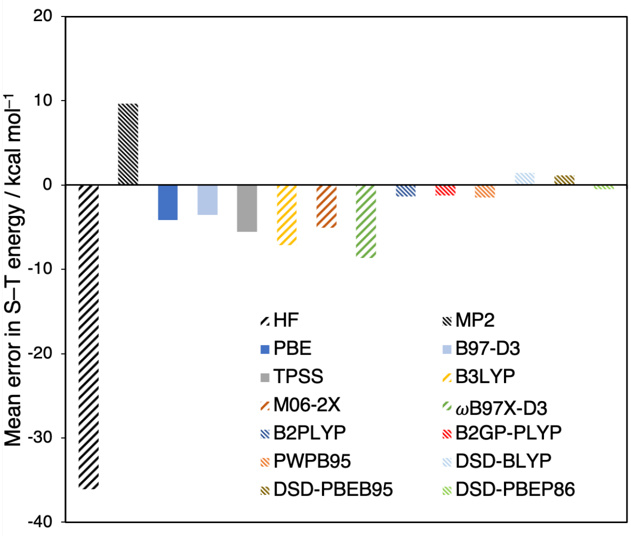

Figure 2.5: Mean errors in singlet-triplet energies ($\Delta E_{\text{S–T}}$, kcal mol^{-1}) compared with DLPNO-CCSD(T), employing a def2-QZVPP basis set. $r_{\text{C1–C3}}$ = 1.54 to 2.00 Å in 9 steps of 0.05 Å.

GGA/meta-GGA density functionals tend to underestimate $\Delta E_{\text{S–T}}$, which is made worse with the inclusion of exact HF exchange in hybrid functionals. While the inclusion of exact exchange often improves the behaviour of pure density functionals,[144] we suspect that the delocalised nature of the interbridgehead C–C bond diminishes the error cancellation that would usually result in more localised electronic structures. Despite the poor performance of single-hybrids, all double-hybrid functionals tested performed well. The inclusion of MP2-like correlation may improve the description of the system by including the important double-excitation featured in the CASSCF wavefunction. In general, we anticipate that functionals in which $\Delta E_{\text{S–T}}$ is underestimated will give activation barriers that are much too low for [1.1.1]propellane, which will be problematic given that electronic activation barriers are likely to already be small for many of these reactions.

Vertical ionisation potential. The reaction of [1.1.1]propellane with cations is likely to involve the donation of electron density out of the propellane cage, and towards the approaching electrophile. In the most extreme case, this is equiv-

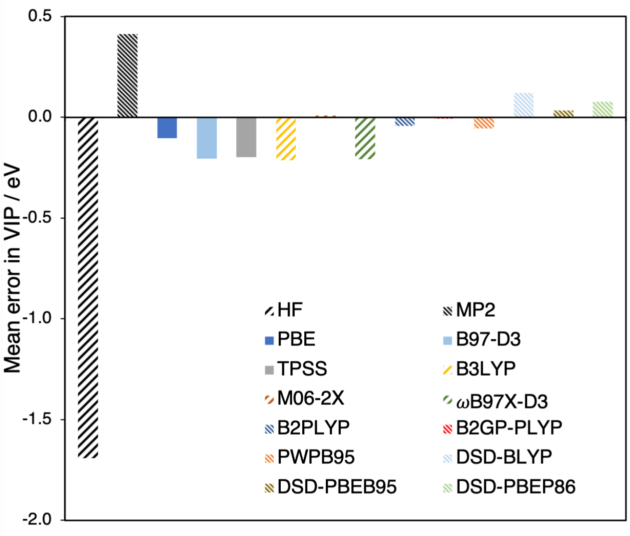

Figure 2.6: Mean errors in the vertical ionisation potential (VIP, eV) compared with DLPNO-CCSD(T), employing a def2-QZVPP basis set.

alent to the ionisation of the propellane cage, which is known to cause rapid fragmentation.[191] We therefore computed the vertical ionisation potential (VIP) for a range of functionals and compared them to the DLPNO-CCSD(T)/def2-QZVPP value (Figure 2.6). HF theory vastly underestimates the VIP of [1.1.1]propellane, in line with our suggestion that this method overestimates electron-electron repulsion in the ground state. On the other hand, MP2 overestimates the VIP, which suggests that the singlet state is over-stabilised. Among the GGA density functionals, PBE is surprisingly accurate, giving an error of only –0.10 eV; however, we suspect this is fortuitous (*vide infra*). Single-hybrid functionals give similar performance to GGA/meta-GGAs, although M06-2X gives almost exact agreement with the reference value. Double-hybrid functionals generally perform well; in particular, B2GP-PLYP led to an error of just –0.01 eV.

Density. To confirm that double-hybrid DFT is correctly describing the electronic structure of the interbridgehead C1–C3 bond of [1.1.1]propellane, we explored the ability of different DFT functionals to reproduce the CASSCF electron density

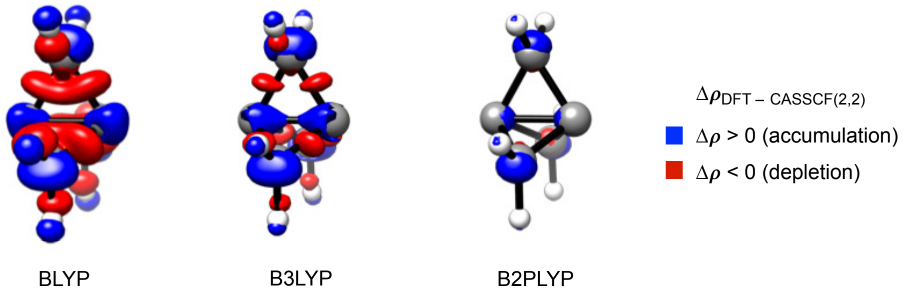

Figure 2.7: Electron density difference plots for [1.1.1]propellane at the DFT level (BLYP, B3LYP and B2PLYP) compared with CASSCF(2,2), employing a def2-QZVPP basis set. Isovalue = 0.01 a.u.

(Figure 2.7). We chose three functionals from different rungs of the DFT Jacob's Ladder[146]: BLYP (GGA), B3LYP (single hybrid GGA) and B2PLYP (double-hybrid GGA).[148,192,193]

As we move up the Jacob's ladder, density differences relative to CASSCF become smaller, in agreement with the improved performance in the singlet-triplet gaps and VIP estimations. For example, employing BLYP results in accumulation of density on the carbon atoms and depletion along the side bonds. This would suggest that repulsion between the side and central bonds is underestimated, therefore σ–π-delocalisation is not properly described. B3LYP, which contains 20% HF exchange,[193] provides a better description, despite HF suffering from overlocalisation problems. Here, accumulation of density is observed on the carbon centres and along the central bond. The double-hybrid B2PLYP functional, which includes 53% HF exchange and 27% PT2 correlation,[148] corrects this error, resulting in a density closely resembling the CASSCF density. The slight overlocalisation on the wing carbon atoms is likely to arise from truncation of the CASSCF orbital space (*i.e.*, neglect of dynamic correlation).

From the results described above, we anticipate that double-hybrid DFT functionals will provide the optimal choice to describe the reactivity of [1.1.1]propellane. While the C1–C3 bond is slightly underestimated, the inclusion of MP2-like correlation significantly improves electronic descriptions, including the singlet-triplet gap, VIP and electron density. For systems where double-hybrids become prohibitively expensive, such as transition state calculations on medium-to-large molecules, single-hybrid functionals will be required, with the expectation that activation barriers will be slightly underestimated due to singlet destabilisation arising from the HF localisation error.

2.2 Rationalising the reactivity of [1.1.1]propellane

Having identified the presence of σ–π-delocalisation in [1.1.1]propellane, we investigated how it might influence reactivity. We suspected that the unusually broad reactivity profile observed with this system might be caused by this delocalisation effect – a small penalty for distorting the electron density in the C1–C3 bond could indicate low activation barriers with nucleophilic species, and the possibility of rapid electronic repulsion-relieving reactions with electrophiles.

We therefore undertook a systematic study of the reactivity of [1.1.1]propellane with three types of system: anionic, radical, and cationic, using a minimal model to achieve high accuracy and efficiency. The applicability of this model was later tested in experimentally-relevant systems.

2.2.1 Reactions with anions

The addition of anionic species to [1.1.1]propellane can be thought of as an S_N2 reaction, in which the leaving group (nucleofuge) is the distal C3 atom of the cage. However, at odds with most S_N2 reactions, there is no requirement to planarise the central atom (C1) due to its pre-existing inverted geometry. As distortion of the electrophile is usually the origin of the TS barrier in S_N2 reactions,[172] one would

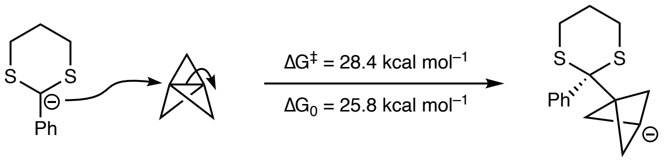

Scheme 2.1: Key step in Walsh's dithiane addition to [1.1.1]propellane, calculated at the SMD(1,4-dioxane)-UM06-2X/6-311+G(d,p)//UB3LYP/6-31+G(d,p) level.

expect low barriers for additions to [1.1.1]propellane, especially considering the strain-release driving force for the reaction. However, counter to this intuition, anionic addition reactions tend to require elevated temperatures and long reaction times; for example, temperatures in excess of 50 °C and reaction times of around 16 h for the addition of turboamide anions to [1.1.1]propellane.[114,194] These requirements were corroborated by Walsh in a combined experimental and computational study on the addition of dithiane anions to [1.1.1]propellane (Scheme 2.1).[115,195] Their calculated activation barriers of $\approx$ 30 kcal mol^{-1} agree with the need for experimental conditions of 80 °C and 16 h reaction time.

Reaction profiles and distortion / interaction analysis

To investigate the origins of TS barriers in anionic additions to [1.1.1]propellane, we constructed a model system with hydride as the nucleophile. This system was first modelled at the CASSCF(4,3)/ ma-def2-QZVPP level of theory. The active orbitals were chosen based on the combination of the doubly-occupied hydride 1s orbital (ϕ_2, Figure 2.8) with the bonding and antibonding combinations of the C1–C3 σ bond (ϕ_1 and ϕ_3). A relaxed scan of the forming C–H bond length (r_1) revealed a single maximum at 1.9 Å, and an overall electronically favourable process with a driving force of –20 kcal mol^{-1}. Over the course of the reaction, the orbital characteristics change from the initial H 1s, σ and [$\sigma^* + \pi$] to the bonding (ϕ_1), non-bonding (ϕ_2) and antibonding (ϕ_3) combinations of two p orbitals (propellane fragment) and the H 1s orbital. Only two significant configuration

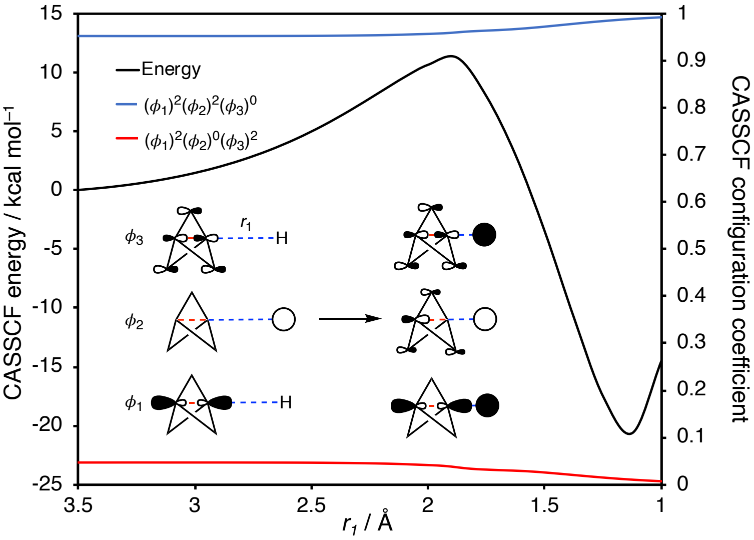

Figure 2.8: Potential energy surface for the addition of hydride to [1.1.1]propellane at the CASSCF(4,3)/ma-def2-QZVPP level (left axis), and the CASSCF(4,3) configuration coefficients for this process (right axis). Inlay: Composition of active orbitals ϕ_{1-3} along the reaction coordinate.

coefficients were observed along the PES, the largest being the $(\phi_1)^2(\phi_2)^2(\phi_3)^0$ configuration, with a smaller contribution from the $(\phi_1)^2(\phi_2)^0(\phi_3)^2$ configuration. In fact, the latter configuration features only at large C–H distances, and corresponds to the double excitation observed in isolated [1.1.1]propellane (*vide supra*). The weight of the coefficient for this doubly-excited configuration decays smoothly over the course of the reaction as orbital mixing occurs, so there is no appreciable multireference character at the TS. We can therefore safely employ DLPNO-CCSD(T) as we did for benchmarking studies. Both ϕ_2 and ϕ_3 retain the contribution of the bridging carbon p orbitals, and near-double occupation of ϕ_2 in the adduct suggests considerable delocalisation of the BCP anion over the cage.

To further analyse this reaction, we carried out a distortion / interaction analysis (DIA) and electron density difference analysis to examine the role of propellane cage distortion and electronic delocalisation in the observed reactivity (Figure 2.9). To our surprise, the distortion energy (ΔE_{dist}) remains close to zero

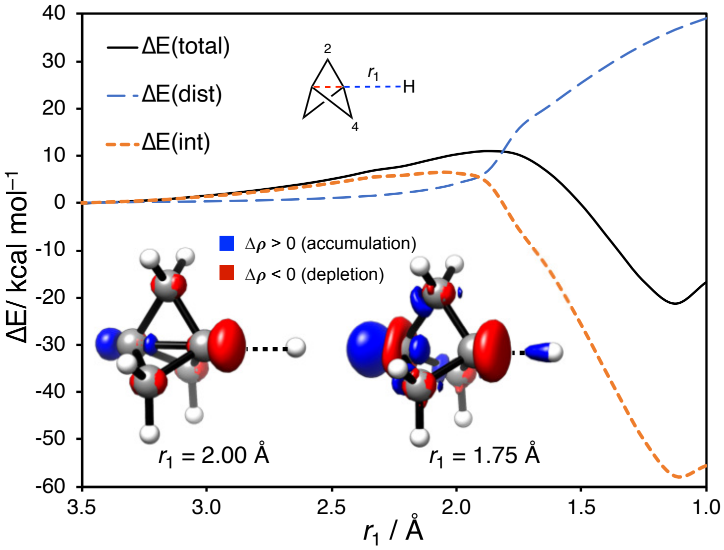

Figure 2.9: Distortion / interaction analysis for the addition of hydride to [1.1.1]propellane, at the SMD(Et_2O)-DLPNO-CCSD(T)/ma-def2-QZVPP level. Inlay: Electron density difference plots (isovalue = 0.01 a.u.) pre- (r_1 = 2.00 Å) and post-TS (r_1 = 1.75 Å), at the CASSCF(4,3) [hydride + [1.1.1]propellane] / CASSCF(2,2) [[1.1.1]propellane] / HF [hydride] levels (ma-def2-QZVPP basis set).

prior to the TS – only when the forming bond reaches 2.5 Å does distortion rise above 1 kcal mol^{-1}. At this point, the total barrier is already 5 kcal mol^{-1} indicating that interaction energy (ΔE_{int}) is positive and responsible for most of the energy barrier, an unusual phenomenon previously noted for some cycloaddition reactions.[172] This ΔE_{int} dominance is only overtaken at the TS, where [1.1.1]propellane distortion rises quickly and ΔE_{int} becomes stabilising. During the formation of the product state, the C2–C4 distance decreases from 2.21 Å to 2.11 Å, and the cage distorts by almost 40 kcal mol^{-1} – a value which we can later use to compare anionic reactivity with that of radicals and cations.

A density difference analysis, using the same fragments and methodology as the DIA (Figure 2.9, inlay), reveals that as the TS is reached, the interbridgehead C1–C3 bond becomes polarised such that charge is depleted from the C1 region facing the hydride anion and accumulated at the back of the cage. We suggest that while this polarisation is disfavoured, the delocalised electron density of the C1–C3 bond reduces the barrier compared with a more localised σ bond.

At the TS, a more substantial change in electronic structure is initiated, featuring an accumulation of density onto the wing carbon atoms. This indicates an increase in σ–π-delocalisation in the product bicyclopentyl anion compared with the starting propellane, which accounts for the observed cage compression from the DIA.

The addition of anions to [1.1.1]propellane can therefore be understood as follows: The energy barrier for anion addition primarily arises due to distortion of the propellane electron density rather than geometry; specifically, from polarisation of the electron density of the C1–C3 bond. Cage geometric distortion is delayed as a result, with most geometric deformation occurring after the TS. Carbanion delocalisation occurs in the product through a similar mechanism to σ–π-delocalisation in the starting [1.1.1]propellane.

Benchmarking an anionic addition

To analyse this reaction in increasingly complex systems, we sought to identify a general, accurate and efficient methodology as an alternative to CASSCF. We performed a relaxed PES scan at the DLPNO-CCSD(T)/ma-def2-QZVPP// CASSCF(4,3)/ma-def2-QZVPP level of theory, and evaluated single point electronic energies with a range of density functionals (Figure 2.10a) . We quantified the overall performance of each based on the mean absolute error (MAE) and maximum error (ME, Figure 2.10b).

As expected, HF theory underestimates the long-range interactions and considerably overestimates the TS barrier. This contrasts with pure density functionals, which underestimate both the activation barrier and overall reaction energy.

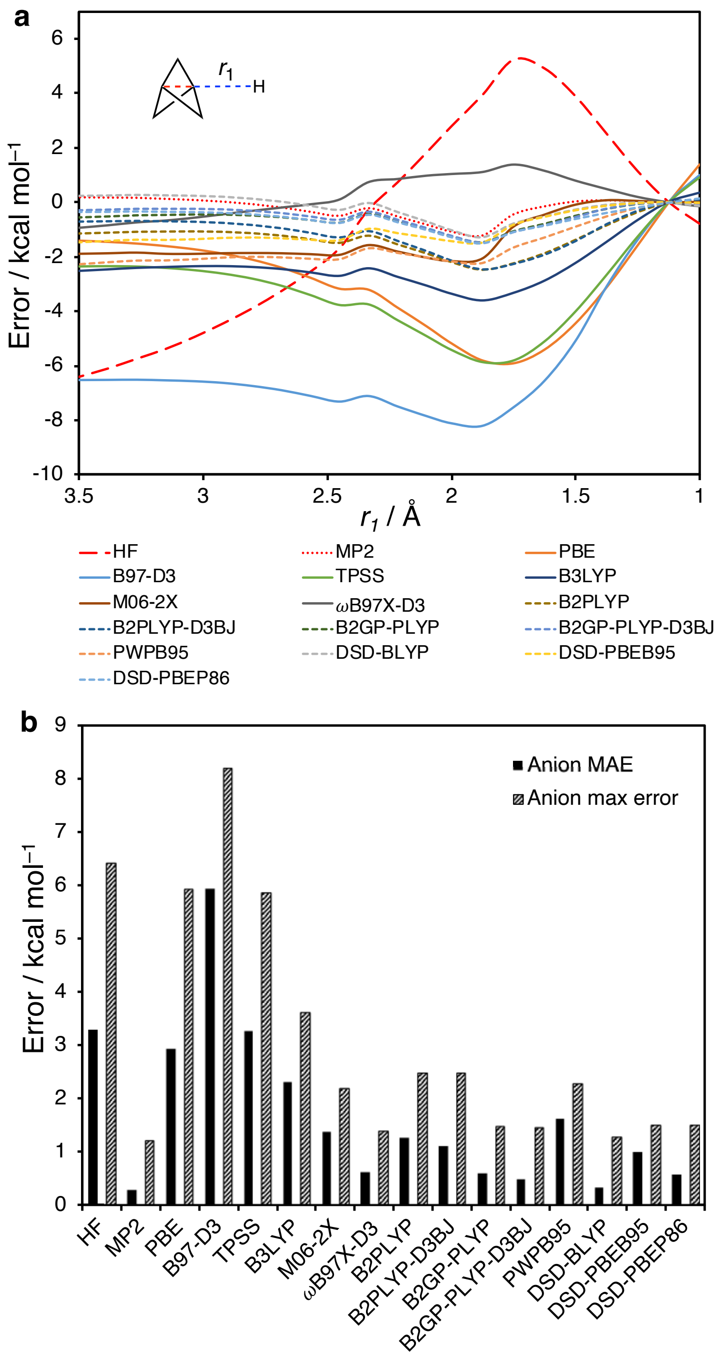

Figure 2.10: a. Potential energy surface errors for the addition of hydride to [1.1.1]propellane, with each method (ma-def2-QZVPP level) referenced to the DLPNO-CCSD(T)/ma-def2-QZVPP energy. **b.** Mean absolute error (MAE) and maximum error for the PESs described in **a**.

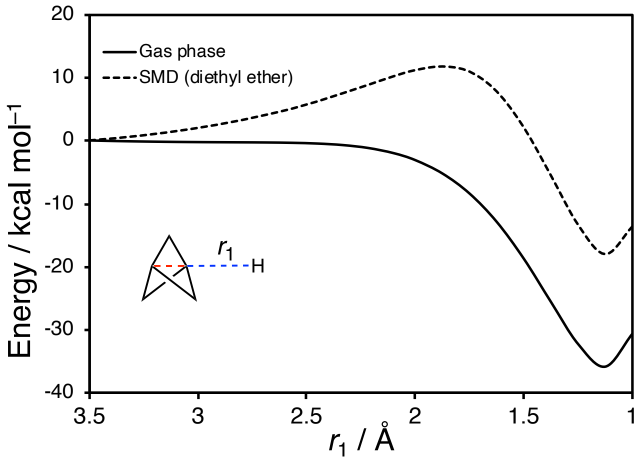

Figure 2.11: Effect of solvation on the addition of hydride to [1.1.1]propellane at the [SMD(Et_2O)]-DLPNO-CCSD(T)/ma-def2-QZVPP level.

The performance of hybrid DFT is much improved, but the TS barrier is non-systematically either over- or underestimated with different functionals. Double-hybrid DFT performs uniformly well over the whole PES. The smallest MAEs and MEs were observed for MP2, B2GP-PLYP-D3BJ, DSD-BLYP and ωB97X-D3, suggesting that any of these methods would be suitable for describing the reactivity of [1.1.1]propellane with anions. However, given the poorer performance of MP2 and ωB97X-D3 for the description of ground state properties, we suggest that double-hybrids will be more reliable in general.

Finally, we evaluated the effect of solvation on the reactivity of **1** employing the SMD implicit solvent model for Et_2O,[157] since ethereal solvents are commonly used in reactions of **1** – either by choice or because **1** is conveniently synthesised and stored in Et_2O.[196] As expected, solvation stabilises the hydride nucleophile relative to the bicyclopentyl anion, resulting in a significant barrier increase (Figure 2.11). For this reason, we employed an implicit solvent model for the subsequent study in which comparison with experiment is to be made.

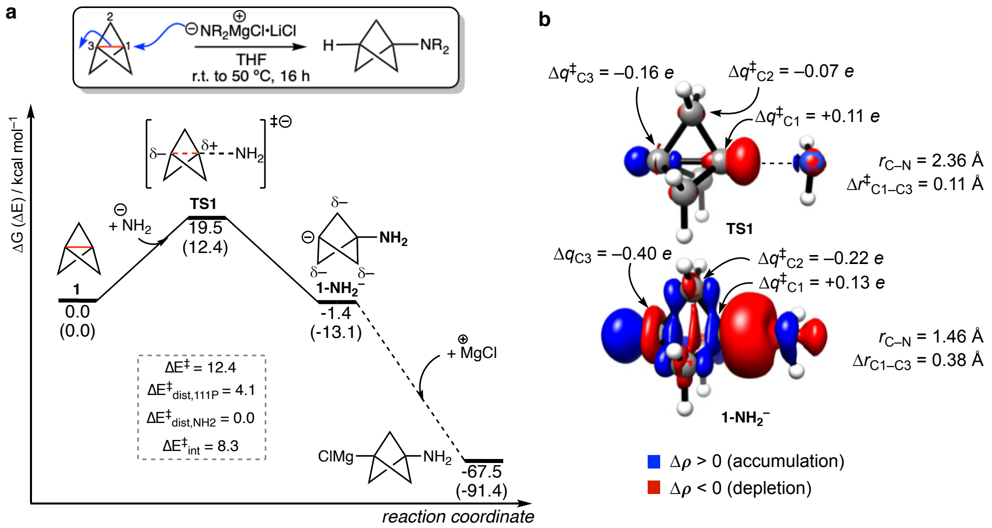

Figure 2.12: a. Potential energy surface for Baran's turboamide addition to [1.1.1]propellane, calculated with NH_2^- as the nucleophile, at the SMD(THF)-DLPNO-CCSD(T)/ma-def2-QZVPP//SMD(THF)-B2GP-PLYP-D3BJ/ma-def2-TZVP level (323.15 K, 1 M). Inlay: Distortion / interaction analysis for **TS1**. **b.** Electron density difference analysis and Hirshfeld partial charges for **TS1** and **1-NH$_2^-$**. $\Delta q^\ddagger = q^\ddagger_{\mathbf{TS1}} - q_{\mathbf{1}}$; $\Delta q = q_{\mathbf{1\text{-}NH_2^-}} - q_{\mathbf{1}}$; $\Delta r^\ddagger = r^\ddagger_{\mathbf{TS1}} - r_{\mathbf{1}}$.

Case study: Strain-release amination

Having identified the important features that determine the reactivity of anions with [1.1.1]propellane, we investigated the seminal strain-release amination reaction which features an amide anion addition to [1.1.1]propellane (Figure 2.12a).[114,194] A model NH_2^- anion was chosen for this study to avoid complications arising from conformational effects. The reaction was modelled using implicit THF with the SMD solvation model to match the experimental conditions.

Addition of NH_2^- to [1.1.1]propellane is only slightly exergonic (ΔG_0 = –1.4 kcal mol^{-1}, **1-NH$_2^-$**), suggesting that much of the strain release effect is cancelled by the instability of the resulting bicyclopentyl anion. Despite this lack of thermodynamic driving force, the activation barrier is low ($\Delta G^\ddagger$ = 19.5 kcal mol^{-1}, **TS1**), a phenomenon that we can explain using our σ–π-delocalisation model introduced above: the activation barrier results from distortion of the delocalised

C1–C3 electron density, which incurs a much smaller penalty than geometric distortion which would feature in a later TS. Only upon quenching the bicyclopentyl anion **1-NH$_2^-$** with a MgCl$^+$ ion does the reaction become exergonic (ΔG_0 = –67.5 kcal mol^{-1}), suggesting that the quenching of charge separation is in fact the reaction driving force, rather than strain release.

DIA of **TS1** reveals that the 12.4 kcal mol^{-1} electronic barrier arises primarily from the destabilising interaction between NH$_2^-$ and [1.1.1]propellane ($\Delta E^{\ddagger}_{\text{int}}$ = +8.3 kcal mol^{-1}), with a much smaller contribution from the distortion of the propellane cage ($\Delta E^{\ddagger}_{\text{dist},\mathbf{1}}$ = 4.1 kcal mol^{-1}) and of the amide anion ($\Delta E^{\ddagger}_{\text{dist,NH}_2^-}$ = 0.0 kcal mol^{-1}). Compared with the hydride anion addition, the contribution of destabilising interaction energy at the TS is even greater.

Electron density difference analysis reveals a build-up of charge primarily on the terminal bridgehead carbon (C3) at the TS and a depletion of the density on the bridgehead carbon facing the amide anion (C1, Figure 2.12b). This qualitative picture is corroborated by the increase in the negative value of the Hirshfeld partial charge at C3 (Δq = –0.16 *e*) and an increase in the value at C1 (Δq = +0.11 *e*). After the TS, density difference analysis suggests a significant increase in charge on the bridging carbon atoms (C2). Strikingly, in the bicyclopentyl anion adduct, the sum of charges on the bridging CH$_2$ units is –0.44 *e*, compared with the –0.51 *e* partial charge on C3 – charge delocalisation appears to be significant in this anion.

Overall, these results challenge the suggestion that release of strain energy causes the facile reaction of nucleophiles with [1.1.1]propellane, since anion instability significantly outweighs any benefits arising from strain release. Instead, we suggest that the polarisability of the C1–C3 bond due to σ–π-delocalisation enables these reactions.

2.2.2 Reaction with radicals

We next investigated the reactivity of [1.1.1]propellane with radicals. This reaction class is widely utilised in the synthesis of functionalised bicyclo[1.1.1]pentanes due to the mild reaction conditions and short reaction times required to achieve high product yields. In general, these reactions occur *via* the attack of a radical species to the interbridgehead C1–C3 bond of [1.1.1]propellane, resulting in the formation of a bicyclopentyl radical. The resultant radical is intercepted by either an H-atom source, a radical trap or an organometallic species to form the bicyclopentane product, or may intercept a second equivalent of [1.1.1]propellane to form a staffane radical. As with the study on anionic addition reactions to [1.1.1]propellane, we first studied a model reaction to identify the key features that define the process using CASSCF calculations, before investigating examples of experimentally-studied reactivity.

Reaction profiles and distortion / interaction analysis

The addition of a methyl radical to [1.1.1]propellane was studied at the CASSCF(3,3)/def2-QZVPP level of theory. The active orbitals were chosen based on the combination of the singly-occupied carbon 2p orbital on the $CH_3^{\bullet}$ fragment with the bonding and antibonding combinations of the C1–C3 σ bond (Figure 2.13). A relaxed scan of the forming C–C bond length (r_1) revealed a single maximum at 2.3 Å, and an overall electronically favourable process with a driving force of –21 kcal mol^{-1}. As in the anionic addition reaction, orbital mixing occurs over the course of the reaction, from their isolated carbon 2p and propellane σ and [$\sigma^* + \pi$] orbitals to the bonding, non-bonding and antibonding combinations of the three 2p orbitals of the methyl radical and propellane C1–C3 σ bond (Figure 2.13, inlay).

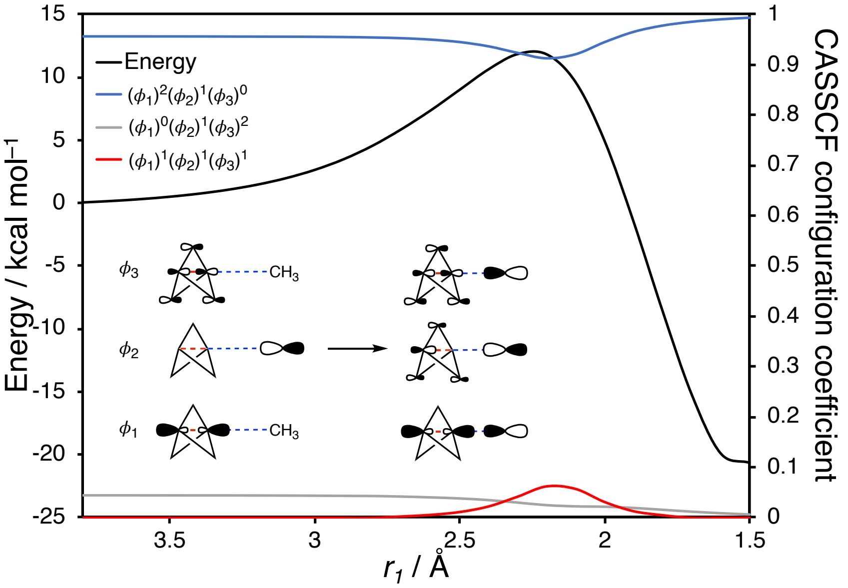

Figure 2.13: Potential energy surface for the addition of $CH_3^{\bullet}$ to [1.1.1]propellane at the CASSCF(3,3)/def2-QZVPP level (left axis), and the CASSCF(3,3) configuration coefficients for this process (right axis). Inlay: Composition of active orbitals ψ_{1-3} along the reaction coordinate.

Three significant configurations feature along the PES, the largest being the $(\phi_1)^2(\phi_2)^1(\phi_3)^0$ configuration, with a smaller contribution from the $(\phi_1)^0(\phi_2)^1(\phi_3)^2$ configuration at large C–C distances (again corresponding to the [1.1.1]propellane double excitation). The third configuration, $(\phi_1)^1(\phi_2)^1(\phi_3)^1$, appears only in the vicinity of the TS, and corresponds to the diradical structure of the propellane interacting with the approaching methyl radical.

In principle, orbital mixing over the course of the reaction should be sufficient to avoid the formation of a diradicaloid. Indeed, no such configuration was seen for the anionic addition. To account for this difference between the anionic and radical CASSCF profiles, we suggest that the polarisation of the C1–C3 electron density for the anionic addition avoids an accumulation of charge inside the cage. However, for the neutral radical addition this polarisation is much less pronounced, resulting in a build-up of charge inside the cage which is alleviated by promotion of an electron into an antibonding orbital.

To further elucidate the origin of the TS barrier for this type of reaction, we investigated the influence of destabilising electronic interactions and distortion on the activation energy via a DIA (Figure 2.14). As for the anionic addition, ΔE_{dist} is close to zero before the TS, only rising above 1 kcal mol^{-1} at $r_1 \approx 2.5$ Å. In this region, ΔE_{int} is positive, which is rationalised as a result of the increase in electronic repulsion inside the cage prior to bond cleavage. After the TS, ΔE_{dist} rises sharply, in contrast to what would be expected from a reaction driven by strain release, where geometric distortion would be anticipated prior to the TS.

During formation of the bicyclopentyl radical, the cage compresses, as evidenced by the decrease in the C2–C4 distance from 2.22 to 2.16 Å (Δr = 0.06 Å). However, this change is less pronounced than for the bicyclopentyl anion (Δr = 0.10 Å). This cage compression in the radical adduct corresponds to only a $\approx$ 15 kcal mol^{-1} increase in distortion energy with respect to the isolated propellane, which is far less than the distortion energy computed for the formation of the bicyclopentyl anion (40 kcal mol^{-1}). This comparison partially explains the enhanced reactivity of [1.1.1]propellane with radicals compared with anions.

To compare anionic and radical additions a density difference analysis was performed. While significant polarisation was seen for the anion, negligible changes are observed for the radical addition (Figure 2.14, inlay), even after the TS. This result supports the argument that the origin of the TS barrier is different for anionic and radical additions to [1.1.1]propellane – in the absence of long-range electronic repulsion, radical addition reactions occur with only mild C1–C3 polarisation, therefore incurring a penalty from charge build-up inside the cage at the TS. The lower barriers observed for radical *vs* anionic additions indicate that this effect appears to be less detrimental than the inter-fragment repulsion observed

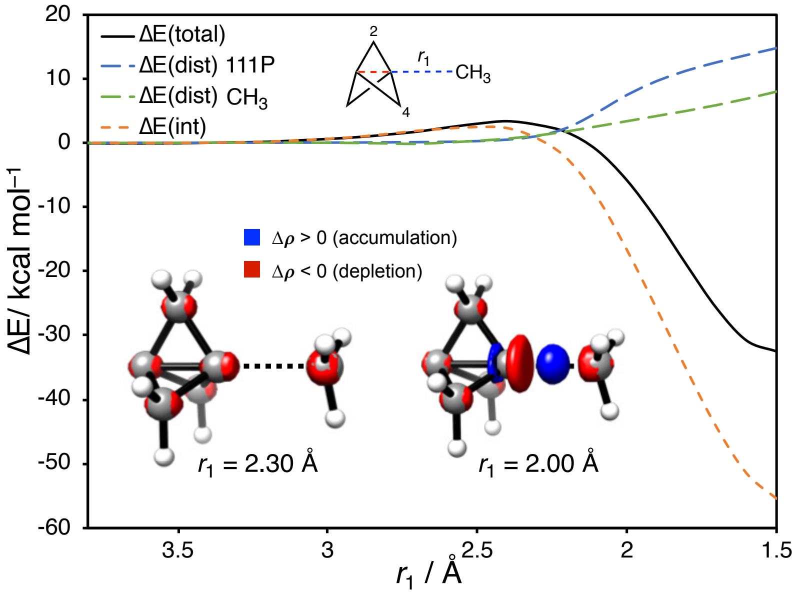

Figure 2.14: Distortion / interaction analysis for the addition of $CH_3^{\bullet}$ to [1.1.1]propellane, at the DLPNO-CCSD(T)/def2-QZVPP level. Inlay: Electron density difference plots (isovalue = 0.01 a.u.) pre- ($r_1 = 2.30$ Å) and post-TS ($r_1 = 2.00$ Å), at the CASSCF(3,3) ($CH_3^{\bullet}$ + [1.1.1]propellane) / CASSCF(2,2) ([1.1.1]propellane) / HF ($CH_3^{\bullet}$) levels (def2-QZVPP basis set).

for anionic addition reactions.

Benchmarking a radical addition

A similar benchmark analysis to the one carried out for anionic addition was performed for the addition of $H^{\bullet}$ to [1.1.1]propellane, with the DLPNO-CCSD(T)/def2-QZVPP//CASSCF(3,3)/def2-QZVPP level of theory as a reference (Figure 2.15). Truncated coupled cluster methods can fail to describe diradical species due to their single determinant nature.[197] However, since the maximum weight of the diradical configuration from the CASSCF calculation is small (6%), DLPNO-CCSD(T) should provide an excellent reference for benchmark studies.

Unrestricted HF (UHF) theory substantially overestimates the TS barrier, which can be attributed to its lack of electron correlation which would otherwise alleviate charge build-up inside the cage. However, the introduction of dynamic correlation

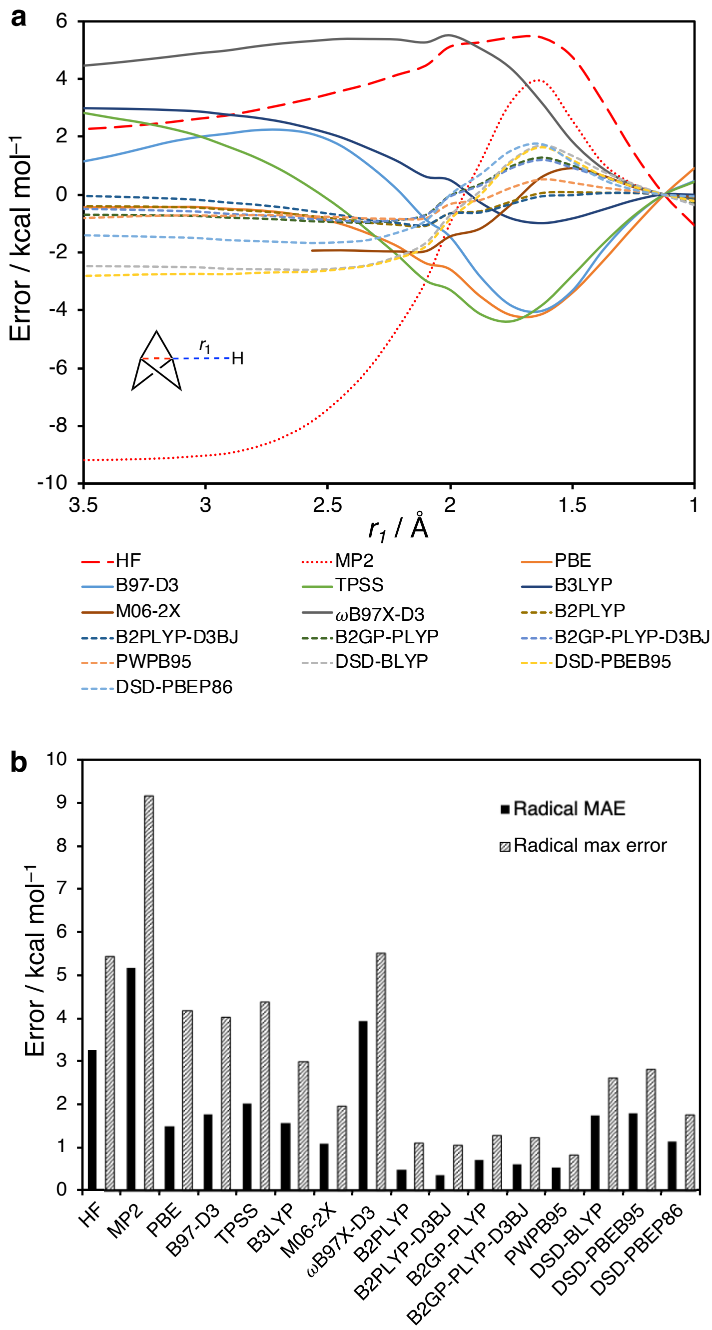

Figure 2.15: **a.** Potential energy surface errors for the addition of H$^\bullet$ to [1.1.1]propellane, with each method (def2-QZVPP level) referenced to the DLPNO-CCSD(T)/def2-QZVPP energy. **b.** Mean absolute error (MAE) and maximum error for the PESs described in **a**. All wavefunctions are unrestricted.

with MP2 results in severe failures, underestimating the energy prior to the TS and overestimating at the TS. We suspect this is due to the near-degeneracy problem encountered by MP2, and the underlying UHF wavefunction deviates in $\langle \mathcal{S}^2 \rangle$ by up to 0.21. Pure density functionals generally overestimate the interaction energy prior to the TS, resulting in TS barriers that are too low. Hybrid functionals offer varied accuracy, and while M06-2X performs best, it suffers from convergence failures at larger values of r_1. This result suggests that this functional may not provide a robust and generally-applicable approach to model radical reactivity. Once again, double hybrid functionals perform well, with the B2PLYP and B2GP-PLYP functionals offering low error. While this is perhaps surprising considering the poor performance of MP2, it indicates that the correlation introduced with the KS orbitals alleviates problems arising from using a poor reference determinant. From its excellent performance in the different reactions, we suggest that B2PLYP or B2GP-PLYP with D3BJ dispersion are likely to offer the best overall performance.

Finally, we evaluated the effect of solvent on the calculated PES. As expected for a neutral reaction, the inclusion of solvent has a negligible impact on the shape of the PES (Figure 2.16); therefore, it is likely not necessary to include solvent in the calculation of neutral radicals with [1.1.1]propellane. However, to be consistent with the study on the anionic reactivity profile and to reproduce the conditions used experimentally, we employed the SMD solvent model for Et_2O in the subsequent investigations.

Case study: Diiodination of [1.1.1]propellane

The reaction of iodine with [1.1.1]propellane has been widely employed as a titration technique.[196] We expected its mechanism to follow that of carbon- and nitrogen-centred radical reactions with [1.1.1]propellane, where the iodine radi-

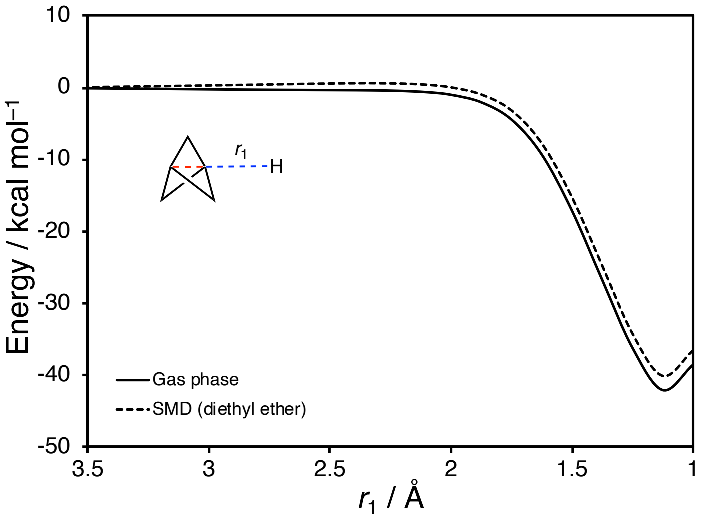

Figure 2.16: Effect of solvation on the addition of H$^\bullet$ to [1.1.1]propellane at the [SMD(Et$_2$O)]-DLPNO-CCSD(T)/def2-QZVPP level.

cal forms a new C–X bond with the propellane and cleaves its interbridgehead bond (Figure 2.17a). The resulting carbon-centred radical is then intercepted by I$_2$, forming diiiodobicyclo[1.1.1]pentane and regenerating the iodine radical chain carrier.

To our surprise, the optimised product from this reaction does not resemble the expected 1-iodo-bicyclo[1.1.1]pentyl radical (Figure 2.17b). Instead, it forms a coordination complex (C–I distance = 2.55 Å compared with 2.13 Å in diiodobicyclo[1.1.1]pentane), with little appreciable change in propellane cage geometry ($\Delta r_{\text{C1–C3}}$ = +0.02 Å). The formation of this complex is electronically barrierless and accompanied by a free energy change of ΔG = –7.6 kcal mol^{-1} (ΔH = –10.4 kcal mol^{-1}). The spin density of this complex is delocalised onto both the iodine atom and the distal (C3) carbon atom, such that the C1–C3 bond is weakened, surprisingly without altering the cage geometry. Interception of this delocalised radical by I$_2$ then occurs at the C3 position in a second electronically barrierless process (Figure 2.17c), in which C3–I bond formation (r_1) and C1–C3 bond lengthening (r_2) occur simultaneously.

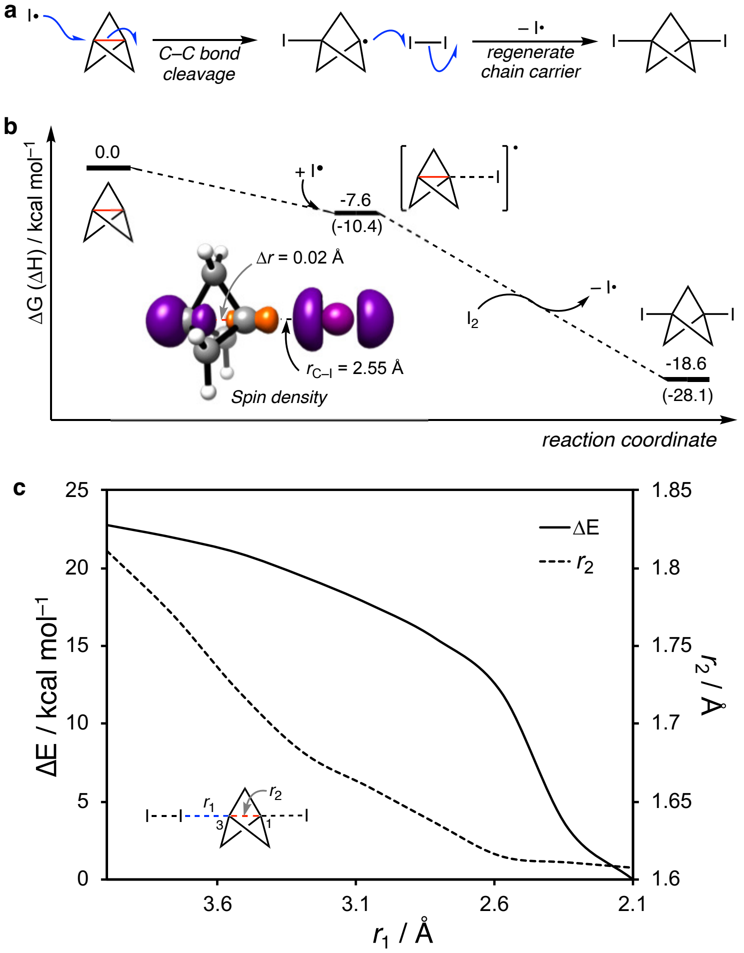

Figure 2.17: **a.** Anticipated mechanism for the diiodination of [1.1.1]propellane. **b.** Potential energy surface for the diiodination of [1.1.1]propellane, calculated at the SMD(Et_2O)-DLPNO-CCSD(T)/def2-QZVPP//SMD(Et_2O)-B2PLYP/def2-TZVP level. Inlay: Calculated structure of I—BCP$^•$ structure and its spin density (isovalue = 0.01 a.u.). **c.** Potential energy surface (left axis) for interception of I—BCP$^•$ as a function of the forming C3–I bond (r_1). Right axis indicates the length of the C1–C3 bond (r_2) as a function of r_1.

Therefore, we suggest that the initial I$^•$ coordination is facilitated by delocalisation and is not related to strain release. The subsequent trapping of the radical complex by I_2 is where the strain energy is relieved and causes this process to be electronically barrierless. This explanation is consistent with the findings from both the anionic and radical addition processes explored above – but in the case of iodine radical addition, the increased polarisability of $I^\bullet$ and the weakness of the C–I bond results in the expected TS instead being found as an intermediate on the PES. It is likely that the through-bond / through-space interaction of the BCP C-centred radical with the C–I σ^* weakens the C–I bond, disfavouring full C–I bond formation in the adduct.

Halogen and chalcogen radical additions. To test the idea that the strength of the forming C–X bond might affect the likelihood of full C–C cleavage *vs* the formation of a radical complex, we calculated the PES for the addition of halide ($F^\bullet$, $Cl^\bullet$, $Br^\bullet$ and $I^\bullet$) and chalcogen hydride ($HO^\bullet$, $HS^\bullet$, $HSe^\bullet$ and $HTe^\bullet$) radicals to [1.1.1]propellane (Figure 2.18). The extent of C–X bond formation was measured by taking the relative C–X distance with respect to the C–X length in the saturated bicyclopentyl product.

The 1-fluorobicyclopentyl radical behaves much as the 1-methylbicyclopentyl radical – there is no appreciable difference in the C–F bond length compared with the saturated product. However, moving down the group, the C–X distance in the radical adduct increases, reaching its largest value of $\Delta r \approx 0.4$ Å for the iodobicyclopentyl radical discussed above. This can be interpreted in terms of bond strengths and resonance structures: as the C–X bond weakens down the group, the contribution of the resonance form with the intact C–C bond increases (Scheme 2.2). Equivalently, the C3-centred bicyclopentyl radical donates into the C–X σ^* orbital with increasing efficiency as the C–X bond becomes weaker. There is then a balance between the C–X and C–C bond strengths (the latter being determined by σ–π-delocalisation).

The chalcogen hydrides follow a similar trend, with the C–X distance of the lowest energy structure increasing down the group. However, the PES for $HTe^\bullet$ addition deserves more attention. While the global minimum on the $HTe^\bullet$ PES is found at

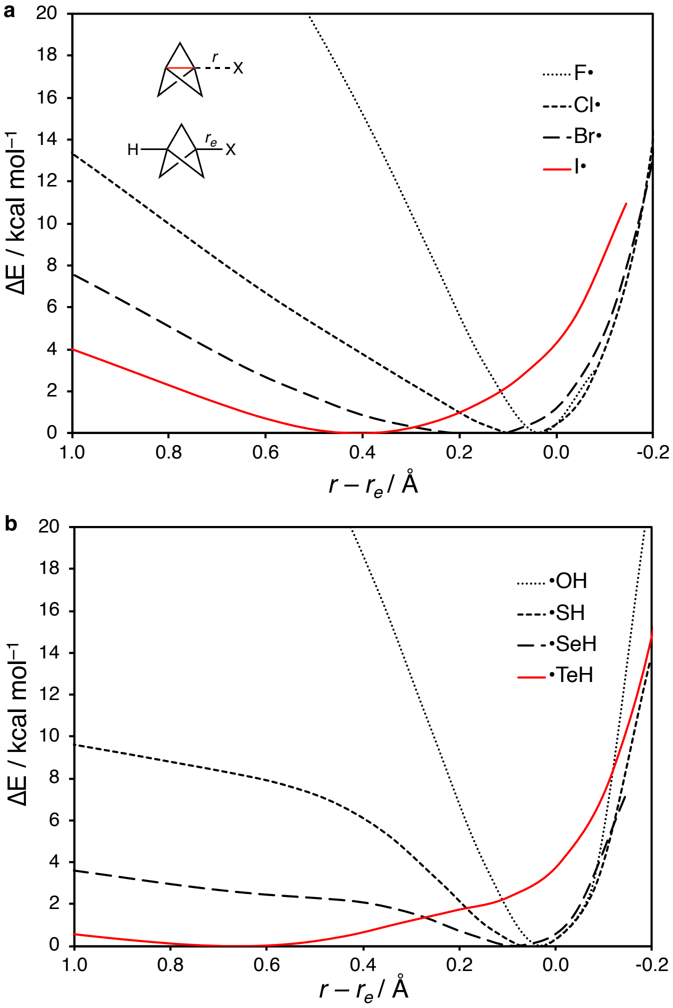

Figure 2.18: Potential energy surface for the addition of halogen (**a**) and chalcogen hydride (**b**) radicals to [1.1.1]propellane as a function of $r - r_e$, where r is the length of the forming C–X bond and r_e is the length of the equilibrium C–X bond in the saturated bicyclopentyl adduct. Calculations at the SMD(Et_2O)-B2PLYP-D3BJ/def2-TZVP level.

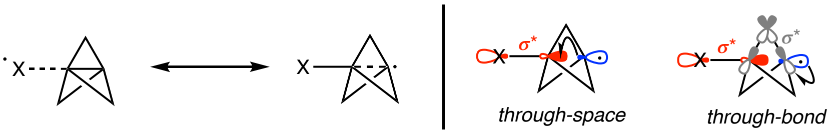

Scheme 2.2: Resonance forms ([$X^\bullet \cdots$ C–C] and [X–C$\cdots C^\bullet$]) for BCP radical adducts (left), and the possible through-space and through-bond orbital interactions that lead to different resonance weights.

$\Delta r \approx 0.6$ Å, corresponding to the radical complex as observed for the $I^\bullet$ adduct, a second plateau is seen approaching $\Delta r \approx 0.1$ Å. This second geometry corresponds to the bicyclopentyl adduct with the fully-cleaved C–C bond. We propose that the contributions of the two resonance forms ([$X^\bullet \cdots$ C–C] and [X–C$\cdots C^\bullet$]) are different for the two geometries, with the distortion of the propellane cage and loss of σ–π-delocalisation responsible for the preference for the radical complex. This 'double-minimum' phenomenon may be thought of as a type of bond-stretch isomerism, and the equilibrium position could be biased through variation of the tellurium substituent.

Through this study of the reactivity of [1.1.1]propellane with various radicals, a key feature can be identified: minimal polarisation of the C1–C3 bond upon radical approach results in accommodation of electron density within the propellane cage. The extent to which a radical may add to [1.1.1]propellane will depend on the C–X bond strength relative to stabilisation due to σ–π-delocalisation – for weak C–X bonds, bicyclopentyl radical back-donation increases the equilibrium C–X distance, giving rise to radical complexes.

2.2.3 Reactions with cations

For both anionic and radical reactions with [1.1.1]propellane, the increase in electron density inside the propellane cage is suggested to cause the activation barrier. This leads to the question of what would happen if electron density was instead lost from the cage, for example in the reaction of [1.1.1]propellane with a cationic species. Experimental studies on the ionisation of [1.1.1]propellane have shown that the radical cation undergoes a low-barrier C1–C2 fragmentation followed by two additional C–C bond fragmentations, remarkably leaving the C1–C3 bond intact in the product.[191] Similarly, protonation of [1.1.1]propellane leads to similar C1–C2 cleavage, at odds with the exclusive C1–C3 cleavage observed for the anionic and radical reactivity modes.[82]

Reaction profiles and distortion / interaction analysis

We investigated the origin of this reactivity difference by constructing a model system of the reaction of [1.1.1]propellane with a cation. Initial studies were carried out on the addition of a proton to propellane, using the CASSCF/def2-QZVPP method. We envisaged using an active space of two electrons in three orbitals (the unoccupied H 1s orbital and the bonding and antibonding combinations of the C1–C3 σ bond) in the same manner as our study on anionic and radical reactions. However, a scan of the forming C–H distance revealed complete charge transfer from the propellane to the proton, even at large separation. This is shown by the degeneracy of the singlet and triplet states at $r_1 \geq 3.5$ Å (Figure 2.19a) and the active orbital composition consisting of the bonding (ϕ_1) and antibonding (ϕ_2) combinations of the H 1s orbital with the C1–C3 bond of [1.1.1]propellane. All attempts to restrict this charge transfer by selecting different active spaces were unsuccessful, which points to the unique oxidising power of a gas-phase proton. As a result, this charge transfer mechanism will likely not represent the general reactivity profile of propellane with electron-deficient species in solution.

We therefore instead employed a methyl cation as the electron-deficient species, using CASSCF(2,3)/def2-QZVPP. This time, selection of the C 2p orbital on the CH_3^+ fragment (instead of the H 1s) and the bonding and antibonding combinations of the C1–C3 σ bond resulted in the desired orbital space (Figure 2.19b). A relaxed scan of the forming C–C bond length (r_1) reveals a smooth energy decrease from 3.8 to 1.5 Å separation and an overall driving force of –82 kcal mol^{-1}. Surprisingly, the C1–C3 distance decreases over the course of the addition, from 1.58 Å at r_1 = 3.80 Å to 1.54 Å at r_1 = 1.60 Å, in stark contrast with the increase seen for both radical and cationic reactions.

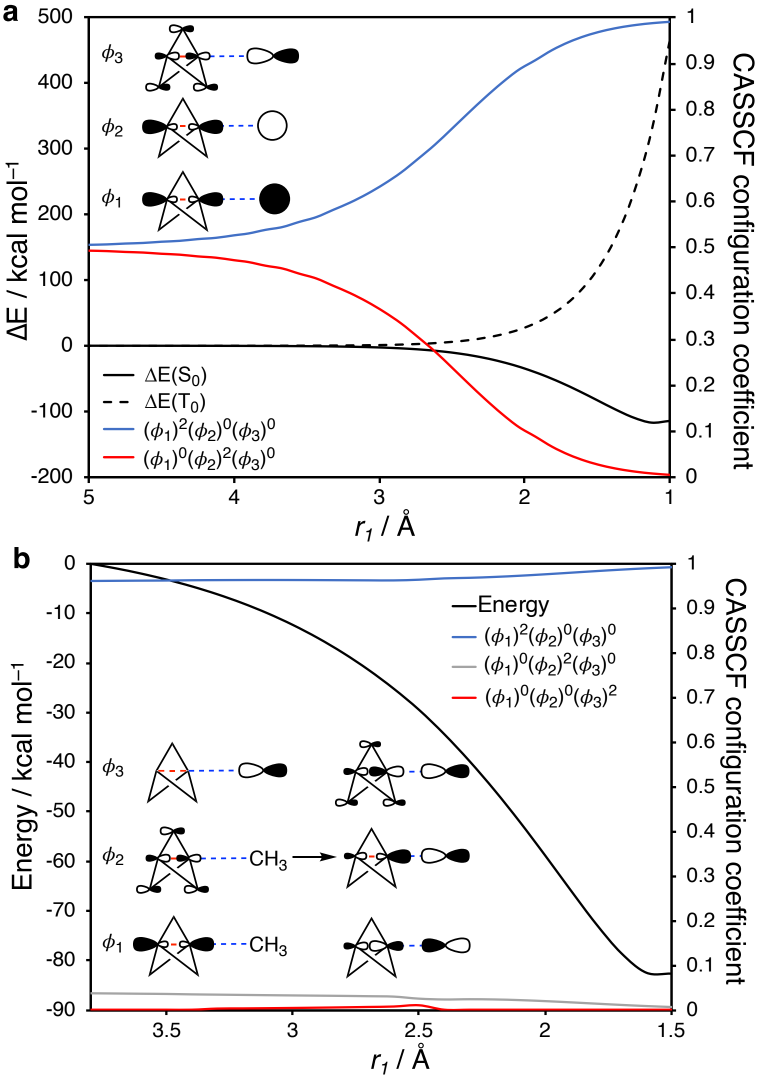

Figure 2.19: Potential energy surface for the addition of H^+ (**a**) and CH_3^+ (**b**) to [1.1.1]propellane at the CASSCF(2,3)/def2-QZVPP level (left axis), and the CASSCF(2,3) configuration coefficients for these processes (right axis). Inlay: Composition of active orbitals ϕ_{1-3} along the reaction coordinate.

As in the anionic and radical addition reactions, the orbitals mix from their initial identity as isolated methyl 2p and propellane σ and $[\sigma^* + \pi]$ orbitals, this time to the bonding and antibonding combinations of the methyl 2p with the propellane σ orbital, and the bonding combination of the carbon 2p / propellane $[\sigma^* + \pi]$ orbitals. Two significant configurations feature along the PES, the largest being the $(\phi_1)^2(\phi_2)^0(\phi_3)^0$ configuration, with a smaller contribution from the $(\phi_1)^0(\phi_2)^2(\phi_3)^0$ configuration at large C–C distances (corresponding to the [1.1.1]propellane double excitation). A third configuration, $(\phi_1)^0(\phi_2)^0(\phi_3)^2$, appears at $r_1 \approx 2.5$ Å, however, we attribute this to numerical noise rather than the behaviour of the physical system. The lack of significant multireference character indicates that this type of reaction is well-described by DLPNO-CCSD(T).

DIA reveals a slow increase in distortion over the course of the addition (Figure 2.20). The lack of TS for this PES means that ΔE_{int} is stabilising at all C–C distances, following closely the total energy curve until $r_1 \approx 2.5$ Å where distortion becomes significant, indicating bond formation. The majority of this distortion originates from pyramidalisation of the methyl cation ($\approx$ 30 kcal mol^{-1} in the adduct) – the propellane cage is only distorted by $\approx$ 5 kcal mol^{-1} over the course of the reaction. Compared with bicyclopentyl radical (15 kcal mol^{-1}) and anion (40 kcal mol^{-1}) distortion, the formation of the bicyclopentyl cation requires very little geometric distortion. While the radical and anion cages are compressed ($\Delta r_{\text{C2–C4}}$ = –0.06 and –0.10 Å, respectively), the bicyclopentyl cation instead slightly expands ($\Delta r_{\text{C2–C4}}$ = +0.01 Å).

We suggest that the formation of the bicyclopentyl cation from a methyl cation and [1.1.1]propellane occurs through charge transfer from the propellane cage to the cation. This process can be followed using a density difference analysis (Figure 2.20, inlay): electron density diminishes from both the inside and the back of the cage (in the vicinity of C3) and accumulates between C1 and the

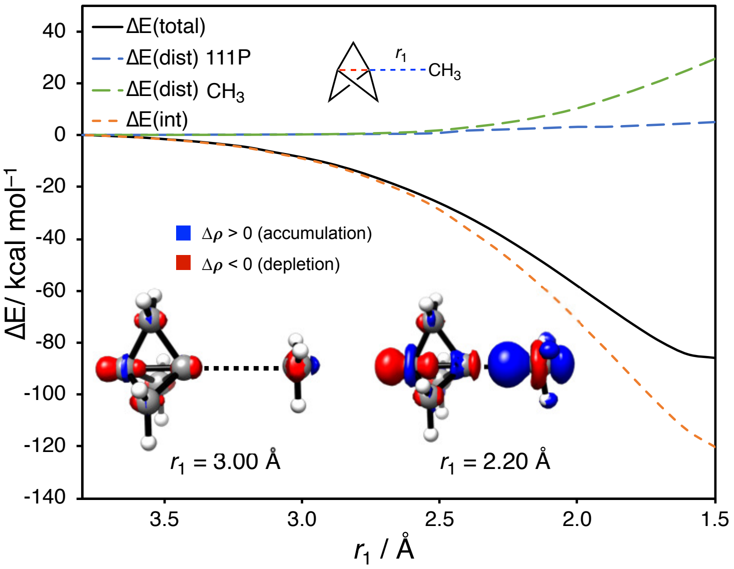

Figure 2.20: Distortion / interaction analysis for the addition of CH_3^+ to [1.1.1]propellane, at the DLPNO-CCSD(T)/def2-QZVPP level. Inlay: Electron density difference plots (isovalue = 0.01 a.u.) at the CASSCF(2,3) [CH_3^+ + [1.1.1]propellane] / CASSCF(2,2) [[1.1.1]propellane] / HF [CH_3^+] levels (def2-QZVPP basis set).

methyl cation (indicating C–C bond formation), and onto the methyl cation itself. This analysis is consistent with our σ–π-delocalisation model, which is based on the premise that there is significant electron accumulation inside the cage, leading to an ‘internal pressure’ effect that inflates the cage like a balloon. Donation of electron density to a cation decreases this internal pressure and shortens the C1–C3 distance.

Benchmarking a cationic addition

For completeness, we benchmarked the addition of a cation to [1.1.1]propellane, although this reactivity mode is less common. The PES for the addition of a methyl cation to [1.1.1]propellane (r_1 = C1–Me) was calculated at the DLPNO-CCSD(T)/def2-QZVPP//CASSCF(2,3)/def2-QZVPP level of theory, where the BCP cation product was taken as the zero energy point since its wavefunction is well-described by a single HF determinant.

HF theory underestimates the interaction between the methyl cation and [1.1.1]propellane at longer r_1 distances as a result of overlocalisation (Figure 2.21). As with the anionic addition, the inclusion of perturbative dynamic correlation with MP2 results in excellent performance – in fact resulting in the lowest error for all methods tested. Pure density functionals are the worst performers, underestimating the interaction between the methyl cation and propellane at all distances. Hybrid functionals give contrasting results, where B3LYP shows poor performance, while both M06-2X and ωB97X-D3 are much improved, likely owing to their more highly parameterised functional forms and dispersion corrections. While the performance of double-hybrids is improved with respect to the single-hybrids, the gain is not as pronounced as for anionic and radical additions. In general, empirical dispersion corrections improve the performance of double-hybrids. Despite not being the best-performer for this system, the B2GP-PLYP-D3BJ functional provides a reliable approach to explore all reactions involving [1.1.1]propellane.

Inclusion of implicit solvent in cation addition to [1.1.1]propellane strongly affects the thermodynamics of the reaction. For methyl cation addition it leads to an increase in the reaction driving force by 12 kcal mol^{-1} (Figure 2.22). This is due to the significant redistribution of charge involved in the process, necessitating the inclusion of solvent effects for the study of this type of reaction.

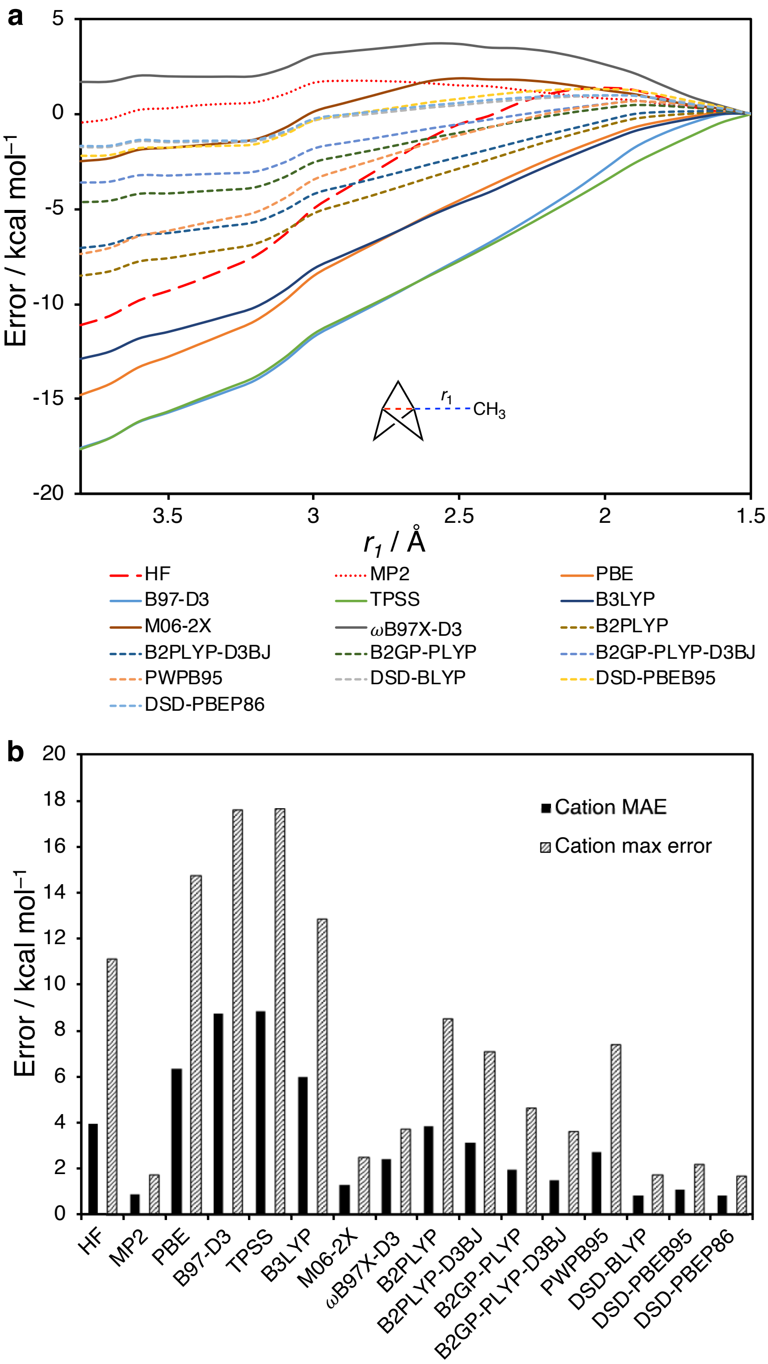

Figure 2.21: a. Potential energy surface errors for the addition of CH_3^+ to [1.1.1]propellane, with each method (def2-QZVPP level) referenced to the DLPNO-CCSD(T)/def2-QZVPP energy. **b.** Mean absolute error (MAE) and maximum error for the PESs described in **a**.

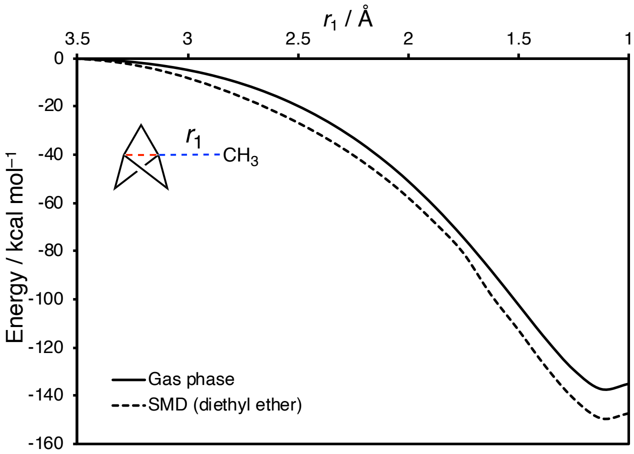

Figure 2.22: Effect of solvation on the addition of CH_3^+ to [1.1.1]propellane at the [SMD(Et_2O)]-DLPNO-CCSD(T)/ma-def2-QZVPP level.

Case study: Cage fragmentation

Our previous analysis of the ground state electronic structure of [1.1.1]propellane suggests electronic repulsion inside the cage gives rise to σ–π-delocalisation, which strengthens the cage through the formation of lateral C1–C2 π-like interactions. The reaction of a cation with [1.1.1]propellane appears to relieve this electronic repulsion, leading to a weaker cage structure and facile fragmentation.

To explore how the cage might fragment over the course of a cation addition, we constructed a More O'Ferrall-Jencks plot (Figure 2.23),[198] using the forming C1–CH_3 bond as r_1 and the breaking C1–C2 bond as r_2. Calculations were carried out at the SMD(Et_2O)-B2GP-PLYP-D3BJ/def2-TZVP level (*vide infra*). We were particularly interested to see whether the cation engaged directly with the C1–C3 bond, or whether it might instead interact to a greater extent with the more localised C1–C2 bond.

The PES that describes the subsequent cage fragmentation is flat, with some indication of a bifurcation point. Path A follows a synchronous bicyclo[1.1.0]-

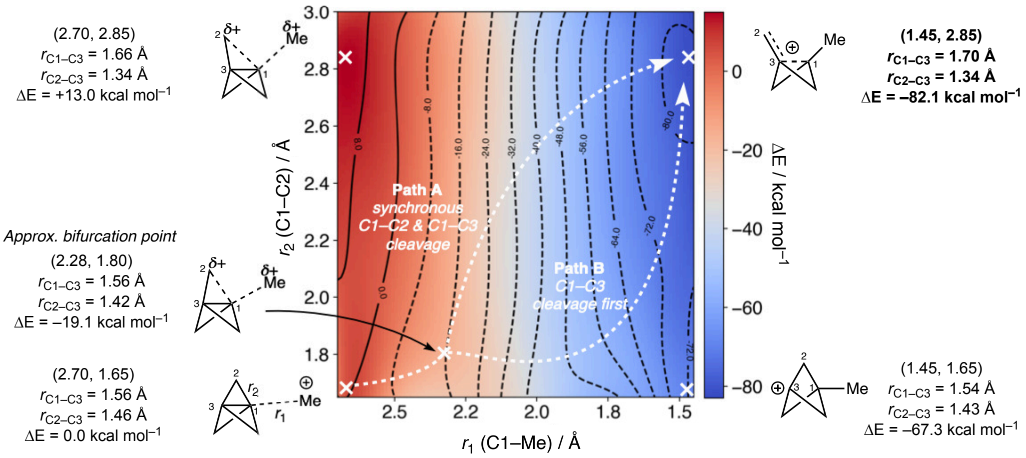

Figure 2.23: More O'Ferrall-Jencks plot for the addition of a methyl cation to [1.1.1]propellane, with r_1 (Å) taken as the forming C1–Me bond and r_2 (Å) taken as the breaking C1–C2 bond. Relative energies (kcal mol^{-1}) are taken with respect to the species at (2.70, 1.65), calculated at the SMD(Et$_2$O)-B2GP-PLYP-D3BJ/def2-TZVP level.

carbinyl cation formation process, in which charge transfer from the C1–C3 bond is accompanied by C1–C2 lengthening to form the carbinyl cation. Alternatively, path B follows C1–C3 cleavage to completion before C1–C2 fragmentation commences in an asynchronous process. Path A and B lead to the same carbinyl cation, in which the C1–C3 bond is partially intact due to stabilisation of the C1 cation by the C2–C3 σ-bond. The flat nature of the PES, with no saddle points observed, suggests that both paths are likely operative, or indeed an alternative low-energy pathway which combines features of both paths. This highlights the lack of structural integrity of the cage upon the loss of σ–π-delocalisation. It is also worth noting that the structure corresponding to the bicyclopentyl cation was not a minimum on the PES, which agrees with experimental findings from the reaction of [1.1.1]propellane with acetic acid,[82] or cationic organometallic species,[199,200] in which no intact bicyclopentane products are observed.

2.3 Conclusions

In this Chapter, we have explored the unusual electronic structure and reactivity of [1.1.1]propellane employing CASSCF, coupled cluster and DFT calculations. CASSCF calculations revealed important electron density donation from the interbridgehead C1–C3 σ bond into the [$\sigma^* + \pi$] system to alleviate strain energy resulting from the extremely compact arrangement of C–C bonds (Figure 2.24a). This effect, which we have described as σ–π-delocalisation, enables the rationalisation of the unexpected reluctance of propellane to cage fragmentation. A localised orbital analysis leads to the same conclusion, where the Lewis structure of [1.1.1]propellane is in resonance with six degenerate alkene/carbene pairs, which stabilises the overall ground state of the molecule. This interpretation is consistent with its large singlet-triplet gap (110 kcal mol^{-1}) and the apparently non-bonding HOMO suggested for [1.1.1]propellane,[179] and previous studies which demonstrate that the propellane cage is unstable towards fragmentation upon one-electron oxidation.[191]

The implications of the σ–π-delocalisation effect on intermolecular reactivity have also been considered, where [1.1.1]propellane is able to undergo addition reactions with anions, radicals and cations. A selection of experimental systems were selected for study, allowing a set of general conclusions to be drawn for each reactivity mode. We suggest that the delocalised nature of the interbridgehead bond reduces the expected barrier to anionic addition through polarisation of the cage electron density, and results in an anion which is delocalised from the bridgehead onto the bridging carbon atoms (Figure 2.24b). Radical additions do not induce the same bond polarisation, therefore some diradical character results at the TS to alleviate electronic repulsion inside the propellane cage. The strength of the forming C–X bond determines the extent of bond formation *vs* radical complex-

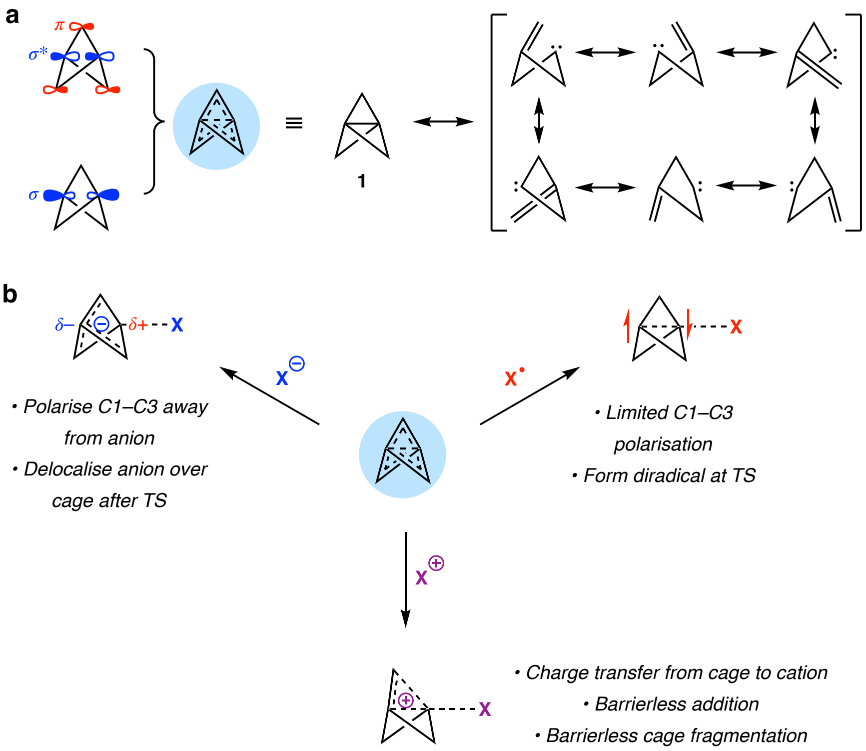

- Polarise C1–C3 away from anion
- Delocalise anion over cage after TS

- Limited C1–C3 polarisation
- Form diradical at TS

- Charge transfer from cage to cation
- Barrierless addition
- Barrierless cage fragmentation

Figure 2.24: a. σ–π-delocalisation in [1.1.1]propellane defined with both MO and resonance models. **b.** Key features of the reactivity of [1.1.1]propellane with anions, radicals and cations.

ation. For the addition of cationic species, charge transfer from the propellane cage alleviates Pauli repulsion, and is therefore a barrierless process. The loss of this repulsion, however, also removes the origin of the propellane cage stability, therefore the cage fragments without a barrier.

These studies were accompanied by a benchmark of the PES for each process. We suggest that double-hybrid density DFT functionals provide an accurate approach with which to calculate thermodynamics and kinetics of reactions of [1.1.1]propellane. In particular, B2PLYP and B2GP-PLYP with an empirical dispersion correction were found to perform well across all reactivity modes. Unfortunately, pure or single-hybrid density functionals did not enjoy the same success, so in cases in which double-hybrids cannot be used due to system size constraints, we would suggest undertaking a small benchmarking study on a model system to ensure the less expensive method accurately reproduces the correct PES.

3 |

Catalytic asymmetric bicyclopentylation of aldehydes

In this Chapter, consequences of σ–π-delocalisation in [1.1.1]propellane (**1**) are realised in its use for the development of a direct synthesis of α-chiral bicyclo[1.1.1]pentanes (BCPs) using photoredox, organocatalysis and H-atom transfer catalysis. The low-barrier addition of an α-iminyl radical cation to the interbridgehead bond of [1.1.1]propellane results in unusual dependence of stereoselectivity on the nature of the photocatalyst. We propose a kinetic model that is consistent with experimental outcomes observed during reaction optimisation, using DFT modelling to investigate the importance of substrate-catalyst non-covalent interactions on selectivity. The work presented here was published in *Nature Communications* in 2021.[128]

3.1 Synthetic development

Bicyclo[1.1.1]pentanes with an α-stereocentre may be considered bioisosteres for benzylic, neopentylic or propargylic stereocentres (Figure 3.1a). Current synthetic approaches towards α-chiral BCPs can be separated into three classes: chiral resolution,[97] stoichiometric / auxiliary-based approaches,[201–205] and catalytic approaches.[206–208] The latter are highly desirable, but to date have been limited to post-functionalisation of pre-formed BCPs. For example, Houk and Davies reported the selective bridgehead C–H functionalisation of monosubstituted BCPs with aryl diazoacetates promoted by a chiral dirhodium complex, giving access to chiral α-bicyclopentyl esters (Figure 3.1b).[206] An alternative strategy by Aggarwal and co-workers featured an iridium-catalysed allylic substitution employing a preformed organometallic BCP complex as the nucleophile.[207] To complement these catalytic approaches, a synthetic strategy in which the stereochemistry is set contemporaneously with the ring-opening of [1.1.1]propellane was envisaged (Figure 3.1c).

3.1.1 Asymmetric radical three-component organophotoredox reactions

The MacMillan[209] group recently described a three-component organophotoredox reaction in which a photocatalytically-generated α-iminyl radical cation adds to a styrene or 1,1-disubstituted alkene, and the resultant benzylic or tertiary radical undergoes H-atom transfer (HAT) with a thiol (Figure 3.2a). The subsequent iminium ion is hydrolysed to reveal an α-chiral aldehyde, which is reduced during the work-up. To motivate the work carried out here, it has previously been noted that radical addition to alkenes follows a similar kinetic profile to that of the interbridgehead C–C bond of [1.1.1]propellane (Figure 3.2b).[119,210] As a result, the addition of an α-iminyl radical cation to [1.1.1]propellane was envisaged for the synthesis of aldehydes with an α-BCP substituent, based upon the conditions developed for styrene by MacMillan. The (wet) experimental part of this project was carried out by DPhil student Marie Wong in the Anderson group, who carried out all optimisation studies and substrate scope that will be mentioned here.[211]

3.1.2 Reaction optimisation

Extensive reaction optimisation by Marie Wong on substrate **5a** led to the identification of a set of conditions that gave α-chiral BCP **6a** in 94% isolated yield

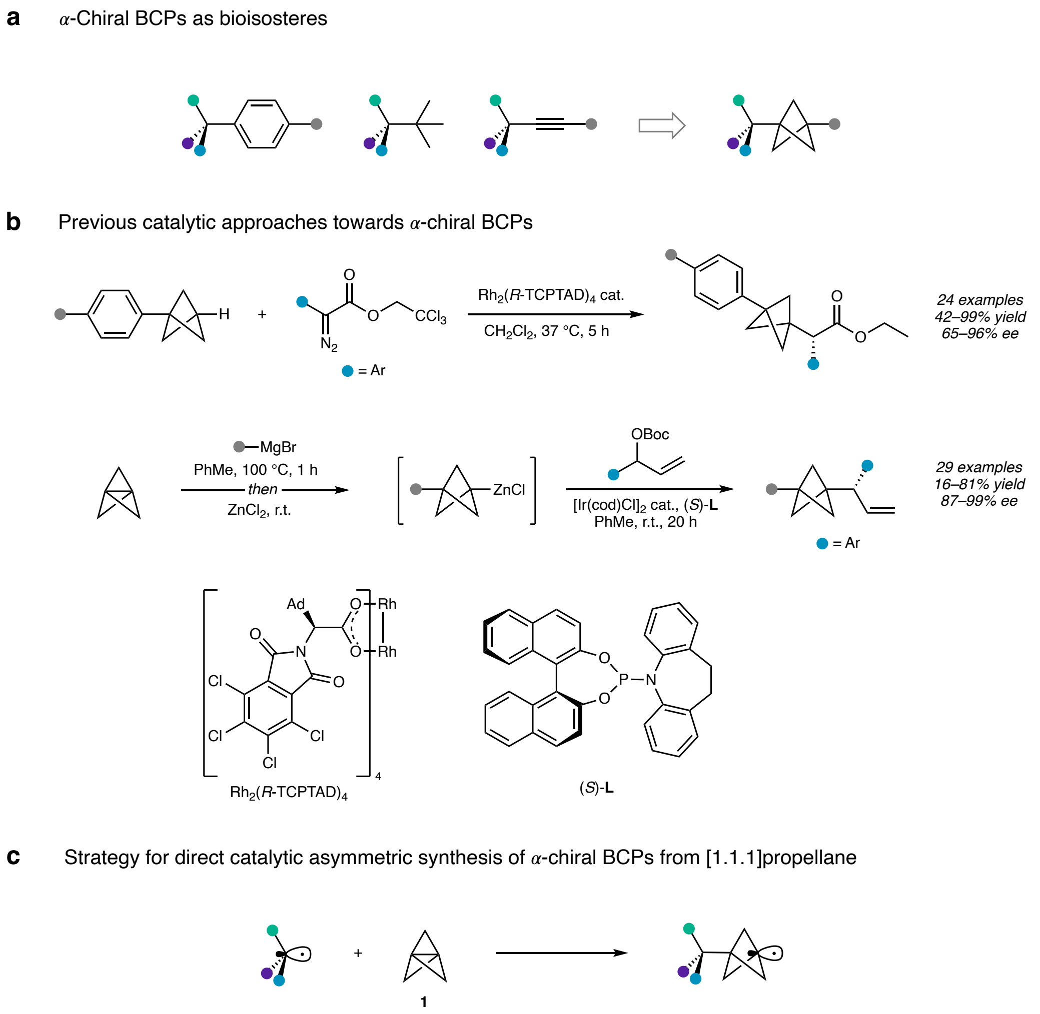

Figure 3.1: a. α-Chiral BCPs may be thought of as surrogates for benzylic, neopentylic and propargylic groups. **b.** Catalytic approaches to α-chiral BCPs through functionalisation of BCP precursors. **c.** Our approach to the synthesis of α-chiral BCPs in which C1–C3 bond cleavage of [1.1.1]propellane sets the stereocentre.

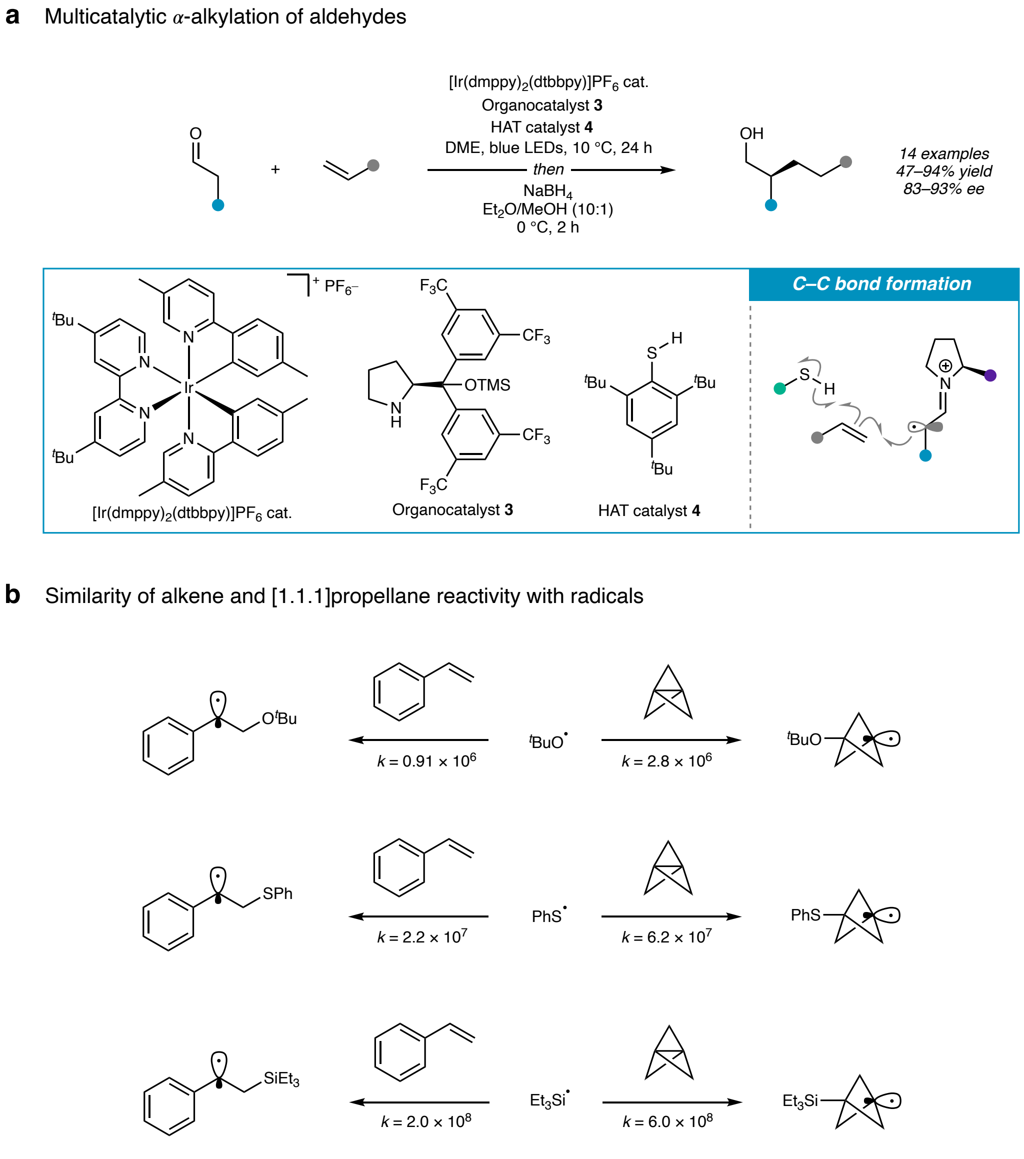

a Multicatalytic α-alkylation of aldehydes

b Similarity of alkene and [1.1.1]propellane reactivity with radicals

Figure 3.2: a. MacMillan's multicomponent reaction for the α-alkylation of simple aldehydes using the merger of photoredox catalysis, organocatalysis and HAT catalysis. **b.** Comparison of the radical reactivity of styrene with [1.1.1]propellane. Rate constants, k, in M^{-1} s^{-1}.

and 89% *ee* (Figure 3.3), where the aldehyde that resulted from the photoredox organocatalytic reaction was reduced *in situ* to avoid risk of racemisation, and aid with purification. Optimisation studies began with identification that diarylprolinol silyl ether organocatalyst **3**, with a pair of 3,5-bis(trifluoromethyl)phenyl groups, was optimal for ensuring high enantioselectivity (86% *ee*) at 25 mol% loading; replacing the trifluoromethyl substituents with hydrogens (i.e. employing the diphenylprolinol silyl ether **7**) resulted in a drop in enantioselectivity to 44% *ee*. The choice of silyl ether was also found to be important, with TMS proving optimal. A 2 mol% loading of iridium photocatalyst $[Ir(ppy)_2(dtbbpy)]PF_6$ was found to give the highest yield (65%) and *ee* (86%) for the reaction. Interestingly, the choice of photocatalyst significantly impacted the product *ee*. The use of 2,4,6-tri-*tert*-butylthiophenol (**4**) as the HAT catalyst provided the desired BCP product **6a** in high yield (65%) and enantioselectivity (86% *ee*) at a loading of only 10 mol%. Other classes of HAT catalyst offered varying results – often providing high *ee* but suffering from reduced yield.

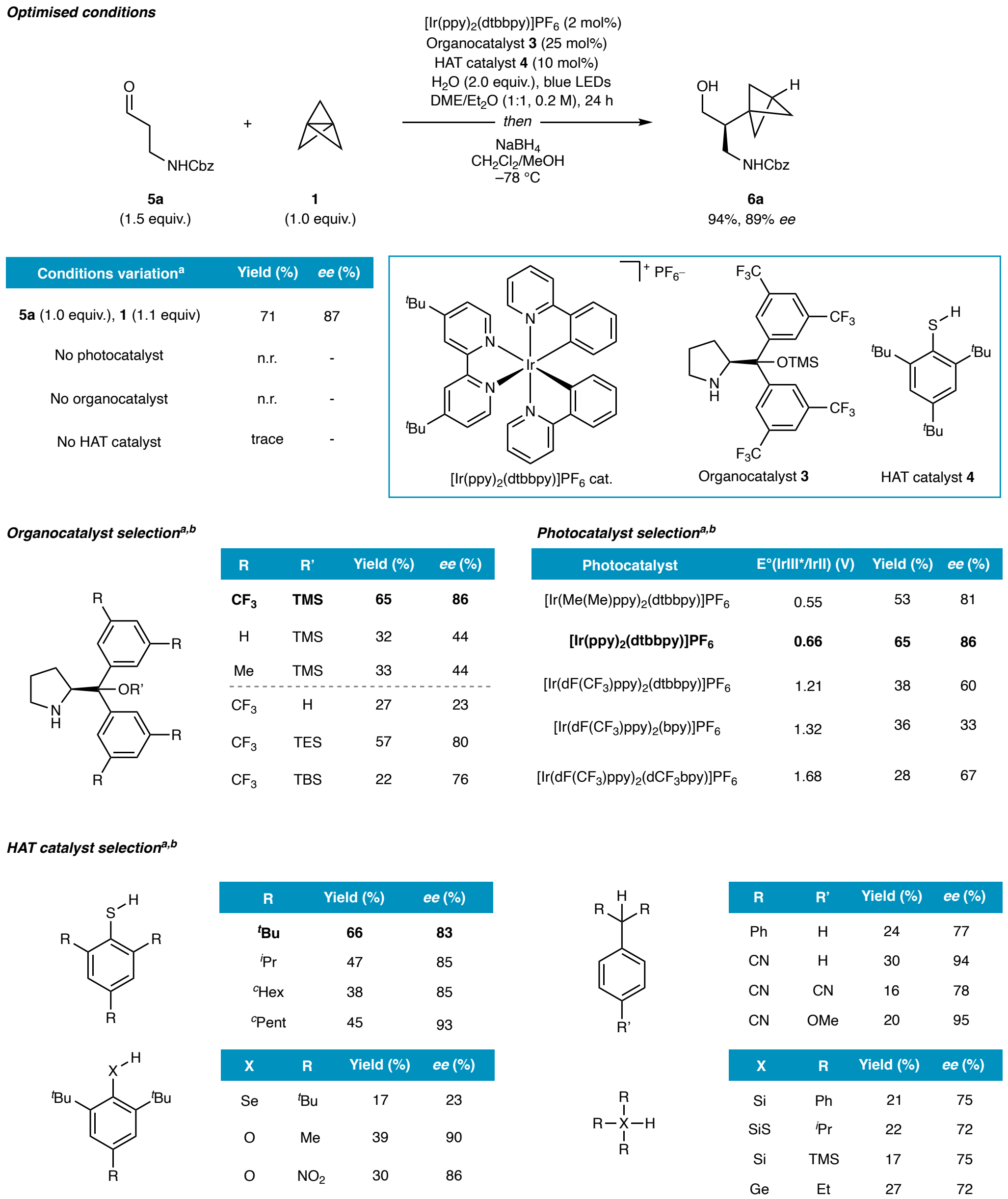

Conditions variation[a]	Yield (%)	*ee* (%)
5a (1.0 equiv.), **1** (1.1 equiv)	71	87
No photocatalyst	n.r.	-
No organocatalyst	n.r.	-
No HAT catalyst	trace	-

Organocatalyst selection[a,b]

R	R'	Yield (%)	*ee* (%)
CF_3	**TMS**	**65**	**86**
H	TMS	32	44
Me	TMS	33	44
CF_3	H	27	23
CF_3	TES	57	80
CF_3	TBS	22	76

Photocatalyst selection[a,b]

Photocatalyst	E°(IrIII*/IrII) (V)	Yield (%)	*ee* (%)
$[Ir(Me(Me)ppy)_2(dtbbpy)]PF_6$	0.55	53	81
$[Ir(ppy)_2(dtbbpy)]PF_6$	**0.66**	**65**	**86**
$[Ir(dF(CF_3)ppy)_2(dtbbpy)]PF_6$	1.21	38	60
$[Ir(dF(CF_3)ppy)_2(bpy)]PF_6$	1.32	36	33
$[Ir(dF(CF_3)ppy)_2(dCF_3bpy)]PF_6$	1.68	28	67

HAT catalyst selection[a,b]

R	Yield (%)	*ee* (%)
^{t}Bu	**66**	**83**
^{i}Pr	47	85
^{c}Hex	38	85
^{c}Pent	45	93

R	R'	Yield (%)	*ee* (%)
Ph	H	24	77
CN	H	30	94
CN	CN	16	78
CN	OMe	20	95

X	R	Yield (%)	*ee* (%)
Se	^{t}Bu	17	23
O	Me	39	90
O	NO_2	30	86

X	R	Yield (%)	*ee* (%)
Si	Ph	21	75
SiS	^{i}Pr	22	72
Si	TMS	17	75
Ge	Et	27	72

Figure 3.3: Summary of optimisation studies. Figure adapted with permission from References [128] and [211]. All optimisation studies carried out by M. Wong. [a]Reactions carried out with a 2:1 mixture of DME / Et_2O. [b]Reactions carried out with 1.0 equiv. **5a** and 1.1 equiv. **1**.

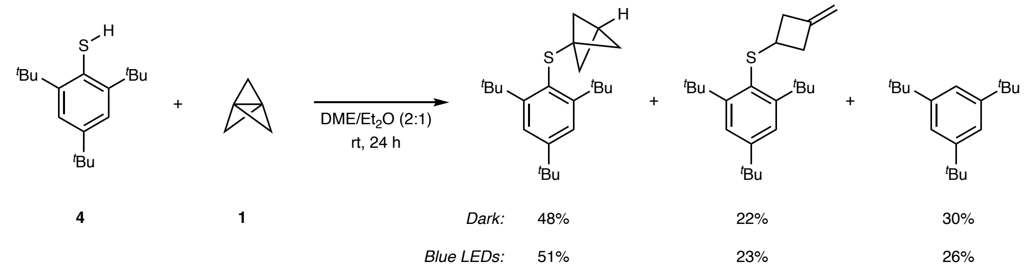

Scheme 3.1: Control reaction of [1.1.1]propellane with thiol **4** either in the dark or under blue LED irradiation. Reaction carried out by M. Wong. Figure adapted from Reference [211].

A control reaction of thiophenol **4** with [1.1.1]propellane in the dark or in the presence of blue LED irradiation (24 h) generated the expected bicyclopentane-thiol adduct, as well as ring-opened methylenecyclobutane and 1,3,5-tri-*tert*-butylbenzene (Scheme 3.1). None of these products were observed under the photoredox organocatalytic reaction conditions, suggesting that either thiyl radical addition is outcompeted by reduction by the reduced photocatalyst, or that thiyl radical addition to [1.1.1]propellane is reversible.

It was also found that maintaining a reaction temperature of 10 °C was important to obtain high enantioselectivity, and that the optimal solvent for the reaction was a 1:1 mixture of DME and Et_2O. This is particularly convenient, since [1.1.1]propellane is commonly synthesised and stored as an ethereal solution, in which it is stable at –20 °C for at least six months. Using [1.1.1]propellane as the limiting reagent, the desired product **6a** was obtained in a slightly increased yield (94%) and the *ee* was maintained (89% *ee*). Finally, control experiments showed that blue LED irradiation, the organocatalyst and the photocatalyst were all required in the reaction, and that only trace product was observed in the absence of the HAT catalyst.

3.1.3 Substrate scope

A variety of simple aldehydes were found to afford good to excellent yields and excellent enantioselectivities (**6b**-**e**, 44–96%, 96–98% *ee*), including primary, secondary and tertiary α-carbonyl substituents (Figure 3.4). The only exception to this was propanal (**5b**), the product from which (**6b**) was formed in 63% yield but only 64% *ee*. β-Carbonyl substituents such as arenes, an alkene, alkyne or heteroatom (sulfur or nitrogen) were also well-tolerated (**6f**-**j**, 50–99%, 89–97% *ee*).

Remote functionality such as a primary alkyl chloride (**6l**, 98%, 86% *ee*), ester (**6m**, 97%, 92% *ee*), ether (**6n**, 83%, 97% *ee*) and acetal (**6o**, 99%, 95% *ee*) also proved successful, and the pharmaceutically-relevant piperidine group[212] also gave high yield and enantioselectivity (**6p**, 83%, 97% *ee*). Heterocyclic substituents including a furan (**6q**), thiophene (**6r**) and pyridine (**6s**) were tolerated and gave high enantioselectivity (90–96% *ee*), although the latter two products suffered from diminished yields (25% and 29%, respectively). An alternative quenching method to the HAT catalyst employed superstoichiometric *N*-(phenylthiol)phthalimide, resulting in the formation of thioBCP **6t** in a 50% yield and 88% *ee*.

It was found that α-aryl aldehydes gave poor conversion and enantioselectivity (Figure 3.5), and α-heteroatom substituents were also not tolerated due to a lack of reactivity. Additionally, β-substituents such as an ester or benzoyl group, or an α-trifluoromethyl aldehyde, resulted in complex mixtures of products.

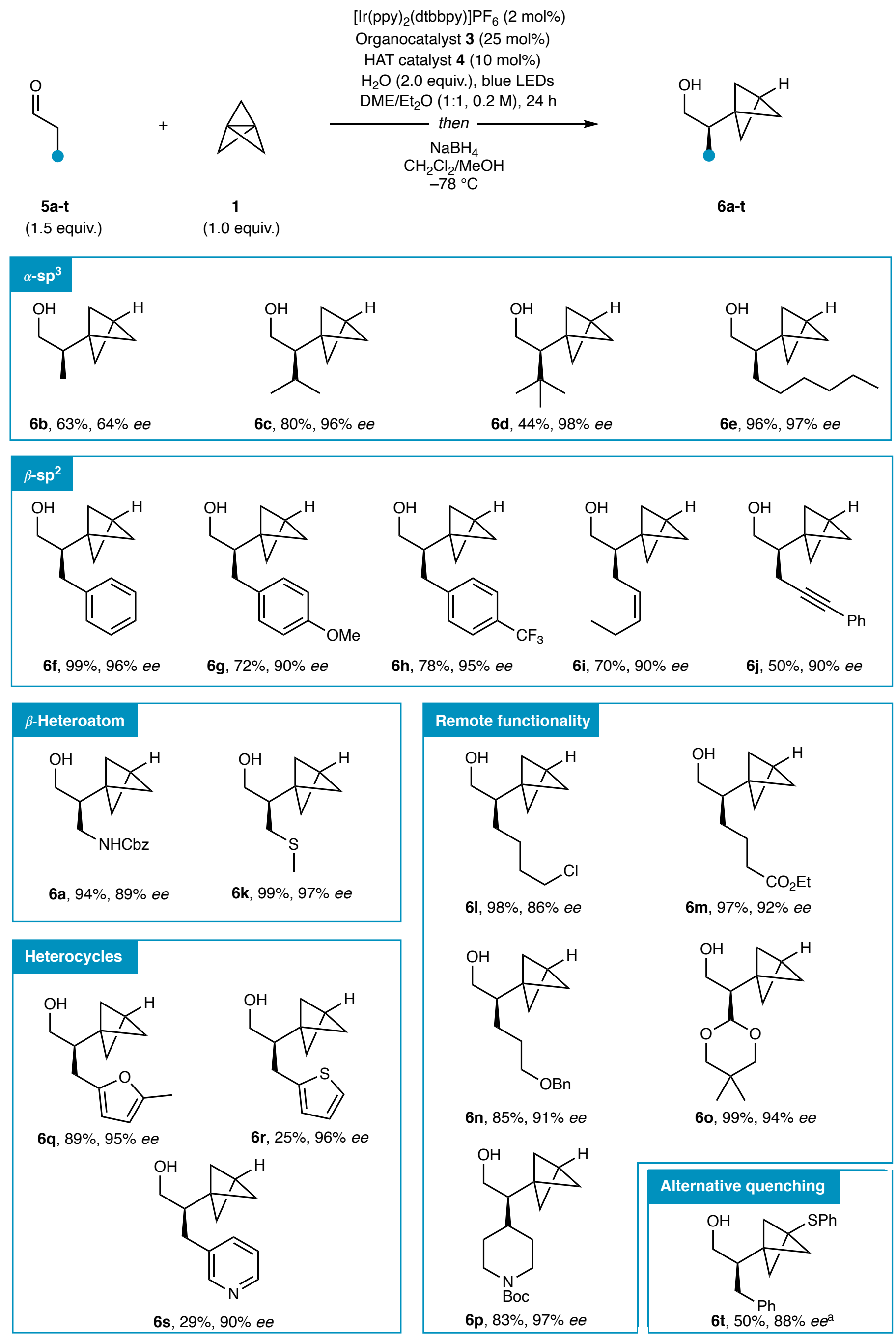

Figure 3.4: Successful substrate scope for the asymmetric ring-opening of [1.1.1]propellane. [a]Quenched with *N*-(phenylthiol)phthalimide. Figure adapted with permission from References [128] and [211].

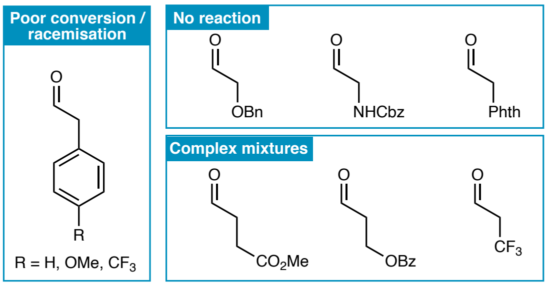

Figure 3.5: Unsuccessful substrates for the asymmetric ring-opening of [1.1.1]propellane. Figure adapted with permission from Reference [211].

3.2 Mechanistic studies

Following the suggestion from the work of MacMillan, we proposed a mechanism that could account for the results of the optimisation study and the observed substrate scope (Figure 3.6). Initial condensation between diarylprolinol organocatalyst **3** and the aldehyde **5** would result in the formation of an enamine (**8**), which could be oxidised by the excited photocatalyst to form an α-iminyl radical cation **9**. [1.1.1]Propellane could then intercept this electron-deficient radical via cleavage of its inter-bridgehead bond, which would set the α-stereocentre and result in a BCP radical **10**, which in turn would undergo HAT with the thiol catalyst **4**. The resultant thiyl radical could then be reduced to regenerate the photocatalyst, and the ensuing thiolate anion could be protonated, for example by the pyrrolidinium ion, to reform the thiol catalyst. Hydrolysis of the product iminium ion **11** would reveal the α-chiral BCP aldehyde (**12**) and regenerate the organocatalyst.

Side-product formation could be envisaged by trapping of BCP radical **10** with a second molecule of [1.1.1]propellane to form a staffane radical (**13**) – a process commonly encountered in atom transfer radical addition (ATRA) reactions involving [1.1.1]propellane. Additionally, the interception of [1.1.1]propellane by thiophenol is well-documented to be facile,[84,111,213] as shown in Scheme 3.1, ex-

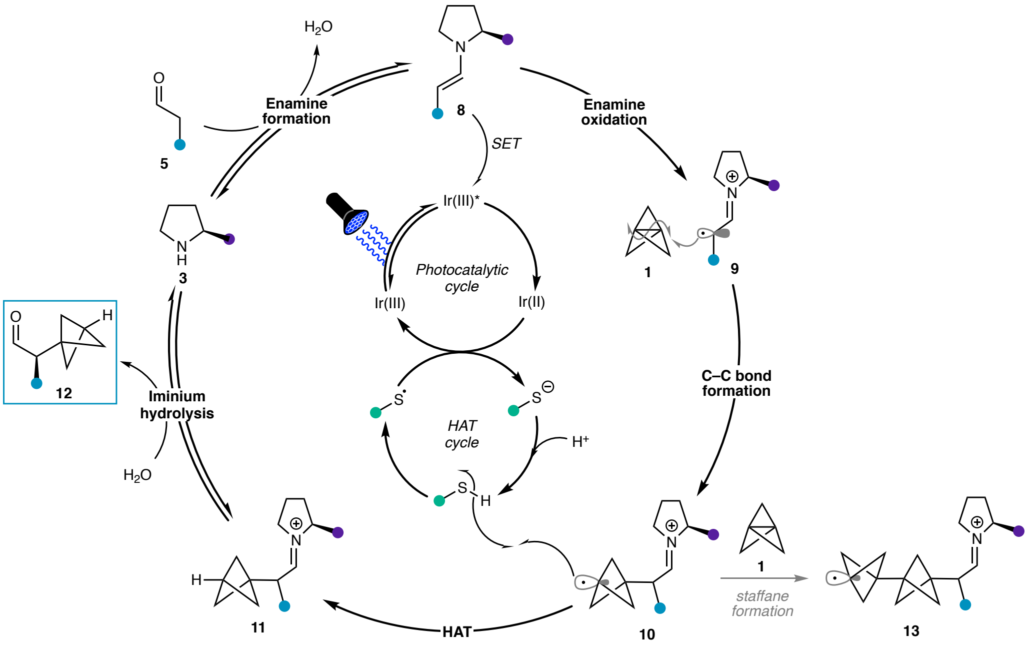

Figure 3.6: Proposed mechanism for the synthesis of α-chiral BCPs from an aldehyde and [1.1.1]propellane.

plaining why the choice of HAT catalyst is crucial to the success of the reaction. It is worth noting that kinetic studies by Scaiano suggest thiyl radical addition to [1.1.1]propellane to be reversible.[214]

Approach. To validate this mechanistic hypothesis, a combination of experimental and computational techniques were used to interrogate specific steps of the mechanism. We first needed to confirm experimentally that the excited photocatalyst was indeed oxidising the enamine, rather than any of the other reaction components (*e.g.*, [1.1.1]propellane or the thiol). Calculations by Luo and co-workers at the IEF-PCM(MeCN)-M06-2X/6-311G(d,p) level revealed an oxidation potential of $E°$(α-iminyl radical cation/enamine) = +0.77 V *vs* SCE for the enamine derived from propanal and organocatalyst **3** in MeCN,[215] and cyclic voltammetry data from Malliaras, Bernhard and co-workers for iridium photocatalyst [Ir(ppy)$_2$(dtbbpy)]PF$_6$ showed an estimated reduction potential for the excited state of $E°$(Ir(III)*/Ir(II) = +0.66 V *vs* SCE in MeCN.[216] From these values a slightly endergonic electron transfer process is predicted ($\Delta E°$ = –0.11 V, ΔG = +2.5 kcal mol^{-1}), necessitating a Stern-Volmer quenching study to investigate if this electron transfer process was indeed occurring in this reaction.

Alongside support for the mechanistic hypothesis, we were also keen to explore the origins of stereoselectivity in the reaction. In particular, we wanted to construct a model that could explain the observations that: (1) the enantioselectivity varies with the nature of the diaryl substituents of the organocatalyst; (2) poor enantioselectivity is observed for propanal, but is excellent for octanal; (3) the enantioselectivity varies with the choice of photocatalyst. Traditional models based on steric shielding appeared to be inconsistent with these findings.[217] We therefore turned to computation, investigating the presumed stereodetermining step of the reaction: C–C bond formation between the α-iminyl radical cation and [1.1.1]propellane.

3.2.1 Stern-Volmer quenching studies

The species which most efficiently quenches the excited state of the excited photocatalyst is likely to be directly involved in the photocatalytic cycle. Using Stern-Volmer quenching (see Section 1.3.5), we could directly interrogate this process by measuring the decrease in the luminescence intensity of the photocatalyst as a function of the concentration of a quencher. By comparing the luminescence quenching for a series of quenchers, the relative efficiency of photocatalyst quenching can be obtained. We therefore systematically tested each component of the reaction mixture to rule in / out its involvement in this cycle (Figure 3.7).

While the organocatalyst **3** showed a small quenching gradient ($k_q\tau_0$) of 2.7 M^{-1} s^{-1}, the aldehyde **5t** displayed enhanced quenching (8.3 M^{-1} s^{-1}); however, a 15:1

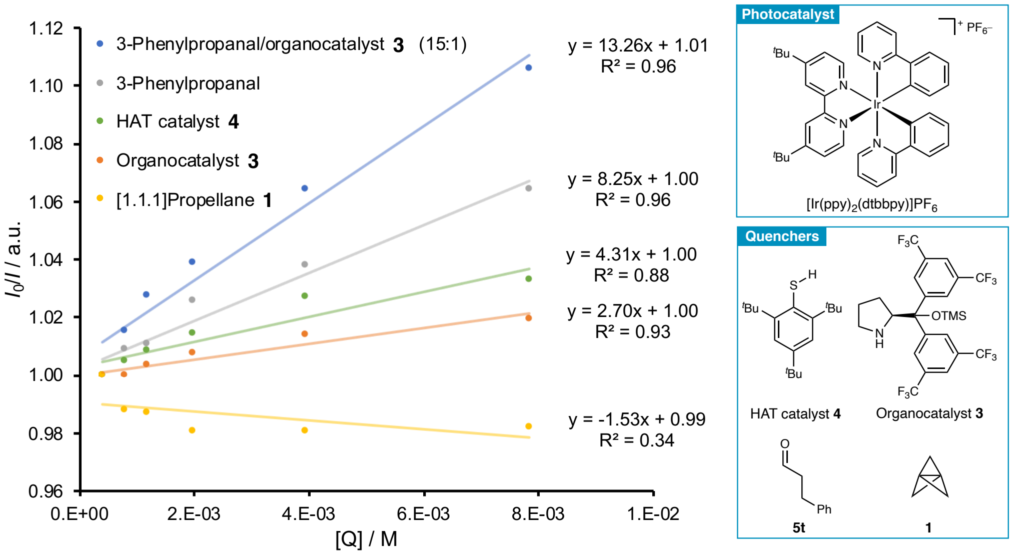

Figure 3.7: Stern-Volmer quenching study for the reaction components in the synthesis of α-chiral BCPs.

mixture of aldehyde and organocatalyst (to ensure complete consumption of the organocatalyst) resulted in a quenching gradient greater than either of the individual components: $k_q\tau_0$ = 13.3 M^{-1} s^{-1}. Adjusting for the $\approx$ 7% concentration of the enamine in this mixture (assuming complete enamine formation), and subtracting the background quenching of the remaining aldehyde, the iminium ion was estimated to quench the excited photocatalyst with a rate 10 $\times$ greater than the next best quencher ($k_q\tau_0$ = 83.4 M^{-1} s^{-1}).

An alternative mechanism for this reaction could involve oxidation of [1.1.1]propellane, however the negligible (and unphysical) quenching gradient ($k_q\tau_0$ = –1.5 M^{-1} s^{-1}) allows us to rule out this mechanism. In fact, Bally and Williams[191] revealed that the propellane radical cation undergoes a series of low-barrier rearrangements to form a 1,1-dimethyleneallene radical cation (**14**, Scheme 3.2), which would likely outcompete any intermolecular processes and result in low / no product yield. As a result, we can rule out any involvement of an oxidation event involving [1.1.1]propellane in this reaction. Additionally, luminescence quench-

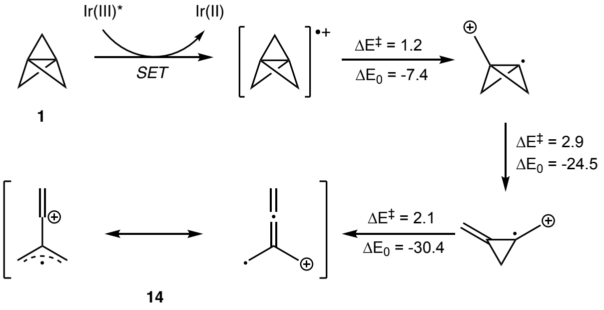

Scheme 3.2: Proposed degradation pathway for the [1.1.1]propellane radical cation, with energies reproduced from Reference [191]. Energies (E_{el} + ZPVE) in kcal mol^{-1} at the CCSD(T)/cc-pVTZ//B3LYP/6-31G* level.

ing by the thiol was also found to be inefficient compared with the enamine ($k_q\tau_0$ = 4.3 M^{-1} s^{-1}), allowing us to also rule out any mechanisms invoking an excited state, or oxidised / reduced, thiol.

Despite the predicted endergonic electron transfer from the enamine to Ir(III)*, our quenching study provides support for the formation of an α-iminyl radical cation in the catalytic cycle. We next turned to computation to investigate the fate of this radical cation, in particular its impact on the enantioselectivity of the reaction.

3.2.2 Reaction profile calculations

To explain the experimentally-observed trends in enantioselectivity, a kinetic model was constructed that would allow us to examine the effect of the organocatalyst, substrate sidechain and photocatalyst on the reaction. An equilibrium mixture of *E*- and *Z*-enamines, defined by K_{eq}, will be oxidised by the excited photocatalyst with rates $k_{\mathrm{SET,E}}$ and $k_{\mathrm{SET,Z}}$, respectively, resulting in a non-equilibrium mixture of *E*- and *Z*-α-iminyl radical cations (Figure 3.8a). These radical cations may then potentially interconvert to their equilibrium populations *via* $\mathrm{TS}_{\mathrm{Z/E}}$. Attack on these α-iminyl radical cations by [1.1.1]propellane can occur through open (*Si*) / closed (*Re*)-face attack to the *E*/*Z* radical cations (Figure 3.8a, box), and these four pathways lead to the two diastereomers of the BCP adduct. It is crucial to know the relative rates of *E*/*Z*-radical cation isomerisation and [1.1.1]propellane addition; if isomerisation is fast ($k_{Z/E} \gg k_{Re\text{-}Z}$), stereoselectivity will be determined entirely in the C–C bond forming step, but if it is slow ($k_{Z/E} \ll k_{Re\text{-}Z}$), both the *E* / *Z* enamine ratio and open / closed face addition preference will determine the stereoselectivity. For this latter scenario, we can imagine two limiting / extreme cases (Figure 3.8b), which are outlined as follows:

Case 1 ($k_{1,E}/k_{1,Z} \ll k_{Si\text{-}E}/k_{Re\text{-}E}$): [1.1.1]Propellane addition occurs exclusively *via* the open face (*Si-E* / *Re-Z* attack) of the α-iminyl radical cation, such that the enantiomeric ratio (*er*) is approximately equal to the ratio of enamine oxidation rates ($k_{1,E}/k_{1,Z}$). The ratio $k_{1,E}/k_{1,Z}$ is defined as the ratio of intrinsic electron transfer rates between the excited photocatalyst and enamine ($k_{\text{SET},E}/k_{\text{SET},Z}$) multiplied by the ratio of *E* and *Z* enamines at equilibrium (K_{eq} = [*E*-enamine]/[*Z*-enamine]).

Case 2 ($k_{1,E}/k_{1,Z} \gg k_{Si\text{-}E}/k_{Re\text{-}E}$): [1.1.1]Propellane addition occurs to both the open (*Si-E* / *Re-Z*) and closed (*Re-E* / *Si-Z*) faces of the α-iminyl radical cations, such that the *er* is approximately equal to $k_{Si\text{-}E}/k_{Re\text{-}E}$.

If $k_{1,E}/k_{1,Z} \approx k_{Si\text{-}E}/k_{Re\text{-}E}$, both *Re-Z* and *Re-E* pathways will contribute to the formation of the minor (*Re*) enantiomer.

We anticipate an energetic preference for the *E*-enamine over *Z*-enamine due to 1,3-allylic strain between the enamine α-substituent and the pyrrolidine ring, which will also be the case for the *Z*-α-iminyl radical cation, and TS_{Re-Z} and TS_{Si-Z}. Additional steric repulsion might be expected between [1.1.1]propellane and the diarylprolinol pyrrolidine substituent, disfavouring $\text{TS}_{Re\text{-}E}$ and TS_{Si-Z} – an effect often cited as the origin of stereoselectivity with the Hayashi-Jørgensen organocatalyst.[218]

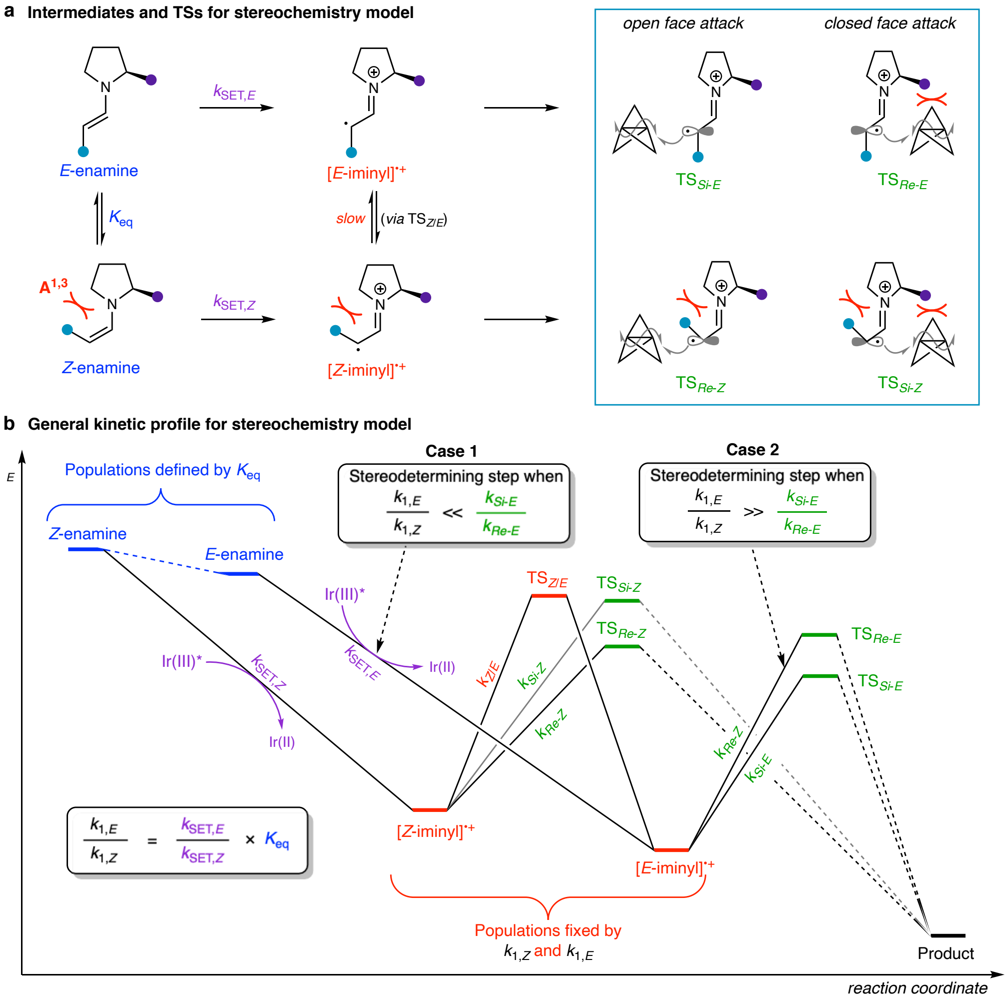

Figure 3.8: **a.** Enamines, α-iminyl radical cations, and C–C bond forming TSs for the stereodetermining step of the catalytic cycle. **b.** Kinetic profile that defines the stereodetermining processes of the catalytic cycle.

C–C bond formation *vs* isomerisation

To investigate the competition between the rates of radical cation isomerisation vs C–C bond formation, we constructed a model system of the α-iminyl radical cation derived from propanal and pyrrolidine (**15**). The reaction pathway was calculated at the SMD(DME)-DLPNO-CCSD(T)/def2-TZVPP//SMD(DME)-PBE0-D3BJ/def2-TZVP level. The E-α-iminyl radical cation ***E*-15** was found to be 4.1 kcal mol^{-1} lower in energy than ***Z*-15**, reflecting the manifestation of 1,3-allylic strain in the latter ($r_{\text{H–H}}$ = 2.25 Å, ∠C1–C2–C3 = 129.9°, Figure 3.9). We found that the activation barrier connecting ***E*-** and ***Z*-15** (**TS$_{Z/E}$-15**) was 17.3 kcal mol^{-1}, presumably reflecting the inevitable loss of radical stabilisation during this interconversion. Addition of [1.1.1]propellane to ***E*-15** was calculated to be slightly endergonic, due to the approximate cancellation of the enthalpic and entropic contributions upon bond formation. The activation free energy for the TS that connects ***E*-15** to adduct **16** (**TS-*E*-15**) was found to be 13.9 kcal mol^{-1}, in comparison with $\Delta G^{\ddagger}$ = 12.9 kcal mol^{-1} for the TS that connects ***Z*-15** to adduct **16** (**TS-*Z*-15**). The finding that C–C bond formation is likely to occur with a lower barrier than isomerisation suggests that we cannot assume an equilibrium population of *E*- and *Z*-α-iminyl radical cations in the reaction, and therefore that the stereoselectivity may be determined by K_{eq} if open-face addition is dominant.

Methodology validation

Initial attempts to calculate TSs for the diarylprolinol silyl ether systems were thwarted by a flat PES, and resultant low barrier, for the addition of [1.1.1]propellane to these α-iminyl radical cations. A pragmatic approach was therefore adopted in which the fully-optimised forming C–C distances from model systems were used as constraints for the TS structures of the full system. This approach requires validation to ensure that such an approximation would still lead to results

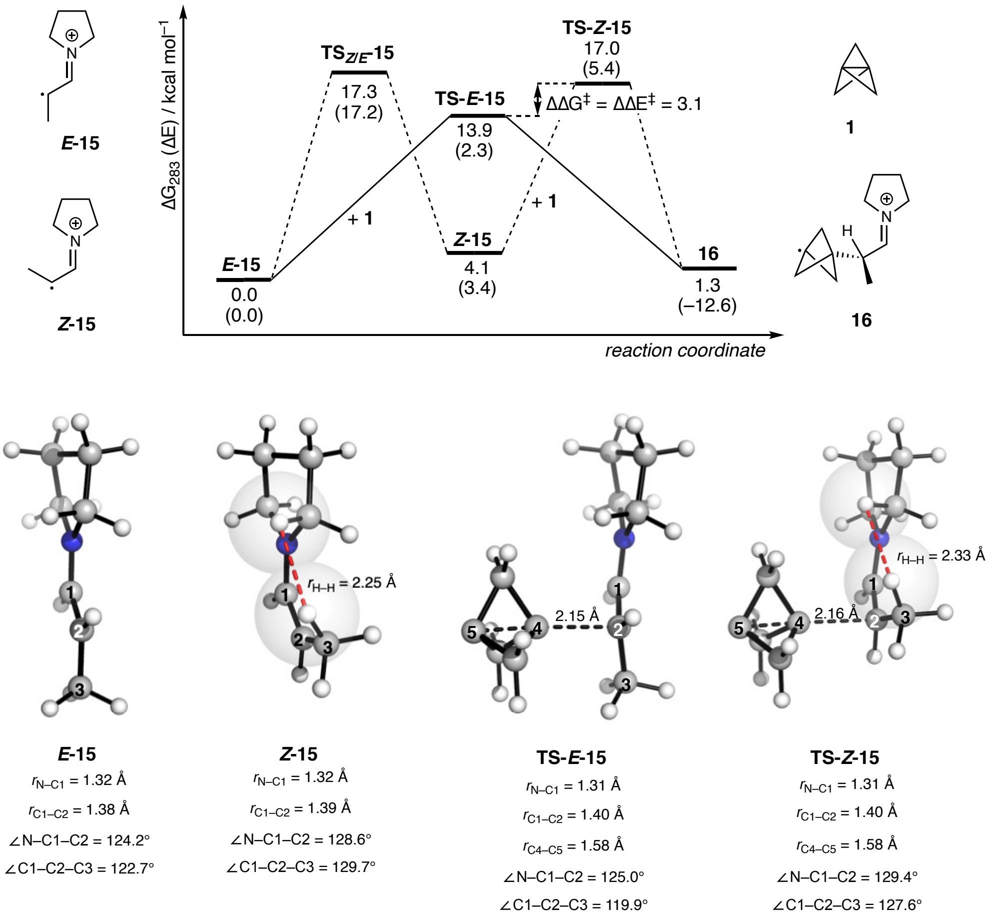

Figure 3.9: Calculated PES for the competition between α-iminyl radical cation *E*/*Z* isomerisation and [1.1.1]propellane addition, at the SMD(DME)-DLPNO-CCSD(T)/def2-TZVPP//SMD(DME)-PBE0-D3BJ/def2-TZVP level. Free energies calculated at 283.15 K and 1 M, distances shown in Å, and angles in degrees.

that are representative of the real system. Unfortunately the use of a constrained TS prevents an estimation of entropic contributions to barrier differences, since the structures are not true minima on the PES; however, the approximation that $\Delta\Delta G^{\ddagger} \approx \Delta\Delta E^{\ddagger}$ for this system is validated below.

Firstly, to validate the use of single-hybrid DFT for optimisation, the forming C–C distance between [1.1.1]propellane and ***E*-15** was scanned using either PBE0 or B2GP-PLYP (both with D3BJ empirical dispersion) with either the def2-SVP or def2-TZVP basis set, and the SMD solvent model for DME (Figure 3.10a). Taking SMD(DME)-B2GP-PLYP-D3BJ/def2-TZVP as the reference, the PBE0 functional with the same basis set and D3BJ dispersion slightly underestimates the activation energy, as expected from the results of Chapter 2. Single point calculations at the SMD(DME)-B2GP-PLYP-D3BJ/def2-TZVPP level for addition TSs with model system **15** at either the SMD(DME)-B2GP-PLYP-D3BJ/def2-TZVP or SMD(DME)-PBE0-D3BJ/def2-TZVP level revealed a discrepancy of < 0.1 kcal mol^{-1}, suggesting that the geometry at the latter level of theory would be adequate.

Unfortunately, decreasing the basis set size artificially increases the driving force (presumably due to basis set superposition error) which lowers the activation energy, and all attempts to calculate TS barriers for the diarylprolinol system were unsuccessful with both the def2-SVP and def2-TZVP basis sets.

To validate the use of constrained TSs for the diarylprolinol system, we built a system of intermediate size (**17**), in which a *tert*-butyl group was used in place of the diaryl / silyl ether pyrrolidine substituent (Figure 3.10b). Relative activation energies, $\Delta\Delta E^{\ddagger}$, for the constrained TSs were compared with those from full optimisation at the SMD(DME)-PBE0-D3BJ/def2-SVP for the *Si*-*E*, *Re*-*E* and *Re*-*Z* approaches, where we found that the relative energies (SMD(DME)-B2GP-

a **Methodology test**

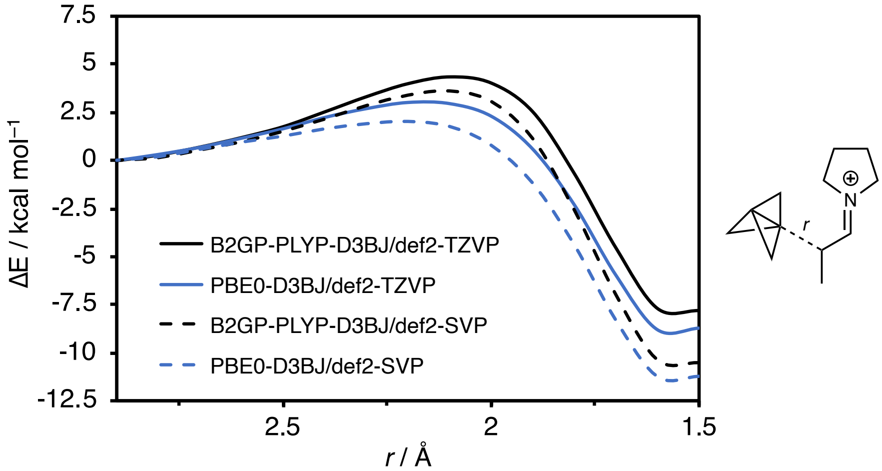

b **Constrained vs fully optimised TS geometries**

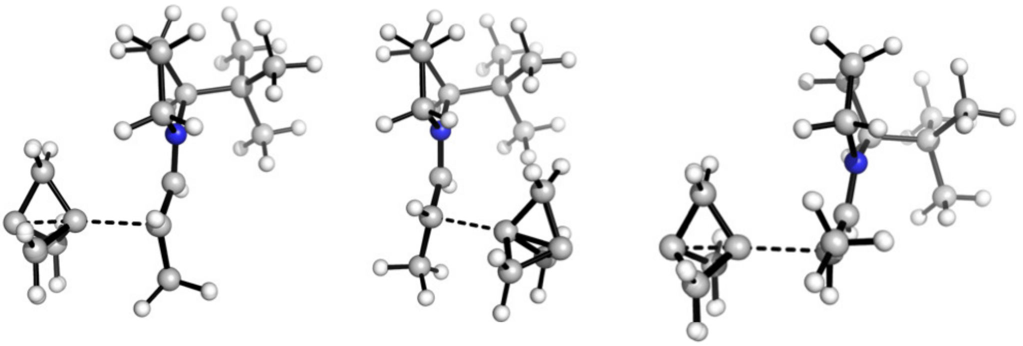

TS-*Si*-*E*-17	**TS-*Re*-*E*-17**	**TS-*Re*-*Z*-17**
$\Delta\Delta G^{\ddagger}_{\text{full}}$ = 0.0	$\Delta\Delta G^{\ddagger}_{\text{full}}$ = 0.2	$\Delta\Delta G^{\ddagger}_{\text{full}}$ = 2.9
$\Delta\Delta E^{\ddagger}_{\text{full}}$ = 0.0	$\Delta\Delta E^{\ddagger}_{\text{full}}$ = 0.1	$\Delta\Delta E^{\ddagger}_{\text{full}}$ = 3.0
$\Delta\Delta E^{\ddagger}_{\text{constrained}}$ = 0.0	$\Delta\Delta E^{\ddagger}_{\text{constrained}}$ = 0.1	$\Delta\Delta E^{\ddagger}_{\text{constrained}}$ = 3.1

Figure 3.10: **a.** PES for the addition of [1.1.1]propellane to ***E*-15** as a function of the forming C–C bond length (*r*) in Å. **b.** Overlaid fully-optimised and constrained TS structures for the addition of [1.1.1]propellane to ***E*-17** and **Z-17**, and relative Gibbs free energies ($\Delta\Delta G^{\ddagger}$) and electronic energies ($\Delta\Delta E^{\ddagger}$) at the SMD(DME)-B2GP-PLYP-D3BJ/def2-TZVPP//SMD(DME)-PBE0-D3BJ/def2-TZVP level. Free energies calculated at 283.15 K and 1 M.

PLYP-D3BJ/def2-TZVPP) of the structures from each of these approaches at the level did not exceed 0.1 kcal mol^{-1}. Additionally, $\Delta\Delta E^{\ddagger}$ and $\Delta\Delta G^{\ddagger}$ showed excellent agreement, with deviations not exceeding 0.1 kcal mol^{-1}, suggesting that our approximations would allow us to gain at the very least qualitative, if not quantitative insight into selectivity in the full system.

Since the nature of the sidechain could impact the TS geometry, we also constructed a third model system (**18**) with a methyl carbamate (Moc) substituent in the place of the methyl substituent, as an analogue of substrate **5a** used for the experimental optimisation studies (Figure 3.11). As for the model system with a methyl sidechain (**15**), there is a thermodynamic preference for the *E*-α-iminyl radical cation over the *Z* geometry, which can again be linked to sidechain / pyrrolidine steric repulsion. The activation barrier for the formation of adduct **19** from ***E*-18** and **1** is similar to that connecting ***Z*-18** and **1** to adduct **19** (10.9 and 10.6 kcal mol^{-1}, respectively). We suggest that the barrier-lowering effect that arises from the reduction in 1,3-allylic strain on reaction with **1** that was seen for **TS-Z-15** (methyl sidechain) is also important for **TS-Z-18**; however, while this effect resulted in a 1 kcal mol^{-1} lowering of the activation barrier for the *Z* isomer of the iminyl radical cation over the *E* isomer for the methyl sidechain, the same magnitude is not seen for the Moc sidechain. A distortion / interaction analysis, along with recognition of an earlier TS for the *E* than *Z* isomer, indicates a slightly stronger interaction between the propellane and ***E*-18** earlier on the PES. This effect may be due to the conformation of the sidechain, where the antiperiplanar relationship between the radical centre and the C–N bond stabilises the TS.

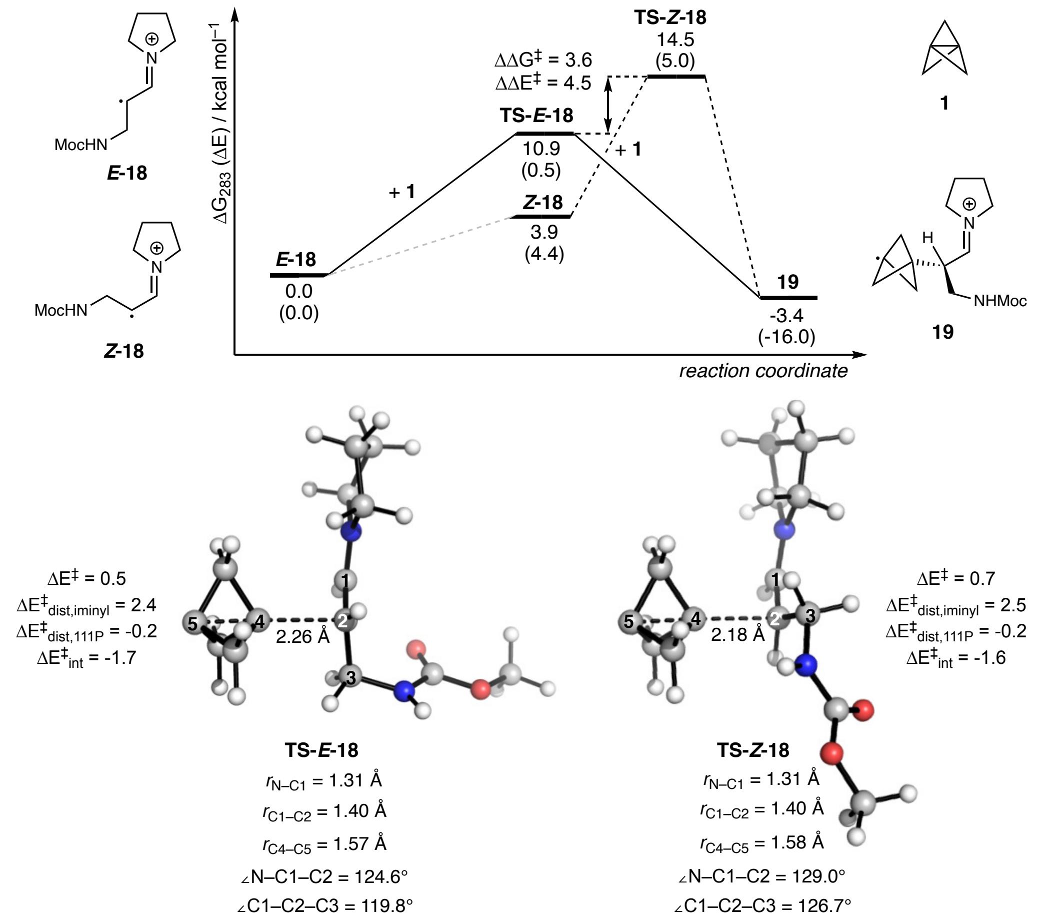

Figure 3.11: Calculated PES for the addition of [1.1.1]propellane to *E*/*Z*-α-iminyl radical cations ***E*-18** and ***Z*-18**, at the SMD(DME)-DLPNO-CCSD(T)/def2-TZVPP//SMD(DME)-PBE0-D3BJ/def2-TZVP level. Free energies calculated at 283.15 K and 1 M, distances shown in Å, and angles in degrees.

Stereoselectivity in the full catalytic system

With a method to calculate relative activation barriers in hand, we could then examine the relationship between equilibrium *E* / *Z* enamine ratios, open / closed face addition, and the observed stereoselectivity. Gibbs free energy changes (ΔG) were calculated for the *E* and *Z* minima at 283 K, and converted to equilibrium constants using the relation $K_{\mathrm{eq}} = \exp^{(-\Delta G/RT)}$. The relative Gibbs free energies of ***E*-20** and ***Z*-20** ($\Delta G_{E/Z}$ = 3.9 kcal mol^{-1}) led to an estimation of $K_{\mathrm{eq}} = 1 \times 10^3$ at 283 K (Figure 3.12a, i). In comparison, the *Si-E* addition pathway is strongly favoured over *Re-E* addition ($\Delta\Delta E_{Si\text{-}E/Re\text{-}E}$ = 4.9 kcal mol^{-1}), giving an estimated $k_{Si\text{-}E}/k_{Re\text{-}E}$ of 6×10^3 at 283 K (Figure 3.12a, ii). Stereoselectivity is therefore likely to be determined by Case 1 – *i.e.*, the enamine *E*/*Z* ratio limits the observed *ee* (as well as a possible contribution from the relative oxidation rates of these enamines, since a value of $K_{\mathrm{eq}} = 1 \times 10^3$ would imply an *ee* of 99.8 % at 283 K, compared with the experimental value of 89%).

Looking more closely at the reason for such a large preference for open-face addition, non-covalent interaction (NCI) analysis reveals stabilising C–H$\cdots$F and C–H$\cdots$O interactions between the Moc sidechain of the α-iminyl radical cation and the diarylprolinol substituents (Figure 3.12a, iii and Appendix B). Closed-face attack would require the loss of these interactions to allow the propellane to approach the radical centre. We hypothesised that these interactions amount to an enhanced steric block of the closed face of the radical cation, and that the absence of these interactions would lead to poorer selectivity.

To test this idea, we replaced the trifluoromethyl substituents on the organocatalyst with hydrogen atoms (**21**, Figure 3.12b). Interestingly, the calculated enamine *E*/*Z* ratio is enhanced compared with the trifluoromethylated organocatalytic system ($\Delta G_{E/Z}$ = 4.8 kcal mol^{-1}, $K_{\mathrm{eq}} = 5 \times 10^3$, Figure 3.12b, i) – perhaps due to stronger

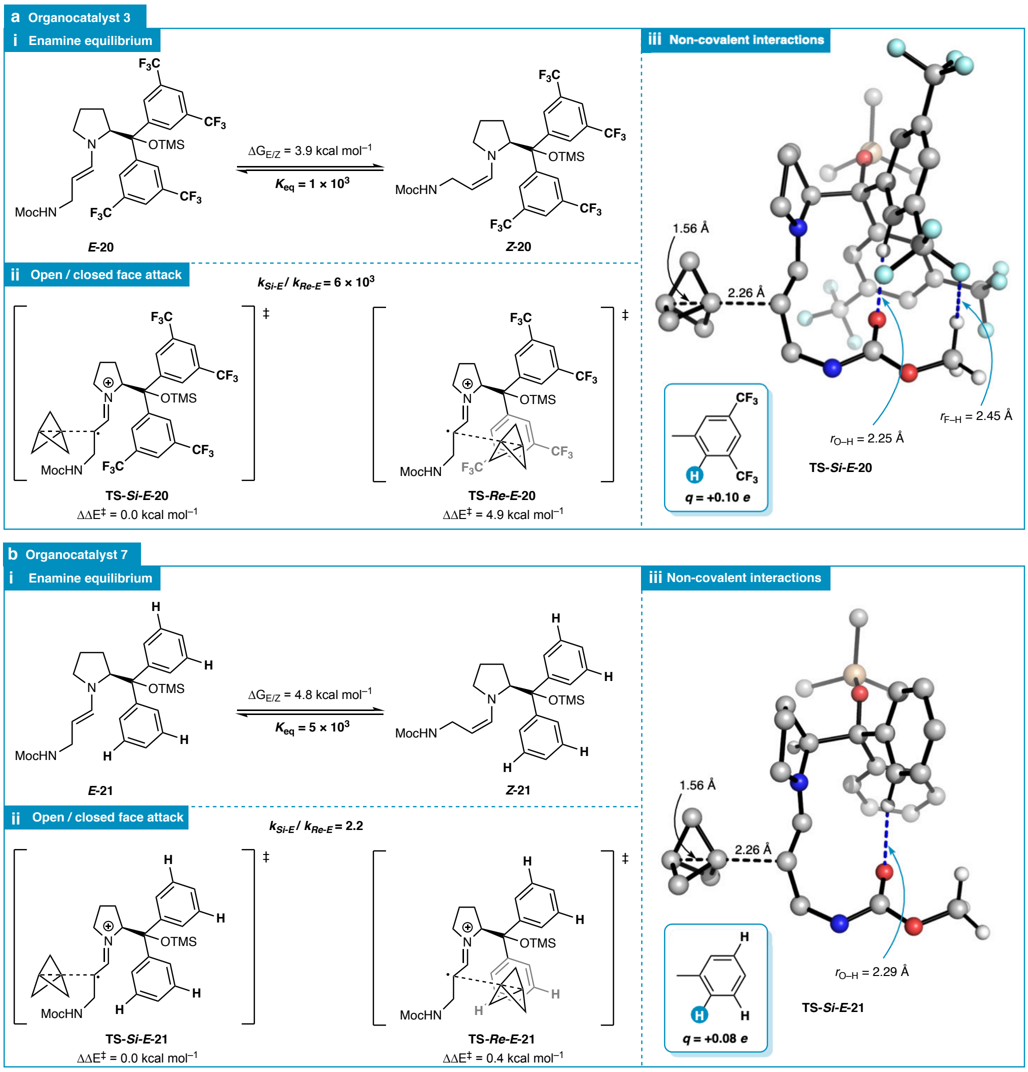

Figure 3.12: Calculated *E*/*Z*-enamine equilibria (i), constrained TSs for [1.1.1]propellane addition (ii) and non-covalent interactions for *Si*-*E* attack (iii) for organocatalysts **3** (**a**) and **7** (**b**). H atoms hidden for clarity. Inlay: H atom Hirshfeld charges for toluene and 3,5-bis-CF3-toluene.

interactions between the sidechain and the aryl substituents in **Z-20**. However, this ratio becomes inconsequential to the selectivity; closed-face (*Re-E*) addition is now disfavoured by only 0.4 kcal mol^{-1} with respect to open-face (*Si-E*) addition, resulting in $k_{Si\text{-}E}/k_{Re\text{-}E}$ = 2.2 at 283 K (Figure 3.12b, ii) – corresponding to a predicted *ee* of 34%. This value is in excellent agreement with the experimental stereoselectivity using this organocatalyst (44% *ee*), and indicates a switch from Case 1 to Case 2, where closed-face addition is the dominant source of the minor enantiomer.

NCI analysis shows a significant reduction in the appearance of stabilising non-covalent interactions between the Moc sidechain and the organocatalyst substituents (Figure 3.12b, iii and Appendix B). Calculated Hirshfeld charges for model systems 3,5-bis-CF_3-toluene and toluene for the crucial H atom involved in the most important C–H$\cdots$O interaction reveals a small (0.02 *e*) decrease in partial charge for the latter molecule (Figure 3.12, inlay), which points to a slightly weaker electrostatic interaction with the carbonyl oxygen of the Moc sidechain. In combination with the reduction in dispersion interactions between the sidechain and diphenylprolinol substituents compared with the CF_3-substituted organocatalyst, a general decrease in interactions between the sidechain and organocatalyst is the proposed cause of poor stereoselectivity with this organocatalyst.

We were also interested to see that high levels of stereoselectivity could be induced in the absence of polar functionality, for example substituting the Moc sidechain for a hexyl chain in substrate **5e** (Figure 3.13a). For this system, K_{eq} was calculated to be 5×10^3 ($\Delta G_{E/Z}$ = 4.8 kcal mol^{-1}, Figure 3.13a, i), and $k_{Si\text{-}E}/k_{Re\text{-}E}$ at 283 K as 70 ($\Delta\Delta E^{\ddagger}_{Si\text{-}E/Re\text{-}E}$ = 2.4 kcal mol^{-1}, Figure 3.13a, ii). These values would suggest a switch to Case 2 – the substantial contribution of 1,3-allylic strain in the *Z*-enamine means $k_{Si\text{-}E}/k_{Re\text{-}E}$ is limiting. The attractive sidechain / diarylprolinol NCIs again enhance the closed face steric block, leading to a predicted ee of 97%

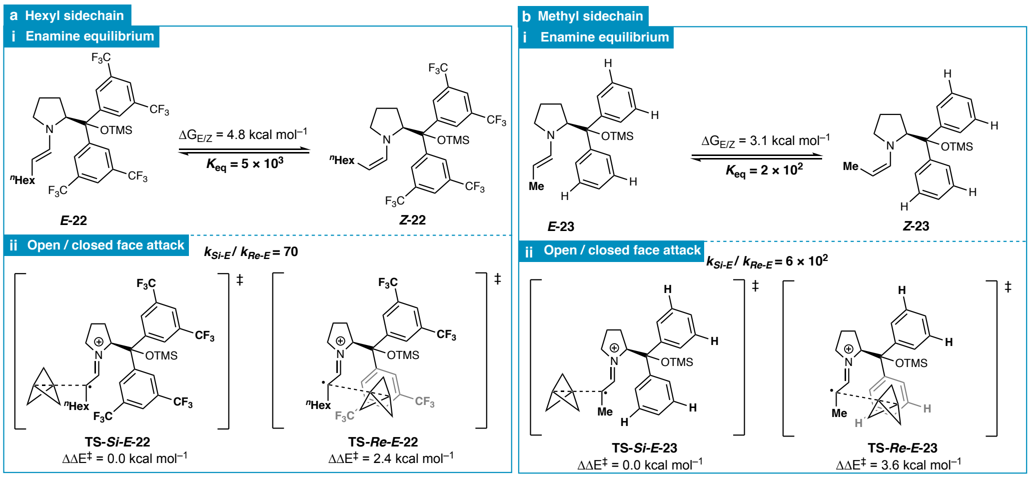

Figure 3.13: Calculated *E*/*Z*-enamine equilibria (i) and constrained TSs for [1.1.1]propellane addition for substrates **5e** (**a** and **5b** **b**.

for this substrate – the same value as that seen experimentally.

The low *ee* of 64% observed experimentally for propanal (*i.e.*, a methyl sidechain) merits further discussion. We anticipated that the methyl sidechain would interact less strongly with the diarylprolinol substituents, and therefore the attack of [1.1.1]propellane to the closed face of the radical cation would be more similar in energy to attack of the open face, resulting in Case 2 (Figure 3.13b, ii). However, this prediction was not borne out by the calculated $k_{Si\text{-}E}/k_{Re\text{-}E}$ value of 6×10^2 at 283 K ($\Delta\Delta E^{\ddagger}_{Si\text{-}E/Re\text{-}E}$ = 3.6 kcal mol^{-1}), which would correspond to an *ee* of 99.7%. In comparison, the calculated enamine *E*/*Z* energies correspond to a K_{eq} of 2×10^2 ($\Delta G_{E/Z}$ = 3.1 kcal mol^{-1}, Figure 3.13b, i), likely suggesting that selectivity is determined not by a reduced preference for open-face addition, but rather by the enamine *E*/*Z* ratio and the subsequent rates of oxidation (Case 1). The reduced *E*/*Z* enamine ratio can be attributed to the small size of the methyl sidechain compared with longer sidechains. However, the small difference between $\Delta\Delta E^{\ddagger}_{Si\text{-}E/Re\text{-}E}$ and $\Delta G_{E/Z}$ prevents any stronger conclusions from being drawn.

Origins of the dependence of stereoselectivity on the photocatalyst

The above studies on the variation of enantioselectivity with the nature of the sidechain and diarylprolinol substituents led to explanations of selectivity being limited either through the irreversible oxidation of equilibrium populations of *E* and *Z* enamines, or by poor selectivity for open-face addition due to a lack of stabilising NCIs between the substrate sidechain and diarylprolinol substituents. However, the use of K_{eq} to predict whether Case 1 or 2 would be dominant implicitly assumes that the *E* and *Z* enamines would be oxidised (irreversibly) at the same rate.

Estimation of K_{eq} for each of the systems mentioned above in which Case 1 is in operation results in a systematic overestimation of reaction stereoselectivity. There are a few reasons that this might be the case, the first of which could be due to an overestimation of $\Delta G_{E/Z}$ from our calculations – which is certainly possible given the difficulty of accurately predicting entropy in large, flexible molecules. However, this would not account for any variation of enantioselectivity with the choice of photocatalyst.

A possible cause of this catalyst dependence is that, while it was assumed that the oxidation of the *E* and *Z* enamines is irreversible, the lack of strong driving force for iminium ion oxidation might suggest that electron transfer could occur from the reduced photocatalyst back to the α-iminyl radical cation. The result of this would be that the *E* and *Z* iminyl radical cations could equilibrate not only through C–C bond rotation, but also by interconversion of the precursor enamines (*via* protonation to the iminium ions). This equilibration would then result in C–C bond formation being stereodetermining, therefore direct competition between *Si-E*, *Re-E* and *Re-Z* attack. However, for the system with a Moc sidechain, *Re-Z* attack is even higher in energy than *Re-E* (Figure 3.14a), so any reversibility in the oxidation step would be inconsequential to the stereoselectivity; the same is true for the *n*-hexyl sidechain (Figure 3.14b). Conversely, *Re*-*Z* attack is lower in energy than *Re*-*E* attack on the α-iminyl radical cation with a methyl sidechain (due to relief of torsional strain and little contribution from NCIs, Figure 3.14c), therefore reversible oxidation could alter the stereoselectivity. However, the value of $\Delta\Delta E^{\ddagger}_{Si\text{-}E/Re\text{-}Z}$ = 2.2 kcal mol^{-1} would still correspond to an *ee* of 96% – significantly more than that observed experimentally (64%). In combination, these results suggest that any reversibility in the oxidation of the enamine has little consequence on the reaction stereoselectivity.

An alternative explanation for at least part of the discrepancy between the predicted and experimental stereoselectivity may, however, come from differing oxidation rates of the *E*- and *Z*-enamines. As mentioned, the *Z*-enamine features greater 1,3-allylic strain between the enamine α-substituent and the pyrrolidine ring (Figure 3.15), which manifests itself as a 3.1° increase in pyramidalisation at the N atom ($\mathrm{N_p}$) for the *Z*-enamine compared with the *E*-enamine. Upon oxidation, both *E*- and *Z*-enamine N atoms approach planarity, and we therefore anticipate enhanced strain relief at the electron transfer TS for the *Z*-enamine. Additionally, upon oxidation, the enamine C=C bond and C3$\cdots$C4 distance lengthens by 0.04 Å and 0.1 Å, respectively, reducing the steric clash between the *Z*-enamine and *Z*-α-iminyl radical cation. Interestingly, the oxidation of the *E*-enamine is calculated to be marginally favoured over the *Z*-enamine ($\Delta\Delta G$ = 1.2 kcal mol^{-1}) which could simply relate to superior product stabilisation. However, the rate of *Z*-enamine oxidation may be greater than for the *E*-enamine, as the former will enjoy greater relief of steric strain along the C1–C2 coordinate at the electron transfer TS.

This proposed difference in oxidation rates of the two enamines could reasonably be expected to vary with the nature of the photoredox catalyst through changes in

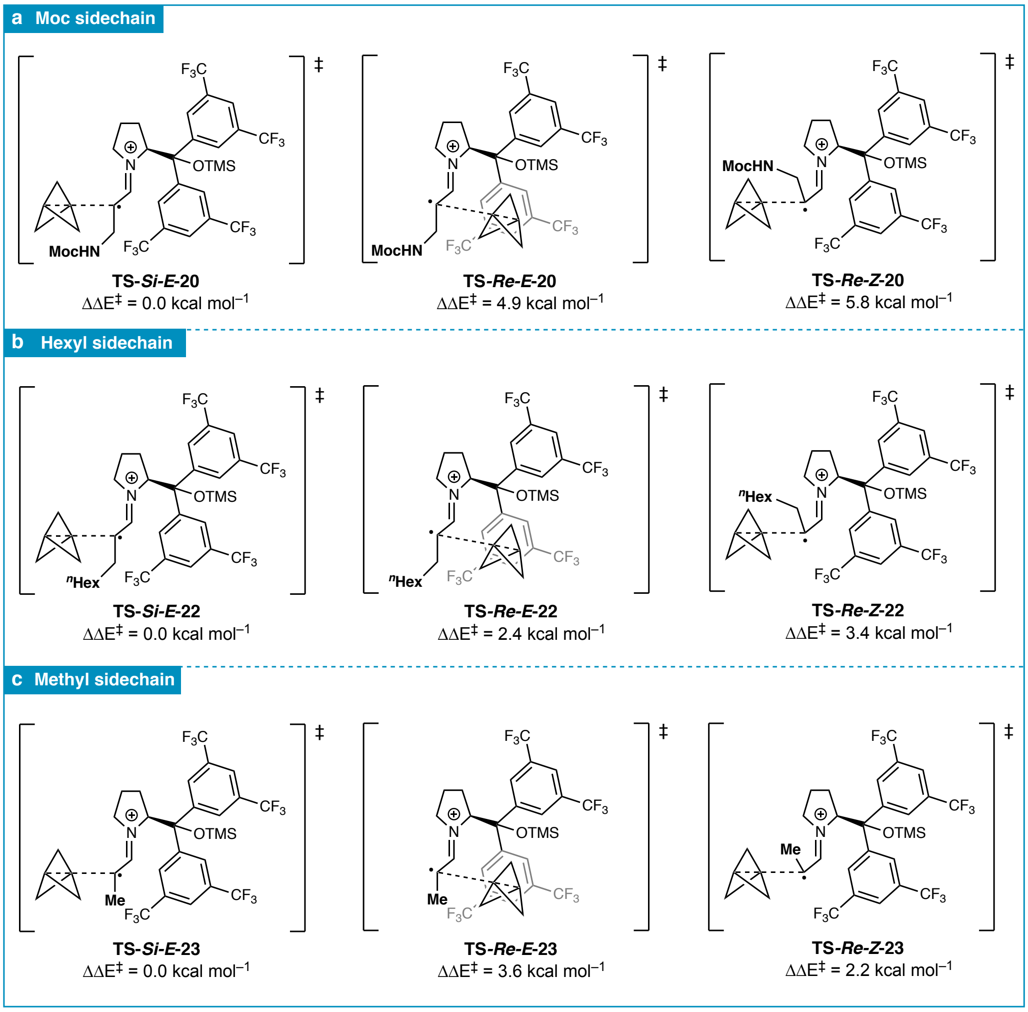

Figure 3.14: Comparison of *Si*-*E*, *Re*-*E* and *Re*-*Z* constrained TS energies for substrates **5a** (Moc sidechain, **a**), **5e** (*n*-hexyl sidechain, **b**) and **5b** (methyl sidechain, **c**).

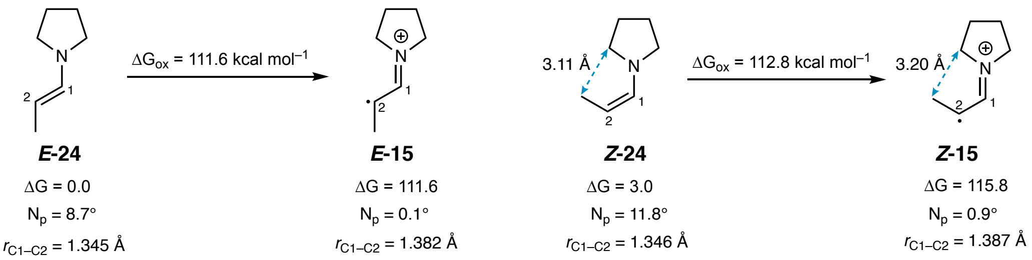

Figure 3.15: Comparison of *E*- and *Z*-enamine oxidation processes, calculated at the SMD(DME)-DLPNO-CCSD(T)/def2-TZVPP//SMD(DME)-PBE0-D3BJ/def2-TZVP level. Free energies calculated at 283.15 K and 1 M.

its excited state oxidation potential or structure – which could explain the unusual variation in *ee* observed experimentally for different photocatalysts. This hypothesis, however, requires further experimental validation, for example through a systematic study on the relative oxidation rates of *E* and Z enamines under geometric constraints with photocatalysts of varying type and redox potential range. The development of computational methods to explicitly calculate intermolecular transfer processes would be required for further theoretical study.

3.3 Conclusions

In this Chapter, a multicatalytic approach for the synthesis of α-chiral bicyclopentyl aldehydes was presented (Figure 3.16a): Photoredox-catalysed one-electron oxidation of an enamine formed from the reaction of an aldehyde and an organocatalyst results in the formation of an α-iminyl radical cation, which cleaves the interbridgehead bond of [1.1.1]propellane to form a chiral bicyclopentyl radical. This radical is then trapped by an H-atom catalyst, and results in the formation of the α-chiral bicyclopentyl aldehyde after hydrolysis of the iminium ion. The reaction was shown to tolerate a range of functionalities on the aldehyde, giving easy access to valuable building blocks for drug design.[128,211]

A combined experimental and theoretical study provided evidence for the proposed mechanistic cycle, including Stern-Volmer luminscence quenching that confirmed the feasibility of the key electron transfer event between the enamine and excited photocatalyst. A model for enantioselectivity in this reaction was proposed that is consistent with experimental observations (Figure 3.16b), and DFT calculations were used to understand the critical role of enamine geometry and NCIs to achieve high stereoselectivity. Crucially, rapid C–C bond formation is enabled by σ–π-delocalisation in [1.1.1]propellane, resulting in a similar reactiv-

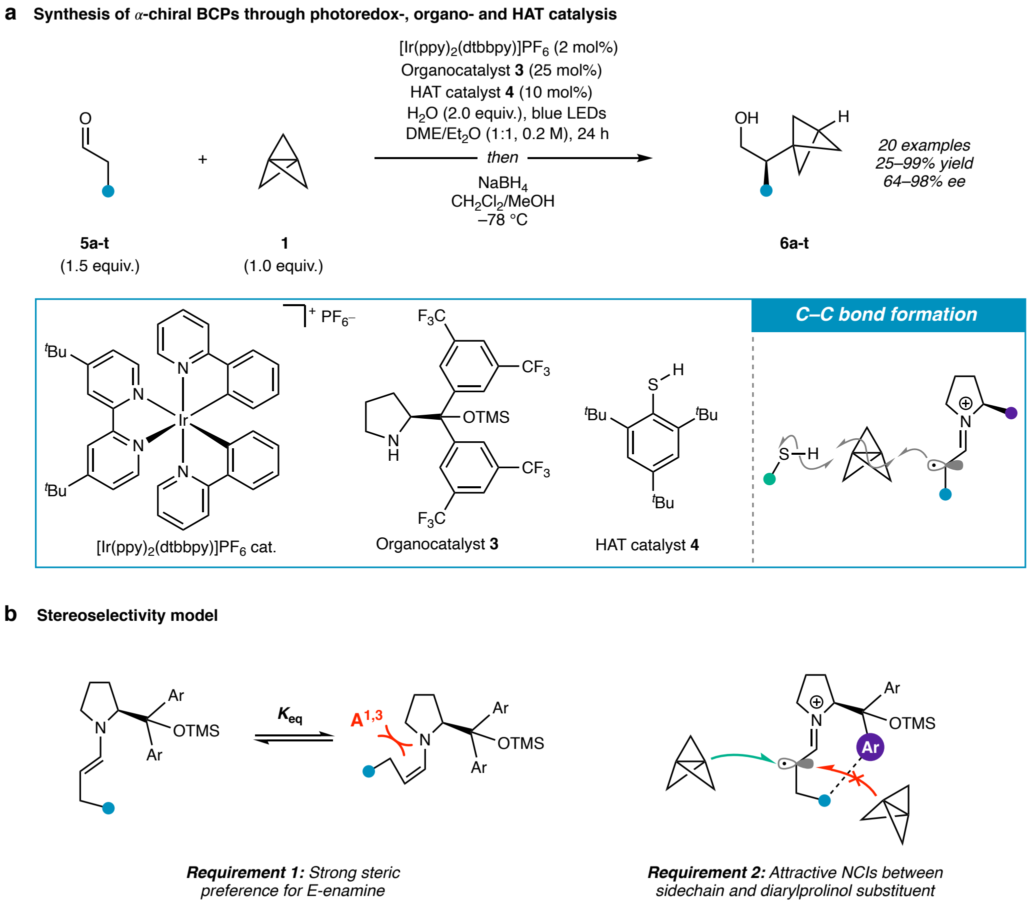

Figure 3.16: **a.** Overview of the α-chiral BCP synthesis developed here. **b.** Model for stereoselectivity for this reaction, with two requirements that must be fulfilled to achieve high stereoselectivity.

ity profile to olefins.

The judicious choice of an organocatalyst that benefits from significant stabilising NCIs between the substrate sidechain and the diaryl prolinol substituents effectively results in enhanced steric shielding of the closed face of the α-iminyl radical cation. In the absence of these NCIs, closed-face addition will be in closer competition with open-face addition, resulting in poorer selectivity. Unexpectedly, with the 'right' organocatalyst these NCIs are sufficient to almost completely block closed-face attack, which changes the stereodetermining step from C–C bond formation to the oxidation of the *E*/*Z* enamines. Since the resultant α-iminyl radical cations interconvert with a rate slower than C–C bond formation, a high *E*/*Z* ratio is then important to ensure high stereoselectivity. It is suspected that the relative rates of *E* and *Z* enamine oxidation vary with the photocatalyst, which could also affect the observed stereoselectivity.

Based on these studies, two conditions are proposed that must be met to ensure high stereoselectivity in this reaction:

1. Sufficient 1,3-allylic strain to disfavour the *Z*-enamine at equilibrium.
2. Sufficient attractive NCIs between the substrate sidechain and diarylprolinol substituents to effectively block addition to the closed face of the radical cation.

It is hoped that the reaction and stereoselectivity models put forward in this Chapter offer both a practical method to access building blocks of value in medicinal chemistry, and further insight into this type of reaction mechanism for future reaction design. The importance of delocalisation-enabled reactivity is realised through the unusual dependence of stereoselectivity on the nature of the photocatalyst.

4 |

Quantifying the roles of delocalisation and strain release on the reactivity of small rings

In Chapter 2 the idea that the interbridgehead C–C bond in [1.1.1]propellane is delocalised over the cage was introduced, conferring both structural stability and enhanced reactivity. However, so far, the connection between delocalisation and reactivity has been qualitative. Moreover, relative importance of the release of the $\approx$ 30 kcal mol^{-1} strain energy and electronic delocalisation is unknown. In this Chapter, a quantitative model that allows the direct comparison of these two effects is proposed. The Bell-Evans-Polanyi principle and Marcus theory confirm that strain energy alone is indeed insufficient to account for the variation in reactivity of a variety of small rings with different connectivity. Building on work by Houk and Hoz,[53,54,56,58,61,62,219] delocalisation in small rings is quantified using NBO theory, and incorporated within the Bell-Evans-Polanyi and Marcus models to generate predictive models able to reproduce experimental reactivity trends. A simple 'rule of thumb' is also proposed, where the fusion of a three-membered ring to a breaking bond lowers the activation energy by $\approx$ 10 kcal mol^{-1} per ring – a rate enhancement of $\approx 10^7$ at 298 K.

4.1 Relationship between strain energy and reactivity

As the driving force for a reaction increases, the rate of that reaction will increase (Figure 4.1a). This idea was first quantified in 1924 by Brønsted who introduced an empirical linear relation-ship between the acidity of a general acid catalyst and the rate of the decomposition of $H_2N_2O_2$.[174] In 1936, Bell, and shortly afterwards Evans and Polanyi, independently investigated the physical origin of this linear relationship,[47,48] resulting in the eponymous Bell-Evans-Polanyi (BEP) principle which determines the activation energy of a reaction using the driving force for that step according to

$$\begin{gathered} \Delta E^{\ddagger} = \Delta E^{\ddagger}_{int} + \alpha \Delta E_r \\ 0 \leq \alpha \leq 1 \end{gathered} \tag{4.1}$$

where $\Delta E^{\ddagger}$ is the potential energy barrier to the reaction, and $\Delta E^{\ddagger}_{int}$ is the intrinsic activation barrier in the absence of a driving force, ΔE_r.

A similar result can be drawn from Marcus theory. Marcus originally investigated the rates of electron transfer using overlapping parabolas to describe the reorganisation of solvent spheres during electron transfer.[49] He later used the same formalism to describe chemical reactions (4.2),[52] where the overlapping parabolas represent the potential energy surface of the bonds being broken and formed over the course of the reaction (Figure 4.1b). The height of the intersection of the parabolas approximates the energy of the transition state (TS) relative to that of the reactants and products, which are found at the minima of the parabolas.

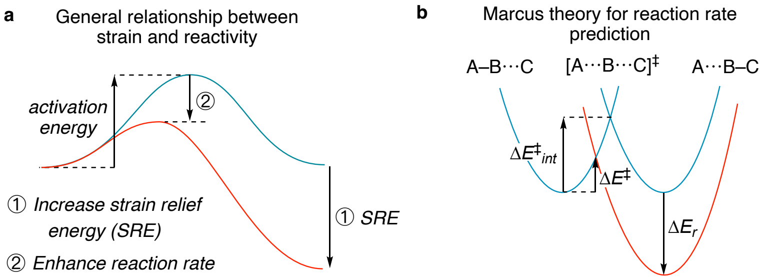

Figure 4.1: **a.** Increasing the reaction driving force through an increase in strain release lowers the activation barrier for that reaction. **b.** Overlapping parabolas describe the reaction PES, allowing the relationship between driving force (ΔE_r) and activation barrier ($\Delta E^{\ddagger}$) to be quantified using Marcus theory.

$$\Delta E^{\ddagger} = \Delta E^{\ddagger}_{int} + \frac{1}{2}\Delta E_r + \frac{\Delta E_r^2}{16\Delta E^{\ddagger}_{int}} \tag{4.2}$$

A comparison of (4.1) and (4.2) reveals that the Bell-Evans-Polanyi principle is an approximation to Marcus theory in which the potential energy surface is described by two overlapping straight lines (instead of parabolas). The two models should therefore give similar results for small changes in ΔE_r.

Both the BEP principle and Marcus theory directly link a reaction driving force and its activation energy. In principle, either of these relationships can be used to investigate the effect of strain release energy on reactivity – the strain release energy is equivalent to increasing the reaction driving force. If strain release were solely responsible for changes in reactivity, a strong linear relationship would be expected between the calculated and predicted activation energies using either (4.1) or (4.2).

The use of linear free energy relationships (LFERs) to investigate strain release reactivity was also identified by Houk and Hoz. Houk employed a BEP-type analysis to identify that [2 + 2 + 2] retro-cycloaddition reactions of cyclohexanes were 16 kcal mol^{-1} lower than expected when substituted with cyclopropanes (Figure

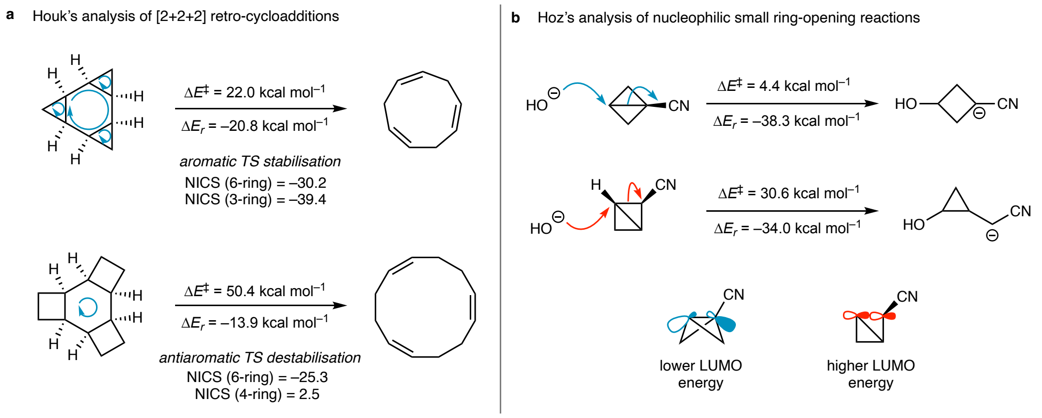

Figure 4.2: **a.** Houk's study on the relative rates of [2 + 2 + 2] retro-cycloadditions of substituted cyclohexanes. **b.** Hoz's study on the addition of nucleophiles to strained hydrocarbons.

4.2a).[57] Hoz, using Marcus theory, identified activation barriers 7–17 kcal mol^{-1} lower for the radical and anionic ring-opening of three-membered rings than expected (Figure 4.2b),[61] naming this strain-independent barrier-lowering effect an "additional factor". The origin of this "additional factor" has been debated. Hoz proposed a distortion-driven rehybridisation effect that lowers the LUMO of the breaking bond, causing earlier bond formation. Houk, using NICS calculations and an orbital interaction through-bond (OITB) model, proposed that aromaticity in TSs featuring three-membered rings causes the barrier-lowering effect, and that the LUMO-lowering effect proposed by Hoz was in fact a consequence of this aromaticity (for further discussion, see Section 1.1.2).

In this Chapter, a complementary and general model is provided that unifies the reactivity of small rings in terms of their bonding and strain release energies. The quantitative power of this model is illustrated in the systematic study of ring-opening reactions of small rings, culminating in analysis of heterosubstituted small rings and a 'rule of thumb' to quickly estimate relative reaction rates based on visual inspection.

4.2 Predicting the reactivity of small rings

A set of 12 hydrocarbons with varying numbers of small rings was constructed (Figure 4.3a), with numbers of three- (n_3) and four-membered (n_4) rings, strain energies and strain release energies summarised in Table D.1. For this set of molecules, TSs and adducts for the addition of a methyl radical, $CH_3^{\bullet}$, to each molecule were calculated at the DLPNO-CCSD(T)/def2-QZVPP//B2PLYP-D3BJ /def2-TZVP level, giving access to activation enthalpies ($\Delta H^{\ddagger}$) and reaction energies (ΔH_r) for the construction of BEP and Marcus models. Enthalpies were used in preference to free energies since strain energies are commonly reported in these terms, however the conclusions from these models were found to be independent of the choice of ΔH or ΔG.

Use of both the BEP and Marcus models for this set of reactions leads to a poor correlation (R^2 = 0.51 and 0.62, respectively, Figure 4.3b/c) and large prediction error (root mean-square error, RMSE = 10.1 and 8.8 kcal mol^{-1}, respectively). These findings are in line with previous studies, where the reaction driving force is insufficient to account for the observed reactivity trend. It is particularly noteworthy that the reaction enthalpies for the ring opening of cyclobutane, cyclopropane and [1.1.1]propellane are very similar (ΔH_r: –26.8, –28.4 and –28.2 kcal mol^{-1}, respectively), yet their activation enthalpies span over 30 kcal mol^{-1} ($\Delta H^{\ddagger}$: 36.1, 26.4 and 5.0 kcal mol^{-1}, respectively). In this case, enthalpic differences effectively determine differences in Gibbs free energies ($\Delta G^{\ddagger}$: 47.0, 36.9 and 15.3 kcal mol^{-1} respectively), which result in estimated rate constants spanning 23 orders of magnitude at 298 K. Clearly strain release is unable to account for this range of reactivity profiles; differences in delocalisation, therefore bonding, were therefore investigated as a means to improve predictions and recover a more complete picture of strain release reactivity.

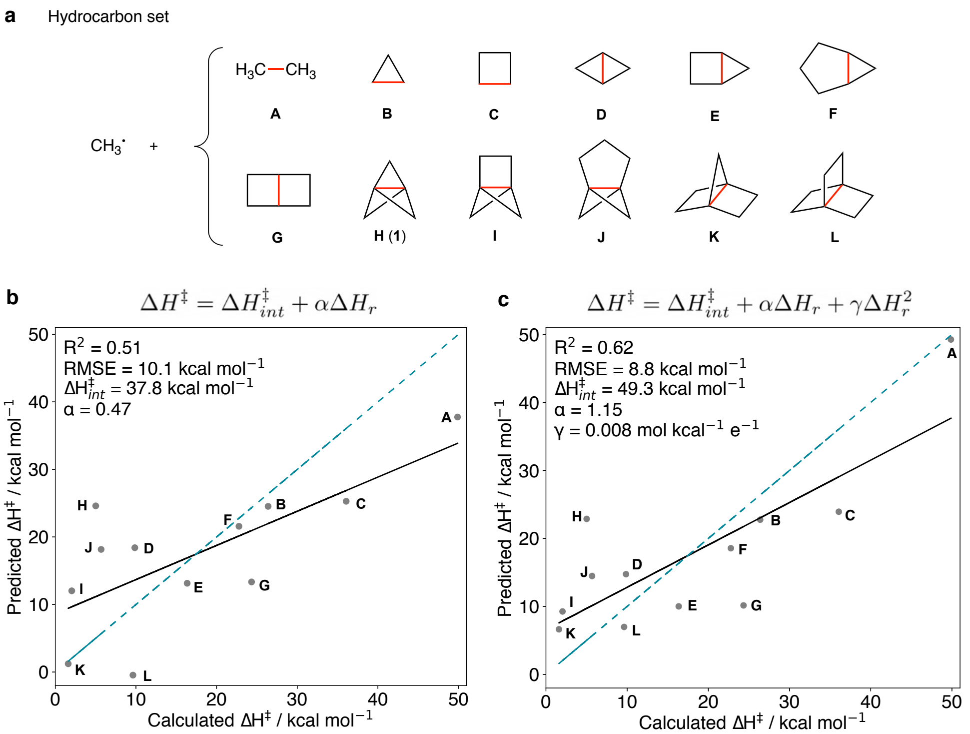

Figure 4.3: **a.** Set of 12 hydrocarbons with varying ring sizes and strain energies, and Bell-Evans-Polanyi (**b**) and Marcus (**c**) plots showing prediction of activation barriers using ΔH_r for this set of 12 hydrocarbons. Blue dashed lines represent perfect correlation, and solid black lines are the regression lines.

4.3 Linking delocalisation to reactivity

Delocalisation is an inherently fuzzy concept, since it is not a physical observable. It is defined here as the extent to which an electron pair in a bond between two atoms is spread over neighbouring atoms or groups, for example through conjugation or hyperconjugation.[220] Intuitively, one can imagine that a more delocalised bond will be easier to break, and therefore result in a lower activation barrier compared with a more localised bond. To investigate this relationship, first a method to routinely calculate the delocalisation associated with a given bond is required, that is both widely applicable and inexpensive to calculate for a range of system sizes. Two methods to obtain such a delocalisation parameter are focused upon here, and a comparison with delocalised MOs is briefly mentioned.

Quantifying delocalisation

The definition of delocalisation above lends itself to a local orbital representation. The Lewis representation of a molecule perfectly localises each bonding electron pair between two atoms.[170] Natural bond orbital (NBO) theory provides a way to quantify the extent of delocalisation, since each NBO represents an electron pair in the Lewis structure, with an orbital occupancy (N_{occ}) of exactly 2. Deviation from 2 indicates delocalisation of the electron pair, therefore 2–N_{occ} can be used to quantify delocalisation. For example, in Chapter 2 an NBO analysis of [1.1.1]propellane was presented, involving resonance between its Lewis structure and resonance forms with six alkene / carbene pairs, suggesting a delocalised electronic structure. 2–N_{occ} for **1** is 0.167, compared with 0.017 for the localised C–C bond in ethane.

For the set of 12 hydrocarbons introduced above, 2–N_{occ} was calculated for each of the bonds being broken and they were ranked by the extent of delocalisation (Figure 4.4). In general, bonds that are part of a three-membered rings are more delocalised than those that are part of the analogous four-membered ring. For example, the C–C bonds of cyclopropane (2–N_{occ} = 0.046) are more delocalised than cyclobutane (0.029), as expected from the analysis of Coulson and Moffitt.[27] Similarly, the interbridgehead bond of bicyclo[1.1.0]butane (0.125) is more delocalised than that of bicyclo[2.1.0]pentane (0.081), which is in turn more delocalised than the interbridgehead bond of bicyclo[2.2.0]hexane (0.045). The maximum number of three-membered rings that a bond can be part of is three, a value achieved by [1.1.1]propellane which gives rise to the maximum value of 2–N_{occ} for the set (0.167). Conversely, the minimum possible number of three-membered rings is trivially zero, which in this set we attribute to ethane with its minimum value of

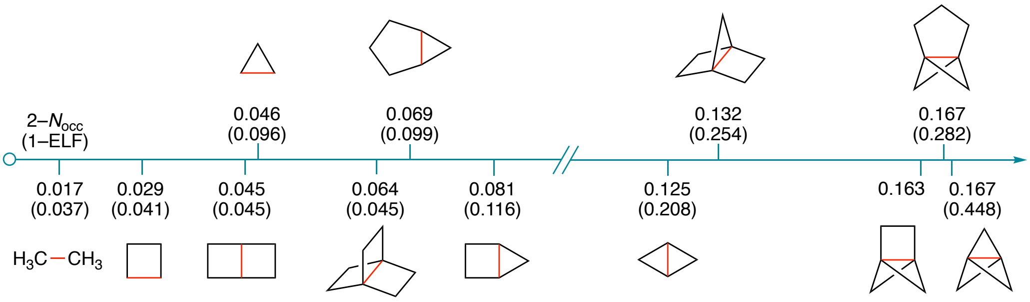

Figure 4.4: Ranking of delocalisation based on 2–Nocc or (1–ELF) of bonds shown in red for the set of 12 hydrocarbons shown in Figure 4.3a.

2–N_{occ} of 0.017.

An alternative scheme to represent the extent of delocalisation associated with a given bond is via the electron density of the molecule. The electron localisation function (ELF) provides one such measure, where the density at a point in space is compared with that of a uniform electron gas.[221] ELF runs from 0.5 (complete delocalisation) to 1 (complete localisation), so to compare directly with the orbital delocalisation measure we took the value of 1–ELF such that a larger value indicates greater delocalisation. The ELF value was calculated at the bond critical point for each of the 12 hydrocarbons, except [2.1.1]propellane for which no bond critical point could be identified. The trend in 1–ELF was found to follow closely that observed with the 2–N_{occ} parameter (Figure 4.4), giving us greater confidence that we are indeed quantifying delocalisation.

Combining strain and delocalisation measures

The delocalisation measure 2–N_{occ} was incorporated into the BEP model using a multiple linear regression (MLR) model. The resultant model (Figure 4.5a) gives an excellent correlation (R^2 = 0.97) and low prediction error (RMSE = 2.5 kcal mol^{-1}). The negative value of the coefficient β indicates that the intrinsic activation barrier decreases as delocalisation increases, independently of the contribution of strain release to the activation barrier. Including the quadratic term in the Marcus model alongside the 2–N_{occ} parameter results in a slight increase in the performance of the model (R^2 = 0.98, RMSE = 2.2 kcal mol^{-1}, Figure 4.5b). The coefficient α is 0.5, as expected from the Marcus equation (4.2), and γ is 0.002 mol kcal^{-1}, in reasonable agreement with the value $(16\Delta H^{\ddagger}_{int})^{-1}$ = 0.001 mol kcal^{-1} predicted by Marcus theory. The modified models are therefore reproducing the physical behaviour of the systems under study. Given the similarity in the behaviour of the BEP and Marcus models, only the BEP model was considered from this point onwards due to its simplicity.

Through the ranking of delocalisation in the 12 hydrocarbons by their delocalisation values, a general trend appears between the number of three-membered rings appended to the breaking bond, n_3, and the delocalisation parameter 2–N_{occ}. The n_3 parameter could be used in the place of 2–N_{occ} to predict the effects on activation barriers simply by visual inspection. The MLR model resulting from this substitution shows an excellent correlation between predicted and calculated activation barriers (R^2 = 0.99, Figure 4.5c) with a low prediction error (RMSE = 1.2 kcal mol^{-1}). The coefficient β using this model represents the decrease in intrinsic activation barrier per additional three-membered ring – in this case $\approx$ 10 kcal mol^{-1}. Since $\Delta\Delta H^{\ddagger} \approx \Delta\Delta G^{\ddagger}$ for this set of similar reactions, a rate enhancement of $\approx 10^7$ per additional three-membered ring is expected at 298 K.

Since the strain release energies of cyclobutane, cyclopropane and [1.1.1]propellane are approximately the same, their starkly different reactivity profiles can be attributed to the extent of bond delocalisation. This delocalisation increases from cyclobutane to [1.1.1]propellane due to the maximisation of n_3. Similarly, the activation energy ordering of bicyclo[2.2.0]butane (n_3 = 0) > bicyclo[2.1.0]pentane (n_3 = 1) > bicyclo[1.1.0]hexane (n_3 = 2) can be rationalised by the same argument. From this model, it is clear that simply varying the number of three-membered

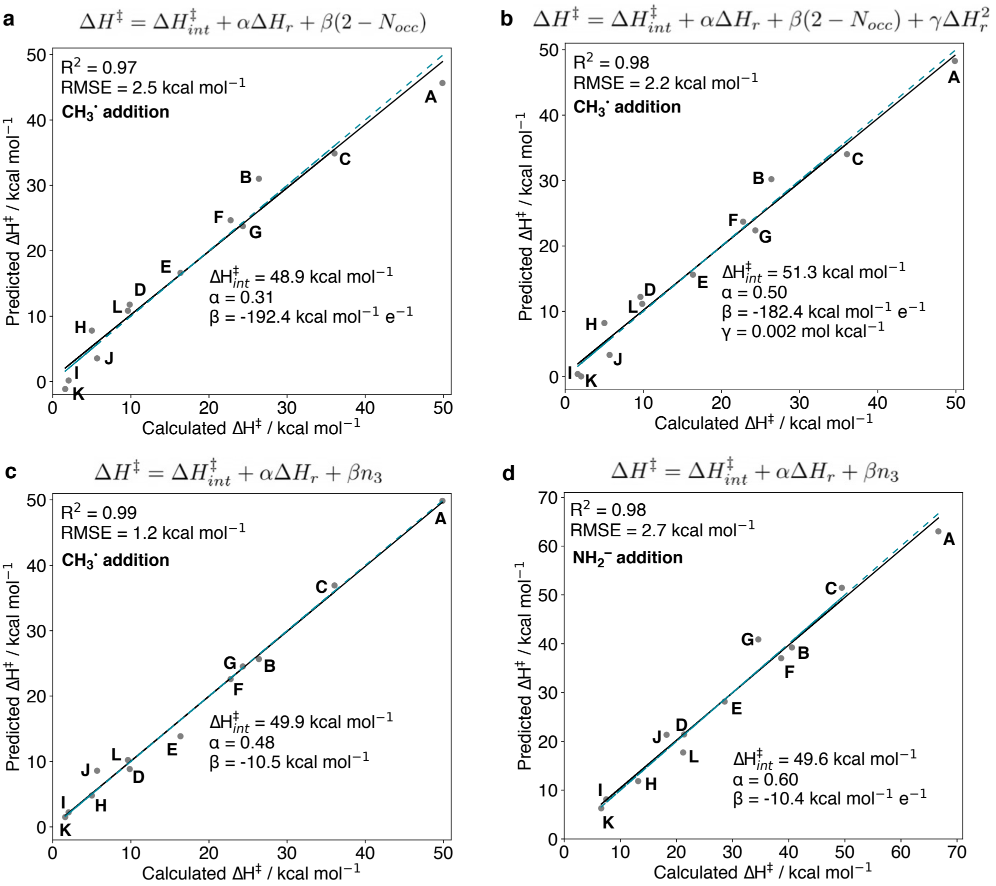

Figure 4.5: Multiple linear regression (MLR) plots for $CH_3^{\bullet}$ addition to the set of 12 hydrocarbons in Figure 4.3 based on the Bell-Evans-Polanyi (**a**) and Marcus (**b**) equations and the 2–N_{occ} parameter to include delocalisation, and MLR Bell-Evans-Polanyi + n_3 plots for $CH_3^{\bullet}$ (**c**) and NH_2^- (**d**) addition. Blue dashed lines represent perfect correlation, and solid black lines are the regression lines.

rings appended to a breaking bond is a powerful way to enhance or suppress reactivity, for example switching the behaviour of the molecule from a highly-reactive bioconjugate warhead (*e.g.*, bicyclo[1.1.0]butane derivatives)[114,222] to an inert lipid tail group (*e.g.*, bicyclo[2.2.0]hexane derivatives).[223]

To test the generalisability of the delocalisation model, the methyl radical was replaced with an amide anion, NH_2^-, as the species to attack each of the 12 molecules in the hydrocarbon set. Amide anion addition to [1.1.1]propellane, bicyclo[1.1.0]butane and bicyclo[2.1.0]pentane derivatives were employed by Baran for the synthesis of substituted amines,[114,194] therefore analysis of these systems would allow exploration of the importance of delocalisation in a further experimentally relevant setting (Figure 4.5d). Activation barriers are accurately predicted once again (R^2 = 0.98, RMSE = 2.7 kcal mol^{-1}), and the coefficient $\beta \approx$ –10 kcal mol^{-1} is in excellent agreement with that obtained for the radical reaction. This result indicates that the contribution of delocalisation to reactivity may be independent of reaction type. Based on this model, if the delocalisation effect were to be somehow removed from [1.1.1]propellane, its activation barrier would increase from 13.2 to 44.4 kcal mol^{-1}, rendering it inert under the reaction conditions. The release of strain energy therefore appears to be insufficient to cause the observed reaction – it is instead delocalisation that weakens the breaking bond, leading to its ‘spring-loaded’ behaviour.[114]

Having established the predictive power of either the $2–N_{occ}$ or n_3 delocalisation parameters in the BEP model, the extent to which Hoz’s LUMO-lowering effect or Houk’s aromaticity / OITB effect describe the same strain-independent reactivity enhancement was explored. The LUMO energy (E_{LUMO}) and HOMO-LUMO gap ($\Delta E_{\text{HOMO-LUMO}}$) were extracted for this set of hydrocarbons and incorporated into the linear model, where the chosen orbitals represented the bonding and antibonding combinations of the breaking C–C bonds. The LUMO energy provides

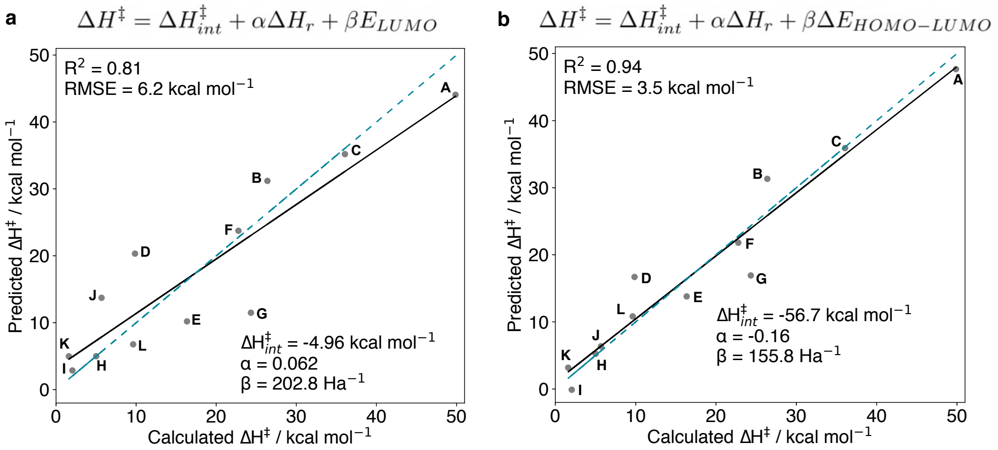

Figure 4.6: Multiple linear regression (MLR) plots for $CH_3^\bullet$ addition to the set of 12 hydrocarbons in Figure 4.3 based on the Bell-Evans-Polanyi principle using the LUMO energy (E_{LUMO}) (**a**) and HOMO-LUMO gap ($\Delta E_{\text{HOMO-LUMO}}$) (**b**). Blue dashed lines represent perfect correlation, and solid black lines are the regression lines.

negligible improvement to the prediction of activation barriers (Figure 4.6a, $R^2 = 0.81$, RMSE = 6.2 kcal mol^{-1}), and results in an unphysical negative intrinsic activation barrier. The positive coefficient β does indicate anticorrelation between the LUMO energy and the strain-independent barrier-lowering effect, implying that in general a lower LUMO energy may be loosely connected to enhanced reactivity. However the overall poor performance of the model, in particular the negative intrinsic activation barrier, suggests that the LUMO energy alone is of little value for the quantitative prediction of reaction rates. Poor model performance likely results from the delocalised nature of this type of MO, where information not directly connected to changes in bonding ‘contaminates’ the relevant information.

The use of the HOMO-LUMO gap significantly improves the correlation and decreases the prediction error of the model (Figure 4.6b, $R^2 = 0.94$, RMSE = 3.5 kcal mol^{-1}). Once again, the positive sign of the coefficient β indicates anticorrelation between the HOMO-LUMO gap and the strain-independent barrier-lowering effect. This finding bolsters the proposal that the OITB model explains the enhanced reactivity of three-membered rings, therefore supporting TS (anti)aromaticity (de)stabilisation. However, a negative intrinsic activation barrier and coefficient α result from this model, indicating divergence from the Bell-Evans-Polanyi principle – an increase in reaction driving force would cause an *increase* in the activation energy. While the HOMO–LUMO gap includes information on the nature of the bond being broken and its direct surroundings, non-physical MO delocalisation will introduce additional chemical information that may be unrelated to changes in bonding at the TS, and therefore introduce noise to the model. As a result, while arguments based on either the LUMO energy or HOMO-LUMO gap provide intuitive qualitative explanations for the enhanced reactivity of small rings independent of the strain contribution, they appear not to be of use within the quantitative model proposed here.

Delocalisation in heterocycles

The facile ring-opening reactivity of heteroatom-containing small rings, such as azetidines and epoxides, is widely exploited in synthetic organic chemistry.[224–226] The four-membered analogues of these rings, however, display diminished reactivity, making them inviting inert building blocks for use in pharmaceuticals.[227,228] To investigate whether delocalisation plays a role in this reactivity difference, a dataset was compiled from Hoz and co-workers that reports the error between the calculated and predicted activation barriers from the Marcus equation (4.2), for anionic and radical ring-opening reactions of carbo-, aza- and oxacycles commonly encountered in synthetic chemistry (Figure 4.7a).[61,62] We found a good correlation between the Marcus prediction error and the number of three-membered rings (n_3, $R^2 = 0.93$, Figure 4.7b), and a low model error (RMSE = 1.6 kcal mol^{-1}). This error is the rate enhancement caused by Hoz's "additional factor", therefore we suggest that the connection between increased reactivity and delocalisation

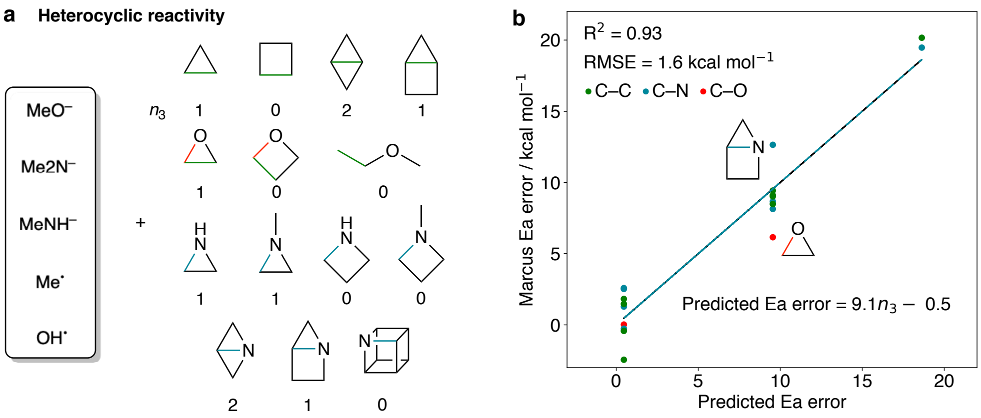

Figure 4.7: a. Set of 14 heterocycles (C, N, O) and their reactions with anions and radicals (for the full set of reactions studied see Figure D.1). Cleaved bonds are colour-coded by type (C–C: green, C–N: blue, C–O: red). **b.** Plot showing the ability of n_3 to predict deviations from activation barriers predicted using Marcus theory. Overlapping blue dashed and black solid lines represent perfect correlation and regression lines, respectively.

in three-membered rings can be generally applied regardless of the type of bond being broken.

As observed for carbocycles, increasing the number of three-membered rings fused to the breaking bond decreases the intrinsic activation barrier. This is illustrated by the comparison of dimethylamide anion addition to *N*-methylaziridine (Marcus error = 8.7 kcal mol^{-1}) and azabicyclo[1.1.0]butane (Marcus error = 19.5 kcal mol^{-1}). Therefore, aza- and carbocycles experience a similar contribution of delocalisation to barrier lowering. However, the equivalent reactivity enhancement for ethylene oxide over oxetane appears to be slightly diminished, with a Marcus error of only 6.2 kcal mol^{-1}. This could either be due to decreased delocalisation as a result of an increase in electronegativity upon changing the nucleofuge from C to O, or a smaller contribution of delocalisation at the TS due to a steeper C–O extension PES. Conversely, the reactivity of azabicyclo[2.1.0]pentane appears to be greater than that predicted by the number of three-membered rings. Specifics of geometry and hybridisation are of course not included in the simple n_3 parameter; therefore, small deviations between predicted and calculated activation barriers are anticipated. A greater amount of data for each bond type would be required to comprehensively investigate the effects of O- and N-substitution. However, the good agreement already achieved despite not accounting for different bond types, geometries and hybridisation suggests that delocalisation still plays a critical role in determining differences in activation barriers in general.

A 'rule of thumb' for small-ring reactivity

Having established a model to explain the enhanced reactivity of more delocalised bonds, a 'rule of thumb' was proposed that could be used to quickly estimate the relative reactivity of small rings. Based on the simple modified BEP model shown in Figure 4.5c, ΔH_r can be approximated by tabulated strain release energies (SREs), and α is taken as 0.5 and β as –10 kcal mol^{-1} for simplicity. Despite the intrinsic activation barrier ($\Delta H^{\ddagger}_{int}$) not being known without explicit calculation, the difference in activation barriers between two substrates ($\Delta\Delta H^{\ddagger}$) can be estimated using

$$\Delta\Delta H^{\ddagger} \approx 0.5\Delta SRE - 10\Delta n_3. \tag{4.3}$$

This simple model was tested on Wiberg and co-workers' 1-halo-3-trichloromethylation of [1.1.1]propellane, bicyclo[1.1.0]butane and bicyclo[2.1.0]pentane with $BrCCl_3$ or CCl_4 (Figure 4.8a).[83,111] While [1.1.1]propellane and bicyclo[1.1.0]butane were found to readily undergo these reactions, bicyclo[2.1.0]pentane showed no reactivity under these conditions. Additionally, competition reactions showed [1.1.1]propellane to undergo a more rapid reaction than bicyclo[1.1.0]butane.

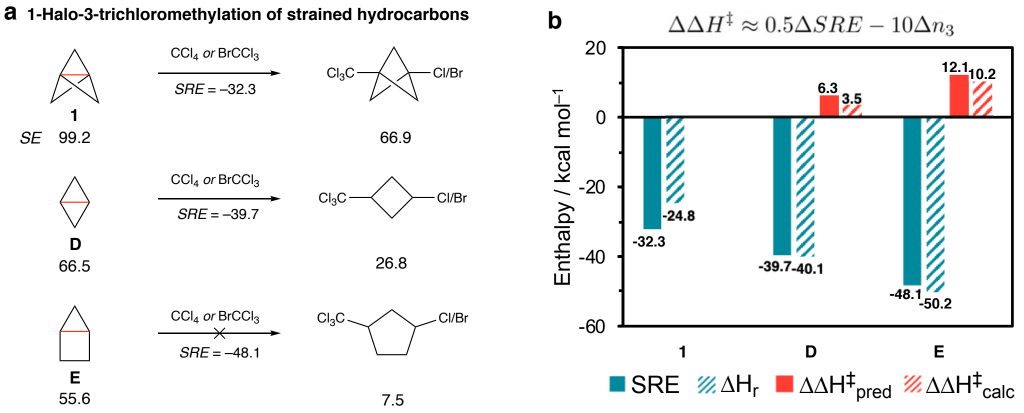

Figure 4.8: a. Wiberg's halotrichloromethylation of [1.1.1]propellane, bicyclo[1.1.0]butane and (unsuccessful) bicyclo[2.1.0]pentane, and the strain energies of the reactants and products from Ref. [24] (W1BD level). **b.** Comparison of calculated [DLPNO-CCSD(T)/def2-QZVPP//B2PLYP-D3BJ/def2-TZVP] and predicted activation energies using the 'rule of thumb' Bell-Evans-Polanyi / n_3 model (4.3).

Wiberg noted that the observed reactivity of these three molecules directly opposed the trend in SRE, and that properties such as the ionisation potential and local charge concentration were also unable to even qualitatively reproduce the reactivity trend.[83,111]

By adding a delocalisation parameter into the BEP model in (4.3), the observed reactivity trend is correctly predicted, with estimated activation barriers relative to [1.1.1]propellane of 6.3 and 12.1 kcal mol^{-1} for bicyclo[1.1.0]butane and bicyclo[2.1.0]pentane, respectively (Figure 4.8b). To test the numerical accuracy of these predictions, activation and reaction enthalpies were calculated for the addition of $CCl_3^\bullet$ to each of these small rings. The lowest barrier was calculated for [1.1.1]propellane ($\Delta H^\ddagger$ = 0.5 kcal mol^{-1}), with addition barriers for bicyclo[1.1.0]butane and bicyclo[2.1.0]pentane greater by 3.5 and 10.2 kcal mol^{-1}, respectively. Considering the simplicity of this model, the small discrepancies between the calculated and estimated barriers are acceptable. In fact, much of the model error can be traced back to the difference between the SRE and ΔH_r for [1.1.1]propellane, rather than from the delocalisation parameter. In addition, quantitative agreement was observed between the trend in activation enthalpies and free energies, as expected for reactions that are similar in nature due to the cancellation of entropic terms.

4.4 Conclusions

The enhanced reactivity of cyclopropane over cyclobutane has long been a puzzle for organic chemists. From a traditional LFER analysis, their similar strain energies should result in similar rates of ring-opening, yet this is not borne out in reality. In this Chapter, a simple explanation has been proposed for the enhanced reactivity of cyclopropane over cyclobutane in terms of delocalisation. In doing so, a quantitative model for ring-opening reactions has been formulated in general, incorporating both strain-driven reactivity enhancement and differences in delocalisation. Inspired by Coulson and Moffitt's work on the electronic structure of cyclopropane,[27] and the LFERs of Bell, Evans, Polanyi and Marcus,[47,48,52] a model in which activation barriers depend on both strain release and delocalisation has been developed – and these two factors work together to enhance reactivity. In terms of Marcus theory, delocalisation induces earlier curve crossing, in effect decreasing the intrinsic activation barrier associated with the cleavage of a more delocalised bond (Figure 4.9).

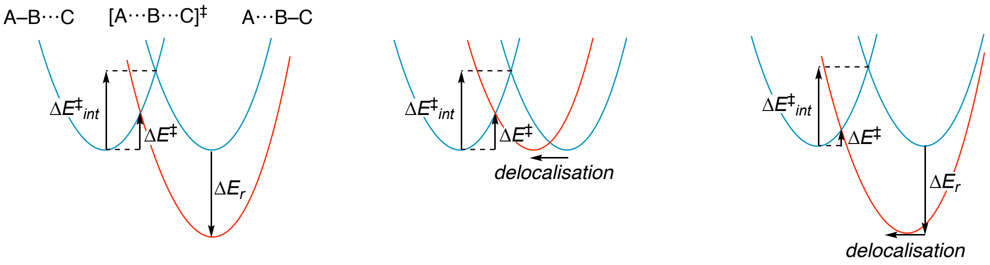

Strain release shifts product curve *vertically*, decreasing activation barrier

Delocalisation shifts product curve *horizontally*, decreasing *intrinsic* activation barrier

Strain release and delocalisation act independently to decrease activation barrier

Figure 4.9: Pictorial representation of the effects of strain release and delocalisation on activation energies within Marcus theory.

Using this model, a systematic study of the ring-opening reactivity of small carbo- and heterocyclic rings has been undertaken, as well as the introduction of a simple 'rule of thumb' to predict relative activation barriers using tabulated strain release energy values and the number of three-membered rings (n_3) appended to the breaking bond. The principles discussed in this Chapter may simplify discussions about strain releasing reactions, and provide an intuitive tool for the design of reactions and molecules.

5 |

Conclusions

5.1 Thesis overview

Over the past decade or so, the development of reactions built upon the attractive idea of strain release has blossomed. These reactions are designed under the premise that the rate of an elementary reaction step will increase if accompanied by a release of strain energy. This hypothesis has been perpetuated through selection bias: a successful reaction in which strain energy has been released has led to the conclusion that the strain release was the cause of the enhanced reactivity, despite similar substrates with similar strain energies being unreactive under the same conditions. This is most clearly seen by comparison of ring-opening reactions of cyclobutane, cyclopropane and [1.1.1]propellane: each enjoys a similar release of strain energy upon ring-opening, yet the relative rates for ring opening can vary by over 20 orders of magnitude. In this Thesis, the role of strain release in such reactions has been clarified by introducing the complementary concept of electronic delocalisation, which accounts for differences in bonding across related substrates (Figure 5.1).

Starting with the archetypal strain release molecule [1.1.1]propellane, investigation of its electronic structure revealed its interbridgehead bond to be delocalised over the cage (Chapter 2 and Figure 5.2). The effect of this delocalisation is two-fold: firstly, it is suggested to provide structural stabilisation that disfavours decomposition; and secondly, this delocalisation is proposed to be the origin of the unusually broad reactivity profile exhibited by [1.1.1]propellane. The impor-

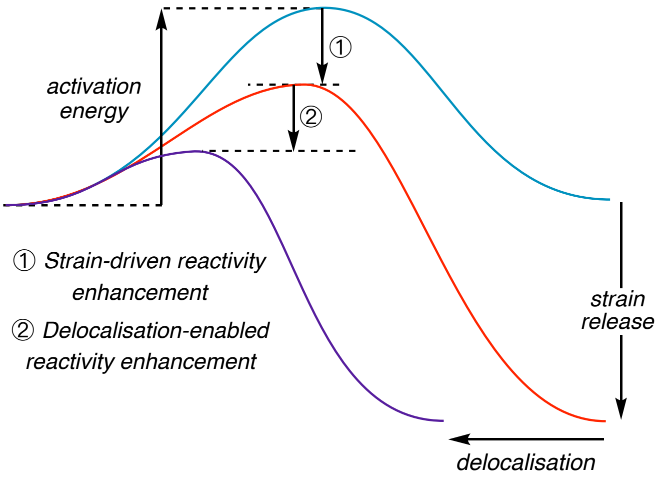

Figure 5.1: Two factors can be engineered to enhance reactivity and selectivity: the extent of strain release, and the amount of bond delocalisation.

tance of this delocalisation-enabled reactivity was shown through investigation of the mechanism of a photoredox / organocatalytic / H-atom transfer catalytic reaction, where facile cleavage of the propellane interbridgehead bond introduces a dependence of the observed enantioselectivity on the nature of the photocatalyst (Chapter 3).

Following these studies, the modulation of reactivity resulting from the interplay of strain release and delocalisation has been systematically investigated (Chapter 4). A coherent model that can quantify the contribution of each effect on the observed activation barrier for ring-opening reactions has been proposed, and a structure-activity relationship which links the number of three membered rings fused to the reactive bond to delocalisation has been identified. Using the framework developed here, many previously developed strain release reactions can be recast in terms of delocalisation-enabled reactivity, for example turboamide addition to [1.1.1]propellane and bioconjugation reactions of bicyclo[1.1.0]butane. Of course, strain release also plays an important role in these reactions, but its impact is often overstated. Bicyclo[2.2.0]butane ring-opening chemistry, for example, is

Chapter 2: Delocalisation explains the stability and reactivity of [1.1.1]propellane

Chapter 3: Delocalisation causes dependence of *ee* on photocatalyst

Chapter 4: Strain release and delocalisation work together to modulate reactivity

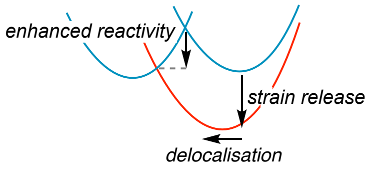

Figure 5.2: Summary of the contribution of Chapter to this Thesis.

far less developed than bicyclo[1.1.0]butane chemistry, despite a > 10 kcal mol^{-1} increase in strain release energy for the former. It could therefore be beneficial to keep both the thermodynamics of strain release and the enhancement of delocalisation in mind when designing such reactions. Further study into synthetic methods through which delocalisation can be maximised using functional group manipulation could provide a complementary framework for reaction development in the future.

5.2 Implication and future avenues

Throughout the development of the strain / delocalisation framework constructed in the course of this Thesis, experimental applications of this model have been sought – both to validate the general approach, and to attempt to assist the strain release community with design of new synthetic methods to access complex molecules for medicinal and materials applications.

Reactions of higher-order propellanes

The strain / delocalisation relationship in propellanes was explored for the series of [*n*.1.1]propellane (*n* = 0–5, Figure 5.3a). CASSCF–HF electron density difference plots indicate that density from the interbridgehead bond of each propellane is only delocalised onto methylene bridges, and that [1.1.1] and [3.1.1]propellane show qualitatively similar delocalisation behaviour (over three and two rings, respectively). According to our model, the reactivity of these two propellanes should therefore be similar. Reactions successfully deployed for bicyclo[1.1.1]pentanes synthesis with [1.1.1]propellane are currently been tested on [3.1.1]propellane both experimentally and using computation by a Masters student, Nils Frank. Preliminary results suggest that the photoredox-catalysed ATRA reaction with alkyl and aryl iodides optimised for [1.1.1]propellane can be readily applied to [3.1.1]propellane for the synthesis of bicyclo[3.1.1]heptanes (BCHs), which could be applied as meta-substituted phenyl bioisosteres, (Figure 5.3b). Perplexingly, organometallic addition reactions, such as the amination reaction described by Baran for [1.1.1]propellane,[114] are yet to afford isolable products. This may be due to the instability of the bridgehead BCH anion formed during the reaction.

New routes to bridge- and hetero-substituted propellanes

Our delocalisation model for [1.1.1]propellane, in particular the idea that the Lewis structure is in resonance with six degenerate alkene / carbene pairs, has also inspired a project in which propellanes might be synthesised directly from exomethylene cyclobutyl carbenes (Scheme 5.1). The synthesis of a propellane by this route was first reported in 1987 by Szeimes,[84] who successfully fragmented and reassembled a bridge-tethered propellane. This approach has the potential to

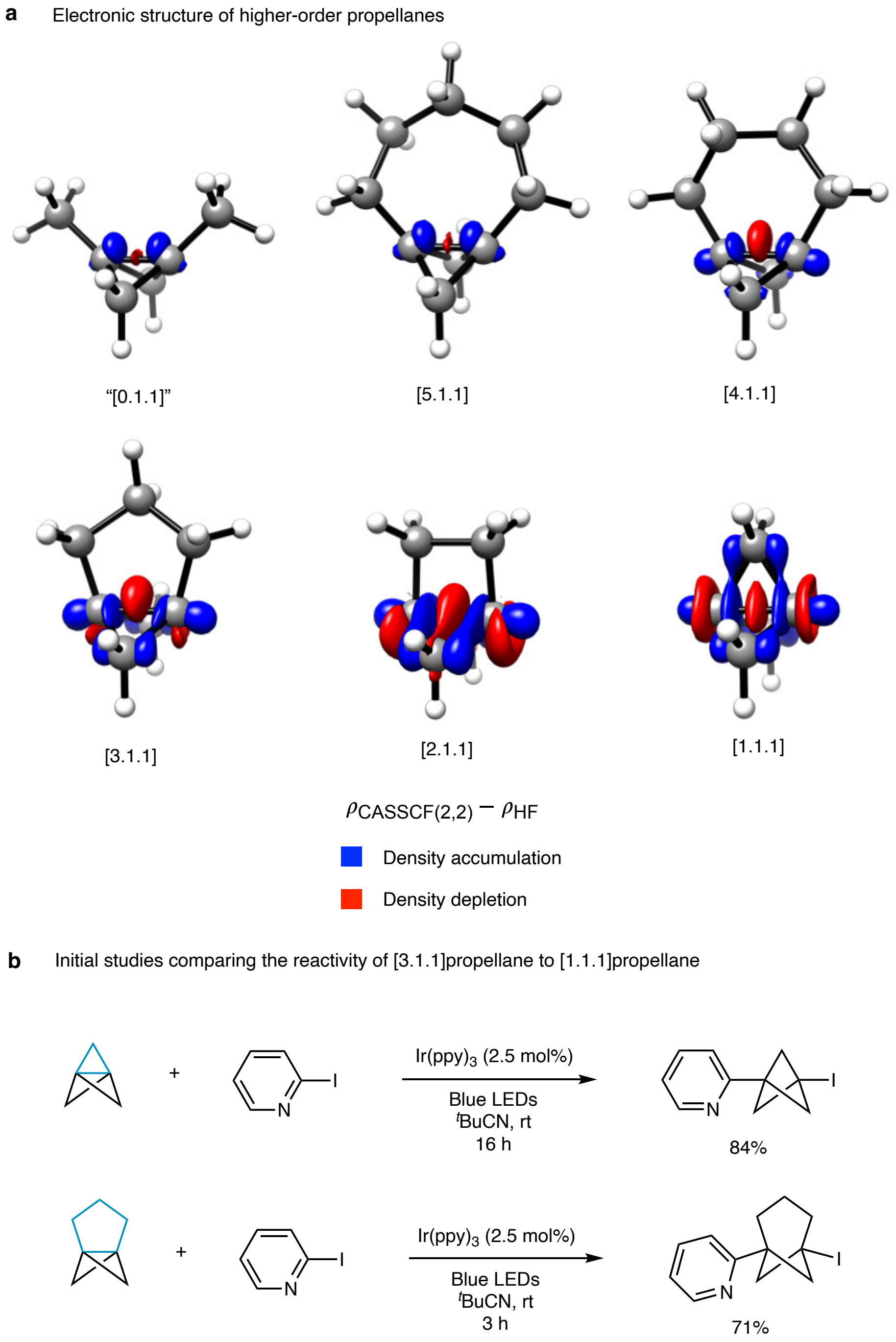

Figure 5.3: **a.** Electron density difference plots for [n.1.1]propellanes (n = 0–5) at the CASSCF(2,2) or HF level with a def2-TZVP basis set and an isovalue of 0.002 a.u. **b.** Photoredox ATRA reaction of 2-iodopyridine with [1.1.1]propellane and [3.1.1]propellane (carried out by Nils Frank).

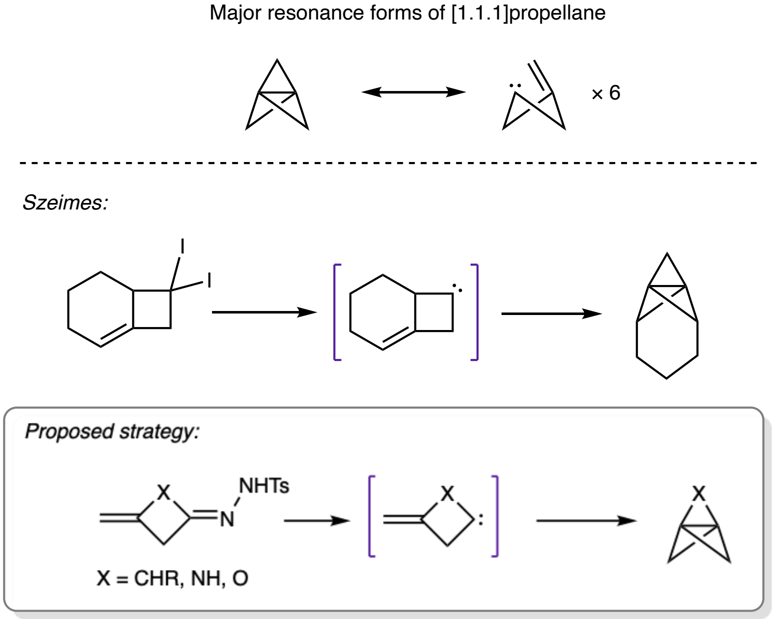

Scheme 5.1: Proposed synthesis of bridge- and hetero-substituted propellanes *via* a cyclobutyl carbene

give access to bridge- and hetero-substituted propellanes. The closure of the cyclobutyl carbene to the propellane is anticipated to be symmetry-allowed and barrierless, which may outcompete 1,2–H migration that would lead to a cyclobutene. Studies to investigate the potential of this strategy are being carried out by a DPhil student, Bethany Shire, in the Anderson group.

Propellane polymerisation

The polymerisation of [1.1.1]propellane, or lack thereof in dilute solution, is a puzzle when compared with the spontaneous polymerisation of [2.1.1] and [2.2.1]-propellane.[82,85,86] Jug and Poredda suggested that the [1.1.1]propellane dimer is formed reversibly, where collision of two singlet monomers and subsequent intersystem crossing results in a bound triplet ground state (Figure 5.4a).[229] The resistance of [1.1.1]propellane towards dimerisation is intriguing; the formation

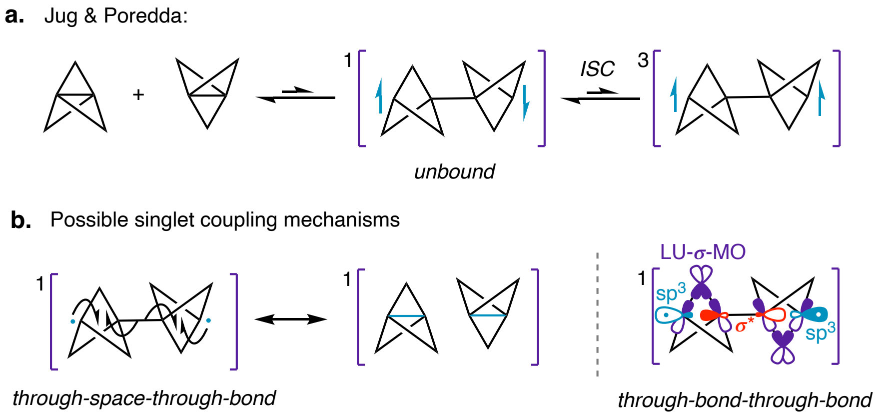

Figure 5.4: **a.** Proposed oligomerisation mechanism of [1.1.1]propellane. **b.** Through-bond and through-space singlet coupling mechanisms.

of an assumed ordinary C(sp^3)–C(sp^3) σ-bond ($\approx$ 85 kcal mol^{-1}),[30] accompanied by two lots of $\approx$ 30 kcal mol^{-1} strain release, may be finely balanced with the cleavage of two weak C–C bonds ($\approx$ 60–80 kcal mol^{-1} each).[82,182] What is perhaps surprising is Jug and Poredda's finding that the triplet dimer is less stable than the singlet at all distances, despite the BCP radical centres being separated by at least 5 Å. We suggest that strong singlet coupling of the terminal electrons *via* the inter-propellane C–C bond may explain this phenomenon, either through-space or through-bond (or a combination of the two mechanisms, Figure 5.4b). Further exploration of this type of singlet coupling mechanism may further our understanding of propellane polymerisation, as well as elucidate further the importance of orbital interactions through-bond. These results may also guide the design of a stable singlet diradical through the judicious choice of propellane substituents.

Generalisation of the strain / delocalisation model

Having established the roles of strain release energy and electronic delocalisation on ring-opening activation barriers of small rings, a more general application of this model to describe reactivity could be envisaged. For example, nucleophilic or radical additions to π bonds (*e.g.*, MacMillan's addition of α-iminyl radical cations to styrenes described in Chapter 3)[209] is commonly associated with the lower bond dissociation energy (BDE) of alkene π bonds. However, the alkene π bond is inherently more delocalised than the corresponding σ bond due to poorer side-on overlap of its side-on p orbitals than the end-on overlap of its sp^2 orbitals within the 'sp^2 + p' bonding model. Assuming the validity of the results presented in Chapter 4, this delocalisation should enhance the reactivity of alkene π bonds more than differences in BDEs would suggest. A computational investigation of the inherent reactivity of alkenes, as well as other delocalised functional groups such as alkynes and arenes, can then be used to test the strain / delocalisation hypothesis. Based on this principle, reactivity could be modulated by optimising bond delocalisation – for example through substitution with 'delocalisation-enhancing' groups that increase (hyper)conjugation.

5.3 Outlook

Strain release is a powerful concept which will undoubtedly continue to play a defining role in the conception of new methods in organic synthesis. However, through the introduction of delocalisation as an additional concept to describe reactivity of small rings, it is our hope that a fuller description of the factors that cause changes in reactivity will result in more efficient reactions that make best use of the individual properties of each system. This Thesis has sought to develop such a full description through the investigation of the electronic structure and reactivity of [1.1.1]propellane, both computationally and experimentally. The lessons learned from these studies ultimately informed the development of a quantitative model for the prediction of small-ring reactivity, culminating in several ongoing experimental studies hoping to make use of these findings. The studies undertaken here might inspire both new theoretical approaches to the study of strain release, and also act as a framework for experimental reaction design for next-generation bioisosteres and materials.

Bibliography

(1) Baeyer, A. Ueber Polyacetylenverbindungen. *Ber. Dtsch. Chem. Ges.* **1885**, *18*, 2269–2281.

(2) Brown, H. C. A New Steric Effect in Organic Chemistry. *Science* **1946**, *103*, 385–387.

(3) Brown, H. C.; Adams, R. M. Studies in Stereochemistry. II. Steric Strains as a Factor in the Relative Stability of Some Etherates of Boron Fluoride. *J. Am. Chem. Soc.* **1942**, *64*, 2557–2563.

(4) Hughes, E. D. Mechanism and kinetics of substitution at a saturated carbon atom. *J. Chem. Soc. Faraday Trans.* **1941**, *37*, 603.

(5) Wiberg, K. B. The Concept of Strain in Organic Chemistry. *Angew. Chem., Int. Ed. Engl.* **1986**, *25*, 312–322.

(6) Christiansen, P. A.; Palke, W. E. A study of the ethane internal rotation barrier. *Chem. Phys. Lett.* **1975**, *31*, 462–466.

(7) Sovers, O. J.; Kern, C. W.; Pitzer, R. M.; Karplus, M. Bond-Function Analysis of Rotational Barriers: Ethane. *J. Chem. Phys.* **1968**, *49*, 2592–2599.

(8) Bader, R. F. W.; Cheeseman, J. R.; Laidig, K. E.; Wiberg, K. B.; Breneman, C. Origin of rotation and inversion barriers. *J. Am. Chem. Soc.* **1990**, *112*, 6530–6536.

(9) Pophristic, V.; Goodman, L. Hyperconjugation not steric repulsion leads to the staggered structure of ethane. *Nature* **2001**, *411*, 565–568.

(10) Quijano-Quiñones, R. F.; Quesadas-Rojas, M.; Cuevas, G.; Mena-Rejón, G. J. The Rotational Barrier in Ethane: A Molecular Orbital Study. *Molecules* **2012**, *17*, 4661–4671.

(11) Allinger, N. L.; Hindman, D.; Hoenig, H. Conformational analysis. 125. The importance of twofold barriers in saturated molecules. *J. Am. Chem. Soc.* **1977**, *99*, 3282–3284.

(12) Hill, T. L. On Steric Effects. *J. Chem. Phys.* **1946**, *14*, 465–465.

(13) Westheimer, F. H.; Mayer, J. E. The Theory of the Racemization of Optically Active Derivatives of Diphenyl. *J. Chem. Phys.* **1946**, *14*, 733–738.

(14) Vanommeslaeghe, K.; Guvench, O.; MacKerell, A. D. Molecular Mechanics. *Curr. Pharm. Des.* **2014**, *20*, 3281–3292.

(15) Pitzer, K. S. The Vibration Frequencies and Thermodynamic Functions of Long Chain Hydrocarbons. *J. Chem. Phys.* **1940**, *8*, 711–720.

(16) Franklin, J. L. Prediction of Heat and Free Energies of Organic Compounds. *Ind. Eng. Chem. Res.* **1949**, *41*, 1070–1076.

(17) Benson, S. W.; Buss, J. H. Additivity Rules for the Estimation of Molecular Properties. Thermodynamic Properties. *J. Chem. Phys.* **1958**, *29*, 546–572.

(18) Knowlton, J. W.; Rossini, F. D. Heats of combustion and formation of cyclopropane. *J. Res. Natl. Bur. Stand.* **1949**, *43*, 113.

(19) Houk, K. N.; Liu, F. Holy Grails for Computational Organic Chemistry and Biochemistry. *Acc. Chem. Res.* **2017**, *50*, 539–543.

(20) Snyder, L. C.; Basch, H. Heats of reaction from self-consistent-field energies of closed-shell molecules. *J. Am. Chem. Soc.* **1969**, *91*, 2189–2198.

(21) Hehre, W. J.; Ditchfield, R.; Radom, L.; Pople, J. A. Molecular orbital theory of the electronic structure of organic compounds. V. Molecular theory of bond separation. *J. Am. Chem. Soc.* **1970**, *92*, 4796–4801.

(22) Wiberg, K. B. Group equivalents for converting *ab initio* energies to enthalpies of formation. *J. Comput. Chem.* **1984**, *5*, 197–199.

(23) Ibrahim, M. R.; Schleyer, P. V. R. Atom equivalents for relating *ab initio* energies to enthalpies of formation. *J. Comput. Chem.* **1985**, *6*, 157–167.

(24) Rablen, P. R. A Procedure for Computing Hydrocarbon Strain Energies Using Computational Group Equivalents, with Application to 66 Molecules. *Chemistry* **2020**, *2*, 347–360.

(25) Estrada, E. Atom–bond connectivity and the energetic of branched alkanes. *Chem. Phys. Lett.* **2008**, *463*, 422–425.

(26) Dunitz, J. D.; Schomaker, V. The Molecular Structure of Cyclobutane. *J. Chem. Phys.* **1952**, *20*, 1703–1707.

(27) Coulson, C.; Moffitt, W. I. The properties of certain strained hydrocarbons. *Philos. Mag.* **1949**, *40*, 1–35.

(28) Cremer, D.; Gauss, J. Theoretical determination of molecular structure and conformation. 20. Reevaluation of the strain energies of cyclopropane and cyclobutane carbon-carbon and carbon-hydrogen bond energies, 1,3 interactions, and σ-aromaticity. *J. Am. Chem. Soc.* **1986**, *108*, 7467–7477.

(29) Dewar, M. J. S.; McKee, M. L. Aspects of cyclic conjugation. *Pure Appl. Chem.* **1980**, *52*, 1431–1441.

(30) McMillen, D. F.; Golden, D. M. Hydrocarbon Bond Dissociation Energies. *Annu. Rev. Phys. Chem.* **1982**, *33*, 493–532.

(31) Coulson, C. A.; Moffitt, W. E. Strain in Non-Tetrahedral Carbon Atoms. *J. Chem. Phys.* **1947**, *15*, 151–151.

(32) Roberts, J. D.; Green, C. Absorption Spectra of Some 2,4-Dinitrophenylhydrazones. *J. Am. Chem. Soc.* **1946**, *68*, 214–216.

(33) Rogers, M. T.; Roberts, J. D. Cyclopropane Derivatives. II. The Electric Moments of Some Alicyclic Compounds. *J. Am. Chem. Soc.* **1946**, *68*, 843–846.

(34) Walsh, A. D. The structures of ethylene oxide, cyclopropane, and related molecules. *J. Chem. Soc. Faraday Trans.* **1949**, *45*, 179.

(35) Walsh, A. D. Structures of Ethylene Oxide and Cyclopropane. *Nature* **1947**, *159*, 165–165.

(36) *Structure of Free Polyatomic Molecules*; Kuchitsu, K., Ed.; Springer Berlin Heidelberg: 1998.

(37) Stanton, J. F. A refined estimate of the bond length of methane. *Mol. Phys.* **1999**, *97*, 841–845.

(38) Cremer, D. Pros and cons of σ-aromaticity. *Tetrahedron* **1988**, *44*, 7427–7454.

(39) Wu, W.; Ma, B.; Wu, J. I.-C.; von Ragué Schleyer, P.; Mo, Y. Is Cyclopropane Really the σ-Aromatic Paradigm? *Chem. Eur. J.* **2009**, *15*, 9730–9736.

(40) Burke, J. J.; Lauterbur, P. C. C^{13} and H^1 Nuclear Magnetic Resonance Spectra of Cycloalkanes. *J. Am. Chem. Soc.* **1964**, *86*, 1870–1871.

(41) Barter, C.; Meisenheimer, R. G.; Stevenson, D. P. Diamagnetic susceptibilities of simple hydrocarbons and volatile hydrides. *J. Phys. Chem.* **1960**, *64*, 1312–1316.

(42) Pelloni, S.; Lazzeretti, P.; Zanasi, R. Assessment of σ-Diatropicity of the Cyclopropane Molecule. *J. Phys. Chem. A* **2007**, *111*, 8163–8169.

(43) Inagaki, S.; Goto, N.; Yoshikawa, K. Antibonding delocalization: geminal interaction of σ-bonds and angle strain. *J. Am. Chem. Soc.* **1991**, *113*, 7144–7146.

(44) Inagaki, S.; Ishitani, Y.; Kakefu, T. Geminal Delocalization of σ-Electrons and Ring Strains. *J. Am. Chem. Soc.* **1994**, *116*, 5954–5958.

(45) Weinhold, F.; Landis, C. R. In *Valency and Bonding*; Cambridge University Press: 2005, pp 89–362.

(46) Brönsted, J. N.; Pedersen, K. Die katalytische Zersetzung des Nitramids und ihre physikalisch-chemische Bedeutung. *Z. Phys. Chem.* **1924**, *108U*, 185–235.

(47) Bell, R. P. The theory of reactions involving proton transfers. *Proc. Math. Phys. Eng. Sci.* **1936**, *154*, 414–429.

(48) Evans, M. G.; Polanyi, M. Inertia and driving force of chemical reactions. *J. Chem. Soc. Faraday Trans.* **1938**, *34*, 11.

(49) Marcus, R. A. On the Theory of Oxidation-Reduction Reactions Involving Electron Transfer. I. *J. Chem. Phys.* **1956**, *24*, 966–978.

(50) Haim, A.; Sutin, N. The Reactions of Isothiocyanatobis(ethylenediamine)-cobalt(III) Complexes with Chromium(II) and the Linkage Isomerization of the Monothiocyanate Complex of Chromium(III)1. *J. Am. Chem. Soc.* **1966**, *88*, 434–440.

(51) Sutin, N. The Kinetics of Inorganic Reactions in Solution. *Annu. Rev. Phys. Chem.* **1966**, *17*, 119–172.

(52) Marcus, R. A. Theoretical relations among rate constants, barriers, and Broensted slopes of chemical reactions. *J. Phys. Chem.* **1968**, *72*, 891–899.

(53) Sella, A.; Basch, H.; Hoz, S. Strain release is not enough. *Tetrahedron Lett.* **1996**, *37*, 5573–5576.

(54) Sella, A.; Basch, H.; Hoz, S. Reactivity of Strained Compounds: Is Ground State Destabilization the Major Cause for Rate Enhancement? *J. Am. Chem. Soc.* **1996**, *118*, 416–420.

(55) Hammond, G. S. A Correlation of Reaction Rates. *J. Am. Chem. Soc.* **1955**, *77*, 334–338.

(56) Sawicka, D.; Li, Y.; Houk, K. N. [2 + 2 + 2]-Cycloreversion reactions: a theoretical elucidation of thermodynamic and through-bond coupling

effects on activation energies. *J. Chem. Soc., Perkin Trans. 2* **1999**, 2349–2355.

(57) Sawicka, D.; Wilsey, S.; Houk, K. N. The 16 kcal/mol Anomaly: Alteration of [2 + 2 + 2] Cycloaddition Rates by Through-Bond Interactions. *J. Am. Chem. Soc.* **1999**, *121*, 864–865.

(58) Sawicka, D.; Houk, K. N. Aromaticity and Antiaromaticity in Small Ring Transition States, Assessed by NICS Values and Energetics. *J. Mol. Model.* **2000**, *6*, 158–165.

(59) Verhoeven, J. W. Sigma-assistance; The modulation of intramolecular reactivity by through-bond interaction. *Recl. Trav. Chim. Pays-Bas* **1980**, *99*, 369–379.

(60) Hoffmann, R.; Imamura, A.; Hehre, W. J. Benzynes, dehydroconjugated molecules, and the interaction of orbitals separated by a number of intervening sigma bonds. *J. Am. Chem. Soc.* **1968**, *90*, 1499–1509.

(61) Wolk, J. L.; Hoz, T.; Basch, H.; Hoz, S. Quantification of the Various Contributors to Rate Enhancement in Nucleophilic Strain Releasing Reactions. *J. Org. Chem.* **2001**, *66*, 915–918.

(62) Wolk, J. L.; Sprecher, M.; Basch, H.; Hoz, S. Relative reactivity of three and four membered rings – the absence of charge effect. *Org. Biomol. Chem.* **2004**, *2*, 1065.

(63) Huisgen, R. 1,3-Dipolar Cycloadditions. Past and Future. *Angew. Chem., Int. Ed. Engl.* **1963**, *2*, 565–598.

(64) Agard, N. J.; Prescher, J. A.; Bertozzi, C. R. A Strain-Promoted [3 + 2] Azide-Alkyne Cycloaddition for Covalent Modification of Biomolecules in Living Systems. *J. Am. Chem. Soc.* **2004**, *126*, 15046–15047.

(65) Siddarth, P.; Gopinathan, M. Strain in heterocycles. *J. Mol. Struct. THEOCHEM* **1989**, *187*, 169–176.

(66) Wong, H. N. C.; Hon, M. Y.; Tse, C. W.; Yip, Y. C.; Tanko, J.; Hudlicky, T. Use of cyclopropanes and their derivatives in organic synthesis. *Chem. Rev.* **1989**, *89*, 165–198.

(67) Crotti, P.; Pineschi, M. In *Aziridines and Epoxides in Organic Synthesis*; Wiley-VCH Verlag GmbH & Co. KGaA: 2006, pp 271–313.

(68) Biletskyi, B.; Colonna, P.; Masson, K.; Parrain, J.-L.; Commeiras, L.; Chouraqui, G. Small rings in the bigger picture: ring expansion of three- and four-membered rings to access larger all-carbon cyclic systems. *Chem. Soc. Rev.* **2021**, *50*, 7513–7538.

(69) Panish, R. A.; Chintala, S. R.; Fox, J. M. A Mixed-Ligand Chiral Rhodium(II) Catalyst Enables the Enantioselective Total Synthesis of Piperarborenine B. *Angew. Chem. Int. Ed.* **2016**, *55*, 4983–4987.

(70) Walczak, M. A. A.; Krainz, T.; Wipf, P. Ring-Strain-Enabled Reaction Discovery: New Heterocycles from Bicyclo[1.1.0]butanes. *Acc. Chem. Res.* **2015**, *48*, 1149–1158.

(71) Fawcett, A.; Biberger, T.; Aggarwal, V. K. Carbopalladation of C–C σ-bonds enabled by strained boronate complexes. *Nat. Chem.* **2018**, *11*, 117–122.

(72) Fawcett, A.; Murtaza, A.; Gregson, C. H. U.; Aggarwal, V. K. Strain-Release-Driven Homologation of Boronic Esters: Application to the Modular Synthesis of Azetidines. *J. Am. Chem. Soc.* **2019**, *141*, 4573–4578.

(73) Silvi, M.; Aggarwal, V. K. Radical Addition to Strained σ-Bonds Enables the Stereocontrolled Synthesis of Cyclobutyl Boronic Esters. *J. Am. Chem. Soc.* **2019**, *141*, 9511–9515.

(74) Bennett, S. H.; Fawcett, A.; Denton, E. H.; Biberger, T.; Fasano, V.; Winter, N.; Aggarwal, V. K. Difunctionalization of C–C σ-Bonds Enabled by the Reaction of Bicyclo[1.1.0]butyl Boronate Complexes with Elec-

trophiles: Reaction Development, Scope, and Stereochemical Origins. *J. Am. Chem. Soc.* **2020**, *142*, 16766–16775.

(75) Guo, L.; Noble, A.; Aggarwal, V. K. α-Selective Ring-Opening Reactions of Bicyclo[1.1.0]butyl Boronic Ester with Nucleophiles. *Angew. Chem. Int. Ed.* **2020**, *60*, 212–216.

(76) Gregson, C. H. U.; Noble, A.; Aggarwal, V. K. Divergent, Strain-Release Reactions of Azabicyclo[1.1.0]butyl Carbinols: Semipinacol or Spiroepoxy Azetidine Formation. *Angew. Chem. Int. Ed.* **2021**, *60*, 7360–7365.

(77) Tyler, J. L.; Noble, A.; Aggarwal, V. K. Strain-Release Driven Spirocyclization of Azabicyclo[1.1.0]butyl Ketones. *Angew. Chem. Int. Ed.* **2021**, *60*, 11824–11829.

(78) Altman, J.; Babad, E.; Itzchaki, J.; Ginsburg, D. Propellanes—I: Tricyclic compounds conjoined in a carbon—carbon single bond. *Tetrahedron* **1966**, *22*, 279–304.

(79) Dilmaç, A. M.; Spuling, E.; de Meijere, A.; Bräse, S. Propellanes–From a Chemical Curiosity to "Explosive" Materials and Natural Products. *Angew. Chem. Int. Ed.* **2017**, *56*, 5684–5718.

(80) Newton, M. D.; Schulman, J. M. Theoretical studies of tricyclo[1.1.1.$0^{1,3}$]-pentane and bicyclo[1.1.1]pentane. *J. Am. Chem. Soc.* **1972**, *94*, 773–778.

(81) Stohrer, W. D.; Hoffmann, R. Electronic structure and reactivity of strained tricyclic hydrocarbons. *J. Am. Chem. Soc.* **1972**, *94*, 779–786.

(82) Wiberg, K. B.; Walker, F. H. [1.1.1]Propellane. *J. Am. Chem. Soc.* **1982**, *104*, 5239–5240.

(83) Wiberg, K. B.; Waddell, S. T.; Laidig, K. [1.1.1]Propellane: Reaction with free radicals. *Tetrahedron Lett.* **1986**, *27*, 1553–1556.

(84) Semmler, K.; Szeimies, G.; Belzner, J. Tetracyclo[5.1.0.0^{1,6}.0^{2,7}]octane, a [1.1.1]propellane derivative, and a new route to the parent hydrocarbon. *J. Am. Chem. Soc.* **1985**, *107*, 6410–6411.

(85) Walker, F. H.; Wiberg, K. B.; Michl, J. [2.2.1]Propellane. *J. Am. Chem. Soc.* **1982**, *104*, 2056–2057.

(86) Wiberg, K. B.; Walker, F. H.; Pratt, W. E.; Michl, J. [2.1.1.]Propellane. Reaction of 1,4-diiodobicyclo[2.1.1]hexane with *tert*-butyllithium and with potassium atoms. *J. Am. Chem. Soc.* **1983**, *105*, 3638–3641.

(87) Levin, M. D.; Kaszynski, P.; Michl, J. Bicyclo[1.1.1]pentanes, [*n*]Staffanes, [1.1.1]Propellanes, and Tricyclo[2.1.0.0^{2,5}]pentanes. *Chem. Rev.* **2000**, *100*, 169–234.

(88) Kaszynski, P.; Michl, J. A practical photochemical synthesis of bicyclo-[1.1.1]pentane-1,3-dicarboxylic acid. *J. Org. Chem.* **1988**, *53*, 4593–4594.

(89) Locke, G. M.; Bernhard, S. S. R.; Senge, M. O. Nonconjugated Hydrocarbons as Rigid-Linear Motifs: Isosteres for Material Sciences and Bioorganic and Medicinal Chemistry. *Chem. Eur. J.* **2019**, *25*, 4590–4647.

(90) Kaszynski, P.; Michl, J. [n]Staffanes: a molecular-size "Tinkertoy" construction set for nanotechnology. Preparation of end-functionalized telomers and a polymer of [1.1.1]propellane. *J. Am. Chem. Soc.* **1988**, *110*, 5225–5226.

(91) Itzhaki, L.; Altus, E.; Basch, H.; Hoz, S. Harder than Diamond: Determining the Cross-Sectional Area and Young's Modulus of Molecular Rods. *Angew. Chem. Int. Ed.* **2005**, *44*, 7432–7435.

(92) de Meijere, A.; Zhao, L.; Belov, V. N.; Bossi, M.; Noltemeyer, M.; Hell, S. W. 1, 3-Bicyclo[1.1.1]pentanediyl: The Shortest Rigid Linear Connector of Phenylated Photochromic Units and a 1,5-Dimethoxy-9,10-di(phenylethynyl)anthracene Fluorophore. *Chem. Eur. J.* **2007**, *13*, 2503–2516.

(93) Kaszynski, P.; Friedli, A. C.; Michl, J. Mesogenic Properties of Telomers of [1. 1. 1]Propellane. *Mol. Cryst. Liq. Cryst. Lett.* **1988**, *6*, 27–33.

(94) Ramireddy, C.; Reddy, V. S.; Munk, P.; Wu, C. N. Liquid-crystalline polymers with a bicyclo[1.1.1]pentane cage in the backbone. *Macromolecules* **1991**, *24*, 1387–1391.

(95) de Meijere, A.; Messner, M.; Vill, V. Liquid Crystalline Bicyclo[1.1.1]-pentane Derivatives. *Mol. Cryst. Liq. Cryst.* **1994**, *257*, 161–167.

(96) Perego, J.; Bracco, S.; Negroni, M.; Bezuidenhout, C. X.; Prando, G.; Carretta, P.; Comotti, A.; Sozzani, P. Fast motion of molecular rotors in metal–organic framework struts at very low temperatures. *Nat. Chem.* **2020**, *12*, 845–851.

(97) Pellicciari, R.; Raimondo, M.; Marinozzi, M.; Natalini, B.; Costantino, G.; Thomsen, C. (S)-(+)-2-(3'-Carboxybicyclo[1.1.1]pentyl)glycine, a Structurally New Group I Metabotropic Glutamate Receptor Antagonist. *J. Med. Chem.* **1996**, *39*, 2874–2876.

(98) Pätzel, M.; Sanktjohanser, M.; Doss, A.; Henklein, P.; Szeimies, G. 3-Aminobicyclo[1.1.1]pentane-1-carboxylic Acid Derivatives: Synthesis and Incorporation into Peptides. *Eur. J. Org. Chem.* **2004**, *2004*, 493–498.

(99) Stepan, A. F.; Subramanyam, C.; Efremov, I. V.; Dutra, J. K.; O'Sullivan, T. J.; DiRico, K. J.; McDonald, W. S.; Won, A.; Dorff, P. H.; Nolan, C. E.; Becker, S. L.; Pustilnik, L. R.; Riddell, D. R.; Kauffman, G. W.; Kormos, B. L.; Zhang, L.; Lu, Y.; Capetta, S. H.; Green, M. E.; Karki, K.; Sibley, E.; Atchison, K. P.; Hallgren, A. J.; Oborski, C. E.; Robshaw, A. E.; Sneed, B.; O'Donnell, C. J. Application of the Bicyclo[1.1.1]pentane Motif as a Nonclassical Phenyl Ring Bioisostere in the Design of a Potent and Orally Active γ-Secretase Inhibitor. *J. Med. Chem.* **2012**, *55*, 3414–3424.

(100) Nicolaou, K. C.; Vourloumis, D.; Totokotsopoulos, S.; Papakyriakou, A.; Karsunky, H.; Fernando, H.; Gavrilyuk, J.; Webb, D.; Stepan, A. F. Synthesis and Biopharmaceutical Evaluation of Imatinib Analogues Featuring Unusual Structural Motifs. *ChemMedChem* **2015**, *11*, 31–37.

(101) Nicolaou, K. C.; Yin, J.; Mandal, D.; Erande, R. D.; Klahn, P.; Jin, M.; Aujay, M.; Sandoval, J.; Gavrilyuk, J.; Vourloumis, D. Total Synthesis and Biological Evaluation of Natural and Designed Tubulysins. *J. Am. Chem. Soc.* **2016**, *138*, 1698–1708.

(102) Makarov, I. S.; Brocklehurst, C. E.; Karaghiosoff, K.; Koch, G.; Knochel, P. Synthesis of Bicyclo[1.1.1]pentane Bioisosteres of Internal Alkynes and *para*-Disubstituted Benzenes from [1.1.1]Propellane. *Angew. Chem. Int. Ed.* **2017**, *56*, 12774–12777.

(103) Measom, N. D.; Down, K. D.; Hirst, D. J.; Jamieson, C.; Manas, E. S.; Patel, V. K.; Somers, D. O. Investigation of a Bicyclo[1.1.1]pentane as a Phenyl Replacement within an LpPLA$_2$ Inhibitor. *ACS Med. Chem. Lett.* **2016**, *8*, 43–48.

(104) Auberson, Y. P.; Brocklehurst, C.; Furegati, M.; Fessard, T. C.; Koch, G.; Decker, A.; La Vecchia, L.; Briard, E. Improving Nonspecific Binding and Solubility: Bicycloalkyl Groups and Cubanes as *para*-Phenyl Bioisosteres. *ChemMedChem* **2017**, *12*, 590–598.

(105) Westphal, M. V.; Wolfstädter, B. T.; Plancher, J.-M.; Gatfield, J.; Carreira, E. M. Evaluation of *tert*-Butyl Isosteres: Case Studies of Physicochemical and Pharmacokinetic Properties, Efficacies, and Activities. *ChemMedChem* **2015**, *10*, 461–469.

(106) Bauer, M. R.; Fruscia, P. D.; Lucas, S. C. C.; Michaelides, I. N.; Nelson, J. E.; Storer, R. I.; Whitehurst, B. C. Put a ring on it: application of small

aliphatic rings in medicinal chemistry. *RSC Med. Chem.* **2021**, *12*, 448–471.

(107) Lovering, F.; Bikker, J.; Humblet, C. Escape from Flatland: Increasing Saturation as an Approach to Improving Clinical Success. *J. Med. Chem.* **2009**, *52*, 6752–6756.

(108) Brown, R. W. Abiotic scaffolds in medicinal chemistry: not a waste of chemical space. *Future Med. Chem.* **2021**, *13*, 211–224.

(109) Wiberg, K. B.; Connor, D. S.; Lampman, G. M. The reaction of 3-bromocyclobutane-1-methyl bromide with sodium : bicyclo[1.1.1]pentane. *Tetrahedron Lett.* **1964**, *5*, 531–534.

(110) Freund, A. Ueber Trimethylen. *J. Prakt. Chem.* **1882**, *26*, 367–377.

(111) Wiberg, K. B.; Waddell, S. T. Reactions of [1.1.1]propellane. *J. Am. Chem. Soc.* **1990**, *112*, 2194–2216.

(112) Della, E. W.; Taylor, D. K.; Tsanaktsidis, J. Unusual bridgehead reactivity: Formation of [1.1.1]Propellane by 1,3-dehydrobromination of 1-bromobicyclo[1.1.1]pentane. *Tetrahedron Lett.* **1990**, *31*, 5219–5220.

(113) Messner, M.; Kozhushkov, S. I.; de Meijere, A. Nickel- and Palladium-Catalyzed Cross-Coupling Reactions at the Bridgehead of Bicyclo[1.1.1]-pentane Derivatives – A Convenient Access to Liquid Crystalline Compounds Containing Bicyclo[1.1.1]pentane Moieties. *Eur. J. Org. Chem.* **2000**, *2000*, 1137–1155.

(114) Gianatassio, R.; Lopchuk, J. M.; Wang, J.; Pan, C.-M.; Malins, L. R.; Prieto, L.; Brandt, T. A.; Collins, M. R.; Gallego, G. M.; Sach, N. W.; Spangler, J. E.; Zhu, H.; Zhu, J.; Baran, P. S. Strain-release amination. *Science* **2016**, *351*, 241–246.

(115) Shelp, R. A.; Walsh, P. J. Synthesis of BCP Benzylamines From 2-Azaallyl Anions and [1.1.1]Propellane. *Angew. Chem. Int. Ed.* **2018**, *57*, 15857–15861.

(116) Kanazawa, J.; Maeda, K.; Uchiyama, M. Radical Multicomponent Carboamination of [1.1.1]Propellane. *J. Am. Chem. Soc.* **2017**, *139*, 17791–17794.

(117) Caputo, D. F. J.; Arroniz, C.; Dürr, A. B.; Mousseau, J. J.; Stepan, A. F.; Mansfield, S. J.; Anderson, E. A. Synthesis and applications of highly functionalized 1-halo-3-substituted bicyclo[1.1.1]pentanes. *Chem. Sci.* **2018**, *9*, 5295–5300.

(118) Nugent, J.; Arroniz, C.; Shire, B. R.; Sterling, A. J.; Pickford, H. D.; Wong, M. L. J.; Mansfield, S. J.; Caputo, D. F. J.; Owen, B.; Mousseau, J. J.; Duarte, F.; Anderson, E. A. A General Route to Bicyclo[1.1.1]-pentanes through Photoredox Catalysis. *ACS Catal.* **2019**, *9*, 9568–9574.

(119) Kim, J. H.; Ruffoni, A.; Al-Faiyz, Y. S. S.; Sheikh, N. S.; Leonori, D. Divergent Strain-Release Amino-Functionalization of [1.1.1]Propellane with Electrophilic Nitrogen-Radicals. *Angew. Chem. Int. Ed.* **2020**, *59*, 8225–8231.

(120) Zhang, X.; Smith, R. T.; Le, C.; McCarver, S. J.; Shireman, B. T.; Carruthers, N. I.; MacMillan, D. W. C. Copper-mediated synthesis of drug-like bicyclopentanes. *Nature* **2020**, *580*, 220–226.

(121) Pickford, H. D.; Nugent, J.; Owen, B.; Mousseau, J. J.; Smith, R. C.; Anderson, E. A. Twofold Radical-Based Synthesis of *N*,*C*-Difunctionalized Bicyclo[1.1.1]pentanes. *J. Am. Chem. Soc.* **2021**, *143*, 9729–9736.

(122) Ma, X.; Han, Y.; Bennett, D. J. Selective Synthesis of 1-Dialkylamino-2-alkylbicyclo[1.1.1]pentanes. *Org. Lett.* **2020**, *22*, 9133–9138.

(123) Zhao, J.-X.; Chang, Y.-X.; He, C.; Burke, B. J.; Collins, M. R.; Bel, M. D.; Elleraas, J.; Gallego, G. M.; Montgomery, T. P.; Mousseau, J. J.; Nair, S. K.; Perry, M. A.; Spangler, J. E.; Vantourout, J. C.; Baran, P. S. 1,2-Difunctionalized bicyclo[1.1.1]pentanes: Long–sought-after mimetics for ortho/meta-substituted arenes. *Proc. Natl. Acad. Sci. U.S.A.* **2021**, *118*, e2108881118.

(124) Yang, Y.; Tsien, J.; Hughes, J.; Peters, B.; Merchant, R.; Qin, T. Synthesis of Multi-Substituted Bicycloalkyl Boronates: An Intramolecular Coupling Approach to Alkyl Bioisosteres. *ChemRxiv (preprint)* **2021**, DOI: `10.26434/chemrxiv.13724827.v1`.

(125) Klopsch, R.; Schlüter, A.-D. A [1.1.1]propellane with an unprotected hydroxy group in the side chain. *Tetrahedron* **1995**, *51*, 10491–10496.

(126) Wiberg, K. B.; McMurdie, N. Formation and Reactions of Bicyclo[1.1.1]-pentyl-1 Cations. *J. Am. Chem. Soc.* **1994**, *116*, 11990–11998.

(127) Sterling, A. J.; Dürr, A. B.; Smith, R. C.; Anderson, E. A.; Duarte, F. Rationalizing the diverse reactivity of [1.1.1]propellane through σ–π-delocalization. *Chem. Sci.* **2020**, *11*, 4895–4903.

(128) Wong, M. L. J.; Sterling, A. J.; Mousseau, J. J.; Duarte, F.; Anderson, E. A. Direct catalytic asymmetric synthesis of α-chiral bicyclo[1.1.1]pentanes. *Nat. Commun.* **2021**, *12*, 1644.

(129) Rivero, P.; Jiménez-Hoyos, C. A.; Scuseria, G. E. Predicting Singlet-Triplet Energy Splittings with Projected Hartree-Fock Methods. *J. Phys. Chem. A* **2013**, *117*, 8073–8080.

(130) Helgaker, T.; Gauss, J.; Jørgensen, P.; Olsen, J. The prediction of molecular equilibrium structures by the standard electronic wave functions. *J. Chem. Phys.* **1997**, *106*, 6430–6440.

(131) Mok, D. K. W.; Neumann, R.; Handy, N. C. Dynamical and Nondynamical Correlation. *J. Phys. Chem.* **1996**, *100*, 6225–6230.

(132) Bendikov, M.; Duong, H. M.; Starkey, K.; Houk, K. N.; Carter, E. A.; Wudl, F. Oligoacenes: Theoretical Prediction of Open-Shell Singlet Diradical Ground States. *J. Am. Chem. Soc.* **2004**, *126*, 7416–7417.

(133) Marquez, A.; Sanz, J. F. *Ab initio* CASSCF study of the electronic structure of the transition-metal alkylidene-like complexes Mo–M'H_2 (M' = C, Si, Ge, Sn). *J. Am. Chem. Soc.* **1992**, *114*, 10019–10024.

(134) Camacho, C.; Yamamoto, S.; Witek, H. A. Choosing a proper complete active space in calculations for transition metal dimers: ground state of Mn_2 revisited. *Phys. Chem. Chem. Phys.* **2008**, *10*, 5128.

(135) Møller, C.; Plesset, M. S. Note on an Approximation Treatment for Many-Electron Systems. *Phys. Rev.* **1934**, *46*, 618–622.

(136) Raghavachari, K.; Trucks, G. W.; Pople, J. A.; Head-Gordon, M. A fifth-order perturbation comparison of electron correlation theories. *Chem. Phys. Lett.* **1989**, *157*, 479–483.

(137) Loipersberger, M.; Bertels, L. W.; Lee, J.; Head-Gordon, M. Exploring the Limits of Second- and Third-Order Møller–Plesset Perturbation Theories for Noncovalent Interactions: Revisiting MP2.5 and Assessing the Importance of Regularization and Reference Orbitals. *J. Chem. Theory Comput.* **2021**, *17*, 5582–5599.

(138) Soydaş, E.; Bozkaya, U. Assessment of Orbital-Optimized MP2.5 for Thermochemistry and Kinetics: Dramatic Failures of Standard Perturbation Theory Approaches for Aromatic Bond Dissociation Energies and Barrier Heights of Radical Reactions. *J. Chem. Theory Comput.* **2015**, *11*, 1564–1573.

(139) Jensen, F., *Introduction to Computational Chemistry*; John Wiley & Sons, Inc.: Hoboken, NJ, USA, 2006.

(140) Ramabhadran, R. O.; Raghavachari, K. Extrapolation to the Gold-Standard in Quantum Chemistry: Computationally Efficient and Accurate CCSD(T) Energies for Large Molecules Using an Automated Thermochemical Hierarchy. *J. Chem. Theory Comput.* **2013**, *9*, 3986–3994.

(141) Riplinger, C.; Neese, F. An efficient and near linear scaling pair natural orbital based local coupled cluster method. *J. Chem. Phys.* **2013**, *138*, 034106.

(142) Thomas, L. H. The calculation of atomic fields. *Math. Proc. Camb. Philos. Soc.* **1927**, *23*, 542–548.

(143) Hohenberg, P.; Kohn, W. Inhomogeneous Electron Gas. *Phys. Rev.* **1964**, *136*, B864–B871.

(144) Mardirossian, N.; Head-Gordon, M. Thirty years of density functional theory in computational chemistry: an overview and extensive assessment of 200 density functionals. *Mol. Phys.* **2017**, *115*, 2315–2372.

(145) Kohn, W.; Sham, L. J. Self-Consistent Equations Including Exchange and Correlation Effects. *Phys. Rev.* **1965**, *140*, A1133–A1138.

(146) Perdew, J. P. In *AIP Conference Proceedings*, AIP: 2001; Vol. 577.

(147) Bao, J. L.; Gagliardi, L.; Truhlar, D. G. Self-Interaction Error in Density Functional Theory: An Appraisal. *J. Phys. Chem. Letters* **2018**, *9*, 2353–2358.

(148) Grimme, S. Semiempirical hybrid density functional with perturbative second-order correlation. *J. Chem. Phys.* **2006**, *124*, 034108.

(149) Grimme, S.; Ehrlich, S.; Goerigk, L. Effect of the damping function in dispersion corrected density functional theory. *J. Comput. Chem.* **2011**, *32*, 1456–1465.

(150) Grimme, S.; Antony, J.; Ehrlich, S.; Krieg, H. A consistent and accurate ab initio parametrization of density functional dispersion correction (DFT-D) for the 94 elements H-Pu. *J. Chem. Phys.* **2010**, *132*, 154104.

(151) Boys, S. F. Electronic wave functions - I. A general method of calculation for the stationary states of any molecular system. *Proc. R. Soc. Lond. A* **1950**, *200*, 542–554.

(152) Weigend, F.; Ahlrichs, R. Balanced basis sets of split valence, triple zeta valence and quadruple zeta valence quality for H to Rn: Design and assessment of accuracy. *Phys. Chem. Chem. Phys.* **2005**, *7*, 3297.

(153) Neese, F. An improvement of the resolution of the identity approximation for the formation of the Coulomb matrix. *J. Comput. Chem.* **2003**, *24*, 1740–1747.

(154) Neese, F.; Wennmohs, F.; Hansen, A.; Becker, U. Efficient, approximate and parallel Hartree–Fock and hybrid DFT calculations. A 'chain-of--spheres' algorithm for the Hartree–Fock exchange. *Chem. Phys.* **2009**, *356*, 98–109.

(155) Stoychev, G. L.; Auer, A. A.; Neese, F. Automatic Generation of Auxiliary Basis Sets. *J. Chem. Theory Comput.* **2017**, *13*, 554–562.

(156) Neese, F. Software update: the ORCA program system, version 4.0. *Wiley Interdiscip. Rev. Comput. Mol. Sci.* **2017**, *8*, e1327.

(157) Marenich, A. V.; Cramer, C. J.; Truhlar, D. G. Universal Solvation Model Based on Solute Electron Density and on a Continuum Model of the Solvent Defined by the Bulk Dielectric Constant and Atomic Surface Tensions. *J. Phys. Chem. B* **2009**, *113*, 6378–6396.

(158) Hirshfeld, F. L. Bonded-atom fragments for describing molecular charge densities. *Theor. Chim. Acta* **1977**, *44*, 129–138.

(159) Mulliken, R. S. Electronic Population Analysis on LCAO–MO Molecular Wave Functions. I. *J. Chem. Phys.* **1955**, *23*, 1833–1840.

(160) Scerri, E. R. Have Orbitals Really Been Observed? *J. Chem. Educ.* **2000**, *77*, 1492.

(161) Pham, B. Q.; Gordon, M. S. Can Orbitals Really Be Observed in Scanning Tunneling Microscopy Experiments? *J. Phys. Chem. A* **2017**, *121*, 4851–4852.

(162) Itatani, J.; Levesque, J.; Zeidler, D.; Niikura, H.; Pépin, H.; Kieffer, J. C.; Corkum, P. B.; Villeneuve, D. M. Tomographic imaging of molecular orbitals. *Nature* **2004**, *432*, 867–871.

(163) Koopmans, T. Über die Zuordnung von Wellenfunktionen und Eigenwerten zu den Einzelnen Elektronen Eines Atoms. *Physica* **1934**, *1*, 104–113.

(164) Bredas, J.-L. Mind the gap! *Mater. Horiz.* **2014**, *1*, 17–19.

(165) Fukui, K.; Yonezawa, T.; Shingu, H. A Molecular Orbital Theory of Reactivity in Aromatic Hydrocarbons. *J. Chem. Phys.* **1952**, *20*, 722–725.

(166) Klopman, G. Chemical reactivity and the concept of charge- and frontier-controlled reactions. *J. Am. Chem. Soc.* **1968**, *90*, 223–234.

(167) Salem, L. Intermolecular orbital theory of the interaction between conjugated systems. I. General theory. *J. Am. Chem. Soc.* **1968**, *90*, 543–552.

(168) Woodward, R. B.; Hoffmann, R. Stereochemistry of Electrocyclic Reactions. *J. Am. Chem. Soc.* **1965**, *87*, 395–397.

(169) Woodward, R. B.; Hoffmann, R. The Conservation of Orbital Symmetry. *Angew. Chem., Int. Ed. Engl.* **1969**, *8*, 781–853.

(170) Lewis, G. N. The Atom and the Molecule. *J. Am. Chem. Soc.* **1916**, *38*, 762–785.

(171) Foster, J. P.; Weinhold, F. Natural hybrid orbitals. *J. Am. Chem. Soc.* **1980**, *102*, 7211–7218.

(172) Bickelhaupt, F. M.; Houk, K. N. Analyzing Reaction Rates with the Distortion/Interaction-Activation Strain Model. *Angew. Chem. Int. Ed.* **2017**, *56*, 10070–10086.

(173) Johnson, E. R.; Keinan, S.; Mori-Sánchez, P.; Contreras-García, J.; Cohen, A. J.; Yang, W. Revealing Noncovalent Interactions. *J. Am. Chem. Soc.* **2010**, *132*, 6498–6506.

(174) Hammett, L. P. Some Relations between Reaction Rates and Equilibrium Constants. *Chem. Rev.* **1935**, *17*, 125–136.

(175) Boaz, H.; Rollefson, G. K. The Quenching of Fluorescence. Deviations from the Stern-Volmer Law. *J. Am. Chem. Soc.* **1950**, *72*, 3435–3443.

(176) Hedberg, L.; Hedberg, K. The molecular structure of gaseous [1.1.1]propellane: an electron-diffraction investigation. *J. Am. Chem. Soc.* **1985**, *107*, 7257–7260.

(177) Wiberg, K. B.; Dailey, W. P.; Walker, F. H.; Waddell, S. T.; Crocker, L. S.; Newton, M. Vibrational spectrum, structure, and energy of [1.1.1]propellane. *J. Am. Chem. Soc.* **1985**, *107*, 7247–7257.

(178) Seiler, P. The crystal structure of [1.1.1]propellane at 138 K. *Helv. Chim. Acta* **1990**, *73*, 1574–1585.

(179) Honegger, E.; Huber, H.; Heilbronner, E.; Dailey, W. P.; Wiberg, K. B. The PE spectrum of [1.1.1]propellane: evidence for a non-bonding MO? *J. Am. Chem. Soc.* **1985**, *107*, 7172–7174.

(180) Jarret, R. M.; Cusumano, L. ^{13}C–^{13}C Coupling in [1.1.1]Propellane. *Tetrahedron Lett.* **1990**, *31*, 171–174.

(181) Jackson, J. E.; Allen, L. C. The C_1-C_3 Bond in [1.1.1]Propellane. *J. Am. Chem. Soc.* **1984**, *106*, 591–599.

(182) Feller, D.; Davidson, E. R. Ab initio studies of [1.1.1]- and [2.2.2]propellane. *J. Am. Chem. Soc.* **1987**, *109*, 4133–4139.

(183) Wiberg, K. B.; Bader, R. F. W.; Lau, C. D. H. Theoretical analysis of hydrocarbon properties. 1. Bonds, structures, charge concentrations, and charge relaxations. *J. Am. Chem. Soc.* **1987**, *109*, 985–1001.

(184) Kar, T.; Jug, K. Origin of the bridge bond in [1,1,1]propellane. *Chem. Phys. Lett.* **1996**, *256*, 201–206.

(185) Polo, V.; Andres, J.; Silvi, B. New insights on the bridge carbon–carbon bond in propellanes: A theoretical study based on the analysis of the electron localization function. *J. Comput. Chem.* **2007**, *28*, 857–864.

(186) Wu, W.; Gu, J.; Song, J.; Shaik, S.; Hiberty, P. The Inverted Bond in [1.1.1]Propellane is a Charge-Shift Bond. *Angew. Chem. Int. Ed.* **2009**, *48*, 1407–1410.

(187) Harmony, M. D. The equilibrium carbon–carbon single-bond length in ethane. *J. Chem. Phys.* **1990**, *93*, 7522–7523.

(188) Messerschmidt, M.; Scheins, S.; Grubert, L.; Pätzel, M.; Szeimies, G.; Paulmann, C.; Luger, P. Electron Density and Bonding at Inverted Carbon Atoms: An Experimental Study of a [1.1.1]Propellane Derivative. *Angew. Chem. Int. Ed.* **2005**, *44*, 3925–3928.

(189) Foster, J. M.; Boys, S. F. Canonical Configurational Interaction Procedure. *Rev. Mod. Phys.* **1960**, *32*, 300–302.

(190) Li, C.; Zheng, X.; Su, N. Q.; Yang, W. Localized orbital scaling correction for systematic elimination of delocalization error in density functional approximations. *Natl. Sci. Rev.* **2017**, *5*, 203–215.

(191) Müller, B.; Bally, T.; Pappas, R.; Williams, F. Spectroscopic and Computational Studies on the Rearrangement of Ionized [1.1.1]Propellane and Some of its Valence Isomers: The Key Role of Vibronic Coupling. *J. Am. Chem. Soc.* **2010**, *132*, 14649–14660.

(192) Lee, C.; Yang, W.; Parr, R. G. Development of the Colle-Salvetti correlation-energy formula into a functional of the electron density. *Phys. Rev. B* **1988**, *37*, 785–789.

(193) Becke, A. D. Density-functional thermochemistry. III. The role of exact exchange. *J. Chem. Phys.* **1993**, *98*, 5648–5652.

(194) Lopchuk, J. M.; Fjelbye, K.; Kawamata, Y.; Malins, L. R.; Pan, C.-M.; Gianatassio, R.; Wang, J.; Prieto, L.; Bradow, J.; Brandt, T. A.; Collins, M. R.; Elleraas, J.; Ewanicki, J.; Farrell, W.; Fadeyi, O. O.; Gallego, G. M.; Mousseau, J. J.; Oliver, R.; Sach, N. W.; Smith, J. K.; Spangler, J. E.; Zhu, H.; Zhu, J.; Baran, P. S. Strain-Release Heteroatom Functionalization: Development, Scope, and Stereospecificity. *J. Am. Chem. Soc.* **2017**, *139*, 3209–3226.

(195) Trongsiriwat, N.; Pu, Y.; Nieves-Quinones, Y.; Shelp, R. A.; Kozlowski, M. C.; Walsh, P. J. Reactions of 2-Aryl-1, 3-Dithianes and [1.1.1]Propellane. *Angew. Chem. Int. Ed.* **2019**, *58*, 13416–13420.

(196) Mondanaro, K. R.; Dailey, W. P. [1.1.1]Propellane. *Org. Synth.* **1998**, *75*, 98.

(197) Bartlett, R. J.; Musiał, M. Coupled-cluster theory in quantum chemistry. *Rev. Mod. Phys.* **2007**, *79*, 291–352.

(198) O'Ferrall, R. A. M. Relationships between $E2$ and $E1cB$ mechanisms of β-elimination. *J. Chem. Soc. B* **1970**, *0*, 274–277.

(199) Yu, S.; Noble, A.; Bedford, R. B.; Aggarwal, V. K. Methylenespiro[2.3]-hexanes via Nickel-Catalyzed Cyclopropanations with [1.1.1]Propellane. *J. Am. Chem. Soc.* **2019**, *141*, 20325–20334.

(200) Lasányi, D.; Tolnai, G. L. Copper-Catalyzed Ring Opening of [1.1.1]Propellane with Alkynes: Synthesis of Exocyclic Allenic Cyclobutanes. *Org. Lett.* **2019**, *21*, 10057–10062.

(201) Kondo, M.; Kanazawa, J.; Ichikawa, T.; Shimokawa, T.; Nagashima, Y.; Miyamoto, K.; Uchiyama, M. Silaboration of [1.1.1]Propellane: A Storable Feedstock for Bicyclo[1.1.1]pentane Derivatives. *Angew. Chem. Int. Ed.* **2020**, *59*, 1970–1974.

(202) Yu, S.; Jing, C.; Noble, A.; Aggarwal, V. K. 1,3-Difunctionalizations of [1.1.1]Propellane via 1,2-Metallate Rearrangements of Boronate Complexes. *Angew. Chem. Int. Ed.* **2020**, *59*, 3917–3921.

(203) Ni, S.; Garrido-Castro, A. F.; Merchant, R. R.; de Gruyter, J. N.; Schmitt, D. C.; Mousseau, J. J.; Gallego, G. M.; Yang, S.; Collins, M. R.; Qiao, J. X.; Yeung, K.-S.; Langley, D. R.; Poss, M. A.; Scola, P. M.; Qin, T.; Baran, P. S. A General Amino Acid Synthesis Enabled by Innate Radical Cross-Coupling. *Angew. Chem. Int. Ed.* **2018**, *57*, 14560–14565.

(204) Ni, S.; Padial, N. M.; Kingston, C.; Vantourout, J. C.; Schmitt, D. C.; Edwards, J. T.; Kruszyk, M. M.; Merchant, R. R.; Mykhailiuk, P. K.; Sanchez, B. B.; Yang, S.; Perry, M. A.; Gallego, G. M.; Mousseau, J. J.; Collins, M. R.; Cherney, R. J.; Lebed, P. S.; Chen, J. S.; Qin, T.; Baran, P. S. A Radical Approach to Anionic Chemistry: Synthesis of Ketones, Alcohols, and Amines. *J. Am. Chem. Soc.* **2019**, *141*, 6726–6739.

(205) Wong, M. L. J.; Mousseau, J. J.; Mansfield, S. J.; Anderson, E. A. Synthesis of Enantioenriched α-Chiral Bicyclo[1.1.1]pentanes. *Org. Lett.* **2019**, *21*, 2408–2411.

(206) Garlets, Z. J.; Sanders, J. N.; Malik, H.; Gampe, C.; Houk, K. N.; Davies, H. M. L. Enantioselective C–H functionalization of bicyclo[1.1.1]pentanes. *Nat. Catal.* **2020**, *3*, 351–357.

(207) Yu, S.; Jing, C.; Noble, A.; Aggarwal, V. K. Iridium-Catalyzed Enantioselective Synthesis of α-Chiral Bicyclo[1.1.1]pentanes by 1,3-Difunctionalization of [1.1.1]Propellane. *Org. Lett.* **2020**, *22*, 5650–5655.

(208) Vyas, V. K.; Clarkson, G. J.; Wills, M. Enantioselective Synthesis of Bicyclopentane-Containing Alcohols via Asymmetric Transfer Hydrogenation. *Org. Lett.* **2021**, *23*, 3179–3183.

(209) Capacci, A. G.; Malinowski, J. T.; McAlpine, N. J.; Kuhne, J.; MacMillan, D. W. C. Direct, enantioselective α-alkylation of aldehydes using simple olefins. *Nat. Chem.* **2017**, *9*, 1073–1077.

(210) McGarry, P. F.; Scaiano, J. C. The absolute kinetics for radical addition and electronic energy transfer to [1.1.1]propellane. *Can. J. Chem.* **1998**, *76*, 1474–1489.

(211) Wong, M. L. J. Synthesis and Functionalization of α-Chiral Bicyclo[1.1.1]-pentanes. Ph.D. Thesis, University of Oxford, 2020.

(212) Vitaku, E.; Smith, D. T.; Njardarson, J. T. Analysis of the Structural Diversity, Substitution Patterns, and Frequency of Nitrogen Heterocycles among U.S. FDA Approved Pharmaceuticals. *J. Med. Chem.* **2014**, *57*, 10257–10274.

(213) Bär, R. M.; Kirschner, S.; Nieger, M.; Bräse, S. Alkyl and Aryl Thiol Addition to [1.1.1]Propellane: Scope and Limitations of a Fast Conjugation Reaction. *Chem. Eur. J.* **2017**, *24*, 1373–1382.

(214) McGarry, P. F.; Johnston, L. J.; Scaiano, J. C. Addition of oxygen- and sulfur-centered radicals to [1.1.1]propellane. *J. Org. Chem.* **1989**, *54*, 6133–6135.

(215) Li, Y.; Wang, D.; Zhang, L.; Luo, S. Redox Property of Enamines. *J. Org. Chem.* **2019**, *84*, 12071–12090.

(216) Lowry, M. S.; Goldsmith, J. I.; Slinker, J. D.; Rohl, R.; Pascal, R. A.; Malliaras, G. G.; Bernhard, S. Single-Layer Electroluminescent Devices and Photoinduced Hydrogen Production from an Ionic Iridium(III) Complex. *Chem. Mater.* **2005**, *17*, 5712–5719.

(217) Sterling, A. J.; Zavitsanou, S.; Ford, J.; Duarte, F. Selectivity in organocatalysis—From qualitative to quantitative predictive models. *Wiley Interdiscip. Rev. Comput. Mol. Sci.* **2021**, *11*, e1518.

(218) Franzén, J.; Marigo, M.; Fielenbach, D.; Wabnitz, T. C.; Kjærsgaard, A.; Jørgensen, K. A. A General Organocatalyst for Direct α-Functionalization of Aldehydes: Stereoselective C–C, C–N, C–F, C–Br, and C–S Bond-Forming Reactions. Scope and Mechanistic Insights. *J. Am. Chem. Soc.* **2005**, *127*, 18296–18304.

(219) Wolk, J. L.; Rozental, E.; Basch, H.; Hoz, S. Strain Energy Release and Intrinsic Barriers in Internal Nucleophilic Reactions. *J. Org. Chem.* **2006**, *71*, 3876–3879.

(220) Feixas, F.; Matito, E.; Poater, J.; Solà, M. Understanding Conjugation and Hyperconjugation from Electronic Delocalization Measures. *J. Phys. Chem. A* **2011**, *115*, 13104–13113.

(221) Becke, A. D.; Edgecombe, K. E. A simple measure of electron localization in atomic and molecular systems. *J. Chem. Phys.* **1990**, *92*, 5397–5403.

(222) Tokunaga, K.; Sato, M.; Kuwata, K.; Miura, C.; Fuchida, H.; Matsunaga, N.; Koyanagi, S.; Ohdo, S.; Shindo, N.; Ojida, A. Bicyclobutane Carboxylic Amide as a Cysteine-Directed Strained Electrophile for Selective Targeting of Proteins. *J. Am. Chem. Soc.* **2020**, *142*, 18522–18531.

(223) Damsté, J. S. S.; Strous, M.; Rijpstra, W. I. C.; Hopmans, E. C.; Geenevasen, J. A. J.; van Duin, A. C. T.; van Niftrik, L. A.; Jetten, M. S. M. Linearly concatenated cyclobutane lipids form a dense bacterial membrane. *Nature* **2002**, *419*, 708–712.

(224) Schneider, C. Synthesis of 1,2-Difunctionalized Fine Chemicals through Catalytic, Enantioselective Ring-Opening Reactions of Epoxides. *Synthesis* **2006**, *2006*, 3919–3944.

(225) Lu, P. Recent developments in regioselective ring opening of aziridines. *Tetrahedron* **2010**, *66*, 2549–2560.

(226) Akhtar, R.; Naqvi, S. A. R.; Zahoor, A. F.; Saleem, S. Nucleophilic ring opening reactions of aziridines. *Mol. Divers.* **2018**, *22*, 447–501.

(227) Burkhard, J. A.; Wuitschik, G.; Rogers-Evans, M.; Müller, K.; Carreira, E. M. Oxetanes as Versatile Elements in Drug Discovery and Synthesis. *Angew. Chem. Int. Ed.* **2010**, *49*, 9052–9067.

(228) Brandi, A.; Cicchi, S.; Cordero, F. M. Novel Syntheses of Azetidines and Azetidinones. *Chem. Rev.* **2008**, *108*, 3988–4035.

(229) Jug, K.; Poredda, A. Polymerization mechanisms of propellanes. *J. Am. Chem. Soc.* **1991**, *113*, 761–764.

A |

Computational and experimental methods

A.1 Methods for Chapter 2

All calculations were carried out using the ORCA suite of programs (v. 4.1.1).[1] Both optimizations and single-point energy calculations were carried out using "Tight" convergence criteria, corresponding to tolerances of 1.0×10^{-8} Ha for the SCF energy change, and 1.0×10^{-6} Ha for the optimisation step. To speed up the calculations, the resolution-of-identity (RI) chain-of-spheres exchange (RI-JCOSX) approximation was employed.[2] MP2 calculations were employed with the RI approximation as default for the calculation of correlation integrals. The integration grid "Grid5" was employed for DFT energies, corresponding to a Lebedev-434 angular grid, and a radial integral accuracy (IntAcc) of 5.01. Calculations employing a RI approximation utilized the "GridX6" procedure, corresponding to IntAcc = 4.34 and a Lebedev-194 angular grid. For calculations of triple-ζ basis set quality, calculation of correlation integrals used the def2-TZVP/C auxiliary basis set. All calculations using a quadruple-ζ basis set employed the AutoAux[3] procedure developed by Neese and co-workers, which generates large auxiliary basis sets for the Coulomb, exchange and correlation integral calculations. Treatment of 28 core electrons with the def2 effective core potential (def2-ECP) was employed for iodine and tellurium.[4] All intermediate structures were verified to be minima by the absence of imaginary frequencies upon calculation of the Hessian. Grimme's quasi-RRHO approach was used to calculate free energies at 298.15 K. A 1 atm to 1 M standard state correction was applied by adding $RT\ln(24.5) = 1.89$ kcal mol^{-1} to the calculated free energy of each species.[5] Persistent spurious imaginary frequencies for rotations below 35 cm^{-1} in magnitude were ignored, since they are indicative of noise due to the use of numerical grids.

The Domain-based Local Pair Natural Orbital coupled cluster method with singles, doubles and perturbative triples (DLPNO-CCSD(T)) was used as a benchmark for the potential energy surface.[6] DLPNO-CCSD(T) calculations were run using "NormalPNO" cut-offs,[7] corresponding to T_{CutPairs} = 10^{-5} Hartrees, T_{CutPNOs} = 3.33×10^{-7} and T_{CutMKN} = 10^{-3}, where T_{CutPairs} is the correlation threshold for inclusion of a given electron pair in the CCSD calculation, T_{CutPNOs} is the occupation threshold for each PNO (pair natural orbital) formed from an expansion of projected atomic orbitals (PAOs), and T_{CutMKN} determines the threshold for the inclusion of each localized MO in the PNO expansion based on Mulliken population. To ensure the validity of this method, energies were also calculated at the CCSD(T)/(ma-)def2-SVP level of theory and compared to those obtained at the DLPNO-CCSD(T)/(ma-)def2-SVP level, and relative energy differences did not exceed 1 kcal mol^{-1}.

Dispersion corrections to DFT energies were implemented using Grimme's D3 empirical method with Becke-Johnson damping (D3BJ).[8,9] For ωB97X-D3, Chai's bespoke reparameterisation of Grimme's D3 correction was used.[10]

Data for Chapter 2 is available in the 'Chapter2_data' directory of 'Sterling_thesis_data.zip', including tables of raw and processed data ('chapter2_data.xlsx'), and coordinates of optimised structures ('chapter2_coords.zip'). The Python script and csv file to generate the More O'Ferrall Jencks plot is provided in the 'MOJ_plot' directory.

A.2 Methods for Chapter 3

QM calculations were run using ORCA (v. 4.1.1).[1] Optimisation and frequency calculations were carried out at the PBE0-D3BJ/def2-TZVP level of theory[11] using the SMD[12] implicit solvent model for DME (user-defined parameters from Ref. [13]: Epsilon = 7.54, Refrac = 1.3772, Rsolv = 1.30, Soln = 1.3813, Soln25 = 1.3739, Sola = 0.00, Solb = 0.00, Solg = 0.0246, Solc = 0.00, Solh = 0.00). Grimme's D3 empirical dispersion correction with Becke-Johnson (BJ) damping was applied,[8] along with the RIJCOSX approximation using the appropriate auxiliary basis sets,[2] and 'tight' optimization criteria (10^{-8} Ha tolerance for SCF, 10^{-6} Ha tolerance for optimisation step). The accuracy of this method was tested through comparison with results obtained at the B2GP-PLYP-D3BJ/def2-TZVP level of theory[14] with the same solvent model / resolution of the identity / optimization criteria, which we have previously shown to provide accurate geometries and energetics for intermediates in reactions of [1.1.1]propellane **1**.[15] Single point energies were calculated at the DLPNO-CCSD(T)/def2-TZVPP level of theory, using the same solvent model, and 'tight' PNO cut-offs ($T_{\text{CutPairs}} = 10^{-5}$, $T_{\text{CutPNOs}} = 10^{-7}$, $T_{\text{CutMKN}} = 10^{-4}$). All calculations used Grid6 / GridX6, corresponding to Lebedev-590 angular grid, and a radial integral accuracy (IntAcc) of 5.34. Stationary points for the model systems were characterised through calculation of the Hessian. Spurious imaginary frequencies below 30 cm^{-1} in magnitude were ignored, as these correspond to numerical errors due to the integration grid, and all frequencies below 100 cm^{-1} were subsequently damped through the use of Grimme's quasi-RRHO approximation.[5] Free energy corrections were applied for a 1 M standard state at 283.15 K, using the *otherm* Python package.[16]

Conformational sampling was carried out using GFN2-xTB (v. 6.1), using the simulated annealing algorithm with the GBSA implicit solvent model for dichloromethane.[17] Conformers were generated for each compound in triplicate, where each run consisted an initial 16.67 ps molecular dynamics (Δt = 4 fs) at 149.07 K, followed by annealing from 298.15 K to 1000.00 K in three steps of 50 ps (150 ps total). Each conformer was then optimised at the GFN2-xTB level, and conformers above 20 kcal mol^{-1} of the lowest energy were removed. The structures from the three runs ($\approx$ 450 per system) were combined, and conformers with RMSD $<$ 0.7 Å on heavy atoms were removed using the RMSD filter built into the Python package *autodE*.[18] Single point energy calculations on the surviving conformers were obtained at the PBE-D3BJ/def2-SV(P) level of theory using the SMD solvent model for DME, and conformers within 3 kcal mol^{-1} of the lowest were optimised for 10 cycles at the SMD(DME)-PBE0-D3BJ/def2-SVP level of theory. The lowest energy conformer from this process was then reoptimised with 'tight' optimization criteria at the same level of theory.

Distortion / interaction analysis (DIA, also referred to as activation / strain analysis) was carried out on the model addition system,[19] where the barrier to addition ($\Delta E^{\ddagger}$) is divided into the distortion of the fragments required to adopt the transition state (TS) geometry ($\Delta E^{\ddagger}_{\text{dist}}$) and the interaction of the two fragments in this distorted geometry ($\Delta E^{\ddagger}_{\text{int}}$). NPA charges and spin populations were calculated using NBO v. 7.0. Non-covalent interaction (NCI) isosurfaces were calculated using Multiwfn v. 3.6,[20] and are shown at an isovalue of 0.6 a.u.

For the Stern-Volmer quenching studies, emission spectra were recorded at 20 °C using an Edinburgh Instruments FS5 spectrofluorimeter, equipped with a xenon arc lamp (400 nm excitation), an SC-20 thermostatic sample holder, and a Hamamatsu R13456 PMT detector measuring at 425 – 800 nm. A quartz cuvette (10 mm path length) was charged with 2.5 mL of a 5 μM solution of photocatalyst Ir[(ppy)$_2$(dtbbpy)]PF$_6$ dissolved in a 1:1 mixture of anhydrous DME/Et$_2$O and was degassed by sparging with argon for 10 minutes. The appropriate volume of a 0.5 M solution (1:1 DME/Et_2O) of each quencher was added sequentially and the emission of the solution was measured. The quenching constant of the enamine derived from 3-phenylpropanal and organocatalyst **3** was obtained from the measurement of a 15:1 solution of this aldehyde and organocatalyst in which the amine was assumed to be completely consumed. The quenching constant for this enamine was then calculated by adjustment for concentration and background aldehyde quenching, to obtain a value of 83.4 M^{-1}. These measurements show that the enamine is the most efficient quencher of $Ir[(ppy)_2(dtbbpy)]PF_6$ of the components in the reaction.

Data for Chapter 3 is available in the 'Chapter3_data' directory of 'Sterling_thesis_data.zip', including tables of raw and processed experimental and computational data ('chapter3_data.xlsx'), and coordinates of optimised structures ('chapter3_coords.zip').

A.3 Methods for Chapter 4

All calculations were carried out using ORCA (v. 4.2.1).[1] Minima and TSs for the reactive systems were initially identified using *autodE* (v. 1.0.0b3),[18] before refinement at the [DLPNO-CCSD(T)/def2-QZVPP (TightPNO)//B2PLYP-D3BJ/def2-TZVP] level of theory ($CH_3^{\bullet}$ reactions) or [SMD(THF)/DLPNO-CCSD(T)/ma-def2-QZVPP (TightPNO)//SMD(THF)/B2PLYP-D3BJ/def2-TZVP (ma-def2-TZVP on N)] level of theory (NH_2^- reactions).[11,12,21,22] All calculations used the resolution of the identity approximation (RIJCOSX),[2] with the appropriate auxiliary basis sets.[3] 'Tight' optimization criteria (10^{-8} Ha tolerance for SCF, 10^{-6} Ha tolerance for optimisation step) were employed along with Grid6 / GridX6, corresponding to a Lebedev-590 angular grid, and a radial integral accuracy (IntAcc) of 5.34. Stationary points for the model systems were characterised through calculation of the Hessian. NBO occupation numbers were calculated using the NBO program (v. 7.0), and density-based descriptors were calculated with Multiwfn (v. 3.6).[20]

All data processing was carried out using the Scikit-learn package in Python 3.7,[23] and MLR plots were generated with Matplotlib.[24]

Data for Chapter 4 is available in the 'Chapter4_data' directory of 'Sterling_thesis_data.zip', including tables of raw and processed data ('chapter4_data.xlsx'), and coordinates of optimised structures ('chapter4_coords.zip'). The Python script and csv files to generate MLR plots are provided in the 'MLR_plots' directory.

B |

Non-covalent interaction analysis

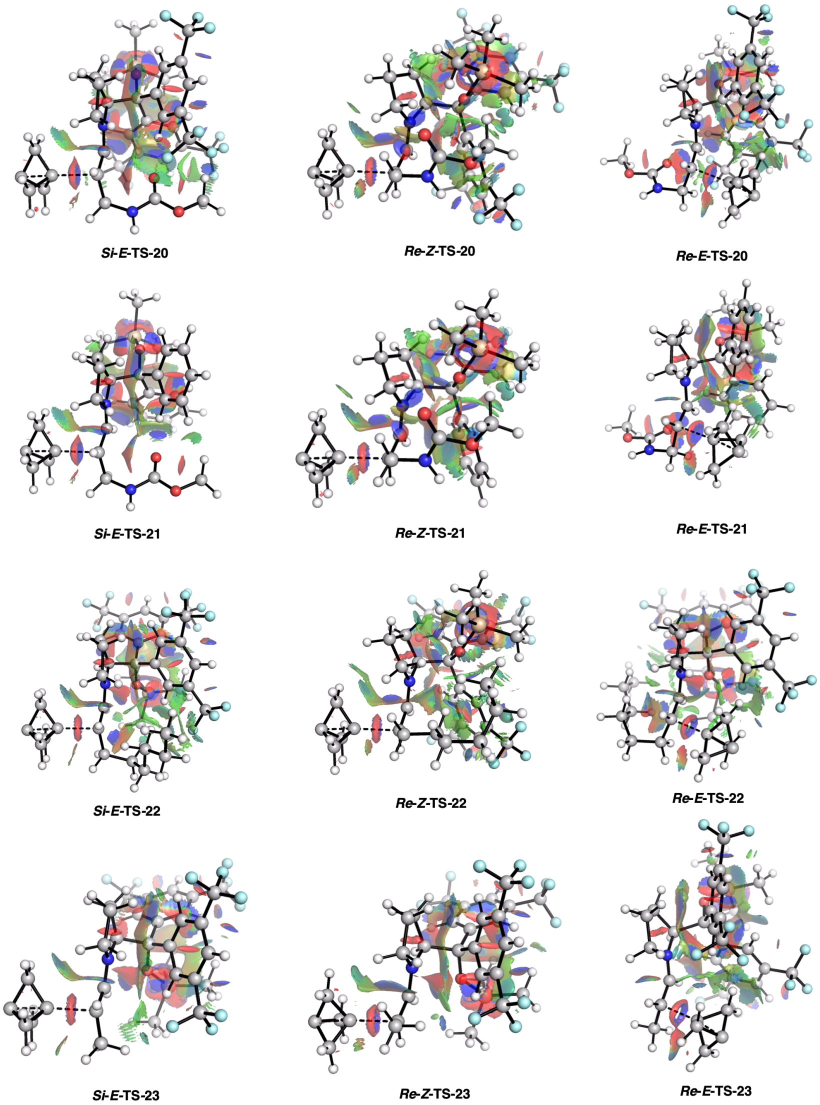

Si-*E*-TS-20 *Re*-*Z*-TS-20 *Re*-*E*-TS-20

Si-*E*-TS-21 *Re*-*Z*-TS-21 *Re*-*E*-TS-21

Si-*E*-TS-22 *Re*-*Z*-TS-22 *Re*-*E*-TS-22

Si-*E*-TS-23 *Re*-*Z*-TS-23 *Re*-*E*-TS-23

Figure B.1: Non-covalent interactions (NCIs) present in each constrained TS analogue for **TS-20**, **TS-21**, **TS-22** and **TS-23**, calculated at the SMD(DME)-PBE0-D3BJ/def2-SVP level of theory. Red indicates repulsion, green in dispersion and blue is attraction. Isovalue = 0.6 a.u.

C |

Luminescence quenching plots

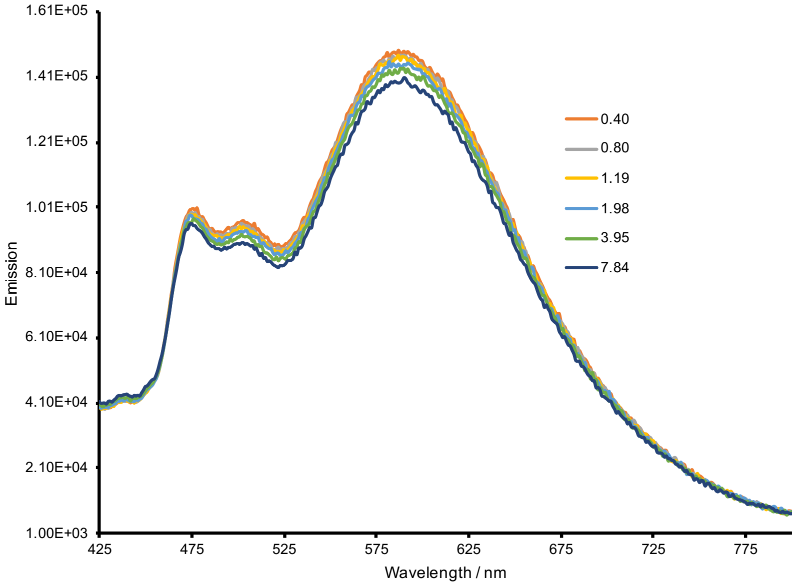

Figure C.1: Luminescence quenching titration for 3-phenylpropanal with a 5 μM solution of Ir[(ppy)$_2$(dtbbpy)]PF$_6$. Quencher concentraions reported in mM.

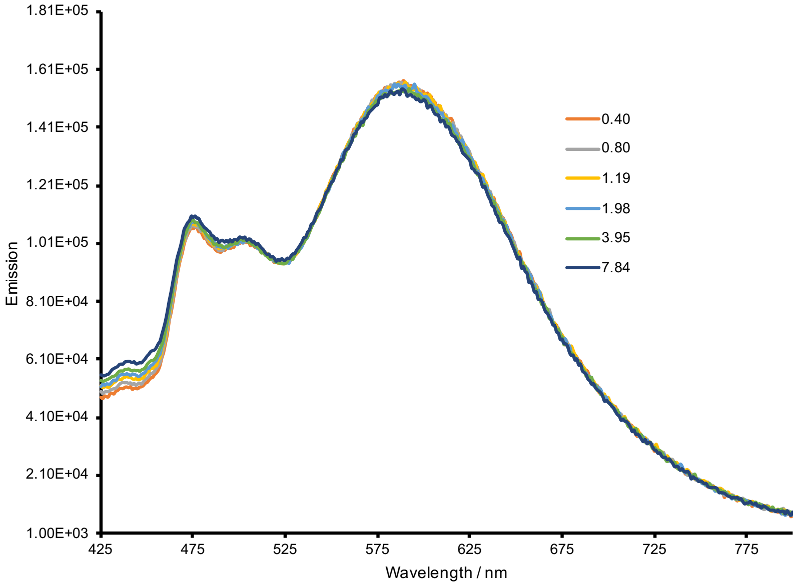

Figure C.2: Luminescence quenching titration for organocatalyst **3** with a 5 μM solution of Ir[(ppy)$_2$(dtbbpy)]PF$_6$. Quencher concentraions reported in mM.

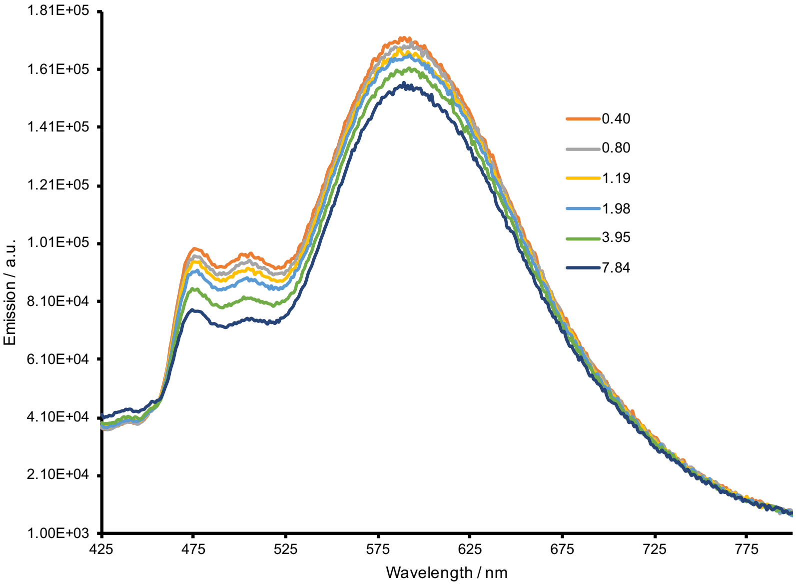

Figure C.3: Luminescence quenching titration for a 15:1 solution of 3-phenylpropanal and organocatalyst **3** with a 5 μM solution of Ir[(ppy)$_2$(dtbbpy)]PF$_6$. Quencher concentraions reported in mM.

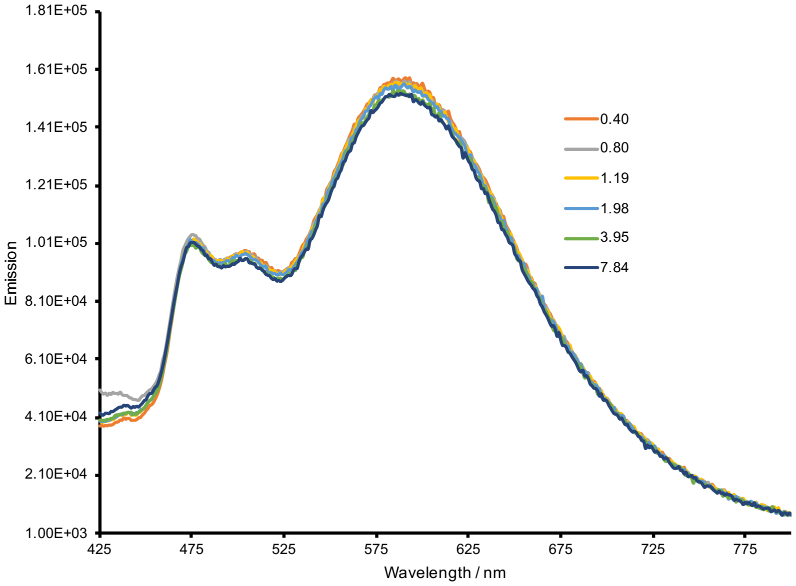

Figure C.4: Luminescence quenching titration for HAT catalyst **4** with a 5 μM solution of Ir[(ppy)$_2$(dtbbpy)]PF$_6$. Quencher concentraions reported in mM.

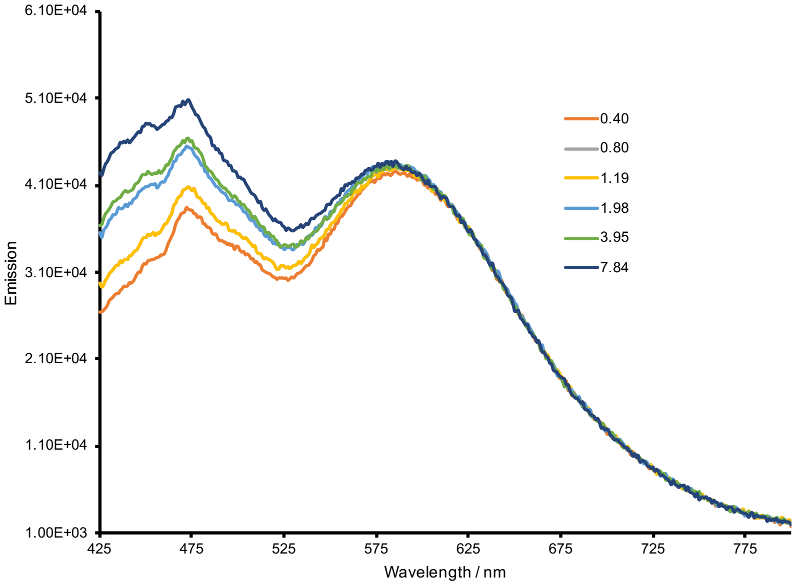

Figure C.5: Luminescence quenching titration for [1.1.1]propellane **1** with a 5 μM solution of Ir[(ppy)$_2$(dtbbpy)]PF$_6$. Quencher concentraions reported in mM.

D |

Hydrocarbon strain release dataset

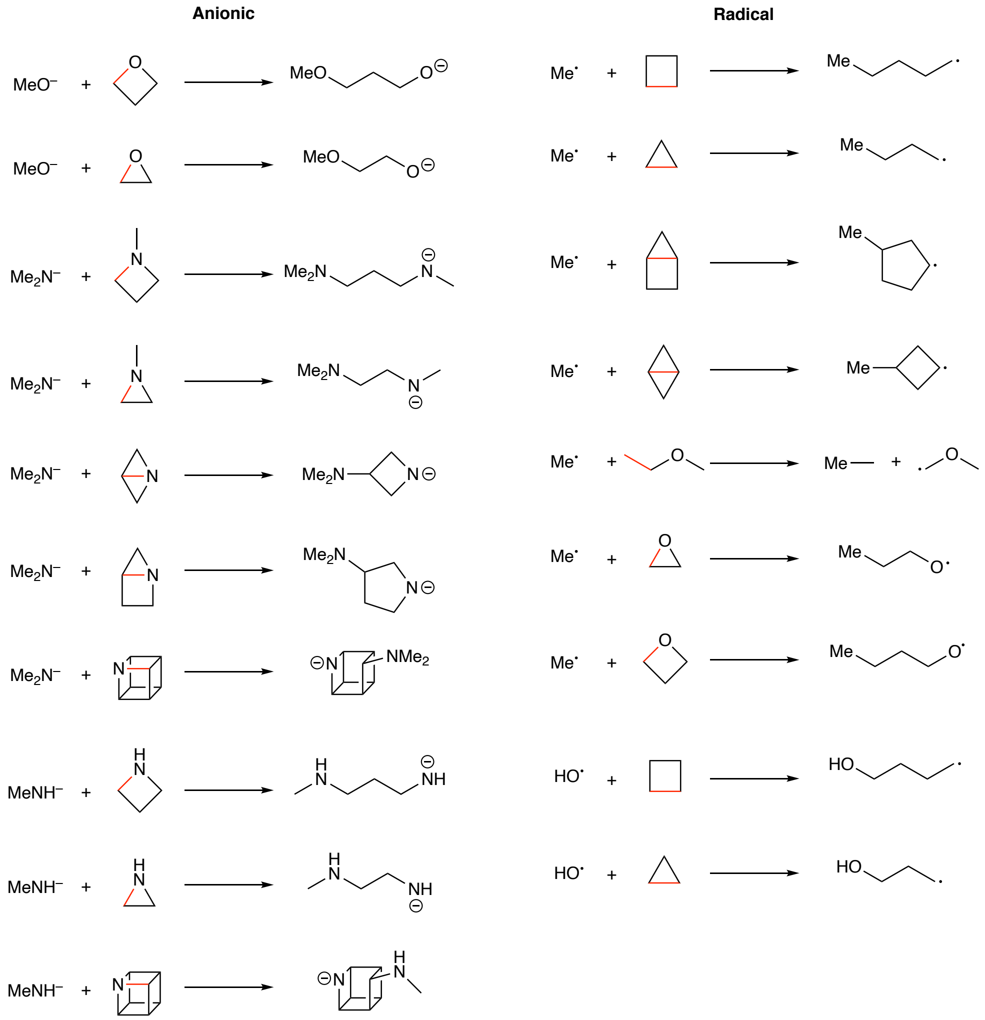
Anionic

Radical

Figure D.1: List of reactions used to construct Figure 4.7, from Refs. [25, 26].

Table D.1: Set of 12 hydrocarbons with varying ring sizes and strain energies. ΔH_r and $\Delta H^\ddagger$ refer to the addition of $CH_3^\bullet$ for the SRE process specified.

Molecule	n_3[a]	n_4[b]	**SE[c] / kcal mol^{-1}**	**SRE[d] / kcal mol^{-1}**	ΔH_r[e] **/ kcal mol^{-1}**	$\Delta H^\ddagger$[e] **/ kcal mol^{-1}**
Ethane (**A**)	0	0	0.0	0.0	0.0	0.0
Cyclopropane (**B**)	1	0	27.9	–27.9 (to *n*-propane)	–28.4	26.4
Cyclobutane (**C**)	0	1	26.8	–26.8 (to *n*-butane)	–26.8	36.1
Bicyclo[1.1.0]butane (**D**)	2	1	66.5	–39.7 (to cyclobutane)	–41.6	9.9
Bicyclo[2.1.0]pentane (**E**)	1	1	55.6	–48.1 (to cyclopentane)	–52.9	16.4
Bicyclo[3.1.0]hexane (**F**)	1	0	32.4	–30.6 (to cyclohexane)	–34.8	22.8
Bicyclo[2.2.0]hexane (**G**)	0	2	54.1	–52.3 (to cyclohexane)	–52.4	24.3
[1.1.1]Propellane (**H / 1**)	3	3	99.2	–32.3 (to bicyclo[1.1.1]pentane)	–28.2	5.0
[2.1.1]Propellane (**I**)	2	1	99.6	–61.6 (to bicyclo[2.1.1]hexane)	–55.3	2.0
[3.1.1]Propellane (**J**)	2	1	76.4[f]	–43.3[f] (to bicyclo[3.1.1]heptane)	–42.1	5.7
[2.2.1]Propellane (**K**)	1	2	99.7	–83.8 (to bicyclo[2.2.1]heptane)	–78.5	1.6
[2.2.2]Propellane (**L**)	0	3	93.9	–82.3 (to bicyclo[2.2.2]octane)	–82.1	9.6

[a] Number of three-membered rings. [b] Number of four-membered rings. [c] Strain energy obtained from Ref. [27]. [d] Strain release energy ($SE_{product}$ – $SE_{reactant}$ obtained from Ref. [27]). [e] DLPNO-CCSD(T)/def2-QZVPP//B2PLYP-D3BJ/def2-TZVP. [f] Calculated at the W1BD level using the procedure described in Ref. [27].

E |

Electronic structure theory

E.1 Determinants, configuration state functions and configurations

Before discussing the electronic structure methods employed in this Thesis, we will briefly define some important terms. Firstly, we will define spatial and spin orbitals, and mention their importance in computational chemistry. We will then distinguish between a *Slater determinant*, a *configuration state function* (CSF) and a *configuration*. Finally, we will introduce the electronic Hamiltionian. The definitions and discussion here are based on those from Szabo and Ostlund's *Modern Quantum Chemistry*.[28]

An orbital is a one-particle wavefunction that completely describes the properties of that particle, which will be an electron for all further discussions here. For example, a spin orbital, $\chi_i(\mathbf{x})$, comprises the product of a spatial part, $\psi_i(\mathbf{r})$, and a spin part, $\sigma(\omega)$. The spatial orbital contains information on the position of the electron based on the position vector $\mathbf{r}$, such that we can describe the probability of finding the electron in the small volume element $d\mathbf{r}$ surrounding $\mathbf{r}$ with the expression $|\psi_i(\mathbf{r})|^2 d\mathbf{r}$. The spin part of $\chi_i(\mathbf{x})$ denotes whether the electron spin is up ($\alpha(\omega)$) or down ($\beta(\omega)$). It is often convenient for the spin (and therefore spatial) orbitals to form an orthonormal set, such that

$$\langle \chi_i | \chi_j \rangle = \delta_{ij} \tag{E.1}$$

$$\langle \psi_i | \psi_j \rangle = \delta_{ij} \tag{E.2}$$

$$\langle \sigma_i | \sigma_j \rangle = \delta_{ij} \tag{E.3}$$

A Slater determinant (often simply described as a determinant) is an antisymmetrised wave-function of N electrons arranged in M orbitals

$$\begin{aligned} |\Phi\rangle &= \frac{1}{\sqrt{N!}} \begin{vmatrix} \chi_1(\mathbf{x}_1) & \dots & \chi_M(\mathbf{x}_1) \\ \vdots & \ddots & \vdots \\ \chi_1(\mathbf{x}_N) & \dots & \chi_M(\mathbf{x}_N) \end{vmatrix} \\ &= \frac{1}{\sqrt{N!}} \sum_{i=1}^{N!} (-1)^{p_i} \hat{P}_i \{\chi_1(\mathbf{x}_1)\chi_2(\mathbf{x}_2) \dots \chi_M(\mathbf{x}_N)\} \end{aligned} \tag{E.4}$$

where $\chi_i(\mathbf{x_1})$ denotes electron 1 occupying spin orbital i. $\hat{P}_i$ is an operator that generates the ith permutation of electrons 1, 2, ..., N (corresponding to switching rows of the determinant), and p_i is the number of row interchanges required to achieve a given electron permutation. For example, switching electrons 1 and 2 requires a single row switch, so $p_i = 1$ and the function takes a negative sign. This is the equivalent of saying that exchanging two electrons changes the sign of the wavefunction, such that the electrons described by this wavefunction are fermions. This determinant construction of the wavefunction ensures that the Pauli exclusion principle is obeyed – no two electrons may have the same quantum numbers (*e.g.*, electrons in the same spatial orbital may not have the same spin) simultaneously.

To be used in a calculation, for example with the Hartree Fock (HF) method, the wavefunction must be an eigenfunction of the electronic Hamiltionian $\hat{H}$, which is fulfilled when the wave-function is also an eigenfunction of the spin operator $\mathcal{S}^2$. Not all determinants fulfil this requirement, however we can form configuration state functions (CSFs) from linear combinations of determinants. For example, neither of the restricted singly-excited determinants of H_2

$$\begin{aligned} |\Psi_{\bar{1}}^{\bar{2}}\rangle &= |\psi_1(1)\alpha(1)\psi_2(2)\beta(2)\rangle \\ |\Psi_{1}^{2}\rangle &= |\psi_2(1)\alpha(1)\psi_1(2)\beta(2)\rangle \end{aligned} \tag{E.5}$$

are eigenfunctions of $\mathcal{S}^2$, but taking linear combinations (and normalising the resultant wave-functions) yields two CSFs which now have well-defined spin quantum numbers, one of which is a singlet and the other a triplet

$$\begin{aligned} |{}^1\Psi_{1}^{2}\rangle &= \frac{1}{\sqrt{2}}(|\Psi_{\bar{1}}^{\bar{2}}\rangle + |\Psi_{1}^{2}\rangle) \\ &= \frac{1}{\sqrt{2}}(\psi_1(1)\psi_2(2) + \psi_2(1)\psi_1(2)) \times (\alpha(1)\beta(2) - \beta(1)\alpha(2)) \end{aligned} \tag{E.6}$$

$$\begin{aligned} |{}^3\Psi_{1}^{2}\rangle &= \frac{1}{\sqrt{2}}(|\Psi_{\bar{1}}^{\bar{2}}\rangle - |\Psi_{1}^{2}\rangle) \\ &= \frac{1}{\sqrt{2}}(\psi_1(1)\psi_2(2) - \psi_2(1)\psi_1(2)) \times (\alpha(1)\beta(2) + \beta(1)\alpha(2)) \end{aligned} \tag{E.7}$$

The nomenclature for representing excitations follows the rule that the lower number is the spatial orbital being excited from, and the upper number is the orbital being excited to (in this case an electron is promoted from orbital 1 to orbital 2). Bars over numbers are used to represent the spin of the electron in that spatial orbital, and α and β represent up and down spin electrons, respectively.

A configuration, often confusingly used interchangeably with determinant, is an electronic state that may comprise several CSFs. For example, the excited triplet H_2 configuration $(\sigma_g)^1(\sigma_u)^1$ comprises the CSFs

$$|^3\Psi_{\bar{1}}^{2}\rangle = \frac{1}{\sqrt{2}}(\psi_1(1)\psi_2(2) - \psi_1(2)\psi_2(1))(\alpha(1)\alpha(2)) \tag{E.8}$$

$$|^3\Psi_{1}^{\bar{2}}\rangle = \frac{1}{\sqrt{2}}(\psi_1(1)\psi_2(2) - \psi_1(2)\psi_2(1))(\beta(1)\beta(2)) \tag{E.9}$$

$$|^3\Psi_{1}^{2}\rangle = \frac{1}{\sqrt{2}}(\psi_1(1)\psi_2(2) - \psi_2(1)\psi_1(2))(\alpha(1)\beta(2) + \beta(1)\alpha(2)) \tag{E.10}$$

In this Thesis we have made every attempt to be consistent with the terminology to avoid ambiguity.

Before moving on to electronic structure calculations, we will introduce the electronic Hamiltonian, $\hat{H}$ – an operator whose action on a wavefunction returns the energy of the state described by that wavefunction according to the equation

$$\hat{H}\Psi = E\Psi \tag{E.11}$$

This is the non-relativistic time-independent Schrödinger equation. The time-dependent Schrödinger equation will not be discussed here. The electronic Hamiltonian is defined as

$$\hat{H} = -\frac{1}{2}\sum_{i=1}^{N}\nabla_i^2 - \sum_{i=1}^{N}\sum_{A=1}^{M}\frac{Z_A}{r_{iA}} + \sum_{i=1}^{N}\sum_{j>i}^{N}\frac{1}{r_{ij}} \tag{E.12}$$

where the first term defines the electron kinetic energy, the second term defines the electron-nuclear Coulomb attraction, and the third term defines the electron-electron Coulomb repulsion. We have made the Born-Oppenheimer approximation, where the nuclei are assumed to move far more slowly than the electrons and therefore the nuclear kinetic energy is assumed to be zero, and the repulsion between nuclei is assumed to be a constant.

E.2 Hartree-Fock theory

Having introduced orbitals, determinants and the electronic Hamiltonian, we can now introduce a method with which to calculate the approximate energy of a many-electron system. Generally, exact calculations on many-electron wavefunctions are intractable, but we can make an approximation where the electrons are assumed to behave independently (the 'independent-electron' approximation, for example the Hartree Product wavefunction). Interactions between these electrons are then reintroduced, for example within Hartree-Fock (HF) theory where the wavefunction is required to be antisymmetric with respect to the exchange of electrons through the use of a Slater determinant.

The energy of each orbital within the HF wavefunction can be obtained with the Fock operator

$$f(1)|\chi_i\rangle = \mathcal{E}_a|\chi_i\rangle \tag{E.13}$$

$$f(1) = h(1) + v_{HF}(1) \tag{E.14}$$

$$h(1) = -\frac{1}{2}\nabla_1^2 - \sum_{A=1}^{M}\frac{Z_A}{r_{A1}} \tag{E.15}$$

$$v_{HF}(1) = \sum_{b}^{N}(\hat{J}_b(1) - \hat{K}_b(1)) \tag{E.16}$$

where we have introduced the one-electron operator $h(1)$, which calculates the kinetic energy of the electron and its attraction to each nucleus, and the two electron operators $\hat{J}_b(1)$ and $\hat{K}_b(1)$, where the index b denotes the interaction of electron 1 with each of the remaining $N-1$ electrons. $\hat{J}_b(1)$, the Coulomb operator, is defined as

$$\hat{J}_b(1) = \int d\mathbf{x}_2 |\chi_b(2)|^2 \frac{1}{r_{12}} \tag{E.17}$$

and represents the repulsion between electron 1 and the averaged position of electron 2. The second of the two-electron operators, the exchange operator $\hat{K}_b(1)$, is defined as

$$\hat{K}_b(1) = \int d\mathbf{x}_2 \chi_b^*(2) \frac{1}{r_{12}} \chi_a(2) \tag{E.18}$$

and has the effect of swapping (exchanging) electrons 1 and 2. This integral is positive, so the negative sign that accompanies it in $v_{HF}(1)$ lowers the total energy. While this effect has no simple classical explanation, we can interpret the lowering of energy based on exchange as a correction to the independent electron approximation: The Hartree Product allows electron 1 and electron 2 to be found in the same volume element regardless of their spin, violating the Pauli exclusion principle if their spins are the same. By antisymmetrising the wavefunction in HF theory, electrons of the same spin are necessarily found further apart (‘Fermi correlation’), so the Coulomb repulsion between these electrons decreases. This decrease in repulsion is provided by the exchange operator. We note that even with antisymmetrisation, it is still possible to find electrons 1 and 2 in the same volume element simultaneously if their spins are opposed – giving HF theory the moniker ‘uncorrelated’ (despite Fermi correlation being accounted for). Methods to correct for this lack of (Coulomb) correlation will be discussed in subsequent sections.

E.3 Electron correlation

In this Thesis, we examine the electronic structure of [1.1.1]propellane from first principles. Discussions about the importance of diradical character necessarily require an electronic structure method which is able to describe electron correlation, in particular static correlation. Static correlation arises from the (near-)degeneracy of occupied and unoccupied orbitals, the classic example being bond dissociation of minimal basis H_2. In this case, we have two orbitals (ψ_1 and ψ_2) corresponding to the gerade (bonding) and ungerade (antibonding) combinations of the two H 1s orbitals, respectively. At short H–H distances, the bonding combination is far lower in energy than the antibonding combination, but as the H–H bond stretches to infinity ψ_1 and ψ_2 become degenerate. While restricted (R)HF theory correctly describes H2 in the short H–H regime, at long H–H distances it incorrectly assigns both electrons to one of the H atoms (to give hydride and a proton). However, unrestricted (U)HF theory permits the correct asymptotic behaviour where one electron ends up on each atom, but cannot describe the whole PES for H_2. To fully describe the full spectrum of H–H bond distances, we need to consider not only the ground state HF wavefunction

$$|\Psi_0\rangle = |\psi_1\bar{\psi_1}\rangle = |1\bar{1}\rangle \tag{E.19}$$

but also the five excited determinants (four singles and one double) that correspond to all possible combinations of placing the electrons into both the bonding and antibonding orbitals

$$|\Psi_{1}^{2}\rangle = |\psi_2\bar{\psi}_1\rangle = |2\bar{1}\rangle \tag{E.20}$$

$$|\Psi_{\bar{1}}^{\bar{2}}\rangle = |\psi_1\bar{\psi}_2\rangle = |1\bar{2}\rangle \tag{E.21}$$

$$|\Psi_{\bar{1}}^{2}\rangle = |\psi_1\psi_2\rangle = |12\rangle \tag{E.22}$$

$$|\Psi_{1}^{\bar{2}}\rangle = |\psi_{\bar{2}}\psi_{\bar{1}}\rangle = |\bar{2}\bar{1}\rangle \tag{E.23}$$

$$|\Psi_{1\bar{1}}^{2\bar{2}}\rangle = |\psi_2\psi_{\bar{2}}\rangle = |2\bar{2}\rangle \tag{E.24}$$

These six determinants then sum to form the full configuration interaction (FCI) wavefunction

$$|\Phi_0\rangle = |\Psi_0\rangle + c_{1}^{2}|2\bar{1}\rangle + c_{\bar{1}}^{\bar{2}}|1\bar{2}\rangle + c_{\bar{1}}^{2}|12\rangle + c_{1}^{\bar{2}}|\overline{21}\rangle + c_{1\bar{1}}^{2\bar{2}}|2\bar{2}\rangle \tag{E.25}$$

The fourth and fifth terms are triplets, therefore they do not contribute to the ground state (singlet) wavefunction. The sixth term is a doubly excited determinant and is therefore a closed-shell singlet, so has a non-zero contribution to the ground state. The second and third terms are not eigenfunctions of the $\mathcal{S}^2$ operator, so we need take their linear combinations with a positive and negative sign to form spin-adapted CSFs

$$|^1\Psi_{1}^{2}\rangle = 2^{-1/2}(|2\bar{1}\rangle + |1\bar{2}\rangle) \tag{E.26}$$

$$|^3\Psi_{1}^{2}\rangle = 2^{-1/2}(|2\bar{1}\rangle - |1\bar{2}\rangle) \tag{E.27}$$

In the same manner as before, the triplet CSF (E.27) does not contribute to the ground state, so we are left with the FCI wavefunction

$$|\Phi_0\rangle = |\Psi_0\rangle + c_1^2|^1\Psi_1^2\rangle + c_{1\bar{1}}^{2\bar{2}}|2\bar{2}\rangle \tag{E.28}$$

The HF and doubly-excited determinants have gerade symmetry for H_2, but the singly-excited CSF has ungerade symmetry – the latter term therefore also does not contribute to the ground state wavefunction, leaving us with our final FCI wavefunction for the ground state of H_2 as

$$\begin{aligned}|\Phi_0\rangle &= |\Psi_0\rangle + c_{1\bar{1}}^{2\bar{2}}|2\bar{2}\rangle \\ &= |\Psi_0\rangle + c_{1\bar{1}}^{2\bar{2}}|\Psi_{1\bar{1}}^{2\bar{2}}\rangle\end{aligned} \tag{E.29}$$

The magnitude of the coefficient of the doubly-excited determinant is crucial to understand the importance of static correlation in the system, and therefore potential success or failure of a single-determinant method (such as MP2 or DFT). For a system well-described by a single determinant, for example H_2 at equilibrium, the coefficient will approach zero – in other words, the wavefunction is described almost entirely by placing two electrons in the bonding combination of H 1s orbitals. As the H–H bond is stretched, the doubly-excited coefficient will approach 1 (in this*intermediate normalised form*) – there is an equal contribution of the bonding and antibonding combinations of H 1s orbitals, allowing the system to smoothly dissociate from the bonded H_2 state into two H atoms, each with a single electron.

The H_2 problem allows us to introduce a second flavour of electron correlation: dynamic correlation. The RHF solution (STO-3G) for H_2 at its equilibrium geometry necessarily places two electrons in ψ_1, with a total energy (-1.11751 Ha) arising from nuclear-nuclear repulsion, electron kinetic energy, electron-nuclear attraction and electron-electron Coulomb repulsion. However, the FCI energy is -1.13685 Ha, almost 0.02 Ha lower than the RHF solution. The FCI wavefunction for this basis set is

$$|\Phi_0\rangle = 0.989|\Psi_0\rangle + 0.011|\Psi_{1\bar{1}}^{2\bar{2}}\rangle \tag{E.30}$$

While the weight of the HF determinant is almost 1, there is a small contribution from the doubly-excited determinant. This contribution, worth about 1% of the total energy, describes the correlated motion of the two electrons. In the mean-field HF theory, the first electron feels only the repulsion of the average position of the second, but in reality the position of the first electron will depend on the instantaneous position of the second. The result of this effect is that electron-electron repulsion is overestimated by HF theory, and the electrons are overlocalised in the regions between nuclei. Qualitatively, by mixing in the doubly-excited configuration to the wavefunction, *i.e.*, through population of the antibonding orbital, the two electrons can avoid each other, lowering the overall energy of the system.

While the introduction of an excited determinant might seem a counter-intuitive way of lowering the energy, it is the overall reduction of electron-electron repulsion that results in this effect. This can be seen by expressing the energy difference between FCI and RHF (= E_{corr}) in terms of one- and two-electron integrals

$$\begin{aligned} E_{corr} &= \Delta - \sqrt{\Delta^2 + K_{12}^2} \\ \Delta &= h_{22} - h_{11} + \frac{1}{2}(J_{22} - J_{11}) \end{aligned} \tag{E.31}$$

The Δ term, which includes the difference in kinetic energy and electron-nuclear attraction ($h_{22} - h_1 1$) and electron-electron Coulomb repulsion ($J_{22} - J11$) between the ground state and doubly-excited determinants, will be > 0 - in line with our classical expectation that mixing in an excited determinant would increase the total energy. However, the doubly-excited determinant in the FCI wavefunction introduces a K_{12} exchange contribution, allowing electron 1 to further interact with (*i.e.*, avoid) electron 2. In essence, Pauli repulsion is introduced by allowing an electron in determinant 1 to interact with an electron of the same spin in determinant 2 via the off-diagonal terms in the Hamiltonian matrix

$$\begin{aligned}\mathbf{H} &= \begin{pmatrix} \langle \Psi_0 | \hat{H} | \Psi_0 \rangle & \langle \Psi_0 | \hat{H} | \Psi_{1\bar{1}}^{2\bar{2}} \rangle \\ \langle \Psi_{1\bar{1}}^{2\bar{2}} | \hat{H} | \Psi_0 \rangle & \langle \Psi_{1\bar{1}}^{2\bar{2}} | \hat{H} | \Psi_{1\bar{1}}^{2\bar{2}} \rangle \end{pmatrix} \\ &= \begin{pmatrix} 2h_{11} + J_{11} & K_{12} \\ K_{12} & 2h_{22} + J_{22} \end{pmatrix}\end{aligned} \tag{E.32}$$

The energy-lowering exchange term (K_{12}) then slightly outweighs the energy-raising Δ term, leading to the overall lowering of the total energy through the inclusion of Coulomb correlation into the wavefunction.

E.4 Methods to approximate electron correlation

From our discussion of electron correlation based on the FCI wavefunction, it is clear that an artificial distinction has been made between static and dynamic correlation – for H_2, for example, a doubly-excited determinant is used to introduce both flavours of correlation. The only difference that can be drawn is from the contribution of this excited determinant: a small contribution (usually ≤ 0.02) indicates dynamic correlation, but a larger contribution (usually ≥ 0.02) can indicate static correlation. The way in which each type of correlation is treated computation-ally can vary.

Up to this point, the coefficients of all possible excitations in the FCI wavefunction have been optimised variationally to obtain the lowest energy for a given basis set. This approach quickly becomes intractable as the system size (number of electrons and orbitals) increases. Several methods have been developed to approximate the correlation energy, generally split into multi-configurational (multideterminental) and single-configuration (single-determinant) methods.

Truncated configuration interaction methods

The most natural approach for limiting the number of configurations to be calculated in the CI wavefunction is to limit the number of spin orbitals that may differ between the excited determinant and the ground state HF determinant – for example, by only including singly- and doubly-excited determinants (CISD, configuration interaction with single and double excitations) to include dynamic correlation. Starting from a single HF determinant, the CI coefficient for each excited determinant is variationally optimised. Unfortunately, any truncated CI approach suffers from a lack of size consistency, where the energy of a system with two monomers at infinite separation is not equal to the energy of the two monomers in isolation. This is most easily seen with the CID (configuration interaction with double excitations) description of two non-interacting molecules of H_2, where double excitations cannot occur within both molecules simultaneously (as this would correspond to a quadruple excitation). A consequence of this size-consistency problem is that truncated CI methods become progressively less accurate with increasing system size – for an infinite system of non-interacting molecules, the correlation energy tends to zero. Since these truncated CI methods are based upon a single HF determinant, if this determinant does not qualitatively describe the electronic structure, then the subsequent CI expansion will also be qualitatively wrong. These problems limit the applicability of truncated CI methods based on restrictions on the types of excitations.

Complete active space self-consistent field theory

An alternative approach to the truncation described in the previous section is to limit the size of the orbital subspace, and use the FCI wavefunction only for a small portion of the orbitals. Within the complete active space self-consistent field (CASSCF) method, the orbital space is divided into three subspaces: an inactive subspace (fully-occupied canonical HF orbitals), an active subspace (FCI treatment to give natural orbitals, see below) and a virtual subspace (unoccupied orbitals). Both the orbitals and FCI coefficients are variationally optimised with this method. CASSCF is particular useful when dealing with (near-)degeneracy that is confined to particular regions of the orbital space – for example to describe bond cleavage, or transition metal complexes with multiple low-lying excited states. However, selection of the active orbitals for the calculation can often seem quite non-systematic. As a general rule, orbitals with a natural occupancy less than 0.02 but greater than 1.98 can be diagnostic of static correlation, and should be included in the calculation; orbitals with occupancy of almost 2 or 0 can often be discarded from the active space. Additional problems with the use of CASSCF can occur due to poor convergence, sometimes requiring expensive brute-force approaches. It is also worth noting that while the active space is treated at the FCI level, orbitals outside this subspace are treated at the RHF level and are therefore void of Coulomb correlation. Truncated CI approaches (*e.g.*, MRCI, multireference configuration interaction), as well as perturbative or coupled cluster approaches (discussed in the following sections for single-reference methods), can be used on top of the CASSCF wavefunction to calculate the missing correlation for the entire system.

As mentioned above, natural orbitals are used for the active space in a CASSCF calculation. Before we can define a natural orbital, we must first introduce the one-electron reduced density matrix (1-RDM).[29] For a given N-electron system, the probability of finding electron 1 within the volume element $d\mathbf{x}_1$ at position $\mathbf{x}_1$, independent of electrons 2 to N, is given by the reduced density function

$$\rho(\mathbf{x}_1) = N \int d\mathbf{x}_2 \cdots d\mathbf{x}_N \Phi(\mathbf{x}_1, \ldots, \mathbf{x}_N)\Phi^*(\mathbf{x}_1, \ldots, \mathbf{x}_N) \tag{E.33}$$

Since the position of electron 1 is continuous, we can ask a more general question about the position of electron 1 by defining the 1-RDM

$$\gamma(\mathbf{x}_1, \mathbf{x}_1') = N \int d\mathbf{x}_2 \cdots \mathbf{x}_N \Phi(\mathbf{x}_1, \mathbf{x}_2, \ldots, \mathbf{x}_N)\Phi^*(\mathbf{x}_1, \mathbf{x}_2, \ldots, \mathbf{x}_N) \tag{E.34}$$

where the diagonal elements of the matrix (*i.e.*, $\mathbf{x}_i' = \mathbf{x}_i$) are $\rho(\mathbf{x}_1), \rho(\mathbf{x}_2), \ldots, \rho(\mathbf{x}_N)$ and the trace of the matrix is N. By integrating out electrons 2 to N, the remaining part of the right hand side of the equation describes only electron 1 and its position in space. Expanding the wavefunctions into products of spin orbitals allows us to form a discrete representation of the position of electron 1 in terms of the spin orbitals that it occupies (instead of its continuous position in space)

$$\gamma(\mathbf{x}_1, \mathbf{x}_1') = \sum_{ij} \chi_i(\mathbf{x}_1)\gamma_{ij}\chi_j^*(\mathbf{x}_1') \tag{E.35}$$

$$\gamma_{ij} = \int d\mathbf{x}_1 d\mathbf{x}_1' \chi_i^*(\mathbf{x}_1)\gamma(\mathbf{x}_1, \mathbf{x}_1')\chi_j(\mathbf{x}_1') \tag{E.36}$$

In essence, we are asking how much of electron 1 is found in a given orbital. From this definition, for a single HF determinant the 1-RDM will take the form

$$\gamma^{HF}(\mathbf{x}_1, \mathbf{x}_1') = \sum_i \chi_i(\mathbf{x}_1)\chi_i^*(\mathbf{x}_1') \tag{E.37}$$

with ones along the diagonal, since each electron occupies only a single orbital in a single determinant. This is not generally true for all wavefunctions – for example an excited configuration will partially populate χ_r at the expense of χ_a, resulting in off-diagonal terms in the γ_{ij} matrix. However, we can diagonalise any 1-RDM to form a set of transformed orbitals (natural orbitals) which are defined as the orbitals of maximum occupancy for a given system. The 1-RDM in the basis of natural orbitals is defined as

$$\gamma(\mathbf{x}_1, \mathbf{x}_1') = \sum_i \lambda_i \eta_i(\mathbf{x}_1)\eta_i^*(\mathbf{x}_1') \tag{E.38}$$

where λ_i is the occupancy number and η_i is the ith natural orbital. Natural orbitals have the useful property that they result in the most compact CI expansion for a given system, and is therefore the most rapidly convergent.[29]

Perturbation theory

If the leading determinant in the FCI wavefunction dominates over the weights of all other determinants in the expansion, we can use Rayleigh-Schrödinger perturbation theory. This approach, which brings in the dynamic correlation missing from HF theory, was first applied to N-electron systems by Møller and Plesset,[30] resulting in the common abbreviation MPn, where n is the order of the perturbation. A substantial advantage of MPn theory over truncated CI expansions is that it is exactly size consistent, and can therefore be easily applied to chemical reactions.

The underlying principle behind MPn theory is that the HF solution for a given system is al-most correct, such that only a small perturbation is required to achieve the exact result

$$\hat{H}|\Phi_i\rangle = (\hat{H}_0 + \lambda\hat{V})|\Phi_i\rangle = \mathcal{E}_i|\Phi_i\rangle \tag{E.39}$$

$$|\Phi_i\rangle = |\Psi_i^{(0)}\rangle + \lambda|\Psi_i^{(1)}\rangle + \lambda^2|\Psi_i^{(2)}\rangle + \cdots \tag{E.40}$$

$$\mathcal{E}_i = E_i^{(0)} + \lambda E_i^{(1)} + \lambda^2 E_i^{(2)} + \cdots \tag{E.41}$$

where $\hat{V}$ is the perturbation, the superscript number indicates the order of perturbation, and λ is an arbitrary ordering parameter to keep track of the order of perturbation. The aim is then to express the higher-order determinants and energies in terms of the perturbation, $\hat{V}$, and the unperturbed determinant, $|\Psi_i^{(0)}\rangle$. To calculate the correlation energy, E_{corr}, we can take the perturbation as

$$\hat{V} = \sum_{i<j} \frac{1}{r_{ij}} - \sum_i v^{HF}(i) \tag{E.42}$$

Using this perturbation, we obtain the zeroth, first and second order energies

$$E_0^{(0)} = \sum_a \epsilon_a \tag{E.43}$$

$$E_0^{(1)} = -\frac{1}{2}\sum_{ab}\langle ab||ab\rangle \tag{E.44}$$

$$E_0^{(2)} = \frac{1}{2}\sum_{abrs} \frac{|\langle ab||rs\rangle|^2}{\epsilon_a + \epsilon_b - \epsilon_r - \epsilon_s} \tag{E.45}$$

where ϵ_i is the HF orbital energy, a and b represent occupied orbitals, and r and s represent virtual orbitals. Since

$$E_{HF} = \sum_{a} \epsilon_a - \frac{1}{2} \sum_{ab} \langle ab || ab \rangle \tag{E.46}$$

the first correction to the HF energy comes from the second order perturbation, which includes double excitations.

In practise, MP2 (*i.e.*, truncating the MPn expansion at the second term) is the most commonly-employed perturbation method due to its relative inexpense compared with higher-order methods yet generally excellent performance. In fact, the MPn series does not necessarily improve upon the MP2 correlation energy for higher orders of n, since the series can oscillate and even diverge.[31] A significant limitation of any MPn method is the dependence of the correlation energy on the difference in orbital energies (*i.e.*, the $\epsilon_a + \epsilon_b - \epsilon_r - \epsilon_s$ denominator) – in cases of near-degeneracy, this term approaches zero causing the correlation energy to diverge. In any case, near-degeneracy would be expected to cause significant contributions from excited determinants in the FCI wavefunction, therefore the assumptions underlying the derivation of MPn-based approaches are no longer valid.

Coupled cluster theory

An attractive approach to estimating the correlation energy of a many-electron system is to calculate the correlation energy between pairs of electrons independently in the HF potential of the remaining electrons (Independent Electron Pair Approximation, IEPA).[32,33] This approach is reasonably accurate, and is size-consistent, but is not variational. It also has the distinct disadvantage that the correlation energy is not invariant under a unitary transform of degenerate molecular orbitals,[34] and interactions between excited pairs are neglected. To address these shortcomings, in particular the neglect of interactions between excited pairs, the Coupled Cluster (CC) approximation recovers the contribution from simultaneous double excitations through the inclusion of quadruple excitations into the wavefunction. To do this, we introduce a cluster operator, $\mathcal{T}$, where

$$
\begin{aligned}
|\Phi_0\rangle &= \exp(\mathcal{T})|\Psi_0\rangle && \text{(E.47)}\\
&= (1 + \mathcal{T} + \frac{1}{2!}\mathcal{T}^2 + \cdots)|\Psi_0\rangle && \text{(E.48)}\\
\mathcal{T} &= \mathcal{T}_1 + \mathcal{T}_2 + \mathcal{T}_3 + \cdots && \text{(E.49)}
\end{aligned}
$$

and the operator $\mathcal{T}_n$ results in

$$
\begin{aligned}
\mathcal{T}_1|\Psi_0\rangle &= \sum_{a,r} c_a^r|\Psi_a^r\rangle && \text{(E.50)}\\
\mathcal{T}_2|\Psi_0\rangle &= \sum_{\substack{a<b\\ r<s}} c_{ab}^{rs}|\Psi_{ab}^{rs}\rangle && \text{(E.51)}\\
\mathcal{T}_3|\Psi_0\rangle &= \sum_{\substack{a<b<c\\ r<s<t}} c_{abc}^{rst}|\Psi_{abc}^{rst}\rangle && \text{(E.52)}
\end{aligned}
$$

and so on – each operator results in the excitation indicated by the index. The strength of the coupled cluster approach comes from the power series implicit within the exponent, where for example

$$\mathcal{T}_2^2|\Psi_0\rangle = \sum_{\substack{a<b<c<d\\r<s<t<u}} c_{ab}^{rs}c_{cd}^{tu}|\Psi_{abcd}^{rstu}\rangle \tag{E.53}$$

From this equation we can see that coupled cluster up to second order connected excitations (CCSD) will include quadruple excitations via the product of double excitations.[35] As a result, coupled cluster theory is size extensive,[36] providing a significant advantage over any truncated CI approximation. For small molecules with up to tens of electrons, CCSDT (coupled cluster with connected single, double and triple excitations) can be employed, however the scaling of $\mathcal{O}(n^3N^5)$ (where n is the number of electrons and N the number of basis functions) severely limits the maximum system size possible to compute.[35] Molecules with tens of atoms can be approached with the CCSD method, which scales as $\mathcal{O}(n^2N^4)$,[35] however at a significant loss of accuracy. A compromise arose with the incorporation of perturbative triple excitations into the CCSD method [CCSD(T)] which scales as $\mathcal{O}(n^2N^4N_{it} + n^3N^4)$ (where N_{it} is the number of CC iterations),[37] now commonly referred to as the "gold standard" for molecular calculations.

Significant effort has been put into finding ways to make coupled cluster methods less computationally expensive. Progress has been made by capitalising on the idea that the correlation between electrons localised in different regions of a molecule will be negligible, leading to the use of localised orbitals to estimate which interactions between excited state configurations can be excluded from the calculation. In this Thesis, we make use of the domain-based local pair natural orbital (DLPNO) approximation, developed by Neese and co-workers.[21] As mentioned above, natural orbitals (NOs) diagonalise the 1-RDM and provide the most rapidly convergent CI expansion for a given system. Pair natural orbitals (PNOs) then define a set of NOs for each electron pair in turn, resulting in a set of orbitals which are non-orthogonal with other PNO sets.[21] Using a parameter to truncate the number of PNOs used for each electron pair, Neese and co-workers developed the local pair natural orbital (LPNO) approach, which was shown to be reasonably efficient and applicable to the CCSD method for systems not more than 100 atoms.[2] However, further savings were found to be possible by making use of local virtual orbitals, rather than the canonical (HF) virtual orbitals employed in the LPNO method. This DLPNO approximation makes use of projected atomic orbitals (PAOs) to define the local virtual orbital subspaces, where PAOs are found by projecting the atomic orbitals onto the canonical orbital space.[38] PNOs are then generated from these PAOs by first doing a local MP2 calculation in which off-diagonal terms are neglected, then constructing and diagonalising a 'pair density' matrix in which the interaction of each excited pair is included. This yields the PNOs and their occupation numbers, analogously to the process described for obtaining NOs from the 1-RDM. These PNOs are then used as the basis for the coupled cluster equations, leading to almost linear scaling. Three cut-offs are defined that limit the number of PAOs that contribute to each PNO (T_{CutMKN}), the number of electron pairs to consider for the CCSD iterations based on the estimated correlation energy from the local MP2 calculation ($T_{CutPairs}$), and the minimum population of the PNOs to be considered for the CCSD iterations (T_{CutPNO}). Judicious choice of these cut-offs allows the desired accuracy for a given system size to be tuned, depending on the types of interactions present in the system.[39]

F |

Linear regression worked example

F.1 Linear regression

The pK_as of five carboxylic acids, their Hammett σ_p constants, and their Swain-Lupton $\mathcal{F}$ (field) and $\mathcal{R}$ (resonance) parameters are shown in Table F.1.[40]

Table F.1: pKas of substituted carboxylic acids and physical organic parameters taken from Ref. [40].

Substituent	pK_a	σ_p	$\mathcal{F}$	$\mathcal{R}$
C_6H_5	4.20	0.0	0.03	0.0
$MeOC_6H_4$	4.47	–0.27	0.29	–0.56
ClC_6H_4	3.99	0.23	0.42	-0.19
$O_2NC_6H_4$	3.44	0.78	0.63	0.13
$Me_3N^+C_6H_4$	3.43	0.82	0.86	–0.04

Using (1.19), a linear equation can be set up between the dependent variable, pK_a, and the independent variable, σ_p

$$\mathrm{p}K_a = \beta_0 + \beta_1\sigma + \epsilon_i. \tag{F.1}$$

Using this equation, the data from Table F.1 sets up five simultaneous equations

$$4.2 = \beta_0 + \epsilon_1 \tag{F.2}$$

$$4.47 = \beta_0 - 0.27\beta_1 + \epsilon_2 \tag{F.3}$$

$$3.99 = \beta_0 + 0.23\beta_1 + \epsilon_3 \tag{F.4}$$

$$3.44 = \beta_0 + 0.78\beta_1 + \epsilon_4 \tag{F.5}$$

$$3.43 = \beta_0 + 0.82\beta_1 + \epsilon_5 \tag{F.6}$$

which, when rearranged and taken as the sum of squares using (1.21) gives the residual

$$SS_{res} = 5\beta_0^2 + 3.12\beta_0\beta_1 - 39.06\beta_0 + 1.4066\beta_1^2 - 10.4132\beta_1 + 77.1395. \tag{F.7}$$

Minimisation of this equation with reference to β_0 and β_1 in turn leads to values of $\beta_0 = 4.21$ and $\beta_1 = -0.964$, or

$$\mathrm{p}K_a = 4.21 - 0.964\sigma_p. \tag{F.8}$$

This result can be interpreted chemically: the negative value of β_1 indicates that an electron-donating group (*e.g.*, $MeOC_6H_4$) will increase the pK_a relative to phenyl, and an electron-withdrawing group (*e.g.*, $O_2NC_6H_4$) will decrease the pK_a. To determine the quality of this linear model, R^2 can be calculated from $SS_{res} = 0.0005$ and $SS_{tot} = 0.85532$ using (1.24) to obtain a value of 0.9994 – a very strong correlation. The MAE and RMSE, calculated using (1.25) and (1.26), are 0.008 and 0.010, respectively.

F.2 Multiple linear regression

The Swain-Lupton parameters $\mathcal{F}$ and $\mathcal{R}$ can be used as independent variables for an MLR model

$$\mathrm{p}K_a = \beta_0 + \beta_1\mathcal{F} + \beta_2\mathcal{R} + \epsilon_i \tag{F.9}$$

which leads to

$$\begin{align} 4.2 &= \beta_0 + 0.03\beta_1 + \epsilon_1 \tag{F.10}\\ 4.47 &= \beta_0 + 0.29\beta_1 - 0.56\beta_2 + \epsilon_2 \tag{F.11}\\ 3.99 &= \beta_0 + 0.42\beta_1 - 0.19\beta_2 + \epsilon_3 \tag{F.12}\\ 3.44 &= \beta_0 + 0.63\beta_1 + 0.13\beta_2 + \epsilon_4 \tag{F.13}\\ 3.43 &= \beta_0 + 0.86\beta_1 - 0.04\beta_2 + \epsilon_5. \tag{F.14} \end{align}$$

Rearranging and summing the square errors gives

$$\begin{split} SS_{res} = 5\beta_0^2 + 4.46\beta_0\beta_1 - 1.32\beta_0\beta_2 - 39.06\beta_0 + 1.3979\beta_1^2 - 0.3894\beta_1\beta_2 \\ -16.4302\beta_1 + 0.3682\beta_2^2 + 5.9026\beta_2 + 77.1395. \end{split} \tag{F.15}$$

which, when minimised and solved for β_0, β_1 and β_2, results in the linear model

$$\mathrm{p}K_a = 4.22 - 0.986\mathcal{F} - 0.979\mathcal{R}. \tag{F.16}$$

The values of β_0, β_1 and β_2 results in $SS_{res} = 0.0016$, and SS_{tot} is unchanged, leading to an R^2 value of 0.998, a MAE of 0.015, and an RMSE of 0.018. This model is again chemically interpretable – an inductively withdrawing group will lower the pK_a to the same extent as a mesomerically-withdrawing group, which makes sense since the π system of the carboxylate anion is not conjugated with that of the arene.

Appendix bibliography

(1) Neese, F. Software update: the ORCA program system, version 4.0. *Wiley Interdiscip. Rev. Comput. Mol. Sci.* **2017**, *8*, e1327.

(2) Neese, F.; Wennmohs, F.; Hansen, A.; Becker, U. Efficient, approximate and parallel Hartree–Fock and hybrid DFT calculations. A 'chain-of--spheres' algorithm for the Hartree–Fock exchange. *Chem. Phys.* **2009**, *356*, 98–109.

(3) Stoychev, G. L.; Auer, A. A.; Neese, F. Automatic Generation of Auxiliary Basis Sets. *J. Chem. Theory Comput.* **2017**, *13*, 554–562.

(4) Peterson, K. A. Systematically convergent basis sets with relativistic pseudopotentials. I. Correlation consistent basis sets for the post-d group 13–15 elements. *J. Chem. Phys.* **2003**, *119*, 11099–11112.

(5) Grimme, S. Supramolecular Binding Thermodynamics by Dispersion-Correected Density Functional Theory. *Chem. Eur. J.* **2012**, *18*, 9955–9964.

(6) Liakos, D. G.; Neese, F. Is It Possible To Obtain Coupled Cluster Quality Energies at near Density Functional Theory Cost? Domain-Based Local Pair Natural Orbital Coupled Cluster vs Modern Density Functional Theory. *J. Chem. Theory Comput.* **2015**, *11*, 4054–4063.

(7) Liakos, D. G.; Sparta, M.; Kesharwani, M. K.; Martin, J. M. L.; Neese, F. Exploring the Accuracy Limits of Local Pair Natural Orbital Coupled-Cluster Theory. *J. Chem. Theory Comput.* **2015**, *11*, 1525–1539.

(8) Grimme, S.; Antony, J.; Ehrlich, S.; Krieg, H. A consistent and accurate ab initio parametrization of density functional dispersion correction (DFT-D) for the 94 elements H-Pu. *J. Chem. Phys.* **2010**, *132*, 154104.

(9) Grimme, S.; Ehrlich, S.; Goerigk, L. Effect of the damping function in dispersion corrected density functional theory. *J. Comput. Chem.* **2011**, *32*, 1456–1465.

(10) Lin, Y.-S.; Li, G.-D.; Mao, S.-P.; Chai, J.-D. Long-Range Corrected Hybrid Density Functionals with Improved Dispersion Corrections. *J. Chem. Theory Comput.* **2012**, *9*, 263–272.

(11) Weigend, F.; Ahlrichs, R. Balanced basis sets of split valence, triple zeta valence and quadruple zeta valence quality for H to Rn: Design and assessment of accuracy. *Phys. Chem. Chem. Phys.* **2005**, *7*, 3297.

(12) Marenich, A. V.; Cramer, C. J.; Truhlar, D. G. Universal Solvation Model Based on Solute Electron Density and on a Continuum Model of the Solvent Defined by the Bulk Dielectric Constant and Atomic Surface Tensions. *J. Phys. Chem. B* **2009**, *113*, 6378–6396.

(13) PubChem Compound Summary for CID 8071, 1,2-Dimethoxyethane, Available at `https://pubchem.ncbi.nlm.nih.gov/compound/1_2-Dimethoxyethane` (2021/09/17).

(14) Karton, A.; Tarnopolsky, A.; Lamère, J.-F.; Schatz, G. C.; Martin, J. M. L. Highly Accurate First-Principles Benchmark Data Sets for the Parametrization and Validation of Density Functional and Other Approximate Methods. Derivation of a Robust, Generally Applicable, Double-Hybrid Functional for Thermochemistry and Thermochemical Kinetics. *J. Phys. Chem. A* **2008**, *112*, 12868–12886.

(15) Sterling, A. J.; Dürr, A. B.; Smith, R. C.; Anderson, E. A.; Duarte, F. Rationalizing the diverse reactivity of [1.1.1]propellane through σ–π-delocalization. *Chem. Sci.* **2020**, *11*, 4895–4903.

(16) Young, T. duartegroup/otherm: Major symmetry improvements, version 1.0.0 beta, 2020.

(17) Bannwarth, C.; Ehlert, S.; Grimme, S. GFN2-xTB—An Accurate and Broadly Parametrized Self-Consistent Tight-Binding Quantum Chemical Method with Multipole Electrostatics and Density-Dependent Dispersion Contributions. *J. Chem. Theory Comput.* **2019**, *15*, 1652–1671.

(18) Young, T. A.; Silcock, J. J.; Sterling, A. J.; Duarte, F. autodE: Automated Calculation of Reaction Energy Profiles— Application to Organic and Organometallic Reactions. *Angew. Chem. Int. Ed.* **2020**, *60*, 4266–4274.

(19) Bickelhaupt, F. M.; Houk, K. N. Analyzing Reaction Rates with the Distortion/Interaction-Activation Strain Model. *Angew. Chem. Int. Ed.* **2017**, *56*, 10070–10086.

(20) Lu, T.; Chen, F. Multiwfn: A multifunctional wavefunction analyzer. *J. Comput. Chem.* **2011**, *33*, 580–592.

(21) Riplinger, C.; Neese, F. An efficient and near linear scaling pair natural orbital based local coupled cluster method. *J. Chem. Phys.* **2013**, *138*, 034106.

(22) Grimme, S. Semiempirical hybrid density functional with perturbative second-order correlation. *J. Chem. Phys.* **2006**, *124*, 034108.

(23) Duchesnay, É. Scikit-learn: Machine Learning in Python. *J. Mach. Learn. Res.* **2011**, *12*, 2825–2830.

(24) Hunter, J. D. Matplotlib: A 2D Graphics Environment. *Comput. Sci. Eng.* **2007**, *9*, 90–95.

(25) Wolk, J. L.; Hoz, T.; Basch, H.; Hoz, S. Quantification of the Various Contributors to Rate Enhancement in Nucleophilic Strain Releasing Reactions. *J. Org. Chem.* **2001**, *66*, 915–918.

(26) Wolk, J. L.; Sprecher, M.; Basch, H.; Hoz, S. Relative reactivity of three and four membered rings – the absence of charge effect. *Org. Biomol. Chem.* **2004**, *2*, 1065.

(27) Rablen, P. R. A Procedure for Computing Hydrocarbon Strain Energies Using Computational Group Equivalents, with Application to 66 Molecules. *Chemistry* **2020**, *2*, 347–360.

(28) Szabo, A.; Ostlund, N. S., *Modern quantum chemistry*; Dover Publications: Mineola, N.Y., 1996.

(29) Löwdin, P.-O. Quantum Theory of Many-Particle Systems. I. Physical Interpretations by Means of Density Matrices, Natural Spin-Orbitals, and Convergence Problems in the Method of Configurational Interaction. *Phys. Rev.* **1955**, *97*, 1474–1489.

(30) Møller, C.; Plesset, M. S. Note on an Approximation Treatment for Many-Electron Systems. *Phys. Rev.* **1934**, *46*, 618–622.

(31) Jensen, F., *Introduction to Computational Chemistry*; John Wiley & Sons, Inc.: Hoboken, NJ, USA, 2006.

(32) Sinanoğlu, O. In *Adv. Chem. Phys.* John Wiley & Sons, Inc.: 1964, pp 315–412.

(33) Nesbet, R. K. In *Adv. Chem. Phys.* John Wiley & Sons, Inc.: 1965, pp 321–363.

(34) Bender, C.; Davidson, E. Unitary transformations and pair energies. *Chem. Phys. Lett.* **1969**, *3*, 33–34.

(35) Bartlett, R. J.; Musiał, M. Coupled-cluster theory in quantum chemistry. *Rev. Mod. Phys.* **2007**, *79*, 291–352.

(36) Bartlett, R. J.; Purvis, G. D. Many-body perturbation theory, coupled-pair many-electron theory, and the importance of quadruple excitations for the correlation problem. *Int. J. Quantum Chem.* **1978**, *14*, 561–581.

(37) Raghavachari, K.; Trucks, G. W.; Pople, J. A.; Head-Gordon, M. A fifth-order perturbation comparison of electron correlation theories. *Chem. Phys. Lett.* **1989**, *157*, 479–483.

(38) Krause, C.; Werner, H.-J. Comparison of explicitly correlated local coupled-cluster methods with various choices of virtual orbitals. *Phys. Chem. Chem. Phys.* **2012**, *14*, 7591.

(39) Liakos, D. G.; Sparta, M.; Kesharwani, M. K.; Martin, J. M. L.; Neese, F. Exploring the Accuracy Limits of Local Pair Natural Orbital Coupled-Cluster Theory. *J. Chem. Theory Comput.* **2015**, *11*, 1525–1539.

(40) Hansch, C.; Leo, A.; Taft, R. W. A survey of Hammett substituent constants and resonance and field parameters. *Chem. Rev.* **1991**, *91*, 165–195.